Synthesis, Characterization and Energy Applications of Supported Mixed-Metal Oxides

QUAID-I-AZAM UNIVERSITY

ISLAMABAD

Submitted

By

Irsa Tariq

Department of Chemistry

Quaid-i-Azam University

Islamabad, Pakistan

2024

Synthesis, Characterization and Energy Applications of Supported Mixed-Metal Oxides

A dissertation submitted to the Department of Chemistry,

Quaid-I-Azam University, Islamabad, Pakistan, in partial fulfilment of

the requirements for the degree of

Doctor of Philosophy

In

Inorganic/Analytical Chemistry

By

Irsa Tariq

Supervised by

Dr. Ali Haider

Department of Chemistry
Quaid-i-Azam University
Islamabad, Pakistan

2024

بسم الله الرحمن الرحيم

Dedicated to

"My Beloved Friend

Sania Parveen (Late)"

List of Publications

1. Tariq I, Asghar M A, Ali A, Badshah A, Abbas S M, Iqbal W, Zubair M, Haider A, Zaman S, (2022) Surface reconstruction of cobalt-based polyoxometalate and CNT fiber composite for efficient oxygen evolution reaction. *Catalysts*, *12*(10), 1242.
2. Tariq I, Ali A, Haider A, Iqbal W, Asghar M A, Badshah A, Mansoor M A, Nisar T, Wagner V, Abbas S M, Talat R, (2024) Nickel-Foam-and Carbon-Nanotubes-Fiber-Supported Bismuth Oxide/Nickel Oxide Composite; Highly Active and Stable Bifunctional Electrocatalysts for Water Splitting in Neutral and Alkaline Media. *Energy Technology*, 2301504.

FOREIGN EXAMINERS

This dissertation entitled "*Synthesis, Characterization and Energy Applications of Supported Mixed-Metal Oxides*" by *Miss Irsa Tariq*, Department of Chemistry, Quaid-i-Azam University, Islamabad, Pakistan, has been evaluated by following panel of foreign examiners and adjudged suitable for the award of PhD degree in Analytical/Inorganic Chemistry.

1. **Emeritus Prof. Dr. Guenter Grampp**

   Institute of Physical and Theoretical Chemistry

   Graz University of Technology, Austria.

   Email: grampp@tugraz.at

2. **Prof. Dr. Janusz Ryczkowski**

   Faculty of Chemistry

   Institute of Chemical Sciences, Department of Chemical Technology

   Maria Curie-Sklodowska University, Lublin, Poland.

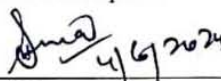   E-mail: janusz.ryczkowski@mail.umcs.pl

DECLARATION

This is to certify that this dissertation entitled *"Synthesis, Characterization and Energy Applications of Supported Mixed-Metal Oxides"* submitted by *Ms. Irsa Tariq* , is accepted in its present form by the Department of Chemistry, Quaid-i-Azam University, Islamabad, Pakistan, as satisfying the partial requirement for the award of degree of *Doctor of Philosophy in Inorganic/Analytical Chemistry.*
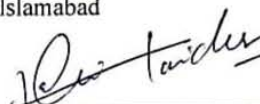
External Examiner (I):

Dr. Nasir Khalid
Deputy Chief Scientist (R)
H.No. 157, Ayub Khan Evenue Ext.
Chaklala Scheme III Rawalpindi

External Examiner (II):

Dr. Farhat Huma
Deputy Chief Manager (DCM), NESCOM,
Plot No. 94, H-11/4
Islamabad

Supervisor :

Dr. Ali Haider
Department of Chemistry
Quaid-i-Azam University
Islamabad.

Head of Section:

Prof. Dr. Syed Munir Hussain Shah
Department of Chemistry
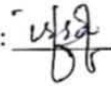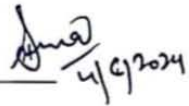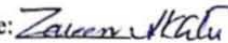Quaid-i-Azam University
Islamabad.

Chairman:

Prof. Dr. Mrs. Zareen Akhter
Department of Chemistry
Quaid-i-Azam University
Islamabad.

Certificate of Approval

This is to certify that the research work presented in this thesis, entitled **"Synthesis, Characterization and Energy Applications of Supported Mixed-Metal Oxides"** was conducted by **Ms. Irsa Tariq** under the supervision of **Dr. Ali Haider**

No part of this thesis has been submitted any where else for any other degree. This thesis, is submitted to the **Departme nt of Chemistry Quaid-i-Azam University Islamabad** in partial fulfillment of the requirements for the Doctor of Philosophy in Field of **Inorganic/Analytical Chemistry, Department of Chemistry, Quaid-i-Azam University, Islamabad.**

Student Name   Ms. Irsa Tariq   Signature: _____

Examination Committee:

1. External Examiner: **Dr. Nasir Khalid**   Signature: _____
Deputy Chief Scientist (R)
H.no. 157, Ayub Khan Evenue Ext,
Chaklala Scheme III Rawalpindi

2. External Examiner: **Dr. Farhat Huma**   Signature: _____ 4/6/2024
Deputy Chief Manager (DCM), NESCOM,
Plot No. 94 , H-11/4,
Islamabad

3. Internal Examiner: **Prof. Dr. Syed Munir H. Shah**   Signature: _____
Department of Chemistry
Quaid-i-Azam University
Islamabad.

Supervisor: **Dr. Ali Haider**   Signature: _____

Head of Department: **Prof. Dr. Zareen Akhter**   Signature: _____

AUTHOR'S DECLARATION

I, **Ms. Irsa Tariq** hereby state that my Ph.D. thesis titled "**Synthesis, Characterization and Energy Applications of Supported Mixed-Metal Oxides**" is my own work and has not been submitted previously by me for taking any degree from this University (Quaid-i-Azam University Islamabad) or anywhere else in the country/world.

At anytime if my statement is found to be incorrect even after my Graduation the University has the right to withdraw my Ph.D. degree.

Name of student: **Ms. Irsa Tariq**

PLAGIARISM UNDERTAKING

I solemnly declare that, the research work presented in the thesis titled **"Synthesis, Characterization and Energy Applications of Supported Mixed-Metal Oxides"** is solely my research work with no significant contribution from any other person. Small contribution/help wherever taken has been duly acknowledged and that complete thesis has been written by me.

I understand the zero tolerance policy of the HEC and **Quaid-i-Azam University Islamabad** towards plagiarism. Therefore, I as an Author of the above titled thesis declare that no portion of my thesis has been plagiarized and any material used as reference is properly referred/cited.

I undertake that if I am found guilty of any formal plagiarism in the above titled thesis even after award of Ph.D. degree, the university reserves the rights to withdraw/revoke my Ph.D. degree and that HEC and the University has the right to publish my name on the HEC/University website on which names of students are placed who submitted plagiarized thesis.

Student/Author Signature: _____

Name: **Ms. Irsa Tariq**

Acknowledgements

Table of Contents

Chapter-2   Experimental   46

List of Tables

List of Figures

List of Abbreviations

Abbreviation	Description
ASTM	American Society for Testing and Materials
BET	Brunauer-Emmett-Teller
BJH	Barrett-Joyner-Halenda
C_{dl}	Double Layer Capacitance
CNTF	Carbon nanotube Fiber
CTAB	Cetyl Trimethyl Ammonium Bromide
CV	Cyclic Voltammetry
D_{avg}	Crystallite Size
DFT	Density Functional Theory
EASAC	European Academy Science Advisory Council
ECSA	Electrochemical Surface Area
EDX	Energy Dispersive X-ray
EIS	Electrochemical Impedance Spectroscopy
ELSD	Evaporative Light Scattering Detection
EMA	Engine Manufacturing Association
ε_m	Micro Strain
FAAE	Fatty Acid Alkyl Ester
FAME	Fatty Acid Methyl Ester
FE	Faradaic Efficiency
FFAs	Free Fatty Acid
FT-IR	Fourier Transform Infrared
FWHM	Full Width Half Maxima
GC	Gas Chromatography
HER	Hydrogen Evolution Reaction
HPLC	High-Performance Liquid Chromatography
IPPS	Independent Power Plant
j	Current Density

KESC	Karachi Electric Supply Company
LSV	Linear Sweep Voltammogram
MCM-41	Mobil Composition of Matter
η	Overpotential
NiF	Nickel Foam
NMR	Nuclear Magnetic Resonance
OECD	Organisation for Economic Cooperation and Development
OER	Oxygen Evolution Reaction
PBS	Phosphate Buffered Solution
PBSC	Layered Perovskite $PrBa_{0.5}Sr_{0.5}Co_2O_{5+\delta}$
PEM	Proton Exchange Membrane
POMs	Polyoxometalates
PV	Photovoltaic
PXRD	Powder X-ray Diffraction
R_{ct}	Charge Transfer Resistance
R_s	Solution Resistance
RDS	Rate Determining Step
RF	Roughness Factor
RHE	Reversible Hydrogen Electrode
δ_D	Dislocation Density
SBA-15	Santa Barbara Amorphous
SEM	Scanning Electron Microscopy
TEOS	Tetra Ethyl Ortho Silicate
TG	Triglycerides
TMDs	Transition Metal Disulphides
UHV	Ultra-High Vacuum
WAPDA	Water and Power Development Authority
XPS	X-ray Photoelectron Spectroscopy
XRD	X-ray Diffraction

Abstract

The researchers are continuously investigating sustainable energy sources because of the significant rise in the usage of fossil fuels and the associated environmental risks caused by greenhouse gases. Hydrogen and biodiesel are among the sustainable fuel routes to encounter rapidly growing energy demands. Noble metal-based catalysts have so far been developed as state-of-the-art materials for hydrogen production while strong acids/bases are used for biodiesel production from different feedstocks. However, the high cost of noble metals and the corrosion/soap formation by strong acids/bases limit the practical applications of these catalysts. This research work focuses on the synthesis of environmentally friendly, cost effective and stable mixed-metal oxides over different porous materials as catalysts for water splitting and biofuel production applications. For the water splitting application, bifunctional composites based on post transition-metal oxide (Bi_2O_3) and 3d-transition metal oxides (Ni, Co, Fe, Mn) were synthesized and characterized through multitude analytical techniques including powder X-ray diffraction analysis (PXRD), scanning electron microscopy coupled energy dispersive X-ray analysis (SEM/EDX) and X-ray photoelectron spectroscopy (XPS). Composites were supported on nickel foam (NiF) and carbon nanotube fiber (CNTF) as electrode materials for oxygen evolution reaction (OER) in basic medium (1M KOH) while OER/hydrogen evolution reaction (HER) in neutral (1M PBS) medium. The electrochemical OER results revealed that Bi_2O_3/NiO-CNTF based electrodes outperformed in 1M KOH (467 mV@150 mA/cm^2) compared to other NiF and CNTF based fabricated electrodes. Similarly, for OER and HER in 1M PBS, Bi_2O_3/NiO-CNTF also outperformed (164 mV@20 mA/cm^2 and 268 mV@50 mA/cm^2, respectively) than the other fabricated electrodes. Keeping in view the performance of mixed metal oxides, three different transition metal-based polyoxometalates (POMs) were also synthesized and fabricated on the surface of CNTF. The electrochemical water oxidation activity in 1M KOH revealed that Ni based POM was more efficient (260 mV@10 mA/cm^2) than other synthesized analogues. For biodiesel production, bifunctional catalysts based on tungsten oxide (WO_3) over mesoporous material MCM-41 impregnated with alkaline earth metal (Mg, Ca, Sr, Ba) oxides were synthesized and characterized through PXRD, SEM-EDX and Brunauer-Emmett-Teller (BET) and Barrett-Joyner-Halenda (BJH) surface area, pore size and volume analysis. These composites were tested for biodiesel production using corn and waste cooking oil as feedstocks. The results revealed that

strontium-based composite was an efficient bifunctional (esterification/trans-esterification simultaneously) catalyst for biodiesel production with 96% and 93% yield from corn oil and waste cooking oil, respectively. Through ^{1}H-NMR spectroscopy, the obtained biodiesel was also characterized.

Chapter-1   Introduction

1.1. Background

To sustain our quality of living, energy specifically electric energy is essential. Human activity used 606.7×10^{18} J of energy globally in 2015. By 2040, it is predicted that demand will have increased by 28% to 776.5×10^{18} J [1]. As anticipated, most of this rise will be attributed to the fast-developing nations known as non-OECD that are in dire need of energy resources to fuel their economies. The requirements of China and India will account for more than half of this rise. By thorough analysis of Pakistan, it is seen that with 241.49 million people, Pakistan's total area is 881,913 km^2. Pakistan generated 87.3 TWh of power as of 2019. By 2023, total installed capacity of electricity was 41,557 MW and consumption was 89,361 GWh. Pakistan is experiencing a serious energy crisis, as shown by the two major facts: firstly, in Pakistan, the production of electricity in 2021 was mostly reliant on the use of fossil fuels, specifically oil and gas, accounting for 64.1% of resource consumption. Secondly, hydropower plants accounted for 24.7% of power production, nuclear power plants for 8.8%, and renewable energy for only 3.9%. It is imperative to devise a plan of action to get out of the current crisis and set a specific objective while keeping in mind the world's declining supply of fossil fuels and the enormous costs associated with importing them. Pakistan's collapsing economy is heavily impacted by the fossil fuel import, which accounts for 60% of its reserves. Fossil fuel consumption is a key contributor to global warming and poses a serious threat to the environment and humans because it produces CO_2 continually. However, by turning CO_2 into practical industrial products or investigating renewable resource sources, the threat can be reduced. So, in a nutshell, alternative energy resources (wind, solar, hydel, vegetable oils and biogas) may be the best choice available given the current circumstances, considering factors like energy security, climate change, sustainable energy supplies, and economic concerns [2].

By establishing different renewable sources plants across the nation, Pakistan's Ministry of Energy and other relevant departments, including the Pakistan WAPDA, KESC, and IPPS are organising and carrying out several renewable energy projects. The current energy resources are being converted from thermal plants (fossil fuels) to renewable energy resources to produce clean energy at a low cost [3]. This change in renewable energy technologies will result in a reduction or

elimination of the primary energy source. There will also be favourable outcomes for the environment in country.

1.2. Different Energy Storage and Conversion Technologies

Commonly, there are four ways that energy can be stored: physically, thermally, in batteries and chemically, [4]. The first choice alludes to pumped hydroelectric storage, which is arguably the oldest large-scale energy storage technology still in use today. The fundamentals of this technology are rather straightforward: using electricity to power turbines, water can be moved upward from a downward reservoir to an upward one, where it is kept in reserve as potential energy. To recover the electricity, the water must be discharged back into the downward reservoir. This releases the potential energy, which is then transformed into kinetic energy and utilised to rotate the turbines in the opposite direction, producing electricity. Sadly, this method would not work well with the sun's daily cycle of energy production, it is not feasible for us to fill and empty large water reservoirs on a regular basis. However, that is outside the purview of this conversation. It could be used as a long-drawn energy storehouse system, serving as a standby to supply electricity in case of an unplanned, urgent need.

Secondly, Thermal storage which is mostly known as Solar Thermal Technology, heats water or other fluids by using sunlight [5]. Small-scale applications include heating a home and providing hot water, but larger structures and even industries, where vapour and heat are needed for numerous operations, might benefit from its utilisation. This is a straightforward and practical solution that, if properly incorporated into the structures, may significantly reduce the amount of fossil fuels used, as it can potentially replace natural gas.

Batteries are still another choice. Although batteries are widely available these days, they are not the ideal means of storing the extra energy generated by solar or wind farms. Their low energy density, which applies to both volume and weight, is the primary cause of this. For small electronics like laptops or cell phones, low battery energy densities are not a huge barrier; but, for larger devices like electric cars, they could be a problem. Additionally, constant charge and discharge gradually erodes a battery's constituent parts, resulting in a persistent decline in storage capacity and, consequently, limited durability. These factors, along with their high cost, make it difficult to recoup their investment over the course of a solar system's normal lifetime.

The storage of energy as chemical bonds is another choice which is very useful in this century. In this instance, the reserved energy is in the kind of chemical bonds, which, when needed, can be selectively broken to liberate energy. In this type of energy storage technology, there are two common sources: water and unsaturated fats. By discussing first, in our search for energy, water is a very full of promise resource that is available everywhere in the world. [5]. It can be broken down into oxygen molecules, electrons, and green protons, which, even at the industrial level, can be used in various redox processes to produce chemical compounds. Even more encouragingly, the protons generated can be converted to molecules of hydrogen (H_2), which is seen to be a good chemical solution to fulfil future energy demands. There are some reasons for this i.e., higher energy density, sustainability, affordability, and clean nature. Of all the fuels, this lightest element has the largest energy content. Unlike fuels based on carbon, when it burns, the only product that emerges from the exhaust is water; no CO_2 is released. Conventionally, there are multiple methods to split it: Firstly, Thermal splitting at temperatures in the range between 2000 to 2500°C. Secondly, Thermochemically water splitting by the chemical cycle as a basis. Lastly, Photo-biological water splitting by using cyanobacteria or green algae.

However, due to several factors including the need for a high temperature, the materials' restricted compatibility, and particularly the biological water splitting process's sluggish conversion efficiency, none of the above-mentioned technologies are economically feasible. Consequently, electrochemical, and photo-electrochemically water splitting is presently the most popular and advanced path to a solar-assisted H_2 based economy. However, huge, highly efficient electrolyzers still require a lot of work to install, and a significant cost scaling down is practically required to be a competitor for available energy sources.

Secondly, unsaturated fats (Vegetable and animal fats) are sustainable biological sources used to make biodiesel, a substituted fuel for diesel engines. The reason is its low emission profiles, biodegradable nature, and nontoxicity, it is advantageous for the environment. Rudolf Diesel had done experiment by using vegetable oil as fuel for engine a century ago [6]. Fuel-suitable crude oil fractions were refined when cheap petroleum became available, and diesel engines and fuels evolved concurrently. In the 1930s and 1940s, vegetable oils were occasionally used as diesel fuels, although usually only in emergency situations. Recent, price rises for crude oil, depletion of fossil fuel reserves, and environmental concerns have brought vegetable and animal fats back into the

3

spotlight as fuel sources for biodiesel. Petroleum use that doesn't stop will worsen local air pollution and exacerbate the effects of CO_2 induced global warming. Biodiesel fuel can lower the number of pollutants and potential or probable carcinogens in a certain situation, such as the discharge of pollutants in underground mines.

1.3. Electrochemical Water Splitting

Through the process of water splitting, hydrogen can be produced directly from the breakdown of water into its constituent parts. The energy needed for water splitting is 237 kJ/mol under standard conditions to split a H-O-H single bond into H_2 and O_2. Moreover, the supply of energy can be provided through two ways i.e., electrochemically, or photochemically also known as electrocatalysis or photocatalysis. Semiconducting materials mimic the naturally occurring photosystem (II) to be used in photocatalysis as energy converters and light harvesters. After being exposed to radiation, the valence band electrons of photo-catalysts are energised to migrate into the conduction-band, where they form pairs of electron-hole, or also known as excitons. In this energy conversion procedure, H_2 generates by employing solar-fuel devices, such as PV materials, PEM, oxidation, and reduction catalysts [7]. Nonetheless, it can be divided into wired and wireless configurations architecturally. In a wireless setup (figure 1.1a) [8], when exposed to direct sunlight, photovoltaic cells and other semiconducting materials trap electrons and holes at opposing poles, which facilitate oxidation and reduction reactions at the catalyst-electrolyte interface. The electrodes in the wired version, on the other hand, have external connection through conducting wire and internal separation by PEM (figure 1.1b). Once the sunlight is caught, the water oxidises at the hole, and electrons travelling to the negative electrode i.e., cathode via an external circuit for the sake of complete the cycle. Direct solar energy collecting and hydrogen storage at the individual electrodes are made possible by both designs. These approaches, while desired and possessing unique benefits and chemistry, are not part of this thesis. Electrochemical water splitting module and their prospects will be our primary areas of study.
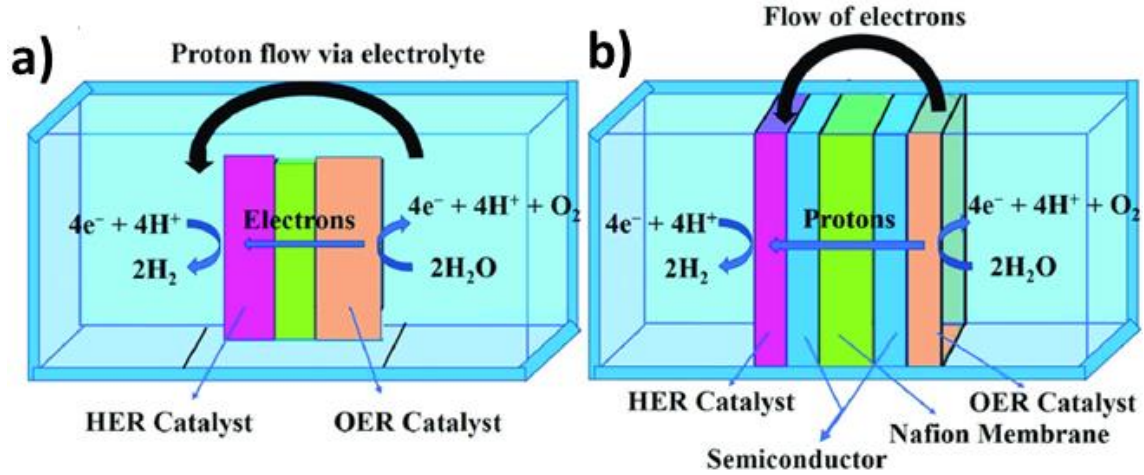
Figure 1.1. Artificial photosynthesis technology: (a) wireless presentation and (b) wired configuration for converting solar energy into hydrogen processes [8].

Basically, the electrolytic cell consists of three components i.e., cathode, anode, and electrolyte, which was initially suggested in 1789 [9]. The overall reaction happening in water splitting is.

$$2H_2O(l) \rightarrow 2H_2(g) + O_2(g) \qquad \text{Eq. 1}$$

This process follows the first law of thermodynamics and thermodynamic potentials. Water electrolysis is typically performed in a two-electrode system i.e., cathode and anode experiencing HER and OER, respectively, as seen in Figure (1.1).

The standard electrode voltage needed to calculate the half-cell reactions occurring at the cathode (HER) and anode (OER) can be represented using the Nernst-equation,

Oxidation reaction at anode, OER

$$2H_2O(l) \rightarrow 4e^- + 4H^+(aq) + O_2(g) \quad E°=1.23 \text{ V vs. RHE} \qquad \text{Eq. 2}$$
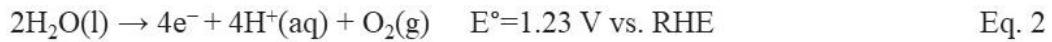
$$E = E° + 0.059/4 \log [H^+]^4$$
$$= E° + 0.059*\log[H^+] = 1.23 + 0.059*pH \qquad \text{Eq. 3}$$

Reduction reaction at cathode, HER

$$4e^- + 4H^+(aq) \rightarrow 2H_2(g) \qquad E° = 0.00 \text{ V vs. RHE} \qquad \text{Eq. 4}$$
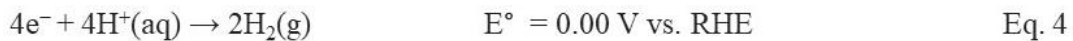
$$E = E° + 0.059/2 \log [H^+]^2$$
$$= E° + 0.059*\log[H^+] = 0.00 + 0.059*pH \qquad \text{Eq. 5}$$

From the above-mentioned equations, it is noted that the whole water splitting process can be completed by supplying at the minimum thermodynamic-potential of 1.23 V versus RHE in both

the energy-intensive and highly thermodynamically demanding OER and HER processes. So, for water splitting, the applied voltage should be greater than 1.23 V which is basically called overpotential (explained in 1.3.2.1 part).

Furthermore, Notably, the reaction media's pH has some substantial effects on the applied cell potential (Figure 1.2). The parameters of pH are bottom-line to determine the potential with potientiostat for half-cell reactions, even though they often cancel one another in the water splitting process. Usually, we measure or normalise the potential against the "RHE" by using Nernst equation ($E_{RHE} = E_{Ag/AgCl} + 0.059*pH$). In this equation, $E_{Ag/AgCl}$ is the electrode potential of silver electrode. With the use of this equation, we can directly evaluate the redox potential for the associated Faradaic reaction and eliminate the pH component. The range of the applied voltage can be systematically decreased or increased by adjusting the pH of the reaction medium, as shown in Figure 1.2 [10]. More specifically, the spike of minus 59.2 mV/pH in the applied cell voltage while raising the pH level by 1° is linked to the slope of the applied voltage vs. pH plot throughout the overall pH i.e., from 0-14 range [11].
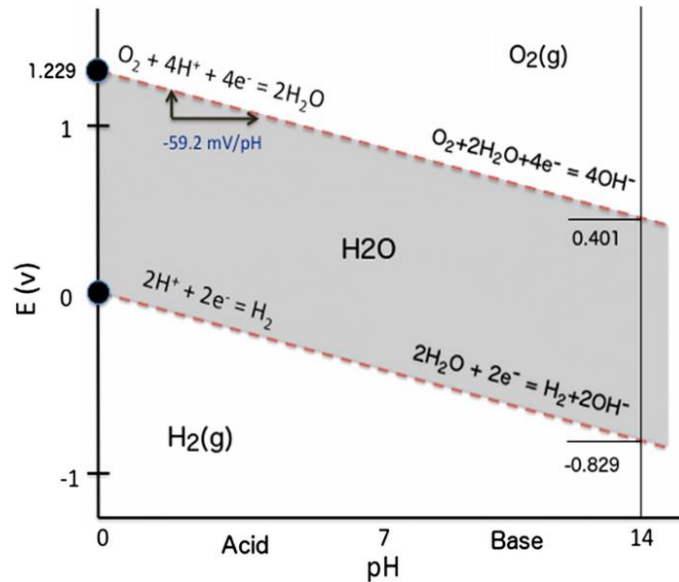
Figure 1.2. Pourbaix diagram for electrochemical water half-cell reaction in saturated media [10]

1.3.1. Hydrogen Evolution Reaction (HER)

The HER is a 2-electron transfer mechanism that produces a single H_2 molecule. HER can be performed in a wide range of pH. However, it is more favourable in acidic media as it has excessive

protons which promote this reaction. In neutral and alkaline media, HER can also be favourable. Basically, two mechanistic steps involved in the HER i.e., Volmer reaction, Heyrovsky or Tafel step. Figure 1.3a shows the HER mechanism in acidic and alkaline medium [12]. It is notable to mention here that in acidic media, the protonation source is H_3O^+, while in basic and neutral media, the source of proton is water molecules. In all medias, first step (Volmer reaction) is common which is hydrogen adsorption H_{ads} on the surface of electrode. In all the below reaction 'M' indicates the metal active sites, H^+ for proton and e^- for electron.

Volmer reaction i.e., electrochemical hydrogen adsorption

$$H^+ + M + e^- \rightarrow MH_{ads} \text{ (in acidic media)} \qquad \text{Eq. 6}$$

$$H_2O + M + e^- \rightarrow MH_{ads} + OH^- \text{(in alkaline and neutral media)} \qquad \text{Eq. 7}$$
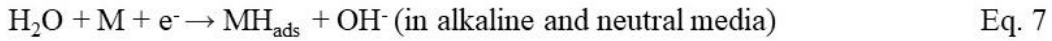
Heyrovsky reaction i.e., electrochemical desorption

$$MH_{ads} + H^+ + e^- \rightarrow M + H_2 \text{ (in acidic media)} \qquad \text{Eq. 8}$$

$$MH_{ads} + H_2O + e^- \rightarrow M + OH^- + H_2 \text{ (in alkaline and neutral media)} \qquad \text{Eq. 9}$$
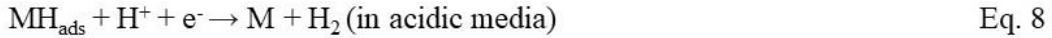
Or

Tafel reaction i.e., chemical desorption

$$2MH_{ads} \rightarrow 2M + H_2 \qquad \text{Eq. 10}$$

Based on the H_{ads}' coverage, the Tafel slope value examines the mechanism via which HER proceeds. The Tafel slope value would be smaller, the faster the reaction kinetics [13].

Tafel slope for Volmer reaction (represented by 'b_v') for Volmer reaction can be calculated by following equation.

$$b_v = 2.303 \, RT/\alpha F \qquad \text{Eq. 11}$$

Tafel slope for Heyrovsky reaction (b_H) can be calculated by,

$$b_H = 2.303 RT / (1+\alpha)F \qquad \text{Eq. 12}$$

Tafel slope for Tafel reaction (b_T) can be calculated by,

$$b_T = 2.303 \, RT / 2F \qquad \text{Eq. 13}$$

Here, R = constant for ideal gas, T = absolute temperature in kelvin, F = faradaic constant and α = symmetry factor which is equivalent to 0.5.

Tafel slopes for Volmer, Heyrovsky or Tafel reactions are 120, 40, and 30 mV/dec, respectively. Other than Tafel slope indicator, the free energy for hydrogen adsorption may serve as a useful marker for an electrocatalyst's HER performance. In 1970, first time Trasatti explained the volcano

plot which was based on the HER exchange current density and metal-hydrogen (M-H) bond strength [14]. Figure 1.3b depicts the volcano plot. It shows that there is a correlation between the strength of the M-H bonds and the HER exchange current densities for different electrocatalysts. At low M-H strength, Volmer step is RDS while at higher M-H strength, because the Volmer reaction quickly absorbs H^+ from the catalysts' active site, and Tafel or Heyrovsky steps are used to desorb the generated H_2, which results in RDS. One possible explanation for the current density drop that occurs after the ideal M-H bond strength is an overstabilization of the absorbed intermediate. For further confirmation of this relationship, Hinnermann et al. in 2005 used estimates of ΔG_{H*} determined by DFT computations [15]. The plot displays a volcanic pattern that is identical to Trasatti, and the metals' positions remain constant. It suggested that ΔG_{H*} with approximately zero value of electrocatalyst would be better for HER.
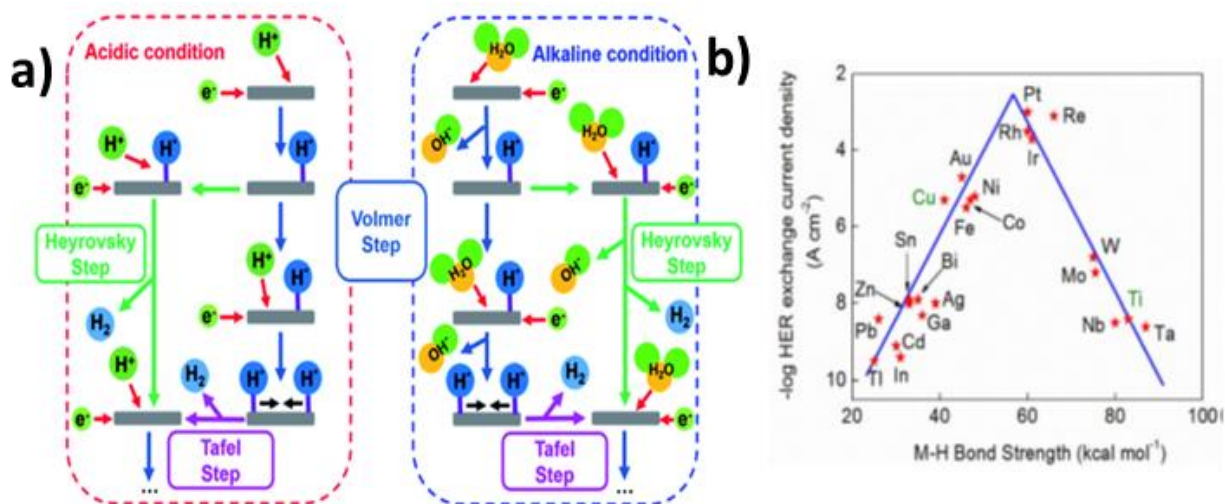
Figure 1.3. a) HER mechanism in acidic and alkaline conditions, b) Trasatti Volcano plot i.e., exchange current density vs. M-H bond strength for HER [12].

1.3.2. Oxygen Evolution Reaction (OER)

Compared to HER, OER is a slow process. The reason is $4e^-$ transfer process at anode. There are several steps involved in four electron transfer that's why, it has sluggish kinetics. Like HER, OER is also favorable in wide variety of pH. In literature, OER proposed mechanism is reported in acidic as well as neutral or alkaline media. Figure 1.4a demonstrates the OER mechanism in alkaline (green) and acidic (red) media, where 'M' shows active sites of metal and there are two pathways (blue and black) for OER mechanism [16]. Generally, in the case of both pathways, the

intermediates are the same as M-OH and M-O. Only the difference occurs at the step which creates oxygen. In one pathway, there is the formation of metal oxyhydroxide intermediate, which breaks down into O_2 and allows the free active sites to regenerate. While in the alternative pathway, two M-O species are combined to directly release M and O_2. Despite this discrepancy, it is generally agreed upon that the electrocatalysis of OER involves four electron transfers, with the number of electrons or protons transferred in each step varying [17]. Equations 12-15 show the steps involved for OER in alkaline or neutral conditions while equations 16-19 explain the OER mechanism in acidic conditions.

In alkaline/neutral media,

$$M + OH^- \rightarrow M\text{-}OH + e^- \hspace{5cm} \text{Eq. 14}$$

$$M\text{-}OH + OH^- \rightarrow M\text{-}O + H_2O + e^- \hspace{4cm} \text{Eq. 15}$$

$$M\text{-}O + OH^- \rightarrow M\text{-}OOH + e^- \hspace{4.5cm} \text{Eq. 16}$$

$$M\text{-}OOH + OH^- \rightarrow M + O_2 + H_2O + e^- \hspace{3cm} \text{Eq. 17}$$

In acidic media,

$$M + H_2O \rightarrow M\text{-}OH + H^+ + e^- \hspace{4.5cm} \text{Eq. 18}$$

$$M\text{-}OH + OH^- \rightarrow M\text{-}O + H_2O + e^- \hspace{4cm} \text{Eq. 19}$$

$$M\text{-}O + H_2O \rightarrow M\text{-}OOH + H^+ + e^- \hspace{3.8cm} \text{Eq. 20}$$

$$M\text{-}OOH + OH^- \rightarrow M + O_2 + H^+ + e^- \hspace{3.5cm} \text{Eq. 21}$$
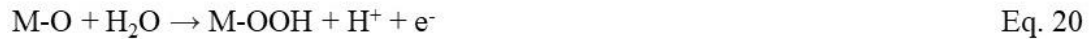
Like the HER, the measured Tafel slope (correlated with the electron transfer coefficient) can be used to determine the OER mechanism on a particular electrocatalyst. Similarly, the more efficient OER kinetics are indicated by the smaller Tafel slope, which points to the OER pathway's RDS. There is another parameter i.e., the Gibbs free energy difference between the intermediates such as M-O and M-OH, may help to better understand the OER mechanism. The OER catalytic activity plot as a function of specific intermediates displays the volcano shape (Figure 1.4b). This suggests that varying the binding energies of the intermediates can lead to the optimal catalytic activity. In other words, the reaction is slowed down when intermediates are too tightly bound by the catalyst surfaces due to the restricted number of accessible surface sites (poisoning effect), whereas the

reaction is slowed down when the surfaces bind oxygen too weakly due to difficulty of further activation.
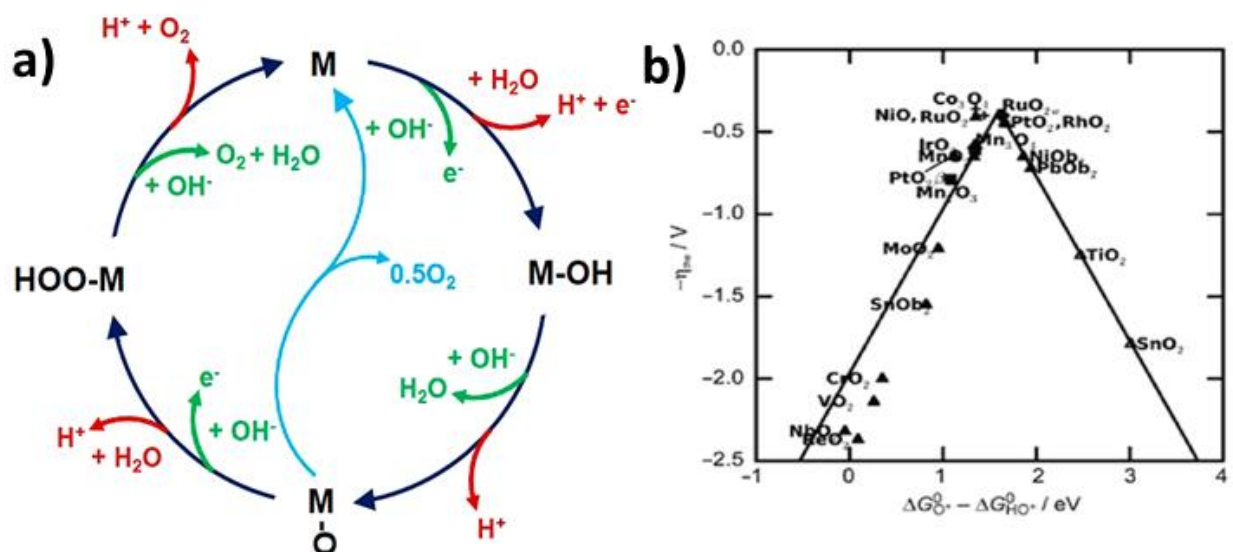
Figure 1.4. a) the OER mechanism in acidic (red line) and basic (green line) media, b) volcano plot for OER; negative values of theoretical overpotential vs. free Gibbs energy difference between M-O and M-OH [16].

1.3.3. Parameters for the Evaluation of Electrochemical Water Splitting

Basically, there should be a proper electrolytic cell with the three electrodes (working, counter, and reference), conducting electrolyte and potential controller. The specific reaction's thermodynamics dictate the potential range in a three-electrode system, which is changed for the reduction or oxidation process across the working electrode. The cathode and anode are the two electrodes which are used in the redox chemical reaction of the overall electrochemical water splitting process. The working electrode in an electrochemical reaction is loaded with the synthesized catalyst and put through a battery of tests to determine their catalytic potential. There are some important parameters which evaluates the electrochemical water splitting i.e., Overpotential, Tafel slope, electrochemical surface area, faradaic efficiency and stability on a constant current or potential (chronoamperometry or chronopotentiometry). All parameters have their own pros and cons.

1.3.3.1.   Overpotential (η)

One of the most important factors to assess the inherent competency and efficiency of the electrocatalyst for the difficult catalysis reaction is overpotential. Theoretically, water splitting always require difference in a voltage i.e., 1.23 V between the positive (anode) and negative electrode (cathode); however, a larger potential is required because of cell resistances and the requirement to overcome kinetic barricades at each electrode. So, the discrepancy among the theoretical and real potentials required to split water is known as the overpotential, and this determines the voltage that we need to apply, which becomes [18]:

$$E_{applied} = 1.23 + \eta_{anode} + \eta_{cathode} + iR \qquad\qquad \text{Eq. 22}$$

There are several possible causes of overpotential, such as resistance, activation, and concentration [19]. By using active catalysts, the activation potential (fundamental characteristic of catalysts), can be decreased. Under specific operational conditions, concentration overpotential occurs during the electrolysis process. A concentration drops at the electrode following the start of the electrolysis process results in an overpotential, most probable due to restricted diffusion and non-homogenized ion dispersal. Nonetheless, it might be somewhat controlled by stirring up the reaction media. On the other hand, junction resistance, or resistance at the system's interfaces, also contributes to the overpotential. Measuring the iR compensation data can eradicate it. Additionally, the overpotential may also be caused by bubbles forming on electrode surfaces and their incorrect detachment.

An electrocatalyst has superior activity or performance if the specific current density demands a lower overpotential. It is also essential to consider the quantity of current density that is acquired above the onset potential (the potential at which the current begins to rise from zero point) to assess electrode materials' steady performance within a limited potential range. The literature frequently uses a current density of 10 mAcm^{-2} to find out the overpotential to evaluate the efficiency of different electrocatalysts for water splitting. But this comparison is only reliable if all catalysts are handled identically, like pH of the electrolyte and the surrounding electrode's temperature [11].

1.3.3.2.   Tafel Slope

The kinetic parameter obtained from the Tafel plot is the Tafel slope. Replotting the polarisation curves, or LSV, as log current density (j) vs. η yields the Tafel plot. Voltage and current are the two basic restrictions on any electrochemical procedure. Nocera et al. confirmed that variations in the

potential range basically correspond to adjusting the driving force between the electrode and electrolyte system [20]. Examining an electrochemical process's kinetics and mechanistic details, basically, known as Tafel slope analysis which is the most employed metric in this regard. The following equation illustrates the relationship between applied potential and steady state current density for multiple step reactions i.e., OER/HER.

$$j = j_o \exp(\alpha F \eta / RT) \qquad \text{Eq. 23}$$

where, j_o = the exchange current density, α = equilibrium coefficient, F = faraday constant, η = overpotential, R = constant used for ideal gas and T = temperature in kelvin.

By taking log of Eq. 23, it is written as.

$$\ln j = \ln j_o + \alpha F \eta / RT \qquad \text{Eq. 24}$$

By taking natural log, it can be written as.

$$2.303 * \log(j) = 2.303 * \log(j_o) + 2.303 * (\log(\alpha F \eta / RT)) \qquad \text{Eq. 25}$$

Dividing by 2.303, it can be written as,

$$\log(j) = \log(j_o) + \log(2.303 * \alpha F \eta / RT) \qquad \text{Eq. 26}$$

The above equation can be rearranged as,

$$\eta = a + b \log j \qquad \text{Eq. 27}$$

Equation 27 is called Tafel slope equation, where a and b are known as constant and Tafel slope $(2.303 * \alpha F \eta / RT)$ respectively.

The linearity in graph plot between logarithm of current density and overpotential determines the Tafel slope value, that is a steady description of an electrode procedure. It offers details on the kinetics of the complete electrochemical reaction as well as the reaction mechanism and RDS. In general, faster charge transfer rate is indicated by smaller Tafel slope values. Since change in Tafel slope can occur by choosing a higher or lower-potential zone for the similar RDS, it's more helpful to calculate it in the onset potential zone [21].

It's crucial to remember, nevertheless, that R_s and R_{ct} could interfere with the OER process's kinetics. More accurately, by exceeding the R_s value from 6 Ω, the catalyst demonstrates a higher current density i.e., ≥ 100 mAcm^{-2}. [22]. Thus, the real kinetics of an electrochemical reaction can be ascertained via EIS. For this reason, data on an extra overpotential of no less than 100 mV must be gathered additionally to the overpotential seen on the cyclic voltammogram image. By providing precise exchange current density at several higher overpotentials, the $1/R_{ct}$ reduces experimental errors often linked to the Tafel slope computed from CV and presents the kinetics of the entire electrode procedure over a wide potential range [23].

1.3.3.3. Electrochemical Active Surface Area (ECSA)

This parameter is calculated through CV performed in non-faradaic region at various scan rates. Then, ECSA can be computed by using the capacitive current response.

$$\text{Double layer charging current } (I_c) = v \, C_{dl} \qquad \text{Eq. 28}$$

where the C_{dl} = double layer capacitance (calculated from the slope of the graph of peak current vs. scan rates) and "v" = scan rate.

$$\text{ECSA} = C_{dl} / C_s \qquad \text{Eq. 29}$$

where C_{dl} = double layer capacitance in the non-Faradic region of the cyclic voltammogram and C_s is the electrocatalyst's specific capacitance as measured in the presence of a specific electrolyte. In literature, C_s value for transition metals is 0.04 mF for acidic, alkaline, and neutral medium [24].

1.3.3.4. Faradaic Efficiency (FE)

It is the electrochemical parameter which can be stated as "It is the ratio of the amount of product collected (measured in moles) to the maximum amount that could be generated from the charge that was passed. It describes how selective an electrochemical process is overall. It can be written as,

$$\gamma_{faradaic} = \Delta n_{effective} / \Delta n_{faradaic} \qquad \text{Eq. 30}$$

O_2 and H_2 gases are generated at the anode and cathode, respectively, during the electrochemical water splitting reaction.

13

In Eq. 30, $\Delta n_{faradaic}$ is calculated by applying Faraday's law, which would be:

For the OER

$$\Delta n_{O_2}^{faradaic} = (\upsilon_{O_2}/\upsilon_e F)*C = (1/4F)*C \qquad \text{Eq. 31}$$

For the HER

$$\Delta n_{H_2}^{faradaic} = (\upsilon_{H_2}/\upsilon_e F)*C = (1/2F)*C \qquad \text{Eq. 32}$$

where C = charge passing during electrolysis, 'n' the number of moles, F = Faraday constant and υ_e is equal to the number of electrons.

There are various techniques to calculate the FE for H_2 and O_2 i.e., for H_2, GC is the best quantitative technique while for O_2, there are many choices like GC, fluorescence-quench methods or O_2-senstive electrodes (Clark electrode) [25]. Furthermore, the simplest procedure is water displacement method which is used to quantify molecular O_2 and H_2 by using the inert gas equation which is PV = nRT. This calibration method assumes that the water oxidation procedure is the only source which produced electrons in the external side circuit and capacitive current is not responsible for charged contribution. More than 95% FE for both OER and HER justifies that the electrocatalyst is active throughout the overall water splitting process [26].

1.3.3.5. Stability

When assessing an electrocatalyst's suitability for large-scale commercial operations, stability is a crucial consideration, as evidenced by an analysis of its activity over an extended period. During electrochemical testing for HER/OER in extreme acidic and basic conditions or by applying higher potential, there are some problems occur like leaching out of the catalytic material from the working electrode. This can reduce the long-term performance of electrocatalyst. Because of this, it is required to evaluate the electrode materials' continuous performance in harsh conditions for at least 24 hours. Majorly, there are two techniques i.e., chronoamperometry (constant current electrolysis) and chronopotentiometry (constant potential analysis). The catalyst maintained constant current density and the applied voltage is computed as a time function during chronoamperometry. On the other hand, chronopotentiometry captures variations in current over time at a fixed applied potential. Other than these, there are two more techniques are employed to investigate the stability of HER and OER by cycling the catalyst within the potential range: CV or

LSV at larger scan rates, it can be called as a galvanostatic or extended potientiostatic electrolysis measurement, or an accelerated degradation test. The number of cycles used to assess the catalytic material's stability varies for OER and HER. In HER, the polarisation curve begins at 0 V vs. RHE and can be carried out for thousands of cycles. In the case of OER, it is doubtful that the accelerated deterioration test will be observed beyond 1000 cycles because there are few reports of OER electrocatalysts with exceptional stability [9].

1.3.4. Electrocatalysts for Electrochemical Water Splitting

Until now, there are various electrocatalysts used for electrochemical water splitting. Detailed periodic classification is given below.

1.3.4.1. s-block Elements-Based Electrocatalysts

s-block elements are all metals with low ionisation enthalpies, strong reactivity, and a tendency to create ionic compounds. They function as potent reducing agents because they are readily oxidised in the presence of air, produce oxides having standard potential in negative. Moreover, Due to the above-mentioned properties, the elements present in s-block have found extensive use in energy conversion and storage applications. The properties i.e., small size of ionic radii and electrode potential in negative increase its capacity to store more energy and allow it to function as an ionic mediator in energy storage devices [27], and other applications. It is noted that lithium is a crucial and important component of modern technology and incorporated lithium as a dopant is observed to enhance electrocatalysis for electrochemical water splitting. In the Li^+-$Ni(OH)_2$-Pt instance, the hydrogen evolution activity was increased due to the Lewis acidic nature of Li^+ [28]. Lee et al., in 2012, explained the structure of $LiCoO_2$ and $LiCoPO_4$, as well as their electrochemical water splitting efficiency in a neutral and basic conditions, demonstrated that how Li is significant in the electrochemical water splitting. 100 continuous cycles between 1.2-1.8 V and 1.0 and 1.7 V vs. RHE at pH 7 and 13, respectively, were observed by the working electrodes at a scan rate of 10 mV/s at 900 rpm. [29]. In 2015, Wang et al., synthesized lithium induced $NiFeO_x$ nanoparticles, supported on carbon fibre paper (CFP) and achieved 10 mA/cm^2 current density at 280 mV for overall water splitting in 1M KOH [30]. Furthermore, Zheng Li et al., in 2020, synthesized magnesium doped RuO_2 by annealing of Ru exchanged Mg-MOF-74 and performed for OER in 0.5M H_2SO_4. Mg–RuO_2 has a good 30-hour lifetime and enhanced OER. Additionally, it exhibited

excellent stability with 10,000 CV cycles and having 228 mV overpotential at 10 mA cm^{-2} [31]. In 2021, Jie Xu et al., prepared two-dimensional Ruthenium beryllium (RuBe) nanosheets and used for the HER in alkaline media and achieved the current density -10 mA cm^{-2} at overpotential of 34.8 mV [32]. In 2021, Lima et al., synthesized Fe doped calcium cobaltite ($Ca_3Co_3 \cdot 2Fe_{0 \cdot 8}O_9$) and tested for OER in 1M KOH. It required the overpotential of 320 mV at 10 mA cm^{-2} [33]. Shi et al., synthesized strontium cobaltite ($SrCoO_3$). For OER in pH 13, it performed best and achieved current density of 2.50 mA cm^{-2} at 500 mV overpotential [34]. According to Mengran Li et al., doping $La(Ni, Fe)O_{3-\delta}$ with Sr^+ improves the crystallinity and electronic structure, also increases OER active sites for cobalt or iron-based perovskite OER electrocatalysts. By raising the amount of Ni^{3+} which is OER active specie, raise up the Ni/Fe surface ratio and boosting the O_2^{2-}/O^-. Due to these changes in structure and substitution, excellent OER occurred. This electrocatalyst needed a lower overpotential of 374 ± 3 mV vs RHE at a current density of 10 mA cm^{-2} [35].

Research is now being done on metal oxides based on Barium for the purpose of water splitting. Xu et al., synthesized Scheelite $BaMoO_4$ through co-precipitation method and further thermal reduction of it cause to change in $BaMoO_3$ perovskite, which increases alkaline HER activity. It is noted that, $BaMoO_3$ required lower overpotential (336 mV at 10 mA cm^{-2}) as compared to the $BaMoO_4$ (561 mV at same current density) [36]. Chen et al., synthesized $BaTiO_3$ through sol-gel method and for OER in alkaline media, it achieved the overpotential of less than 1.6 V(IrO_2) [37].

1.3.4.2. p-block Elements-Based Electrocatalysts

The p-block elements are metals, metalloids, and nonmetals. They have a relatively higher ionisation energy. They show many oxidation states in addition to the group oxidation state. Majorly, Aluminium, Gallium, Indium, Tin and Bismuth are more active elements in electrochemical water splitting.

Due to the benign nature of Al, it is considered a favourable alternative in both acidic and alkaline conditions. They are inexpensive, widely dispersed across the crust, and when water is electrolyzed, they have been demonstrated to yield up to 11 weight percent. Through doping with aluminium, transition metals like cobalt and nickel can acquire electrons from aluminium, facilitating interaction between the aluminium and the transition metal sites. Zhang et al., prepared Al doped CoP (Al-CoP) and supported on carbon cloth (Al-CoP/CC). It is more active

electrocatalyst for HER in acidic conditions while it is good bifunctional electrocatalyst for overall water splitting in basic conditions. In overall water splitting, it achieved current density of η_{10} at overpotential of 330 mV in alkaline media [38]. Furthermore, Zhao Li et al., in 2018, developed P, Al co-doped NiO nanosheets, it exhibited high efficiency as bifunctional electrocatalyst for overall water splitting in 1M KOH by showing 330 mV at 10 mA cm^{-2} [39].

The low melting point and toxicity of gallium have drawn a lot of interest. Gallium, like Al, can self-passivate by creating an ultrathin layer of Ga oxide in the presence of air. In 2019, Kakoria et al., reported Gallium oxide nanofibers (β-Ga_2O_3) for HER in 0.1M KOH. It exhibited low overpotential of 340 mV with a Tafel slope of 70 mV dec^{-1}, and a current density increment greater than Pt/C [40]. In 2019, Ciuan Lim et al., developed the popcorn shaped Gallium platinum ($GaPt_3$) nanoparticles, and tested for HER in acidic media. It is reported that 10 mA cm^{-2} was achieved at only overpotential of 23 mV and highly stable even after stability test for 40 h [41]. Furthermore, through density functional theory (DFT), Tao jing et al., reported Ni doped graphene like 2D-Gallium nitride GaN (Ni/g-GaN) for OER with overpotential of 260 mV [42]. Jiajun Wang et al., recently prepared Indium based ternary spinal selenides ($CoIn_2Se_4$) and used for the OER in 0.1M KOH. It showed exceptional OER activity with overpotential of 315 mV at 10 mA cm^{-2} [43]. Moreover, Shamraiz et al., reported Indium sulfide (In_2S_3) spheres for HER/OER at 239 mV/230mV to achieve 10 mA cm^{-2} current density respectively in 1M KOH [44].

Due to cost effectiveness of Tin (Sn) is also using in electrochemical water splitting. In 2021, Jian et al., reported Sn-Ni(OH)$_2$ for OER (312 mV) and HER (298 mV) at current density of 100 mA cm^{-2} in basic media [45]. Sn doped Nickle sulfide (Sn-Ni_2S_3) nanosheets was developed by Jing Yu et al., it is reported that these nanosheets exhibited 201 mV at η_{10} for HER in 0.5M H_2SO_4 [46]. Furthermore, Lang et al., reported that despite having less stability in acidic media, the Ni–Sn@C core/shell's strong conductivity and wide active surface area provided good electrocatalytic activity towards HER [47].

Because to bismuth's low cost, high electrochemical active sites, compatibility for environment, and potent water splitting electrocatalytic efficiency, 'Bi' based catalysts have been researched for a variety of uses. The metals' synergistic interaction with the oxy/hydroxide phases can boost the activity of Bi-based catalysts, even though they are supposed to have low HER activity. Syah et al., synthesized Bi/Bi_2O_3 and reported for HER in 1M KOH with 180 mV at 1 mA cm^{-2} [48]. S

Khatun et al., reported $Bi_3(FeO_4)(MoO_4)_2$ for OER/HER with 266 mV and 207 mV@10 mA cm^{-2} respectively in alkaline media [49]. Furthermore, Tarik et al, reported the HER of Ce doped α-Bi_2O_3-rGO in alkaline media and achieved current density of 10 mA/cm^2 at overpotential of 337 mV with Tafel slope of 162 mV/dec and same catalyst used for overall water splitting in alkaline media and in two electrode system the catalyst achieved current density of 10 mA/cm^2 at the potential of 1.78 V with a Tefal slope of 158 mV/dec [50].

The metalloids of p-block elements (Boron, Silicon, Germanium, Arsenic, antimony, and Tellurium) were also used for water splitting. Lao et al., developed iron doped Nickel boride grown on 3D-self supported graphene ($Fe_{0.2}Ni_{0.8}B$/SSG). It is used for the overall electrochemical water splitting in alkaline media by showing 1.62 V@10 mA/cm^2) [51]. Transition metal monosilicides (MSi, 'M' is titanium, manganese, iron, ruthenium, nickel, palladium, cobalt, and rhodium) for HER in 0.5M H_2SO_4, these all exhibited very low overpotential in the range of 34-54 mV at 10 mA/cm^2 current density discussed by Yuan He et al., [52]. Mesoporous silica i.e., SBA-15 is also good candidates for HER activity. Chiani et al., synthesized Pd/Cu nanoparticles supported on mesoporous silica and multiwalled carbon nanotubes (Pd/Cu NPs/SBA-15-MWCNTs) and tested for HER in acidic media. It is reported that this electrocatalyst achieved current density of -165.24 mA/cm^2 at overpotential of 36 mV [53]. Hausmann et al., reported intermetallic iron germanide (Fe_6Ge_5) for OER with 272 mV overpotential at 100 mA cm^{-2} in alkaline media [54]. Furthermore, Gauthier et al., discussed transition metal Arsenide (CoAs, MoAs and Cu_3As) in detail and proved through experimentally as well as DFT that Co and Mo based arsenide was more efficient for HER by showing Tafel slope of 76 and 74 mV/dec respectively [55]. Lu et., al explained different transition metal (scandium, titanium, vanadium, chromium, manganese, iron, cobalt, nickel, copper, zinc, ruthenium, rhodium, palladium, silver, cadmium, iridium, palatinum and gold) embedded Sb and reported that Pt@Sb was efficient catalyst for OER by exhibiting 480 mV overpotential [56]. Some metal tellurides (NiTe and CoTe) are also reported as efficient bifunctional electrocatalysts for OER and HER. Between these, CoTe reported as highly efficient for OER and HER. For OER, CoTe achieved current density of 100 mA/cm^2 at 350 mV and for HER, same catalyst exhibited 202 mV at 10 mA/cm^2 [57].

1.3.4.3. d-block Elements-Based Electrocatalysts

d-block elements consist of three rows. First row includes Scandium to Copper, second row from yttrium to silver and third row is form Hafnium to gold. They produce compounds with strong catalytic activity, have high melting and boiling temperatures, exhibit a variety of oxidation states, and form stable complexes. The group classification is mentioned below.

Transition Metal-Based Oxides and Oxyhydroxides

There are many reports on transition metal oxides and oxyhydroxides for electrochemical water splitting. Shi et al., reported hollow nanosphere vanadium oxyhydoxides (VOOH) for overall water splitting in alkaline media by achieving 10 mA/cm^2 at overpotential of 390 mV [58]. Zhang et al., constructed core@shell Ni$_{1-2x}$Mo$_x$Se@NH$_4$NiPO$_4$·6H$_2$O–MoO$_x$/NiF through electrodeposition technique and further tested for HER, OER, and overall water splitting. This novel catalyst was afforded the current density of 10 mA/cm^2 at extremely low overpotential of 31 mV and 205 mV for HER and OER respectively in 1M KOH. For overall electrochemical water splitting, the cell potential was 1.49 V in same media [59]. Furthermore, Zhang et al., reported novel hierarchal PrBa$_{0.5}$Sr$_{0.5}$Co$_2$O$_{5+\delta}$(PBSC)@FeOOH nanoflakes as highly efficient catalyst for HER and OER in 0.1M KOH by achieving the geometric current density of at overpotential of 280 and 390 mV respectively. This much improved electrochemical performance was most likely due to the strong electronic bonds between FeOOH and PBSC, the hierarchical nanostructure, and the high charge-transfer capability [60]. Govind Rajan et al., explained the OER kinetics on iron doped β-NiOOH by depicting the overpotential of 300 mV having Tafel slope value of 76 mV/dec [61]. Tungsten (W^{6+}) doped in Ni(OH)$_2$/NiOOH (W$_{0.1}$Ni(OH)$_2$/NiOOH) was synthesized by Rathore et al., through electrodeposition and reported for HER and OER by reaching at current density of 10 and 50 mA/cm^2 at favorable overpotential of 56 and 293 mV in alkaline media [62]. Zhang et al., synthesized anemone like CoP@CoOOH deposited on carbon paper (CoP@CoOOH/CP) and discovered overall water splitting in alkaline (1.52 V) and neutral (1.65 V) media [63].

A flower-like NiCo$_2$O$_4$ porous material was prepared by Elakkiya et al. as a bifunctional catalyst for the overall water splitting in the alkaline electrolyte. Very good electrocatalytic activity was shown by this catalyst at low overpotential values (360 mV and 370 mV@10 mA cm^{-2} for OER and HER respectively) [64]. Zhang et al., prepared NiCo alloy nanochain arrays deposited on NiF

and tested for overall water splitting. The current density of 10 mA cm^{-2} was obtained for the overall water splitting at cell voltage of 1.688 V [65]. Furthermore, Han et al., synthesized ternary transition metal-based oxide (CoFeNi-O) and supported on various conducting electrodes (glassy carbon (GC) and nickel foam (NiF)). CoFeNi-O/GC was tested only for OER, it exhibited 230 mV overpotential at 10 mA/cm^2 while CoFeNi-O/NiF tested for OER and HER by exhibiting 200 and 57.9 mV@10 mA/cm^2 respectively [66]. Moreover, Liao et al., reported cubic nanoflowers (Ni-Fe-K$_{0.23}$MnO$_2$ CNFs-300) as a bifunctional electrocatalyst for OER (270 mV@10 mA/cm^2) and HER (116 mV@10 mA/cm^2). For overall water splitting, these catalysts exhibited 1.62 cell voltage at 10 mA/cm^2 [67].

Transition Metal-Based Carbides and Nitrides

Transition metal carbides and nitrides are a class of interstitial compound that have been studied extensively in the field of water splitting due to their electronic structure and noble metal-like activity. Yeo et al. synthesized molybdenum carbide (α-Mo$_2$C) and molybdenum nitride (γ-Mo$_2$N) nanoparticles by using the simple urea-glass technique. Between these, α-Mo$_2$C demonstrated exceptional HER performance in alkaline electrolyte by exhibiting low overpotential (176 mV) required to reach 10 mA cm^{-2} [68]. Liu et al., designed Cobalt-Molybdenum carbides oxides (Co$_6$Mo$_6$C$_2$/Co$_2$Mo$_3$O$_8$) and deposited on the N, P doped carbon. He proved that Co$_6$Mo$_6$C$_2$ was the main active phase in the composite and N, P doped carbon enhanced the water splitting activity by exhibiting 220 mV for HER and 403 mV for OER at 10 mA cm^{-2} in 1M KOH [69]. Recently, Zhang et al., synthesized 3D Fe$_x$Mn$_y$ nanoparticles (NPs) and embedded in nitrogen-doped carbon materials (Fe$_x$Mn$_y$@NC) through pyrolysis and further proved the efficient electrocatalyst for overall water splitting by exhibiting 1.628 V@10 mA cm^{-2}[70].

Yu et al. synthesised atomically thin 2D nitrogen-rich hexagonal W$_2$N$_3$ (h-W$_2$N$_3$) nanosheets by using a salt-templated method. This electrocatalyst showed extremely low overpotential of -98.2 mV in an acidic solution at a current density of 10 mA cm^{-2} [71]. Recently, Zhou et al., prepared Fe$_2$P/Co$_2$N. The catalytic activity confirmed that this catalyst was the most efficient for overall water splitting by showing the cell voltage of 1.561 V at 10 mA/cm^2 current density [72]. Peng et al., reported cobalt nanoparticles grafted on vanadium nitride surface (Co/VN) for OER with 320 mV@10 mA/cm^2 in alkaline media [73]. Recently, Wang et al., reported Ni$_{0.2}$Mo$_{0.8}$N/MoO$_2$ for

HER by showing extremely low overpotential of 13 mV at 10 mA/cm^2 current density in 1M KOH [74].

Transition Metal-Based Sulfides and Selenides

TMDs are ideal HER and OER electrocatalysts due to their intrinsic electroactivity, high performance resulting from their metallic and semiconducting nature, various crystal phases, and flexible for insertion of dopant. Antonia et al., reported strong HER activity of MoS$_2$ and WS$_2$ deposition on sulphur-doped graphene i.e., 26 mV and 140 mV respectively in 0.5M H$_2$SO$_4$ [75]. Later, He et al., reported zinc doped nickle sulfide (ZnNi$_3$S$_2$) for HER by exhibiting 78 mV at 10 mA/cm^2 in alkaline conditions [76]. Furthermore, Mao et al., synthesized Co and Fe doped Ni$_3$S$_4$ through hydrothermal method. This electrocatalyst showed high performance for OER i.e., 230 mV@20 mA/cm^2 [77]. Recently, Zhu et al., prepared novel Ir-doped CoNi$_2$S$_4$ nanosheets and reported as highly efficient for overall water splitting by showing cell voltage 1.60 V at 10 mA/cm^2 [78].

Xia et al., synthesized various transition metal selenides (iron, cobalt, nickel, molybdenum, and copper). Among these NiSe$_2$ was the best electrocatalyst for HER and OER [79]. Later, Liu et al., prepared phosphorous doped nickel diselenide (P-NiSe$_2$) and reported as extremely good candidate for HER and whole water splitting by showing 86 mV overpotential and cell voltage of 1.62 V to reach 10 mA/cm^2 respectively in alkaline conditions [80]. Furthermore, Guo et al., reported MOF derived bimetallic NiFe-Se supported on carbon fibre paper (NiFe-Se/CFP) for OER by showing low overpotential of 281 mV at 10 mA/cm^2 [81]. Recently, Wu et al., syntehsized Fe$_{1.2}$(CoNi)$_{1.8}$Se$_x$ medium-entropy metal selenides (Fe$_{1.2}$(CoNi)$_{1.8}$Se$_x$ MESe) through selenylation of MOFs. This catalyst was reported as the most efficient electrocatalyst for overall water splitting i.e., 1.55 V at 10 mA/cm^2 [82].

Transition Metal-Based Phosphides

Transition metal phosphide is another class of electrocatalyst reported for electrochemical water splitting. Yan et al., synthesized zinc and sulphur co-doped CoP nanorods clusters deposited on (Zn, S-CoP NRCs/CP) and reported as highly efficient electrocatalyst for HER, OER, and overall water splitting i.e., 67 mV, 391 mV and 1.70 V@10 mA/cm^2 in 1M PBS [83]. Li et al., prepared Nickle molybdenum phosphide covered with cobalt iron phosphides (P-NM-CF HNRs) for overall

water splitting by exhibiting 1.53 V@10 mA/cm^2 in 1M KOH [84]. Later, Xu et al., reported iron doped cobalt holey nanosheets (Fe-CoP HNSs) for OER and HER by showing the overpotential of 220 mV and 79 mV to reach the current density of 10 mA/cm^2 respectively. The electrolyzer for overall water splitting needed the cell voltage of 1.60 at 20 mA/cm^2 [85]. Recently, Sun et al., constructed cobalt phosphide deposited on nitrogen phosphorus codoped carbon (CoP@NPC) and reported as efficient electrocatsalyst for OER (303 mV) and HER (184.35 mV) at 10 mA/cm^2 in 1M KOH [86].

Transition Metal-Based Polyoxometalates

Polyoxometalates (POMs), also known as polyoxoanions, are polynuclear oxo-bridged anionic clusters of earlier transition metals having higher oxidation states and exhibit a wide range of structural and compositional characteristics [87]. 1n 2017, Luo et al., reported NiCo-POM@NiF for OER by showing 360 mV@10 mA/cm^2 in basic media [88]. Yuan Li et al., in 2019, reported yolk/shell ZIF-67@POM for OER (287 mV@10 mA/cm^2) [89]. In 2021, Gautam et al., prepared POM@ZnCoS/NF and reported for the HER (170 mV at 10 mA/cm^2) and OER (200 mV@20 mA/cm^2) in basic media [90].

Recently, in 2023, Gautam et al., synthesized the composite of well-Dawson POMs and iron zinc LDHs deposited on Nickle foam (ZnFe LDH-P$_2$Mo$_{18}$/NF) through hydrothermal method. This electrocatalyst was reported for OER and HER by exhibiting 275 mV and 330 mV at 20 mA/cm^2 respectively. Moreover, the electrolyzer composed of this catalyst comprised 1.54 V at 10 mA/cm^2 for overall water splitting [91]. Ravi et al., in 2023, prepared hydroxylated POM with Cu complex, and reported as a bifunctional-electrocatalyst for OER and HER by exhibiting 418 mV and 443 mV at current density of 1 mA/cm^2 respectively at neutral pH [92].

1.3.4.4. f-block Elements-Based Electrocatalysts

f-block elements consist of lanthanides and actinides. There are some reports on f-block elements for electrochemical water splitting. Recently, Li et al., incorporated cerium dioxide into nickel cobalt phosphide (CeO$_2$/NiCoP) and reported as a bifunctional electrocatalyst for OER and HER by exhibiting 231 mV and 48 mV at current density of 10 mA/cm^2 respectively at basic pH. Moreover, the reported cell voltage for overall water splitting was 1.46 V at 10 mA/cm^2 in same media [93]. Majhi et al., reported Nd$_2$O$_3$:NdPO$_4$ for HER in 0.5 M H$_2$SO$_4$ (134 mV@10 mA/cm^2) [94]. Furthermore, Quyang et al., reported that doping of Ytterbium (Yb) cation into nickel cobalt

iron based oxyhydroxides (Ni,Co,Yb–FeOOH/CC) increased the electrocatalytic activity for OER by showing the overpotential of 230 mV at 10 mA/cm^2 with the Tafel slope of 22.7 mV/dec [95].

1.4. Biodiesel

Biodiesel is an interesting fuel choice in recent years due to its biodegradability, sustainability, and ability to reduce pollution emissions. Biodiesel is being produced in several nations worldwide using various resources. The renewable source and basic components are the same for all biodiesels. Because they are produced by the photosynthetic conversion of solar energy to chemical energy, they differ from early photosynthetic processes. According to ASTM definitions, "biodiesel" is the term used to describe monoalkyl esters of long-chain fatty acids that are made from triglycerides using methanol and catalyst. These esters can be obtained from edible, non-edible, or waste oils [96]. Transesterification yields glycerin, sometimes referred to as glycerol. Methanol is usually used to manufacture biodiesel since it is easily accessible and reasonably priced. 100% FAME is referred to as B100, whereas B20 and smaller levels are referred to as "biodiesel blends." The foundation of a sustainable bioeconomy is biodiesel, which can only be produced with solar energy. Biodiesel is still largely used in the transportation industry in modern civilizations, even with major technological breakthroughs that allow photovoltaic cells to turn solar energy into electricity. The advantageous physical and chemical qualities of biodiesel, such as its viscosity, flash point, and cetane number, are comparable to those of diesel fuel [97].

1.4.1. Sources of Biodiesel Production; Merits and Demerits

One of the main issues with renewable fuel is the competition for land between food and fuel development. Scientific biodiesel development activities encompass the development of feedstocks, the optimal production process, the improvement of biodiesel quality and quantity, and the building of a carbon-neutral economy. The EASAC report from 2012 states that biodiesel is typically divided into four groups: first, second, and third generations based primarily on the source of the fuel; fourth generation biodiesel is still in the early phases of basic research and is made from biological instruments made by humans. [98].

1.4.1.1. 1st Generation Sources

First generation biodiesels are made from edible feedstocks, which include rapeseed oil, soybean oil, coconut oil, corn oil, palm oil, mustard oil, olive oil, rice oil, etc. At the beginning of the

biodiesel era, producing biodiesel from edible feedstock was a common practise [99]. First generation feedstocks are primarily advantageous due to their crop availability and comparatively easy conversion process. There are several disadvantages to using these feedstocks, the main one being the potential for food price increases due to shortages. The impossibility of producing biodiesel from edible feedstock because of its high cost, small growing area, and inability to adjust to different environmental conditions. Due to these drawbacks, consumers were compelled to turn to more alternative sources to produce biodiesel [100]. Some other edible feedstocks for 1st generations are cashew nut oil, radish oil, walnut oil, cotton seed oil, hazelnut oil, pistachio oil and tigernut oil etc [101-104].

1.4.1.2. 2nd Generation Sources

2nd generation biodiesels are made from non-edible feedstocks such as milk bush oil, rubber seed oil, Mahua indica oil, neem oil, jatropha oil, nagchampa oil, Karanja oil etc [105]. Due to the drawbacks of feedstocks from the first generation, researchers are more interested in non-edible feedstocks. In addition to being less harmful to the environment, second generation biodiesel also eliminates food inequity, requires less space for cultivation, and has lower production costs. The fact that 2nd generation biodiesel doesn't require agricultural space, or the relaying of food plants are the main benefits when used to produce biofuels. One disadvantage of 2nd generation fuels is plant yields, which are lower for important non-edible species such Jatropha oil, Karanja, and jojoba. These feedstocks can thrive on little amounts of land. Therefore, non-edible crops must be grown on agricultural land since they will have an immediate impact on both the production of food and the economy of society [106]. To address the socioeconomic issues surrounding non-edible oil, scientists are concentrating on creative, more accessible, and economically feasible substitutes. An additional drawback of second-generation biodiesel is the need for more alcohol [107].

1.4.1.3. 3rd Generation Sources

3rd generation biodiesel is the kind, made from wasted oil and microalgae. The key benefits of third-generation biodiesel are reduced greenhouse effect, faster development and productivity, less competition for farmed land, a higher percentage of oil, and less effect on the food supply. The main disadvantages include the high cost of investment, the demand for sunlight, the issue with

large-scale production, and the difficulties involved in extracting oil. Presently, studies are being conducted on the manufacture of biodiesel from algal biomass with the aim of enhancing the extraction method and production rate. Fish oil, animal fat, microalgae, and residual cooking oil are the main sources of third-generation biodiesel [108]. The overall practicability of third-generation biodiesel's resources is superior to that of its predecessors' feedstocks in terms of accessibility, adaptability to environmental limitations, and economic feasibility. Microalgae have the potential to produce third-generation biodiesel in the future due to their high lipid content and ability to withstand harsh circumstances [109]. Sources of 3rd generation biodiesel also include waste fish oil, cooking oil, and animal tallow oil. It also reduces water contamination and eases the strain on waste disposal infrastructure [110]. Now, animal fats from pigs, chickens, goats, and cattle are seen to be a reliable and sustainable source for biodiesel production.

1.4.1.4.   4th Generation Sources

In fourth-generation biodiesels, photobiological solar fuels and electro fuels are taken into consideration. Solar energy is converted into biodiesel utilising raw materials to create solar biofuels; this conversion process is a novel area of study. The supply of raw materials is abundant, limitless, and reasonably priced. Innovative technologies that create artificial life forms and fashionable microbes for the direct and efficient conversion of solar energy to fuel are needed for sustainable development. Combining metabolically engineered microbial fuel production with photovoltaic or inorganic water-splitting catalysts is an emerging strategy for efficient development and liquid fuel storage [111]. The major drawback of 4th generation is the high initial investment.

1.4.2. Quality Parameters for Biodiesel

For the analysis of the feedstocks and biodiesel produced, the ASTM mentioned some standards [112] which are mentioned below in Table 1.1.

Table 1.1. physical and chemical properties of feedstocks and biodiesel

Quality parameters	Method i.e., ASTM D	Allowable limits	Units
Density	1298	0.880	at 15°C kg/liter
Kinematic viscosity	445	1.9-6.0	at 40°C cSt
Sulphur	4294	0.05 max.	% wt
Flash point	93	≥ 130 min	°C
Total Acid number	664	0.80 maximum	mg KOH/gm
Pour point	97	-15 to +5	°C
Cetane number	976	47 minimum	Index
Cloud point	2500	From -3 to -12	°C
Water	85	0.05	% Vol
Calorific value	240-14	37.5-42.80	MJ/kg

1.4.3. Technologies Involved in the Production of Biodiesel

Numerous contemporary technologies and procedures are employed in the production of biodiesel. To be used as fuel for diesel engines, vegetable and animal fats must have their viscosities lowered. These procedures use a variety of techniques, which are detailed below:

1.4.3.1. Direct Use and Blending

Vegetable oils have been used as an alternative fuel since 1900, when Dr. Rudolph Diesel, the man who built the diesel engine have experimented with using peanut oil in his compression engine [113]. Using crude vegetable oil directly as fuel for diesel engines is not a very encouraging practise. For usage in diesel engines, crude vegetable oils are either diluted or combined directly with diesel fuel to increase their viscosity. It has been found that the energy consumption of these oils is like that of diesel fuel. The oil to diesel ratios of 1:10 to 2:10 were found to function satisfactorily [114]. Nevertheless, the usage of pure oils or oil blends proved eventually inadequate for direct or indirect use as diesel fuels. The most common issues are carbon deposits, lubricating oil thickening, and polymerization during storage and combustion [115].

1.4.3.2. Micro-Emulsions

Micro-emulsification is a technique for creating microemulsions and a possible remedy for the issue of high vegetable oil viscosity. When one or more ionic or non-ionic amphiphiles interact with two ordinarily immiscible liquids to generate a colloidal equilibrium dispersion of optically isotropic fluid microstructures, a micro-emulsion is spontaneously formed, with diameters typically ranging from 1 to 150 nm [116]. In addition, micro-emulsion-based fuels are often labelled as "hybrid fuels," but the term has also been applied to blends of regular diesel fuel and vegetable oils [117]. Three parts make up microemulsions: an aqueous phase, an oil phase, and a surfactant. These fluids are transparent and steady. Because of this, research on micro-emulsions containing solvents including methyl alcohol, ethyl alcohol, and 1-butanol has been performed. All large carbon chain alcohols i.e., butanol, hexanol, and octanol microemulsions can reach the topmost viscosity limit for engines on diesel. The 200-hour EMA test was passed by a microemulsion that contained soybean oil, methanol, 2-octanol, and cetane improver in the following ratio: 52.7:13.3:33.3:1.0. Vegetable oils micro-emulsion reduced the oil's viscosity, however during a 200-hour laboratory screening endurance test, it also caused significant carbon deposits, inefficient combustion due to low cetane number, and irregular injector needle sticking [114].

1.4.3.3. Pyrolysis of Vegetable Oil

The process of turning one organic material into another by heating it up or using heat and a catalyst is known as pyrolysis. Vegetable oil, animal fat, natural fatty acids, or methyl esters of fatty acids can all be the pyrolyzed material [118]. A practical way to produce biodiesel is to convert vegetable and animal fats, which are mainly composed of triglycerides, using heat cracking techniques. The fact that this process has similarities to traditional petroleum refining makes it especially intriguing in areas where the hydro processing industry is well-established. The thermally broken-down vegetable oil's liquid product fractions are likely to have fuel properties akin to diesel fuels. Several study reports state that triglycerides can be pyrolyzed to create chemicals suitable for diesel engines. Triglyceride pyrolysis research fall into two categories: catalytic and non-catalytic processes. Triglyceride thermal degradation has complex mechanisms because of the wide range of mixed triglyceride structures and reactions that can happen [119].

An investigation of the pyrolysis reactions of castor, palm, and soybean oils was carried out [120]. For small throughputs, the equipment required for thermal cracking and pyrolysis is costly. Furthermore, although though the products' chemical makeup is comparable to that of petrol and diesel made from petroleum, the oxygen removal during thermal processing reduces the ecological advantages of utilising an oxygenized fuel. It occasionally generates a few low-value components together with more petrol than diesel fuel [121].

1.4.3.4. Transesterification/Esterification

Lipids such as vegetable and animal fats react chemically with alcohol to form fatty acid alkyl esters (FAAE i.e., basically biodiesel), a process known as transesterification or esterification [122]. Because of its advantages over other production methods, such as its versatility in using a range of feedstocks, its ability to improve fuel characteristics by lowering its viscosity, its miscibility of biodiesel with any amount of fossil fuel, its affordability, and its high conversion efficiency, transesterification/esterification is the most widely used technique. Glycerol is a byproduct of this procedure that is also a highly valuable molecule [123]. During esterification process, alcohol and FFA mix to generate FAAE and water. Equation 33 depicts the general reaction for esterification reaction. Here R^1 is the alkyl group of fatty acids and R^2 is the alkyl group of alcohol.

$$R^1\text{-COOH} + R^2\text{OH} \rightarrow R^1\text{-COOR}^2 + H_2O \qquad \text{Eq. 33}$$

FFAs   Alcohol   FAAE (Biodiesel)

During transesterification, also known as alcoholysis, ester react with alcohol to form alcohol and ester. This process is similarly to hydrolysis reaction because alcohol is used in place of water. Equation 34 described the general reaction for transesterification.

$$RCOOR^1 + R^2OH \leftrightarrow RCOOR^2 + R^1OH \qquad \text{Eq. 34}$$

Ester   Alcohol   Ester

To produce biodiesel, triglycerides of vegetable oil react with alcohol to form glycerol and FAAE. Triglycerides are sequentially converted to products by reversible stages in the transesterification process. Triglycerides first react with alcohol to form diglycerides, which then react to form

monoglycerides and glycerol, generating one alkyl ester at each stage [124]. Figure 1.5 represents the transesterification reaction of triglycerides to produce FAAE and glycerol.

$$\text{Triglyceride} + \text{R}^1\text{OH} \rightleftharpoons \text{Diglyceride} + \text{RCOOR}^1$$

$$\text{Diglyceride} + \text{R}^1\text{OH} \rightleftharpoons \text{Monoglyceride} + \text{RCOOR}^1$$

$$\text{Monoglyceride} + \text{R}^1\text{OH} \rightleftharpoons \text{Glycerol} + \text{RCOOR}^1$$
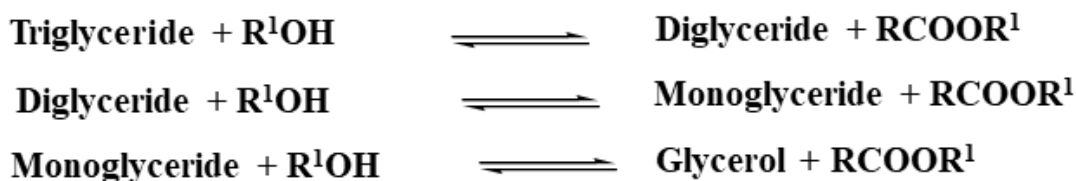
Figure 1.5. The general equation used for the transesterification of triglycerides [124].

One of the reversible reactions is transesterification. Therefore, more alcohol is mandatory to drive the chemical reaction towards equilibrium and the production of the product. During this process, cyclic, long-chain, and short-chain alcohols are used. However, methanol and ethanol are often utilised because of their availability, polarity, cost, and higher reactivity [125]. For esterification, only acid catalysts can be used while for transesterification, both acid and base catalysts can be used. Basically, there are four types involved in transesterification/esterification technology, which are mentioned below.

Acid Catalyzed Esterification

In this process, FFAs reacts with alcohol in the presence of acid catalysts and form methyl esters and water. Most solid acid catalysts were reported to produce the biodiesel through the esterification reaction [126-128].

Figure 1.6 depicts the mechanistic steps involved in the acid catalyzed esterification. Acid catalysts provided the protons needed to first protonate carbonyl carbon. Next, the nucleophilic attack of methanol on the carbonium ion resulted in the creation of a tetrahedral intermediate. FAME was finally produced after the proton migrated, the intermediate collapsed, and the proton was reconstructed [129]. Different acidic species have slightly different routes for esterification reactions. Proton exchange drives the entire chemical reaction. In mechanism, R depicts the alkyl group.
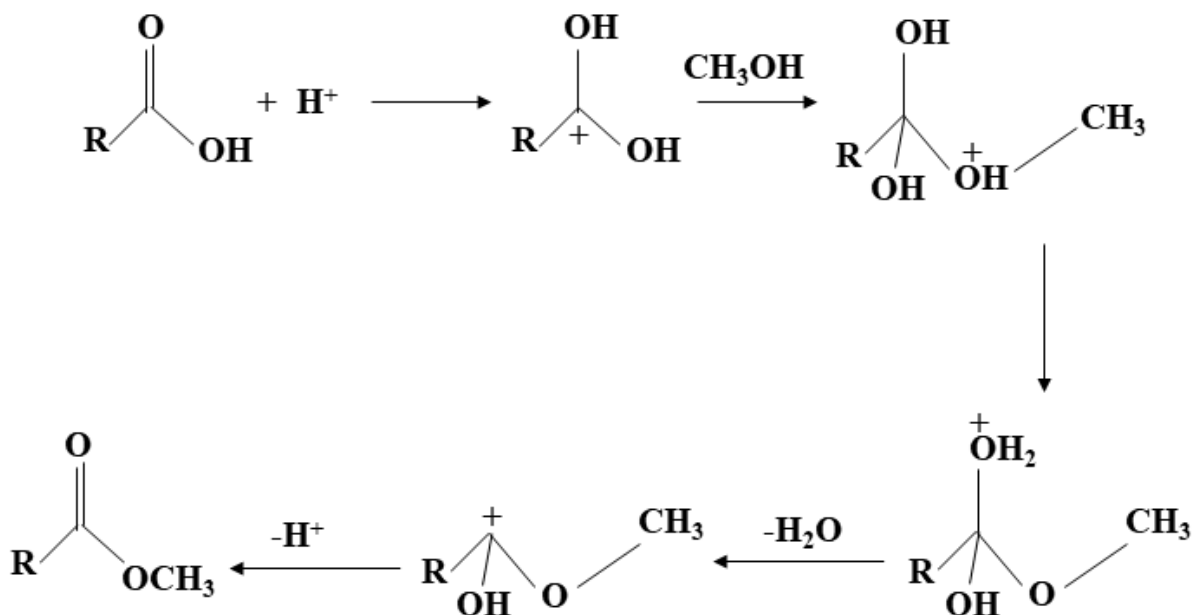
Figure 1.6. Mechanism involved in acid catalyzed esterification reaction [129].

Acid Catalyzed Transesterification

Bronsted acids can catalyse transesterification; sulfonic and sulfuric acids (H_2SO_4), phosphoric acid (H_3PO_4), calcium carbonate ($CaCO_3$) and lipase enzyme etc., work well in this regard. These catalysts produce extremely high yields in alkyl esters, but the reactions are sluggish; it usually takes more than three hours and a temperature above 100°C to finish the conversion [130]. Until now, number of acid catalysts were reported for enhance the transesterification process [131-133]. Figure 1.7 illustrates the mechanism involved for acid-catalyzed vegetable oil transesterification for a monoglyceride. It may be expanded to include diglyceride and triglycerides, though. The ester's carbonyl group is protonated to form the carbocation, which, following an alcohol nucleophilic attack, yields a tetrahedral intermediate. To produce a fresh ester and regenerate the catalyst, this intermediate remove glycerol [134]. In the figure 1.7, R_1 = carbon chain of fatty acids, R_2 = glyceride molecule and R = alkyl group of alcohol.
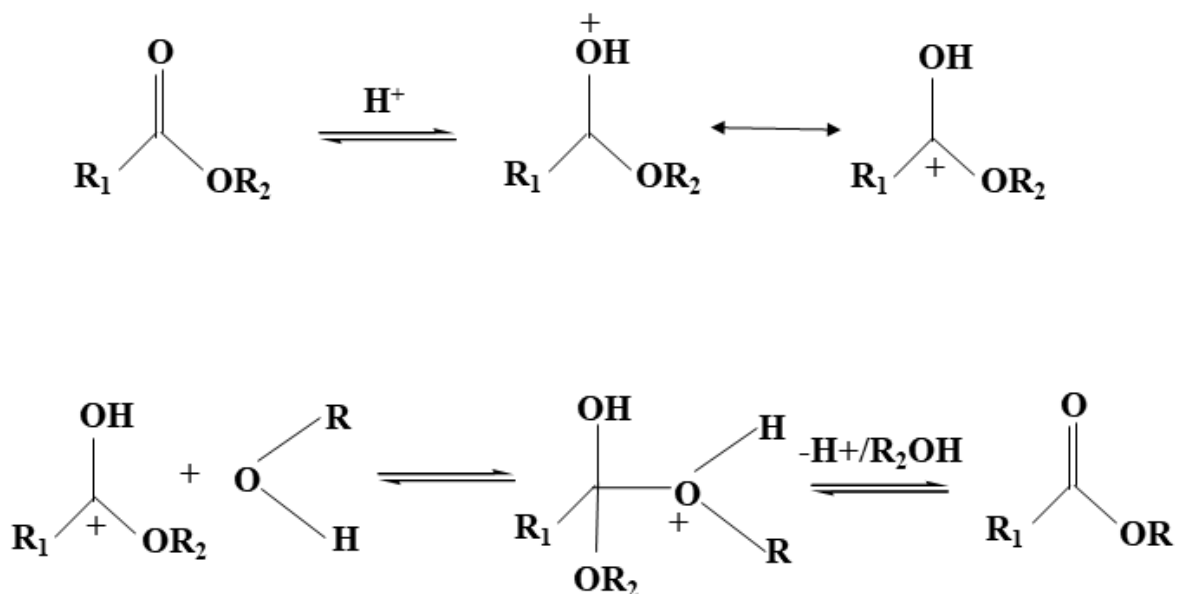
Figure 1.7. Acid catalyzed transesterification mechanism [134].

Base Catalyzed Transesterification

In this process, triglycerides react with methyl alcohol in presence of base catalyst and generate FAAE and glycerol. Majorly NaOH or KOH used in this process due to cheaper and react faster [135]. Later then, there are various reports on other alkaline earth metal oxides used for biodiesel production [136, 137]. Figure 1.8 shows the mechanistic steps involved in base catalyzed transesterification [134]. Pre-step involve the formation of alkoxide ion by reaction between alcohol and base catalyst. During the first step, the alkoxide ion attacks the triglyceride molecule's carbonyl carbon, forming a tetrahedral intermediate. This intermediate produces an alkoxide ion when it combines with an alcohol in the 2nd stage. In the final step, the tetrahedral geometry intermediate is rearranged to provide a diglyceride and an ester.

There are certain benefits to the transesterification, such as inexpensive costs and easy response conditions. Basic catalysts including alkaline hydroxides, methoxides, and carbonates are more frequently used to encourage the reaction because alkali-catalyzed transesterification proceeds far more quickly than acid-catalyzed transesterification [138]. In the figure 1.8, R_1 = fatty acids carbon chain, R_2 = glyceride molecule and R = alkyl group of alcohol.

$$OH^- + ROH \rightleftharpoons RO^- + H_2O$$
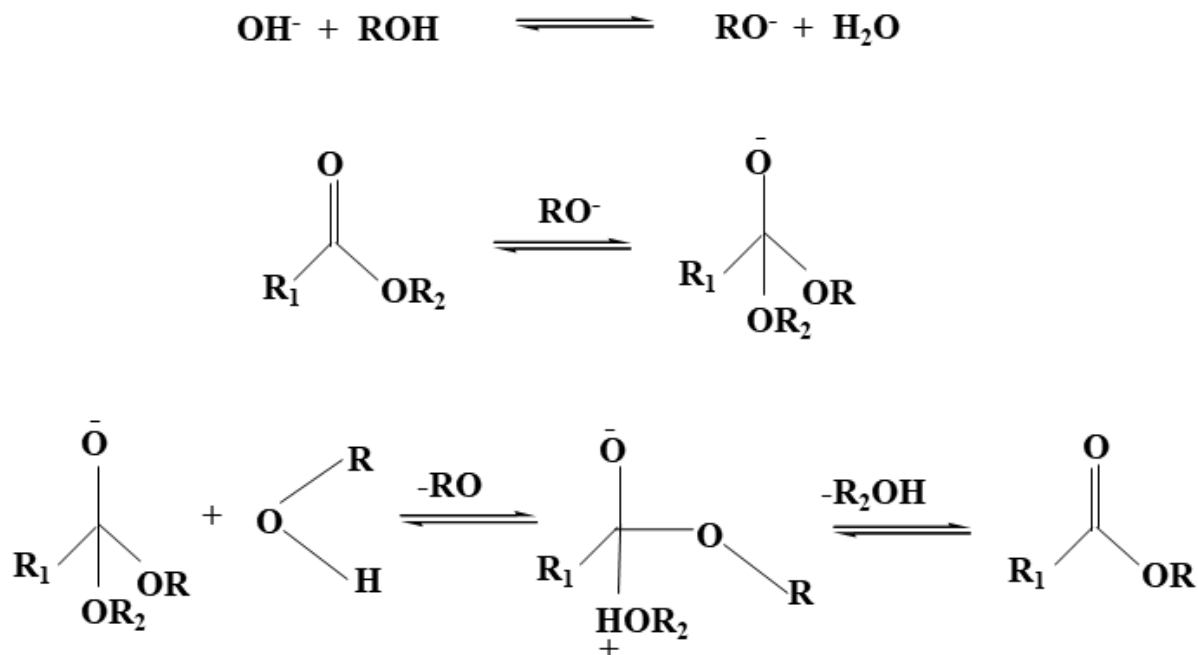
Figure 1.8. Mechanism of base catalyzed transesterification reaction [138].

Base and Acid Catalyzed Trans/Esterification (Two-Step Process)

There are some drawbacks regarding by usage of esterification and transesterification process individually to produce biodiesel. The alkali-catalyzed transesterification procedure produce biodiesel having poor yield due to presence of higher level of FFA in low-cost feedstocks because FFA combines with alkali and cause soap formation, which generally originate the emulsification and separation issues between alkyl esters and glycerol [139]. To address this problem, a two-step catalytic technique for making biodiesel has recently been developed. After an acid catalyst, such as H_2SO_4 or $FeSO_4$, is used in the first stage of feedstock pretreatment to lower the free fatty acid concentration, a basic catalyst is utilised in the second stage to generate biodiesel. A two-step FAME synthesis methodology was used by Wang et al., to convert waste cooking oil into methyl esters. Ferric sulphate is used in the esterification reaction to convert FFA to FAME, while KOH is used in the transesterification reaction to convert triglycerides to FAME [140]. Figure 1.9 depicts the two-step reaction of esterification and transesterification for biodiesel production in which, first step is showing the esterification through acid catalyst and in second step, KOH is used to produce biodiesel [141].
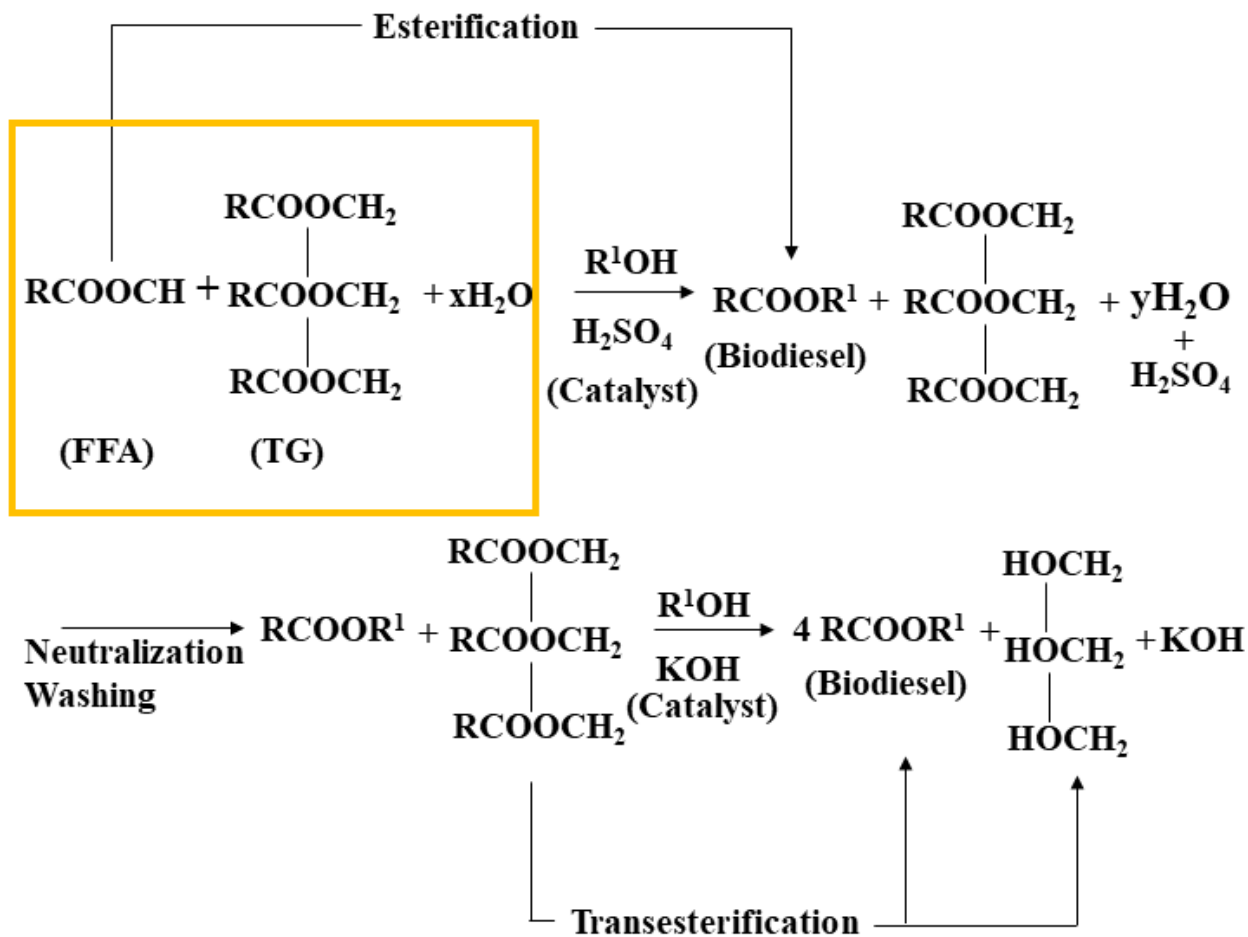
Figure 1.9. Two step reaction of esterification and transesterification for biodiesel production [141].

Although this method can turn waste or unrefined oils into biodiesel, it requires a lot of washing, separation, and reaction stages. To get rid of the extremely strong, acidic, or basic catalysts from the biodiesel product, several washings are needed. This leads to the production of a significant amount of wastewater and a catalyst loss [142]. However, each phase of the two-stage process must also address the catalyst removal issue. The first stage's catalyst removal problem can be overcome by neutralising the acid catalyst and using more alkaline catalyst in the 2nd phase. However, using additional catalyst would increase the cost of manufacturing biodiesel. Engine issues are typically brought on by the biodiesel product's residual acidic or alkaline catalyst. Whereas acid catalysts harm metallic engine parts, alkaline catalysts could produce larger volumes of combustible ash. Consequently, once the process is finished, the two catalysts must always be extracted from the biodiesel [143].

Simultaneous Acid/Base Esterification and Transesterification

Since the primary function of solid acid catalysts is to carry out the esterification of free fatty acids and the primary function of solid basic catalysts is to carry out the transesterification of triglycerides, it would be appropriate to find a solid catalyst that can act as both an acid and a base simultaneously in order to avoid the two-step process issues. Bifunctional solid catalysts are provided as a substitution for the biodiesel production so that the esterification and transesterification reactions can proceed at the same time. There are many reports which showed the simultaneous esterification and transesterification by using bifunctional heterogeneous solid catalyst [144-148].

Figure 1. 10 depicts the mechanism of simultaneous esterification and transesterification by using heterogenous solid catalyst which have both acidic and basic sites [149]. In the mechanism, M^- and A^+ represents the base and acidic site respectively. Using FFA adsorption on the acid site and methanol adsorption on the basic site of catalyst, respectively, esterification and transesterification were generated in the initial stage of this work. Then, at the catalyst for the esterification and transesterification processes, nucleophilic substitution of CH_3^+ and O_2^- at each methanol -OH and triglyceride carbonyl group was produced (step 2). The effect of the nucleophilic substitution would be intermediate. The ultimate product, biodiesel, was produced by the desorption of -OH and alkyl triglycerides from the catalyst when the C-O and -OH bonds were broken, respectively. Meanwhile, the catalyst's deprotonation provided the active species required to initiate the subsequent reaction.
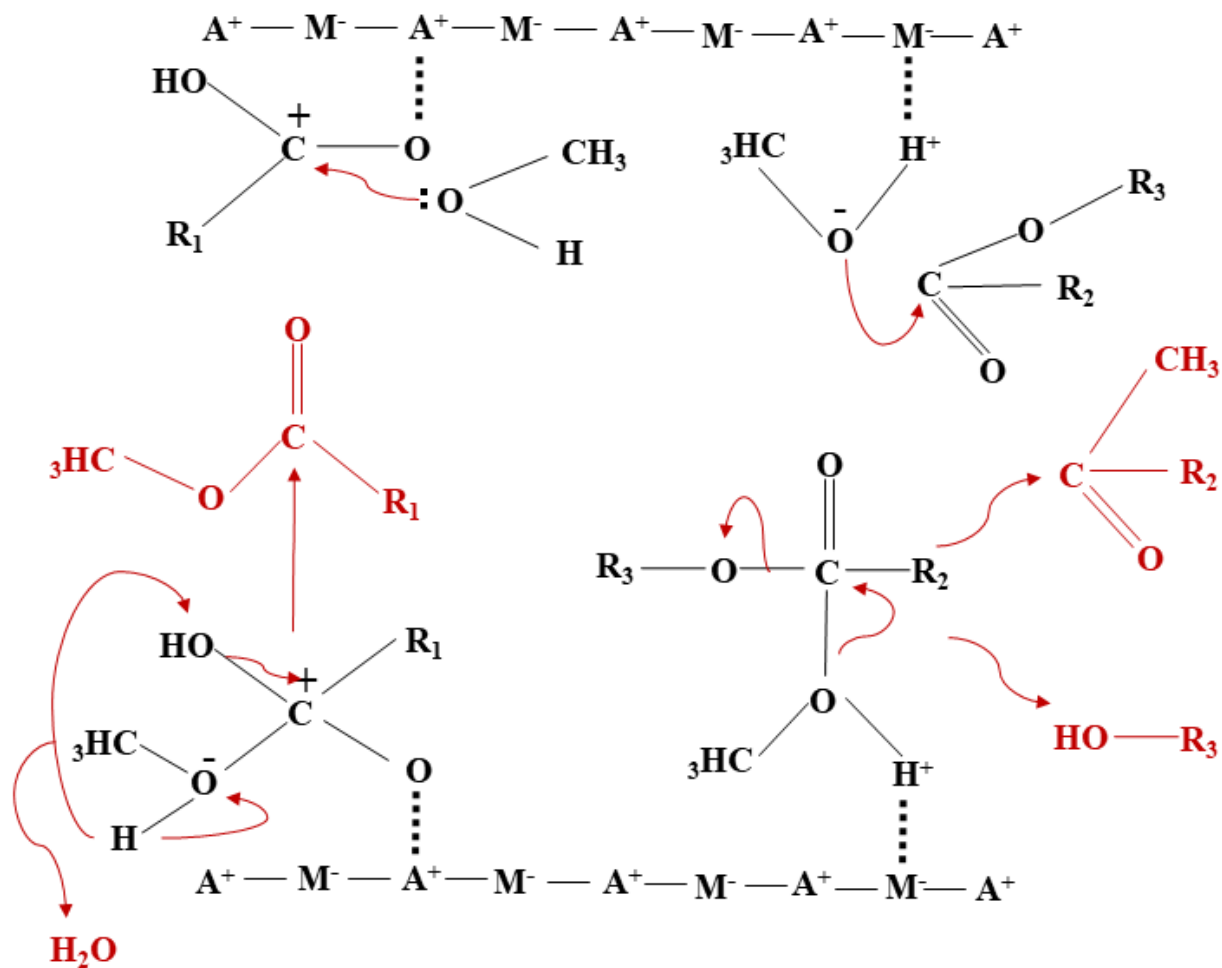
Figure 1. 10. Mechanism of simultaneously esterification and transesterification by using heterogenous solid catalyst having acidic and basic sites [149].

1.4.4. Optimized Parameters Involved in the Evaluation of Biodiesel

There are several factors which affect the biodiesel production that's why optimization needs to be produce highest yield of biodiesel. These factors are mentioned below.

1.4.4.1. Effect of Methanol to Oil Molar Ratio

Methanol to oil molar ratio is critical parameter for the synthesis of biodiesel. By stopping the transesterification process from continuing in a reversible way at the end of the reaction, the alcohol level controls the production of biodiesel. Many alcohols, including butanol, tert-butanol, methanol, and isopropanol, can be used to transesterify oils. This method works well with lower alcohols, including methanol and ethanol. Because they are more expensive, other alcohols are not

often used. Methanol is distinct from other alcohols due to its unique physical and chemical characteristics. For instance, it interacts quickly with triglyceride and dissolves easily in base. In the transesterification reaction, the amount of water in the alcohol is also crucial since too much water could react with the triglyceride and induce saponification [150]. High methanol: oil is thought to improve the conversion of triglycerides to monoglycerides and fastens the transesterification process. In the transesterification process, three moles of fatty acid ester and one mole of glycerol are typically produced for every one mole of triglycerides. However, to maximise the yield of biodiesel, a higher molar ratio is needed to improve the solubility of methyl alcohol and triglyceride molecules as well as the likelihood of their exposure. Moreover, significant quantities of methanol are needed to accelerate and boost output by severing the fatty acid and triglyceride bond. In commercial transesterification techniques, excess dry alcohol (6:1 alcohol-to-oil molar ratio) causes the synthesis of alkyl esters [150].

Glycerol is easily extracted from the reaction slurry by settling or centrifugation since it is insoluble in biodiesel. However, the solubilization of glycerol in biodiesel rises when high molar ratios are used; free glycerol can then either persist in the biodiesel as tiny, dissolved amounts or as suspended droplets. Alcohols can behave like co-solvents, which increases the solubilization of glycerol in biodiesel. Furthermore, to separate and recycle of the leftover methanol at the end of the reaction, there is always need of large amount of energy. As a result, to keep away from the loss of yield and an unproductive methanol reusing process, an acceptable volume of methanol must be specified [150, 151].

1.4.4.2. Effect of Catalyst Dose

One of the important factors in achieving highest biodiesel yield is catalyst loading in the transesterification reaction. Usually, the lowest catalyst concentration is found early in the process and is then increased according to the product content and reaction circumstances. Amani et al., demonstrated that increasing the catalyst loading increased FAME content to a certain extent. Their research indicates that a catalyst loading of 3 weight percent with a FAME content of 90% is ideal. Increased catalyst concentrations decreased the production of biodiesel; in the presence of 4% catalyst, the FAME level fell to 83% [152]. Increasing catalyst loading, according to Ezebor et al., results in product adsorption and, eventually, a decrease in FAME synthesis [153]. The main problem with employing large concentrations of basic catalysts is that the catalyst reacts with FFA

to produce saponification and water, which reduces the output of biodiesel. Additionally, it was found that 86.4% of the biodiesel output was obtained at 3 weight percent H_2SO_4, but the yield of FAME was unaffected by higher catalyst concentrations (5 and 7 weight percent) [154].

1.4.4.3. Effect of Reaction Temperature

Temperatures below the melting point of oil would be unfeasible due to its highly viscous nature. Higher temperatures generally accelerate the process by improving mass transfer. Nevertheless, raising the temperature above a particular point is either not economically viable or has detrimental consequences on the reactants and/or reagents (degradation, side reactions, vaporisation). Therefore, temperature optimisation is essential for both practical biodiesel synthesis and reactor design. It is important to remember that the optimal temperature for the manufacture of commercial biodiesel is lower than the boiling point of alcohol. Because one of the reagents, i.e., alcohol, vaporises at higher temperature, the two characteristics yield, and mass transfer of the biodiesel drop [151].

1.4.4.4. Effect of Reaction Time

When reaction time is increased, biodiesel yield increases, according to Freedman et al (1986). Because of the mixing and dispersion of the alcohol and oil, the reaction is gradual at first. Following that, the reaction is rapid [155]. However, the maximum ester conversion was completed in ninety minutes. Biodiesel/mono alkyl ester is the yield product; longer reaction times have no influence on this product. Furthermore, because transesterification is a reversible reaction that produces soap and resulting in the loss of esters, a longer reaction time lowers the final product (biodiesel) [156].

1.4.5. Analytical Techniques for Biodiesel Production Determination

GC and HPLC are typically used to analyse the most relevant biodiesel parameters (glycerol, fatty mono-alkyl esters, their acyl derivatives, and fatty acids). Because of its excellent precision in quantifying small components, GC has been the most widely utilised technology. GC accuracy, however, can be adversely affected by beginning drift, overlapping signals, and the ageing of standards and samples. Moreover, sample derivatization is often necessary for GC investigations, particularly to produce trimethylsilyl hydroxyl group derivatives. Although this method improves chromatographic separation, the analysis takes longer. The most common detector used in GC is

flame ionisation detection (FID), but mass spectrometers are becoming more popular. The latter removes any ambiguities about the identity of the eluting components, while it may impair quantification. HPLC analysis is less widely employed in characterization of biodiesel than GC analysis, but it is faster and does not require sample derivatization. Furthermore, this technology is better suited for blend analysis than GC and can be used to generate the biodiesel from a various type of feedstock. A variety of detectors for HPLC biodiesel analysis are presented, with ELSD being particularly useful [157].

Most typically, spectroscopic techniques are employed to monitor the transesterification reaction and evaluate the blend level. In these assessments, FT-IR and NMR spectroscopy are regularly used. Because it is a quick and easy detection approach, FT-IR is being used as a new analytical methodology for detecting biodiesel conversion. In the infrared region of the electromagnetic spectrum, raw oils and methyl esters are highlighted as strong absorbers. NMR has been demonstrated as effective tool for judgement of biodiesel grade and quantifying diesel/biodiesel mixtures. Moreover, NMR is an efficient approach, but the instrumentation expenses are somewhat higher [158].

1.4.6. Types of Catalysts for Biodiesel Production

Majorly, there are three types of catalysts reported for biodiesel production i.e., homogenous, heterogenous, and enzymatic catalysts [159]. The prime focus is on heterogeneous catalysts.

1.4.6.1.   Homogeneous Catalysts

In the homogeneous transesterification of oil and alcohols to synthesize biodiesel, there are two types of catalysts used i.e., acidic, and basic catalysts. When compared to acid catalysts, basic catalysts promote quicker reactions (nearly 4000 times faster).

Most studied catalysts are homogeneous base catalysts in the transesterification of vegetable oil to FAME because of the affordability and wide availability. Meng et al., examined biodiesel production by using NaOH from waste cooking oil and reported the biodiesel yield 89.8% under optimum conditions (reaction time; 1.5 hr, methanol/oil; 9/1, reaction temperature; 50°C and catalyst dose 1 wt%) [160]. Furthermore, Rashid et al., used $NaOCH_3$ for biodiesel synthesis from rice bran oil and got 83.3% yield under optimal conditions (methanol/oil; 7.5/1, reaction time; 1 hr catalyst dose 0.99 wt% and reaction temperature; 55°C) [161]. Moreover, Yusup et al., used

KOH and methanol for biodiesel production and under optimum conditions (reaction time; 5 hr, reaction temperature; 55°C, methanol/oil; 8/1 and catalyst dose 2 wt%) total yield was 98% [162]. Later, Atadashi et al., used same alkaline catalyst and examined biodiesel production from roselle oil and according to their findings, under optimal conditions (reaction time; 1 hr, reaction temperature; 60°C, methanol/oil; 8/1 and catalyst dose 1.5 wt% biodiesel yield was 99.4% [163].

Base catalysts are frequently chosen over acid catalysts due to their higher reactivity and lower cost. Nevertheless, during transesterification, base catalysts cause saponification, which could deplete the catalyst reactivity. Up till now, there are various reports on homogenous acidic catalyst (H_2SO_4, HCl, H_3PO_4, HF and sulfonated acids) for biodiesel production from the vegetable oil feedstock [163]. However, there are several disadvantages to acid-catalyzed biodiesel generation, such as a high alcohol-to-oil molar ratio and a slow reaction rate. It has corrosive and environmental problems as well. Acid-catalyzed biodiesel synthesis is less prevalent and studied because of these disadvantages. Veljkovic et al., reported the biodiesel yield of 91% by using H_2SO_4 and feedstock of tobacco seed oil under optimized conditions (reaction time; 25 min, reaction temperature; 60°C, methanol/oil; 18/1 and catalyst dose 1 wt%) [164]. Later then, Miao et al., examined biodiesel production through triflouroacetic acid from soyabean oil with the percent yield of 98.4 under optimized conditions (reaction time; 5 hr, reaction temperature; 120°C, methanol/oil; 20/1 and catalyst dose 2 M) [133]. Moreover, Ehiri at al., used HCl and methanol for biodiesel synthesis from beef tallow and reported the biodiesel yield of 96.3% under optimized conditions (reaction time; 1.5 hr, reaction temperature; 60°C, methanol/oil; 6/1 and catalyst dose 0.5 wt%) [165].

The homogeneous catalyst has several benefits, including high reactivity and low cost, but there are also serious drawbacks when using it to produce biodiesel. These shortcomings include the low-quality level of glycerol that is generated, the difficulty of regenerating the catalyst, and the drawn-out process needed to purify biodiesel. The entire process is therefore ineffective and time-consuming. Because they may be easily reused for multiple cycles of catalytic reaction, heterogeneous catalysts have drawn a lot of interest in recent years for the manufacture of biodiesel. This could reduce the manpower required and the cost of producing biodiesel [166].

1.4.6.2. Heterogeneous Catalysts

Heterogeneous catalysed process is defined as the catalyst and reaction mixture are in different phase and the catalytic surface is the predominant site for the reaction to occur. The heterogenous catalyst mostly used in solid phase. Compared to homogeneous catalysts, heterogeneous catalysts provide several benefits, including easy to separate and reusability. Furthermore, solid catalysts usually use less energy. They are probably less corrosive and less hazardous. As a result, solid catalysts provide an efficient and cost-effective method of producing biodiesel [167]. Basically, heterogenous catalysts divided into two types of catalysts acidic and basic. But now a days synthesizing bifunctional catalysts is more advanced technology due to the simultaneous esterification and transesterification feature for biodiesel production. The classification is mentioned below.

Heterogeneous Acid Catalysts

The heterogeneous acid catalyst is simple to recover throughout the transesterification reaction, has many active sites, is moderately acidic and hydrophobic, reduces diffusion issues, and can significantly increase biodiesel yields. There are two types of acidic sites on heterogeneous acid catalysts i.e., Lewis and Bronsted acid sites. Lewis's acid sites are electron pair acceptor type catalysts and Bronsted acid sites are proton donor type catalysts. Both acidic sites on heterogeneous acid catalysts favour esterification and ester exchange processes [168]. Most commonly, mixed metal oxides, sulfated metal oxides, mesoporous silica, heteropoly acids (HPAs) were used as heterogeneous acid catalysts [169, 170].

There are many reports on mixed metal oxides used for biodiesel production from different edible and non-edible feedstocks. Xie et al., synthesized tin oxide supported on tungsten oxide (WO_3/SnO_2) and used for the biodiesel synthesis from soyabean oil. According to their report, 79.2% methyl esters were produced under optimal conditions (reaction time; 5 hr, reaction temperature; 110°C, methanol/oil; 30/1 and catalyst dose 5 wt%) [171]. Moreover, Zr-Mo based acid catalysts for the FAME production (94.2%) through oleic acid feedstock under optimized conditions (reaction time; 2 hr, reaction temperature; 180°C, methanol/oil; 10/1 and catalyst dose 4 wt%) reported by Zhang et al., [172]. Furthermore, Suzuta et al., synthesized FeO_x/SiO_2 and used for the biodiesel synthesis form jatropha oil. They reported 99% FAME yield under optimal

conditions (transesterification reaction time; 3 hr, reaction temperature; 220°C, methanol to oil ratio; 218/1 and catalyst dose 15 wt%) [173]. Later, Thirunavukkarasu et al., examined $ZnAl_2O_4$ and $ZnFe_2O_4$ for biodiesel synthesis from multiple feedstocks (sunflower oil, waste cooking oil and jatropha oil). In the presence of these catalysts, FAME yield was highest due to the Zn (3d electronic excitation). The reported yield was greater than 90 percent under optimized conditions (reaction time; 10 hr, methanol/oil; 9/1, reaction temperature; 180°C and catalyst dose 5 wt%) [174].

Sulfated inorganic metal oxides are said to possess exceptional acid-base and redox characteristics, as well as being chemically stable and having a super acidity equal to 100% sulfuric acid. Lam et al., investigated sulfated tin oxide supported on silica (SO_4^{2-}/SnO_2-SiO_2) for FAME synthesis from the waste cooking oil and reported the yield (92.3%) under optimum conditions (reaction time; 3 hr, reaction temperature; 150°C, methanol/oil; 15/1 and catalyst dose 3 wt%) [175]. Moreover, Gardy et al., synthesized propyl sulfonic acid supported on titania (TiO_2/$PrSO_3H$) and used for the biodiesel production from waste cooking oil. The yield (98.3%) was reported under the conditions (reaction time; 9 hr, reaction temperature; 60°C, methanol/oil; 15/1 and catalyst dose 4.5 wt%) [176].

Mesoporous materials i.e., MCM-41 and SBA-15 are also reported for biodiesel synthesis. Because of their exceptionally high surface area, which allows for a high concentration of active sites per mass of material, and relatively large pore size, which make easier mass transfer diffusion, ordered mesoporous silica are advantageous supports for heterogeneous catalysis [177]. Furthermore, the amorphous pore walls of mesoporous silica allow for post-synthesis modifications, such as pore size control framework stabilization, compositional changes, or the creation of mesoporous/zeolite composite materials, which greatly increase the flexibility of the material's composition and pore channel structure [178]. Samart et al., used calcium oxide supported on mesoporous silica (CaO/SiO_2) for biodiesel production from soyabean oil and the yield was 95.2% under optimum conditions (reaction time; 8 hr, reaction temperature; 60°C and catalyst dose 5 wt%) [179]. Moreover, Sharma et al., prepared sulfated titanium supported SBA-15 (Ti-SBA-15). From unrefined canola oil, biodiesel was synthesized. The FAME yield (91%) was obtained under the optimized conditions (reaction time; 4 hr, methanol/oil; 15/1, catalyst dose 1 wt%, and reaction temperature; 200°C) [180]. Later then, Karnjanakom et al., examined methyl

sulfonic acid functionalized MCM-41 (SO_3H-MCM-41) for the biodiesel synthesis through para rubber seed oil. It was reported that the biodiesel yield was 95.5% under the optimal conditions (reaction time; 2 hr, reaction temperature; 153°C and catalyst dose 5.06 wt%) [181].

HPAs are among the several solid acid catalysts that are regarded to be particularly useful to produce biodiesel because of their high acidity, high tolerance factor for high FFAs and water content [182]. Monge et al., investigated 12-tungstophoshoric acid supported over zirconia (HPW/ZrO_2) for FAME production through palmitic acid with a yield of above 90% [183]. Recently, Esmi et al., used same HPAs supported on mesoporous aluminosilicates (HPW/MAS) for biodiesel synthesis through the green seed canola oil feedstock with the FAME yield (89%) under optimized conditions (reaction time; 8 hr, reaction temperature; 200°C, methanol/oil; 27.2/1 and catalyst dose 5.9 wt%) [184].

Heterogeneous Basic Catalysts

The reason why basic heterogeneous catalysts have drawn the most interest recently is that they show exceptional catalytic activity under mild reaction conditions and have the potential to overcome the limitations of homogeneous basic catalysts. These catalysts, however, are only appropriate for low-FFA biodiesel feedstock; in other cases, the catalysts will react with the FFA through the saponification reaction, producing soap. This reduces the biodiesel yield by making the process of separating biodiesel from glycerol time-consuming. Commonly, alkaline earth metal oxides, transition metal oxides and mixed metal oxides were used as the heterogeneous base catalysts for the biodiesel synthesis.

Rasouli et al., reported MgO nanoparticles for biodiesel synthesis through goat fat with a yield of 93% under optimum conditions (reaction temperature; 70°C, methanol/oil; 12/1, reaction time; 3 hr and catalyst dose 1 wt%) [185]. Moreover, Zhang et al., prepared SrO-CaO-Al_2O_3 and used for the biodiesel synthesis through transesterification of palm oil. The biodiesel yield was 98.16% under optimized conditions (reaction time; 3 hr, reaction temperature; 65°C, methanol/oil; 18/1 and catalyst dose 7.5 wt%) [186]. Later, Booramurthy et al., used Fe_3O_4/BaO for FAME production through fat extracted from tannery sludge and reported optimum yield (97.6%) under the conditions (reaction temperature; 65°C, methanol/oil; 18/1, reaction time; 5 hr, and catalyst dose 8 wt%) [187]. Furthermore, Hameed et al., used calcium oxide loaded on activated carbon (Ca/AC)

for biodiesel synthesis through waste cooking oil. The FAME yield (96%) was reported under optimized conditions (reaction temperature; 65°C, methanol/oil; 8/1, reaction time; 160 min, and catalyst dose 5 wt%) [188].

Transition metal oxides have been reported for biodiesel synthesis because they are cheaply available, highly stable, and display outstanding catalytic activity. Kaur et al., synthesized Li/NiO and used for biodiesel synthesis by using ethanol as a solvent from waste cottonseed oil. Greater than 98% yield was produced under optimized conditions (reaction time; 3 hr, reaction temperature; 65°C, ethanol/oil; 12/1 and catalyst dose 5 wt%) [189]. Moreover, Baskar et al., synthesized Mn@ZnO for biodiesel synthesis from mahua oil with a yield of (97%) under optimized conditions (reaction time; 50 min, reaction temperature; 50°C, methanol/oil; 7/1 and catalyst dose 8 wt%) [190]. Furthermore, Seffati et al., synthesized $CaO/CuFe_2O_4$ for biodiesel synthesis by using chicken fat. It was reported that the biodiesel yield (94.52%) was under optimized conditions (reaction time; 4 hr, reaction temperature; 70°C, methanol/oil; 15/1 and catalyst dose 3 wt%) [191].

There are several mixed metal oxides reported for biodiesel synthesis. Kawashima et al., synthesized CaO/CeO_2 and used for biodiesel production from rapeseed oil with the yield of 90% under the optimized conditions (reaction time; 10 hr, reaction temperature; 60°C, methanol/oil; 6/1 and catalyst dose 10 wt%) [192]. Later then, Madhuvilakku et al., used TiO_2/ZnO for FAME production from palm oil under the optimized conditions (reaction time; 5 hr, reaction temperature; 60°C, methanol/oil; 6/1 and catalyst dose 14 wt%) with 92% yield [193]. Recently, Banerjee et al., reported Sr-Ce based mixed metal oxides for the transesterification of waste cooking oil to produce biodiesel. They examined the biodiesel yield 99.5% under the optimal conditions (reaction time; 2 hr, reaction temperature; 65°C, methanol/oil; 14/1 and catalyst dose 2 wt%) [194].

Bifunctional Catalysts

Up till now, there have been various reports on bifunctional catalysts for biodiesel production. Farooq et al., synthesized Mo–Mn/γ-Al_2O_3–MgO for FAME production from waste cooking oil under the optimized conditions (reaction temperature; 100°C, methanol/oil; 27/1, reaction time; 4 hr, and catalyst dose 15 wt%) with yield 91.4% [195]. Furthermore, Sulaiman et al., synthesized Cu/Zn/γ-Al_2O_3 and used for the biodiesel production from low grade cooking oil. They reported

the biodiesel yield 88.82% under the optimum conditions (reaction temperature; 65±5°C, methanol/oil; 18/1, reaction time; 3 hr, and catalyst dose 6 wt%) [196]. Later then, Saadi et al., examined SrO-ZnO/Al_2O_3 for the biodiesel production from waste cooking oil with the FAEE yield 95.7% (reaction time; 5 hr, reaction temperature; 75°C, ethanol/oil; 10/1 and catalyst dose 15 wt%) [148]. Moreover, Dai et al., used $LiNbO_3$ for the biodiesel synthesis through soyabean oil with the yield 98.08% under the optimum conditions (reaction temperature; 65°C, methanol/oil; 24/1, reaction time; 6 hr, and catalyst dose 2 wt%) [149]. Recently, Li et al., developed $SrTi_{0.85}Fe_{0.15}O_3$ and used for biodiesel production from palm oil under optimal conditions (reaction time; 3 hr, reaction temperature; 150°C, methanol/oil; 18/1 and catalyst dose 5 wt%) with total experimental yield of 97.52% [197].

1.4.6.3.   Biocatalysts

In recent years, biocatalysts i.e., enzymes have been used for the biodiesel synthesis due to some characteristics (inhibit soap formation, improvement in product separation and environmentally friendly). Rafiei et al., used lipase@ZIF-67 for FAME production from soyabean oil. They reported the experimental yield of 78% under the optimized conditions (reaction time; 60 hr, reaction temperature; 45°C, methanol/oil; 6/1 and catalyst dose 10 wt%) [198]. Furthermore, Jayaraman et al., examined lipase enzymes for biodiesel production through waste cooking oil with the optimum yield of 88% under the conditions (reaction time; 4 hr, reaction temperature; 65°C, methanol/oil; 3/1 and catalyst dose 1.5 wt%) [199].

1.5.   Aims and Objectives

With the increase in energy crisis and environmental issue caused by the rapid consumption and burning of fossil fuels, respectively, the development of green and sustainable energy resources by means of energy conversion and storage technologies is of utmost importance. Hydrogen and biodiesel are among the sustainable fuel routes to encounter rapidly growing energy demands. Noble metal-based catalysts have so far been developed as state-of-the-art materials for hydrogen production while strong acids/bases are used for biodiesel production from different feedstocks. However, the high cost of noble metals and the corrosion/soap formation by strong acids/bases limit the practical applications of these catalysts. Therefore, the presented work aims to synthesize

cheap and environmental friendly bifunctional catalysts over different substrates for water splitting reactions and biodiesel production.

1.6. Plan of Work

In view of the aim of this designed work, it was planned to focus on the synthesis and of bifunctional catalysts for electrochemical water splitting and biodiesel conversion.

Focusing on the first aim, it was intended to synthesize bifunctional catalysts for electrochemical water splitting reaction through solution mixing method. The synthesis of electrocatalysts based on post transition-metal oxide (Bi_2O_3) and 3d-transition metal oxides (Ni, Co, Fe, Mn) was planned for OER and HER reactions. Composites were planned to be supported on NiF and CNTF as electrode materials for OER in basic medium (1M KOH) while OER/hydrogen HER in neutral (1M PBS) medium. It was further planned to synthesize three different transition metal-based POMs and fabricate on the surface of CNTF for OER activity in basic medium.

Furthermore, for the second aim of catalysts for biodiesel production, bifunctional catalysts based on tungsten oxide (WO_3) over mesoporous material MCM-41 impregnated with alkaline earth metal (Mg, Ca, Sr, Ba) oxides were planned to be synthesized. It was further planned to test the synthesized composites for biodiesel synthesis using corn and waste cooking oil as feedstocks under varying conditions of oil to methanol ratio, catalyst doze, reaction temperature and time. The purity of biodiesel produced was planned to be characterized through ^{1}H-NMR spectroscopy.

Chapter-2   Experimental

This chapter discusses the synthetic schemes of all the electrocatalysts, their characterization techniques and electrochemical measurements

2.1. Materials and Chemicals Used

During research work, different chemicals used which are tabulated in table 2.1. It is worth mentioning here that all chemicals were used without further purification.

Table 2.1. Materials and chemicals used in the research work.

Materials/chemicals	Formula	Purity (%)	Supplier
Sodium tungstate dihydrate	$Na_2WO_4.2H_2O$	99	Sigma Aldrich
Glacial acetic acid	CH_3COOH	99.9	Sigma Aldrich
Nickel acetate tetrahydrate	$Ni(CH_3COO)_2.4H_2O$	≥98	Sigma Aldrich
Cobalt acetate tetrahydrate	$Co(CH_3COO)_2.4H_2O$	≥98	Sigma Aldrich
Iron acetate tetrahydrate	$Fe(CH_3COO)_2.4H_2O$	≥98	Sigma Aldrich
Bismuth nitrate pentahydrate	$Bi(NO_3)_2.5H_2O$	≥98	Sigma Aldrich
Nickel nitrate hexahydrate	$Ni(NO_3)_2.6H_2O$	≥98	Sigma Aldrich
Cobalt nitrate hexahydrate	$Co(NO_3)_2.6H_2O$	≥98	Sigma Aldrich
Iron chloride hexahydrate	$FeCl_3.6H_2O$	≥98	Merck
Manganese nitrate hexahydrate	$Mn(NO_3)_2.6H_2O$	≥98	Sigma Aldrich
Disodium hydrogen phosphate	Na_2HPO_4	99.9	Sigma Aldrich
Sodium dihydrogen phosphate	NaH_2PO_4	99.9	Merck
Calcium sulfate dihydrate	$CaSO_4.2H_2O$	≥98	Sigma Aldrich
Magnesium sulfate	$MgSO_4$	≥98	Merck
Strontium nitrate	$Sr(NO_3)_2$	≥98	Sigma Aldrich
Sodium chloride	$NaCl$	99.9	Sigma Aldrich
Barium nitrate	$Ba(NO_3)_2$	≥98	Sigma Aldrich
Cetyl trimethyl ammonium bromide (CTAB)	$C_{19}H_{42}BrN$	≥98	Sigma Aldrich

Tetraethyl ortho silicate (TEOS)	$SiC_8H_{20}O_4$	≥98	Alfa Aesar
Ammonium hydroxide	NH_4OH	≥99	Sigma Aldrich
Potassium hydroxide	KOH	≥99	Sigma Aldrich
Potassium chloride	KCl	≥99	Sigma Aldrich
Nafion	$C_9HF_{17}O_5S$	5% solution	Sigma Aldrich
Ethanol	C_2H_5OH	Absolute	Commercial
Methanol	CH_3OH	Absolute	Commercial
Distilled water	H_2O		In-house distillation plant
Nickel foam (NiF)			Commercial
Carbon nanotube fiber (CNTF)			Huisheng Peng group, China
Teflon tape			Commercial

2.2. Characterization Techniques

The synthesized catalysts for electrochemical water splitting and biodiesel production were characterized through various analytical techniques. The details of these techniques are discussed as follow.

2.2.1. Powder X-ray Diffraction Analysis (PXRD)

The PXRD spectra were recorded using a PAN analytical X′pert equipped with a Cu-Kα radiation source of wavelength 1.54 Å, and 2θ values ranging from 10° to 70°

2.2.2. Fourier Transform Infrared Spectroscopy (FT-IR)

The FT-IR absorption spectra for synthesized solid composites were recorded on Nicolet Summit Lite spectrophotometer (USA) in the frequency range of 1200-500 cm^{-1} was used.

2.2.3. Scanning Electron Microscopy (SEM) and Energy Dispersive X-ray Analysis (EDX)

The morphological features were obtained by SEM using FEI NOVA SEM-450, while elemental analysis was conducted using EDX (INCAX-Act).

2.2.4. X-ray Photoelectron Spectroscopy (XPS)

For the XPS measurements, the samples were first suspended in acetone and subsequently deposited onto highly doped silicon wafers with a natural oxide layer. To prevent any undesired charging during photoelectron measurements, the prepared samples were attached to a sample holder using conducting carbon tape. The affixed samples were then introduced into an ultra-high vacuum (UHV) chamber via an airlock. Inside the UHV chamber, an ultra-low vacuum pressure of 2×10^{-9} mbar was maintained. The UHV chamber contained two main components for the experiment: i) X-ray Excitation Source: A water-cooled X-ray gun, equipped with a double Mg/Al source (Specs XR 50), was employed to generate excitation. ii) Electron Analyzer: Positioned at an angle of 54 degrees relative to the X-ray gun's direction, a hemispheric electron analyzer (Specs Phoebos 100) was used. In this experiment, MgKα radiation (1253.6 eV) served as the source of excitation. For the detection of photoelectrons, a large-area lens mode was employed, and the fixed analyzer transmission was set at a pass energy of 30 eV. Acquired data were processed and analyzed using CASA XPS software. Shirley's method was used to subtract the background signal.

2.2.5. Nitrogen Adsorption and Desorption Analysis

An equipment called the NOVA-4000e was used to record the nitrogen adsorption isotherms. Prior to the measurement, the samples were degassed for 24 hours at 150°C while under vacuum. The BET method was used to evaluate the specific surface areas in the P/P0 range of 0 to 1. The BET specific surface area was calculated in the range of 0.04 to 0.1. The adsorption branch of isotherms data was subjected to the BJH pore analysis, which yielded the pore size distribution and pore volume.

2.2.6. ^{1}H-NMR Spectroscopy

The esterification/transesterification products were confirmed using ^{1}H NMR spectroscopy. A Bruker AC spectrometer was used to record ^{1}H NMR spectra at 300.13 MHz using $CDCl_3$ as a solvent. Reference standard as tetramethyl silane was used.

2.3. Synthesis of Bifunctional Mixed Metal Oxides for Electrochemical Water Splitting Reaction

For the water splitting application, bifunctional composites based on post transition-metal oxide (Bi_2O_3) and 3d-transition metal oxides (Ni, Co, Fe, Mn) were synthesized according to following procedure.

2.3.1. Synthesis of Bismuth Oxide (Bi_2O_3)

To synthesize Bi_2O_3, a reported hydrothermal method was performed [200] with slight modification. Briefly, 25 mL aqueous solutions of 1.45 g (2.98 mmol) $Bi(NO_3)_3 \cdot 5H_2O$ and 0.56 g (3.94 mmol) Na_2SO_4 were prepared separately. Both solutions were mixed and stirred for 20 minutes at room temperature followed by the dropwise addition of 25 mL of 0.71 g (17.75 mmol) NaOH. The reaction mixture was then heated in muffle furnace in an autoclave for 1 h at 120°C. The reaction mixture was cooled to room temperature and the yellow precipitates settled down were filtered and washed thoroughly with ethanol and distilled water. Finally, the product was dried at 80°C in an oven.

2.3.2. Synthesis of Bi_2O_3/NiO

The composite of Bi_2O_3/NiO was prepared by solution mixing method. For that first NiO was synthesized through a reported co-precipitation method with slight modification [201]. Briefly, 0.87 g (4.76 mmol) of $Ni(NO_3)_2 \cdot 6H_2O$ was prepared in 60 mL of deionized water. The solution's pH was maintained at 11 by adding 10 mL NH_4OH (32%) solution. The reaction mixture was heated with constant stirring for 3 h at 80°C and then centrifuged at 2000 rpm for 10 minutes. The light green precipitates settled were filtered and washed with ethanol and distilled water. The product was calcined at 700°C in the air for 4 hours.

After the synthesis of NiO, the composite was synthesized by suspending and sonication of 0.05 g of each Bi_2O_3 (0.11) mmol) and NiO (0.67 mmol) in 25 mL of distilled water. Both the suspended solutions were mixed, and the reaction mixture obtained was sonicated for 1 h. The obtained composite product was separated by centrifugation for 10 minutes at 2000 rpm and then dried at 70°C in an oven.

2.3.3. Synthesis of Bi$_2$O$_3$/Co$_3$O$_4$

For the synthesis of Bi$_2$O$_3$/Co$_3$O$_4$, cobalt oxide (Co$_3$O$_4$) nanoparticles were first synthesized by dissolving 1.0 g (5.46 mmol) of Co(NO$_3$)$_2$.6H$_2$O in 60 mL of distilled water. By dropwise adding 10 mL of NH$_4$OH (32%) solution, the pH of the mixture was maintained at 11. The reaction mixture was heated at 80°C for 10 minutes and then cooled to room temperature. The mixture was centrifuged at 2000 rpm to separate the precipitates. After filtering and washing with distilled water and ethanol, the blackish precipitates settled. The product was calcined at 700°C for 4 h in the air.

By using a simple solution mixing method, Bi$_2$O$_3$/Co$_3$O$_4$ was synthesized. This was accomplished by suspending 0.05 g of Co$_3$O$_4$ (0.21 mmol) and Bi$_2$O$_3$ (0.11 mmol) in 10 mL of distilled water, which were sonicated for 15 minutes. The two suspended solutions were combined, and the resultant reaction mixture was sonicated for an hour. After being separated by centrifugation for 10 minutes at 2000 rpm, the resultant composite product was dried in an oven at 70°C.

2.3.4. Synthesis of Bi$_2$O$_3$/Fe$_2$O$_3$

Fe$_2$O$_3$ nanoparticles were first synthesized by dissolving by 1.25 g (4.62 mmol) of FeCl$_3$.6H$_2$O in 60 mL of distilled water. The pH of the mixture was maintained at 11 by dropwise addition of NH$_4$OH (32%) solution. The reaction mixture was heated to 80°C for 3 h and then centrifuged for 10 minutes at 2000 rpm to separate reddish brown precipitates that was washed with ethanol and distilled water. The product was calcined at 700°C for 4 h.

For the synthesis of Bi$_2$O$_3$/Fe$_2$O$_3$, solution A and B was formed by dissolving 0.05 g of Fe$_2$O$_3$ (0.31 mmol) and 0.05 g Bi$_2$O$_3$ (0.11 mmol) in 10 mL distilled water separately and then sonicated for 15 minutes. Then both the solutions were mixed, and the resultant reaction mixture was sonicated for an hour. The resultant composite was separated by centrifugation for 10 minutes at 2000 rpm, filtered and was dried in an oven at 70°C.

2.3.5. Synthesis of Bi$_2$O$_3$/MnO

MnO nanoparticles were first synthesized by dissolving 1.6 g (5.57 mmol) of Mn(NO$_3$)$_2$.6H$_2$O in 60 mL of distilled water. The pH of reaction mixture was maintained at 11 by using NH$_4$OH (32%) solution. After 3 h of constant stirring at 80°C, the reaction mixture was centrifuged for 10 minutes

at 2000 rpm. After filtration and washing with ethanol and distilled water, black-brown precipitates were calcined for 4 h at 700°C.

For the synthesis of Bi_2O_3/MnO composite, solution A and B was formed by dissolving 0.05 g of MnO (0.70 mmol) and 0.05 g Bi_2O_3 (0.11 mmol) in 10 mL of distilled water separately and sonicated for 15 minutes. Then both solutions were mixed, and the resultant reaction mixture was sonicated for an hour. The composite was separated by centrifugation for 10 minutes at 2000 rpm, and then dried in an oven at 70°C.

2.3.6. Deposition of Bifunctional Catalysts on NiF

Firstly, the NiF (about 1cm x 1cm) was carefully cleaned to remove NiO_X surface layer by sonicating in a 1.0 M HCl solution for 15 minutes followed by washing it with distilled water and absolute ethanol. It was then dried in the air for few minutes. To fabricate the NiF as working electrode, a slurry of 5 mg of catalysts (Bi_2O_3/NiO, Bi_2O_3/Co_3O_4, Bi_2O_3/Fe_2O_3, Bi_2O_3/MnO), 10 mL of analytical grade ethanol, and 5 µl of Nafion as a binder was prepared and sonicated. After sonication, slurry was coated on NiF by using the drop casting technique. The fabricated electrodes were then dried in an oven at 50°C overnight. The labelling of working electrodes is as Bi_2O_3/NiO-NiF, Bi_2O_3/Co_3O_4-NiF, Bi_2O_3/Fe_2O_3-NiF, Bi_2O_3/MnO-NiF.

2.3.7. Deposition of Bifunctional Catalysts on CNTF

2.5 cm long CNTF was tied on to the glass slide by Teflon tape from both ends. The suspended solutions of each Bi_2O_3/NiO, Bi_2O_3/Co_3O_4, Bi_2O_3/Fe_2O_3, Bi_2O_3/MnO (5mg in 5ml ethanol) was drop-casted thrice over the CNTF over the period of 30 minutes and then thermally treated at 200°C for 72 h in a muffle furnace. Later, Teflon tape was removed from one end and silver paste was coated for electrode connection. The labelling of working electrodes is as Bi_2O_3/NiO-CNTF, Bi_2O_3/Co_3O_4-CNTF, Bi_2O_3/Fe_2O_3-CNTF, Bi_2O_3/MnO-CNTF. Figure 2.1 depicts electrode fabrication by drop casting.

Figure 2.1. The schematic illustration of electrode fabrication

2.4. Synthesis of POMs for Electrochemical Water Splitting Reaction

Nickel (Ni), Cobalt (Co) and Iron (Fe) based POMs were synthesized with the slight modification of reported procedure as discussed below.

2.4.1. Synthesis of $Na_{10}[Ni_4(H_2O)_2(PW_9O_{34})_2]$ (Ni₄POM)

For the synthesis of Ni₄POM, 50 mL of distilled water was used to dissolve 11 g (33.35 mmol) of $Na_2WO_4.2H_2O$, 0.52 g (1.93 mmol) of $Na_2HPO_4.7H_2O$, and 1.84 g (7.39 mmol) of $Ni(CH_3COO)_2.4H_2O$. The solution's pH was then brought to 7.8 by adding concentrated acetic acid. The solution mixture was then refluxed for 2 h at 100°C, resulting in a clear green solution. NaCl was added to saturate the solution and the solution was left to cool at room temperature. The green crystals of Ni₄POM were collected by filtration and recrystallized in hot water.

2.4.2. Synthesis of $Na_{10}[Co_4(H_2O)_2(PW_9O_{34})_2]$ (Co₄POM)

For the synthesis of Co₄POM, 16.5 g (50.02 mmol) of $Na_2WO_4.2H_2O$, 1.50 g (5.59 mmol) $Na_2HPO_4.7H_2O$, and 3.2 g (12.81 mmol) $Co(CH_3COO)_2. 4H_2O$ were dissolved in 50 mL of distilled water, and the solution's pH was adjusted to 7.8 with the addition of acetic acid. After that, the solution mixture was refluxed at 100°C for 2 h, resulting in a dark purple solution. After adding NaCl until the solution was saturated, it was left to cool to room temperature. The resultant purple crystals were recovered and recrystallized in hot water.

52

2.4.3. Synthesis of Na$_{10}$[Fe$_4$(H$_2$O)$_2$(P$_2$W$_9$O$_{34}$)$_2$] (Fe$_4$POM)

For the synthesis of Fe$_4$POM, 22 g (66.6 mmol) of Na$_2$WO$_4$.2H$_2$O, 1.2 g (4.47 mmol) Na$_2$HPO$_4$.7H$_2$O, and 4 g (17.62 mmol) Fe(CH$_3$COO)$_2$.4H$_2$O were dissolved in 50 mL of distilled water. The solution's pH was fixed to 7.8 using acetic acid. After that, the solution mixture was refluxed for 2 h at 100°C. NaCl was added to saturate the solution. The orange crystals obtained were separated by filtration and then recrystallized in hot water.

2.4.4. Fabrication of Electrodes by Deposition of POMs on CNTF

About 2.5 cm long CNTF was fixed onto a glass slide by binding both its ends with Teflon tape. The concentrated POM solution (Ni$_4$POM, Co$_4$POM and Fe$_4$POM) was drop-casted thrice onto CNTF, and the glass plate was dried in an oven at 70°C. The fabricated electrodes were then thermally treated at 200°C for 72 h in a furnace followed by washing with water. Lastly, the Teflon tape was removed from one end and sealed with conducting silver paste to establish the electrode connection. The labelling of working electrodes is as Ni$_4$POM-CNTF, Co$_4$POM-CNTF and Fe$_4$POM-CNTF.

2.4.5. Electrochemical Studies

The electrochemical measurements were carried out at room temperature by using Gamry potientiostat/galvanostat 1010e Interface. The electrochemical OER and HER measurements were performed at pH 14 (1M KOH) and pH 7 (1M sodium phosphate buffer; PBS) by using three electrode system. The fabricated electrodes i.e., (Bi$_2$O$_3$/NiO-NiF, Bi$_2$O$_3$/Co$_3$O$_4$-NiF, Bi$_2$O$_3$/Fe$_2$O$_3$-NiF, Bi$_2$O$_3$/MnO-NiF (0.7 cm^2 surface area)), Bi$_2$O$_3$/NiO-CNTF, Bi$_2$O$_3$/Co$_3$O$_4$-CNTF, Bi$_2$O$_3$/Fe$_2$O$_3$-CNTF, Bi$_2$O$_3$/MnO-CNTF (0.056 cm^2 surface area)) were used as working electrodes, platinum sheet (2 × 6 mm) as a counter electrode and Ag/AgCl as a reference electrode. LSV was performed for OER and HER. All the potential values were iR-compensated and converted to RHE using Nernst equation. CV was carried out at various scan rates ranging from 50 to 250 mV/s in the non-faradaic region. Chronoamperometry test was performed at a constant potential corresponding to 150 and 20 mA/cm^2 for basic and neutral pH respectively, for 24 h to determine the stability of the fabricated working electrodes. Moreover, EIS was done in the frequency range of 0.1 to 10^5 Hz at 10 mV AC voltage.

Same setup was used for fabricated electrodes (Ni$_4$POM-CNTF, Co$_4$POM, Fe$_4$POM (0.056 cm^2)). The OER was performed at pH 13 (0.1M KOH). LSV was performed for OER. To calculate the ECSA, CV scans were performed at a scan rate from 50 to 250 mV/s in the non-Faradaic region. The chronoamperometric response was measured at respective voltages for series of electrodes, which was versus RHE for 24 h for the stability tests. The EIS was performed in the frequency range of 0.1–10^5 Hz at a small AC signal of 5 mV.

2.5. Synthesis of Bifunctional Catalysts for Biodiesel Applications

Bifunctional catalysts based on tungsten oxide (WO$_3$) over mesoporous material MCM-41 impregnated with alkaline earth metal (Mg, Ca, Sr, Ba) oxides capable of simultaneous esterification and transesterification were synthesized according to following procedures.

2.5.1. In Situ Synthesis of WO$_3$@MCM-41

WO$_3$@MCM-41 was synthesized according to sol-gel method. In a typical procedure, solution A and B were prepared by dissolving 0.142 g (0.43 mmol) of Na$_2$WO$_4$.2H$_2$O and 0.1 g (0.27 mmol) of CTAB in distilled water separately and stirred until the solution was homogeneous and transparent. Both solutions were mixed and then 10 mL of NH$_4$OH (32 wt%) was gently added to it. It was stirred for 10 minutes, and then 10 mL of TEOS was added dropwise. The gel formation was induced by stirring the reaction mixture overnight at room temperature. Thereafter, the solution was placed in an oven set at 70°C for 12 h. The resulting gel was repeatedly washed with ethanol and distilled water. The final product was calcined at 550°C for 6 h. For comparison, MCM-41 was synthesized by following the same procedure without adding Na$_2$WO$_4$·2H$_2$O.

2.5.2. Synthesis of MgO@WO$_3$@MCM-41 (MgWM)

For the synthesis of MgWM, impregnation method was used [202]. Firstly, 0.1 g (0.83 mmol) of MgSO$_4$ was dissolved in distilled water and then 0.1 g (0.34 mmol) of WO$_3$@MCM-41 was added to it. Impregnation time for magnesium precursor on WO$_3$@MCM-41 support was 1 h. After that the product separated by centrifugation and was dried at 110°C for 6 h followed by calcination at 600°C for 3 h.

2.5.3. Synthesis of CaO@WO₃@MCM-41 (CaWM)

For the synthesis of CaWM, firstly 0.1 g (0.58 mmol) of $CaSO_4.2H_2O$ was dissolved in distilled water. Then, 0.1 g (0.34 mmol) of WO₃@MCM-41 is added to it and impregnated on WO₃@MCM-41 support for 1 h. Through centrifugation, product was separated followed by drying for 6 h at 110°C. Lastly, it was calcined at 600°C for 3 h.

2.5.4. Synthesis of SrO@WO₃@MCM-41 (SrWM)

For the synthesis of SrWM, solution consisted of 0.1 g (0.47 mmol) of $Sr(NO_3)_2$ in distilled water, which was subsequently combined with 0.1 g (0.34 mmol) of WO₃@MCM-41. After 1 h of impregnation, the product was dried for 6 h at 110°C and then calcined for 3 h at 600°C.

2.5.5. Synthesis of BaO@WO₃@MCM-41 (BaWM)

For the synthesis of BaWM, 0.1 g (0.34 mmol) of WO₃@MCM-41 was mixed with a solution of 0.1 g (0.38 mmol) of $Ba(NO_3)_2$ in distilled water. The barium precursor took one hour to impregnate on WO₃@MCM-41 support. After that, the product was dried at 110°C for 6 hours. The material was then calcined at 600°C for 3 h.

2.5.6. Esterification/Transesterification Reaction for Biodiesel Production

For biodiesel production, corn oil and waste cooking oil were the two feedstocks used. The esterification/Transesterification of oils was carried out in a two-neck flask equipped with a magnetic bar, thermometer, and vent condenser. During the esterification/transesterification process, various parameters that include oil to methanol ratio, time, catalyst dose and reaction temperature were varied to obtain the optimized conditions in terms of maximum yield. Briefly, the known amount of dried methanol and preheated oil was mixed by stirring for five minutes followed by the addition of a catalyst. Esterification/transesterification process were carried out at the appropriate temperature and time. The separating funnel was then employed to separate obtained crude oil biodiesel phase which was then rotary evaporated to get the desired product. The obtained biodiesel was calculated using equation 35.

$$\% \text{ yield} = (V_b / V_o)*100 \qquad\qquad \text{Eq. 35}$$

Where V_b is the volume of biodiesel obtained, V_o is the volume of the oil used. The obtained biodiesel yield was also assessed from ^{1}H NMR by employing equation 36.

$$\% \text{ yield} = (2A_{me} / 3A_{CH2})*100 \qquad\qquad \text{Eq. 36}$$

Where A_{me} = integration value of methoxy protons (OCH$_3$) of methyl esters

A_{CH2} = integration value of methylene protons (CH$_2$).

Chapter-3   Results and Discussion

This chapter consist of two parts i.e., first part consists of bifunctional catalysts for electrochemical water splitting and second part consist of bifunctional catalysts for esterification/transesterification reaction for biodiesel production.

3.1. Bifunctional Catalysts for Electrochemical Water Splitting

3.1.1. Bi_2O_3/NiO Based Mixed Metal Oxides

Characterization and electrochemical studies for Bi_2O_3/NiO is given below.

3.1.1.1.Characterization of Materials

Bi_2O_3/NiO based mixed metal oxides were characterized through PXRD, SEM, EDX, elemental mapping and XPS analysis as discussed below.

Powder XRD Analysis

To explore the phase crystallinity and purity, PXRD was performed on the synthesized catalyst. Figure 3.1a represents the PXRD spectra of Bi_2O_3, NiO and Bi_2O_3/NiO which show that the diffraction peaks are strong and sharp, indicating that the Bi_2O_3/NiO have crystallized to a high degree. In the case of Bi_2O_3, all diffraction peaks correlate with the monoclinic phase (α). Bulk monoclinic Bi_2O_3 crystal locations and their relative intensities are in good accord (JCPDS file No.41–1449) [203]. While for NiO, three diffraction peaks, classified as cubic structure with crystal planes (111), (200) and (220), which is in good agreement with JCPDS 78-0423 [204]. Additionally, all peaks of Bi_2O_3 and NiO are present in the composite and no other peaks corresponding to the impurities are observed. Figure 3.1b depicts the PXRD spectrum of Bi_2O_3/NiO-CNTF which shows that due to amorphous phase of CNTF from 20°-30° [87], some prominent peaks of Bi_2O_3/NiO are suppressed. However, the major peaks with hkl planes (120), (200), (302), (242) and (220) confirm its deposition onto CNTF. Using the well-known Debye Scherer equation (D_{avg} =), the average crystallite size (D_{avg}) of Bi_2O_3/NiO and Bi_2O_3/NiO-CNTF is calculated to be 34.4 and 37.8 nm respectively. Dislocation density (δ_D), which determine the amount of crystallographic irregularity or defect inside a crystal structure is calculated by following formula,

$$\delta_D = 1 / (D_{avg})^2 \qquad\qquad \text{Eq. 37}$$

Microstrain (ε_m) is another parameter which describes the alteration in the structure, size, and shape of the particles by following equation 38,

$$\varepsilon_m = \beta\,(\text{Cos}\;\theta)\,/\,4 \qquad\qquad \text{Eq. 38}$$

Smaller values of δ_D and ε_m suggest the good crystallinity of the compounds. Table 3.1 represents all the parameters i.e., crystallite size, dislocation density and micro strain for Bi_2O_3/NiO and Bi_2O_3/NiO-CNTF.
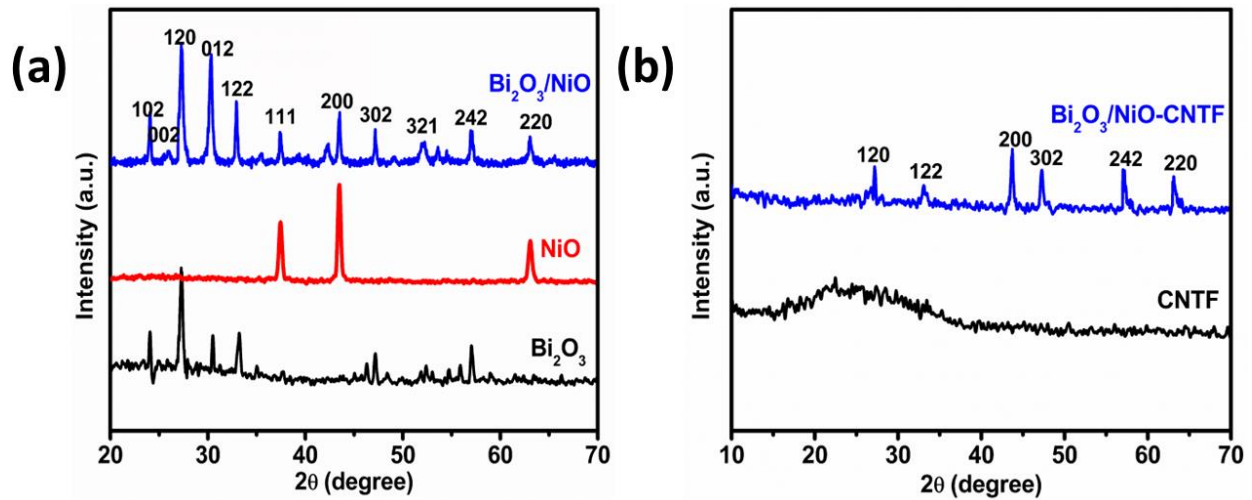
Figure 3.1. PXRD Pattern a) Bi_2O_3/NiO b) Bi_2O_3/NiO-CNTF

Table 3.1. Crystallite size, dislocation density and micro strain

Compound name	hkl	2θ (degree)	FWHM (degree)	FWHM (radians)	D_{avg} (nm)	$\delta_D \times 10^{15}$ (m^{-2})	$\varepsilon_m \times 10^{-3}$
Bi_2O_3/NiO	120	27.27	0.594	0.0103	14.4	4.8	2.0
	012	30.37	0.2214	0.004	37.1	0.72	0.9
	200	43.49	0.1722	0.003	51.7	0.37	0.6
Bi_2O_3/NiO-CNTF	120	27.27	0.2315	0.004	37.1	0.72	0.9
	122	33.01	0.2414	0.0042	36.2	0.76	1.0
	200	43.49	0.2257	0.0039	40.2	0.61	0.9

D_{avg} Bi_2O_3/NiO = 14.4 + 37.1 + 51.7 /3 = 34.4 nm

D_{avg} Bi$_2$O$_3$/NiO-CNTF = 37.1 + 36.2 + 40.2 /3 = 37.8 nm

SEM and EDX Analysis

To observe the structural morphology of synthesized composites i.e., Bi$_2$O$_3$/NiO and Bi$_2$O$_3$/NiO-CNTF, SEM was performed. Figure 3.2(a-c) depicts the SEM images of Bi$_2$O$_3$/NiO at different resolutions, which show the rod like morphology with spherical ends. Figure 3.2d represents the fibrous structure of CNTF spun, whereas figure 3.2(e-f) shows the uniform deposition of Bi$_2$O$_3$/NiO on the surface of CNTF with random orientation.

Furthermore, to determine the elemental and compositional properties, EDX and elemental mapping was performed for Bi$_2$O$_3$/NiO and Bi$_2$O$_3$/NiO-CNTF. Figure 3.3a depicts the EDX spectrum of Bi$_2$O$_3$/NiO revealing that elements i.e., nickel (Ni), bismuth (Bi) and oxygen (O) are all present with high purity in synthesized composite. Figure 3.3b indicates the EDX layered image of Bi$_2$O$_3$/NiO and figure 3c represents the elemental mapping that supports the EDX data. Moreover, EDX spectrum, layered images, and elemental mapping of Bi$_2$O$_3$/NiO-CNTF is shown in figure 3.4(a-c) that supports the deposition of composite over CNTF.
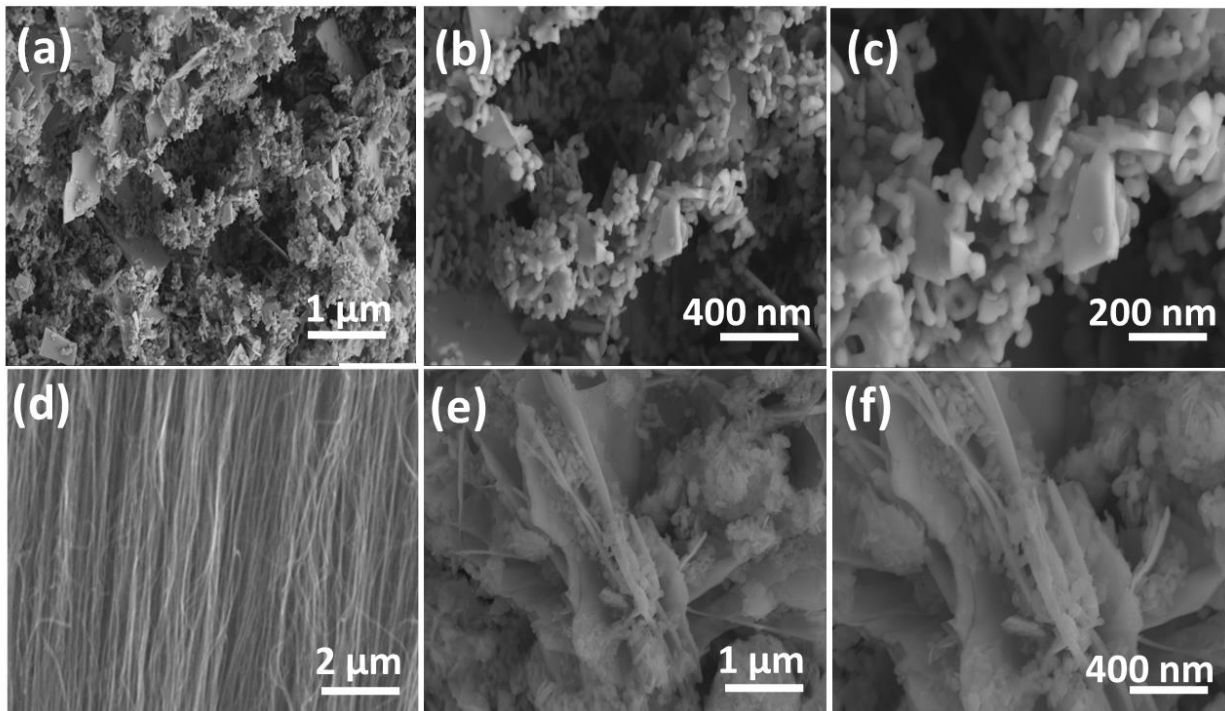
Figure 3.2. SEM images a-c) Bi$_2$O$_3$/NiO composites with different resolution, d) bare CNTF and e-f) Bi$_2$O$_3$/NiO-CNTF with different resolution.
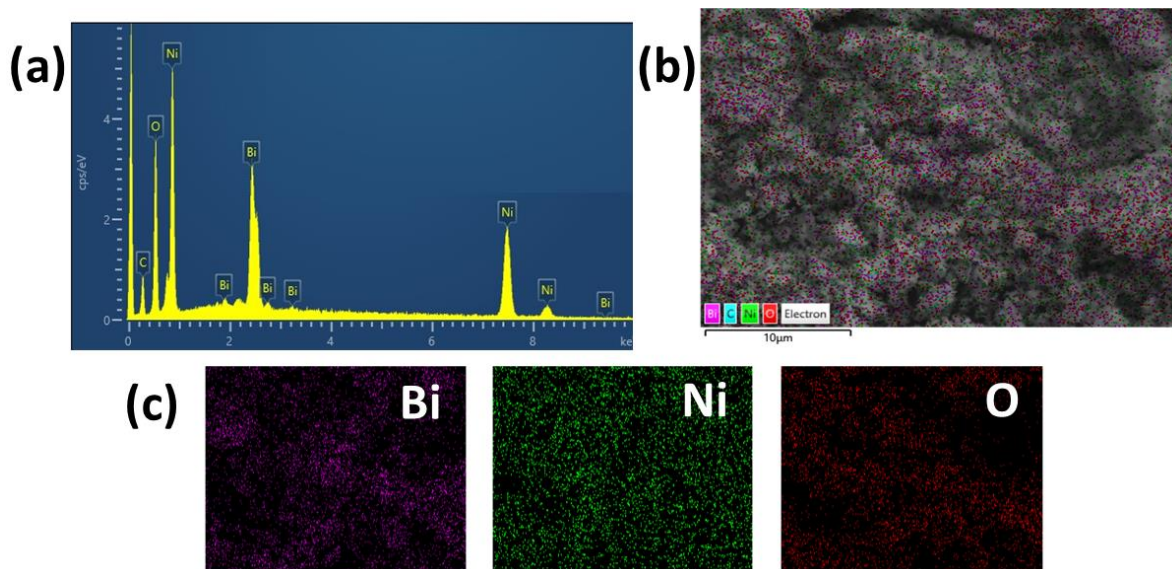
Figure 3.3. EDX spectrum a) Bi_2O_3/NiO, b) EDX layered image of Bi_2O_3/NiO, c) elemental mapping of Bi_2O_3/NiO
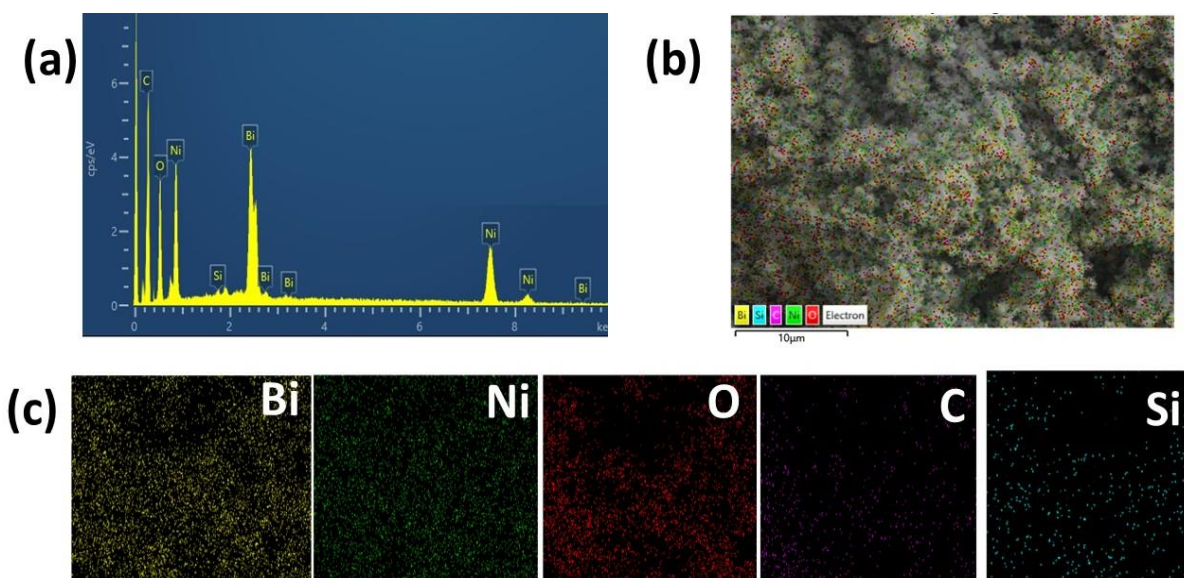
Figure 3.4. EDX spectrum a) Bi_2O_3/NiO-CNTF, b) EDX layered image of Bi_2O_3/NiO-CNTF, c) elemental mapping of Bi_2O_3/NiO-CNTF

XPS Analysis

In figure 3.5a, an overview spectrum of Bi_2O_3/NiO is shown, which contains typical photoelectron and Auger peaks corresponding to nickel, oxygen, bismuth, and carbon. In figure 3.5b, the

spectrum of Bi 4f reveals a doublet with binding energy of 160.8 eV and 166.2 eV for Bi 4f$_{7/2}$ and 4f$_{5/2}$, respectively, which is attributed to the 3+ oxidation state of bismuth in the compound [205]. The figure 3.5c demonstrates the Ni 2p spectrum that exhibits two doublets; the first doublet (blue curve) exhibits binding energy of 855.4 eV and 873.6 eV for Ni 2p$_{3/2}$ and 2p$_{1/2}$, respectively, which corresponds to the 2+ state of nickel [206]. The second doublet has binding energies of 858 eV and 876.2 for Ni 2p$_{3/2}$ and 2p$_{1/2}$, respectively, which is in the range of 3+ state of nickel in the compound [206]. In addition to the main photoelectron peaks in the Ni 2p spectrum, it also contains shakeup satellite peaks. Figure 3.5d demonstrates the O1s spectrum, which exhibits three peaks with the binding energy of 528.8 eV, 530.7 eV and 532. 3 eV for bismuth oxide, nickel oxide and chemisorbed hydroxyl groups.
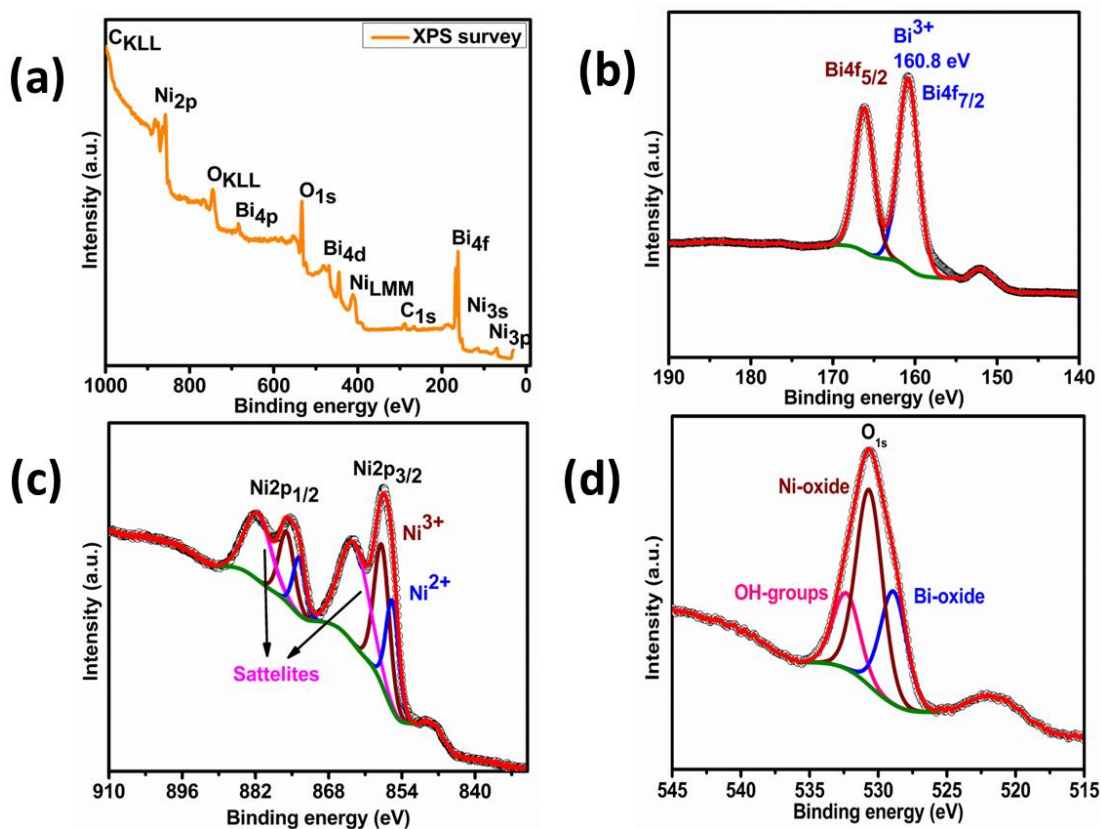
Figure 3.5. XPS spectra; a) survey scan, high resolution spectra of b) Bi 4f, c) Ni 2p and d) O 1s

3.1.1.2. Electrochemical Studies

Electrochemical HER Activity

The HER performance of both series of electrodes was examined in neutral media. LSV polarization curves and Tafel slopes (see Figure 3.6) were used to determine the HER activity of the working electrodes.

Figure 3.6a shows the LSV curves for Bi_2O_3/NiO-NiF in neutral media and it achieved 301 mV at 50 mA/cm^2 which was less than other working electrodes in series and showed Tafel slope of 103.3 mV/dec (figure 3.6b). While Bi_2O_3/NiO-CNTF in neutral media (figure 3.6(c-d) i.e., had low overpotential of 268 mV at 50 mA/cm^2 with a Tafel slope of 81.3 mV/dec. It clearly indicated that Bi_2O_3/NiO-CNTF had better HER performance than Bi_2O_3/NiO-NiF in neutral media. Tarik et al, reported the HER of Ce doped α-Bi_2O_3-rGO in alkaline media and achieved current density of 10 mA/cm^2 at overpotential of 337 mV with Tafel slope of 162 mV/dec [50]. While Yu et al. reported the HER activity of Bi and Ni alloy nanosheets and achieved a current density of 10 mA/cm^2 at overpotential of 183 mV [207], in neutral medium.
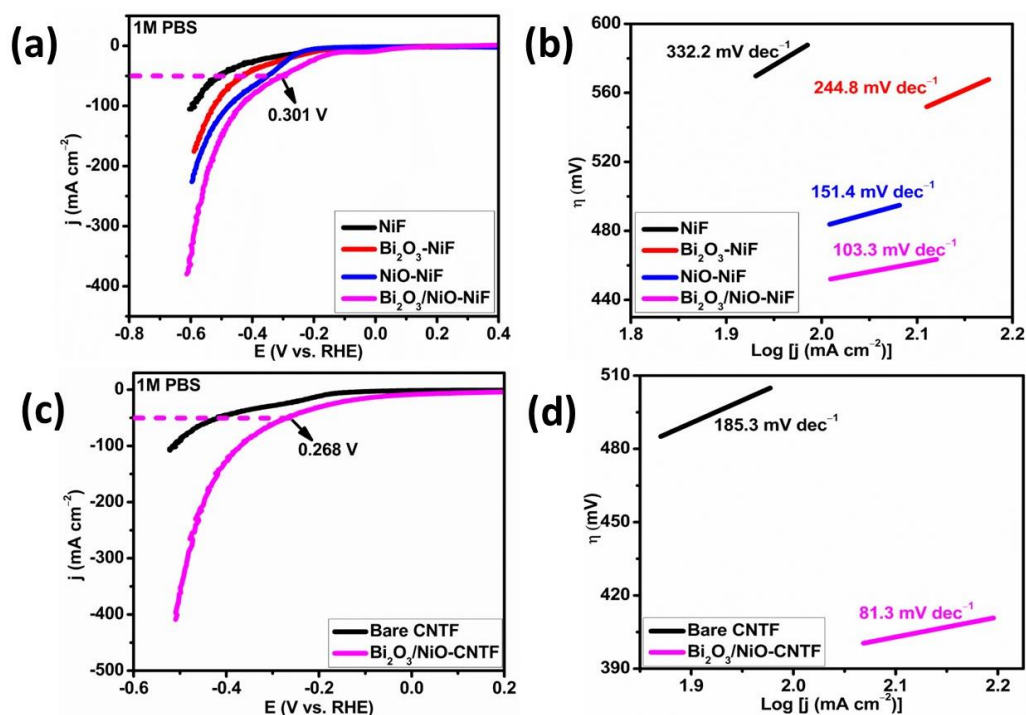
Figure 3.6. HER polarization curves and Tafel plots for a, b) Bi_2O_3/NiO-NiF and c, d) Bi_2O_3/NiO-CNTF in 1M PBS

Electrochemical OER Activity

LSV polarization curves were used to determine the OER performance of NiF based and CNTF based electrodes in basic and neutral media. The LSV data for NiF based electrodes in alkaline media reveals that Bi_2O_3/NiO-NiF exhibited superior performance compared to the other electrodes of its series (see Figure 3.7a). The required overpotential values for Bi_2O_3/NiO-NiF and NiO-NiF to generate a current density of 150 mA/cm^2 are found to be 516 and 552 mV, respectively. While Bi_2O_3-NiF and bare NiF both exhibited very little OER activity. The oxidation of Ni^{2+} to Ni^{3+} is observed as the high anodic peak current in case of Bi_2O_3/NiO-NiF and NiO-NiF between 1.4 - 1.55 V vs. RHE, as compared to other electrodes of this series. According to literature, one of the main active species responsible for the high OER activity for Bi_2O_3/NiO-NiF bimetallic and NiO-NiF catalysts is the oxidized NiOOH species [208]. Tafel plots were further plotted to investigate the kinetics rate of OER activity. Figure 3.7b represents the Tafel slope value of 145.9 mV/dec for Bi_2O_3/NiO-NiF which is the lowest among NiF-based series in basic medium showing faster kinetics and supports the OER activity of Bi_2O_3/NiO-NiF. Furthermore, the electrocatalytic OER activity of bimetallic system over CNTF (see Figure 3.7c-d) exhibited an overpotential of 467 mV at the current density of 150 mA/cm^2 with a Tafel slope value of 78.1 mV/dec which is comparatively much lower than that for Bi_2O_3/NiO-NiF in alkaline media.

Similarly, when the OER activity of Bi_2O_3/NiO-NiF in performed in neutral medium, the results revealed that the Bi_2O_3/NiO-NiF achieved current density of 20 mA/cm^2 at overpotential of 242 mV with Tafel slope value of 157.5 mV/dec, while Bi_2O_3-NiF, NiO-NiF and bare NiF exhibited very little OER activity (see Figure 3.7e-f). Moreover, performing the OER activity on CNTF as a substrate, Bi_2O_3/NiO-CNTF achieved the current density of 20 mA/cm^2 at overpotential of 164 mV with a Tafel slope 94.5 mV/dec (Figure 3.7g-h). The OER results in both media shows that the CNTF-based electrodes exhibited better electrochemical performance than NiF-based electrodes which can be attributed to the tubular channelled structure of CNTF that provides large surface area and more active sites. Table 3.2 shows OER and HER parameters (overpotential and Tafel slope) for both types of working electrodes in alkaline and neutral media. Comparative studies for OER and HER in alkaline and neutral media are shown in table 3.4 and 3.5.
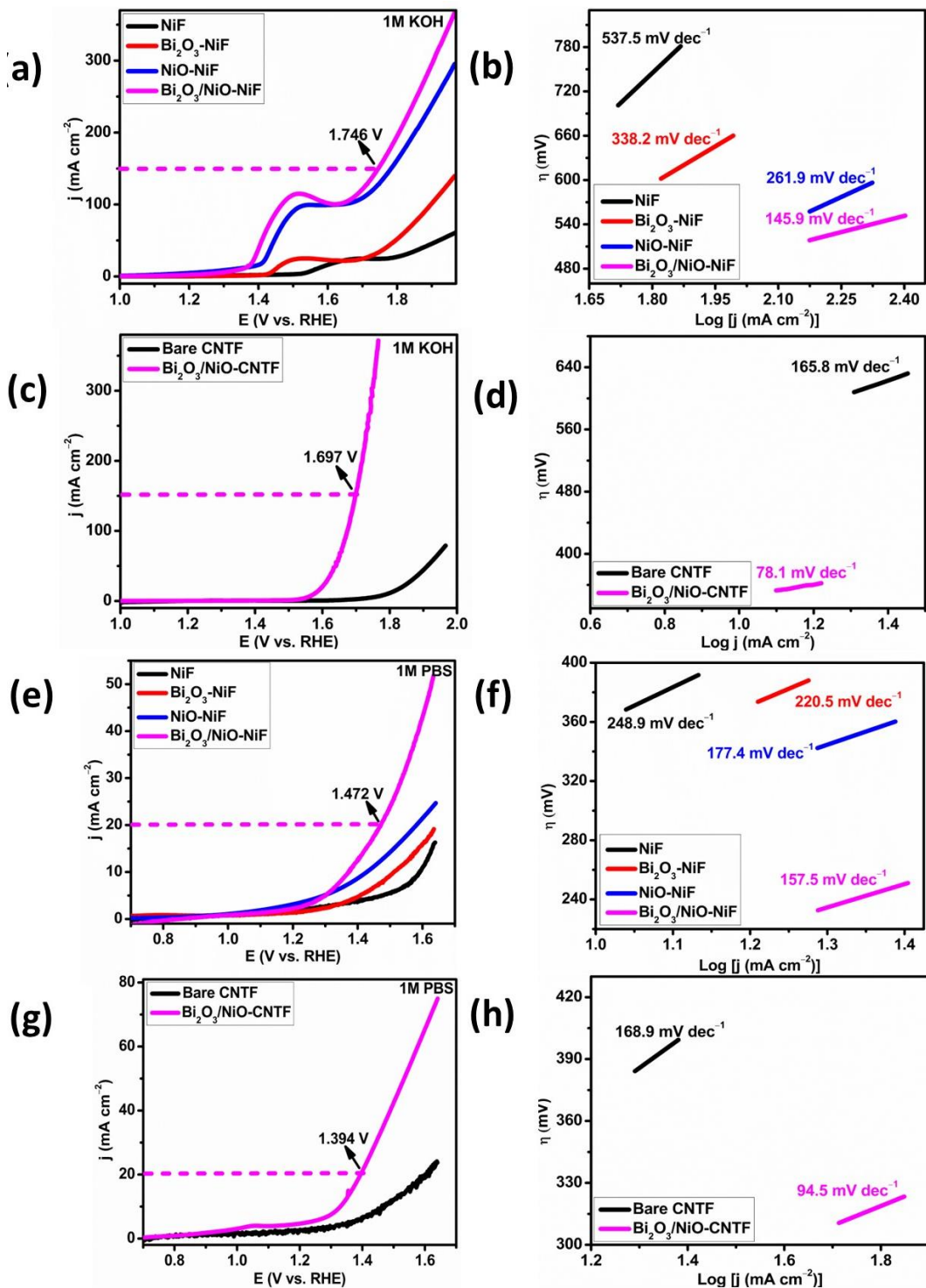
Figure 3.7. OER polarization curves and Tafel plots; a, b) NiF-based electrodes in basic medium, c, d) CNTF-based electrodes in 1M KOH, e, f) NiF-based electrodes in neutral medium, g, h) CNTF-based electrodes in neutral medium

Table 3.2. OER and HER parameters for Bi_2O_3/NiO-NiF and Bi_2O_3/NiO-CNTF in alkaline and neutral medium

Electrocatalyst	Medium	OER		HER	
		Ƞ (mV) @mA/cm²	Tafel slope (mV/dec)	Ƞ (mV) @mA/cm²	Tafel slope (mV/dec)
Bare NiF	Alkaline	703@50	537.5	-	-
Bi_2O_3/NiO-NiF	-	516@150	145.9	-	-
Bare CNTF	-	680@50	165.8	-	-
Bi_2O_3/NiO-CNTF	-	467@150	78.1	-	-
Bare NiF	Neutral	360@10	248.9	508@50	332.2
Bi_2O_3/NiO-NiF	-	242@20	157.5	301@50	103.3
Bare CNTF	-	210@10	168.9	470@50	185.3
Bi_2O_3/NiO-CNTF	-	164@20	94.5	268@50	81.3

Furthermore, CV analysis was performed in non-faradic region at various scan rates ranging from 50 to 250 mV/s for both series of fabricated electrodes in alkaline and neutral media to calculate the electrochemical surface area (ECSA) and double layer capacitance (C_{dl}). The value of C_{dl} is defined from the slope of a graph plotted between anodic current versus scan rates. Figures 3.8a and c depict the CV graphs of Bi_2O_3/NiO-NiF and Bi_2O_3/NiO-CNTF in alkaline media while figures 3.8e and g represent the CV graphs of same electrodes in neutral media. By comparing the C_{dl} values defined from figure 3.8b and d, Bi_2O_3/NiO-CNTF possesses high C_{dl} values than Bi_2O_3/NiO-NiF. The same trend is followed while performing the measurements in neutral media (figures 3.8f and h). The CV and C_{dl} graphs for bare-NiF and -CNTF in different media are given in Figure 3.9 (a-h). Furthermore, ECSA was calculated by the formula (ECSA = C_{dl} / C_s)

where C_s demonstrates the specific capacitance of the monolayer, and its value is 0.04 mF cm². ECSA and C_{dl} are directly correlated; the higher the C_{dl}, the higher the ECSA. Another surface feature is the RF, which is computed using the ratio of ECSA and the surface area of the working electrodes. RF is a crucial parameter for the electrocatalytic activity of the electrode material. RF

is also directly related to the OER activity. Table 3.3 shows the Cdl, ECSA and RF for both types of working electrodes in alkaline and neutral media.

Table 3.3. C_{dl}, ECSA and RF in alkaline and neutral media

Electrocatalysts	Medium	C_{dl} (mF)	ECSA (cm^2)	RF
Bare NiF	Alkaline	0.067	1.675	2
Bi_2O_3/NiO-NiF	-	1.32	33	47
Bare CNTF	-	0.09	2.25	40
Bi_2O_3/NiO-CNTF	-	1.56	39	696
Bare NiF	Neutral	0.026	0.65	1
Bi_2O_3/NiO-NiF	-	1.08	27	38
Bare CNTF	-	0.042	1.05	19
Bi_2O_3/NiO-CNTF		1.27	31.75	567
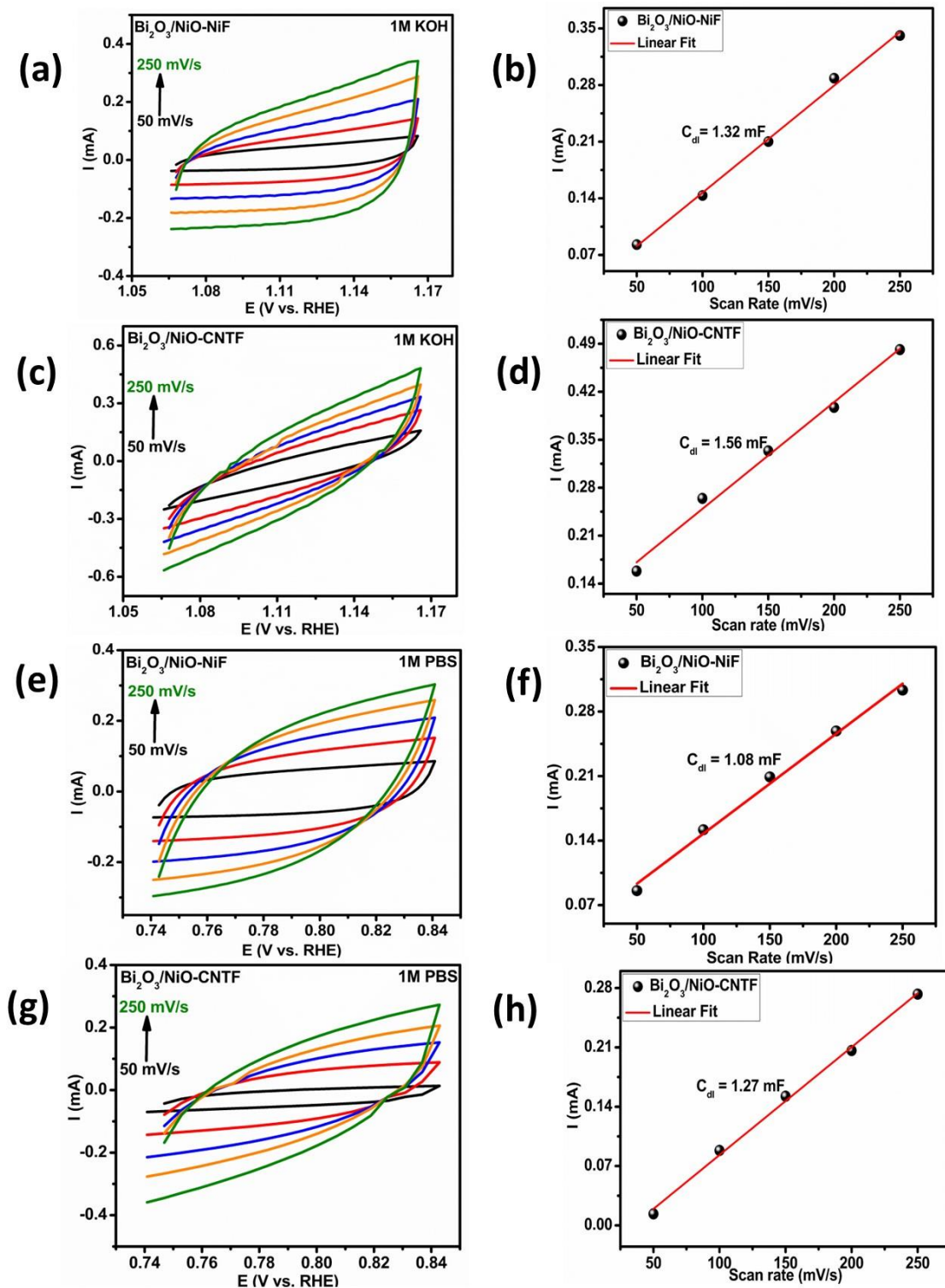
Figure 3.8. CV and C_{dl} plots for a, b) Bi_2O_3/NiO-NiF in 1M KOH c, d) Bi_2O_3/NiO-CNTF in 1M KOH, e, f) Bi_2O_3/NiO-NiF in 1M PBS, g, h) Bi_2O_3/NiO-CNTF in 1M PBS

67
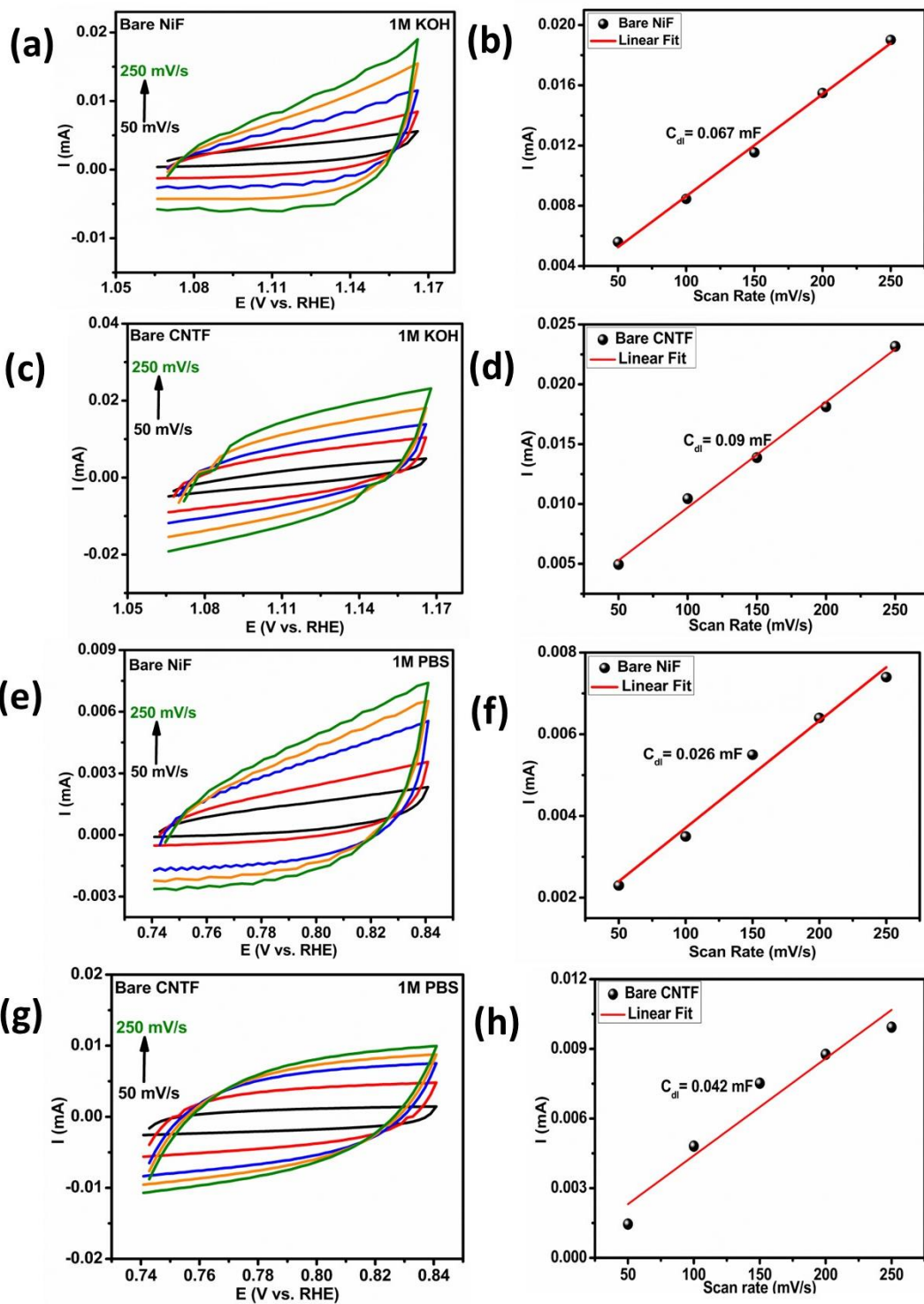
Figure 3.9. CV and C_{dl} plots for Bare NiF in 1M KOH (a-b), Bare CNTF in 1M KOH (c-d), Bare NiF in 1M PBS (e-f), Bare CNTF in 1M PBS (g-h)

To further investigate the OER kinetics, EIS was performed at 0.1 to 10^5 Hz frequency range by applying 10 mV AC voltage. EIS demonstrates the charge transfer resistance (R_{ct}), which is directly related to the semicircle diameter in the Nyquist plot towards high frequency region. Figure 3.10a and b depicts the Nyquist plot for Bi_2O_3/NiO-NiF and Bi_2O_3/NiO-CNTF in alkaline media which clearly reveals that Bi_2O_3/NiO-CNTF had small diameter as compared to the Bi_2O_3/NiO-NiF. The same trend is observed for Bi_2O_3/NiO-NiF and Bi_2O_3/NiO-CNTF in neutral media (see Figure 3.10c and d). A small semicircle justifies the low R_{ct} and faster kinetics.
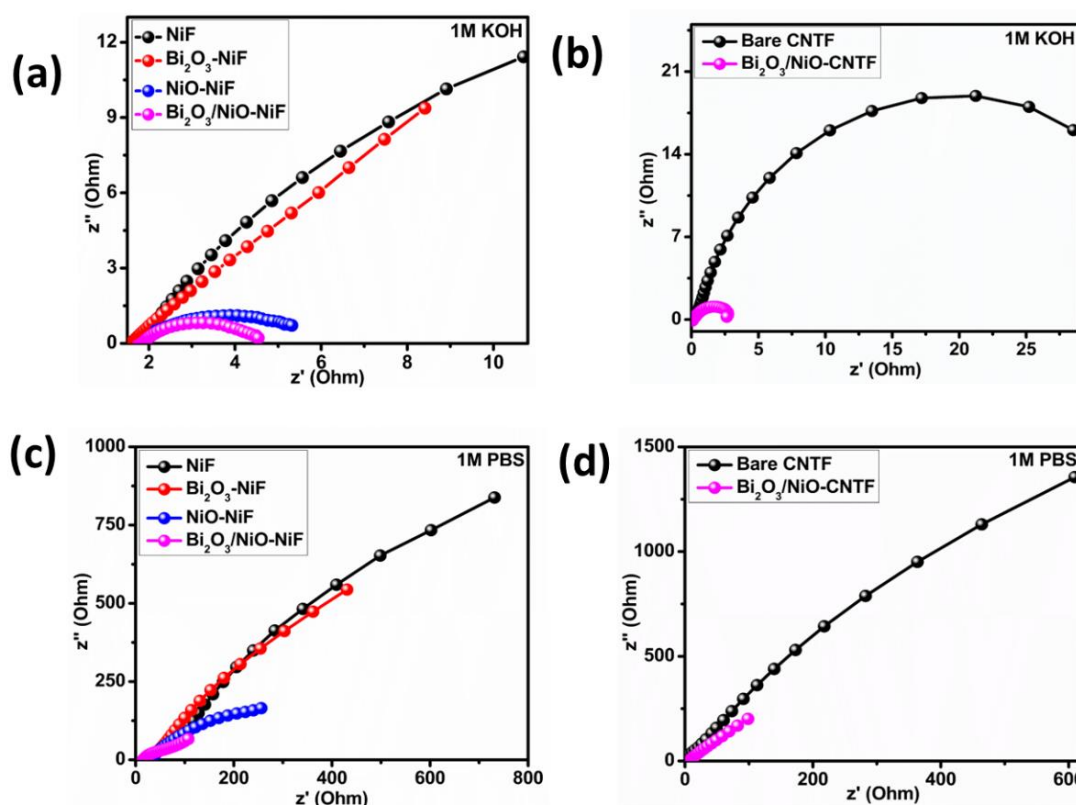
Figure 3.10. Nyquist plots for a) Bi_2O_3/NiO-NiF and b) Bi_2O_3/NiO-CNTF in 1M KOH, c) Bi_2O_3/NiO-NiF and d) Bi_2O_3/NiO-CNTF in 1M PBS

The catalyst's stability is also an important parameter for commercial and industrial water electrolysers. For the stability test, chronoamperometry was performed for Bi_2O_3/NiO-CNTF being the best electrocatalyst among series of fabricated electrodes, for 24 h in both alkaline and neutral media (see Figure 3.11a and b) at the applied potential of 1.697 V (150 mA/cm^2 current density) and 1.394 V (20 mA/cm^2 current density) vs RHE, respectively. The electrocatalyst

maintained for 24 h at the current density of 150 mA/cm^2 and 20 mA/cm^2 in basic and neutral media, respectively with a minor change under constant potentiostatic electrolysis.
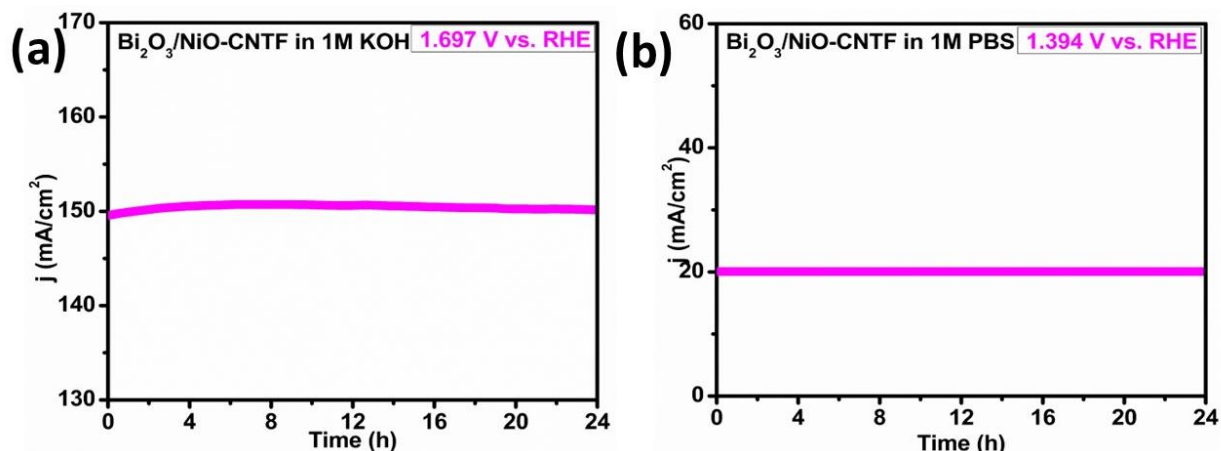
Figure 3.11. Chronoamperometry test for a) Bi$_2$O$_3$/NiO-CNTF in 1M KOH and b) Bi$_2$O$_3$/NiO-CNTF in 1M PBS

Table 3.4. Comparative OER performance of the electrocatalysts in alkaline media with literature.

Electrocatalyst	OER		References
	η (mV)	Tafel slope (mV/dec)	
Pt-NiO	-	-	[209]
NiO@GP	312@10 mA/cm^2	58	[210]
Ce-Bi$_2$O$_3$@Rgo	270@10 mA/cm^2	54.6	[50]
Ni$_{0.82}$Co$_{0.18}$O@C/NF	320@50 mA/cm^2	65	[211]
PA@NiO	310@100 mA/cm^2	36	[39]
A-NiO NPs/rGO	369@10 mA/cm^2	73	[208]
Bi$_{84.8}$Ni$_{15.2}$	479@50 mA/cm^2	74	[207]
Fe-NiO@NiF	206@10 mA/cm2	49.4	[212]
Bi$_2$O$_3$/NiO-NiF	**516@150 mA/cm^2**	**145.9**	**This work**
Bi$_2$O$_3$/NiO-CNTF	**467@150 mA/cm^2**	**78.1**	**This work**

Table 3.5. Comparative OER and HER performance of the electrocatalysts in neutral media with literature.

Electrocatalyst	OER		HER		References
	η (mV)	Tafel slope (mV/dec)	η (mV)	Tafel slope (mV/dec)	
$Bi_{84.8}Ni_{15.2}$	-	-	183@10 mA/cm^2	-	[207]
S-NiFe$_2$O$_4$/NiF	494@10 mA/cm^2	118.1	197@10 mA/cm^2	81.3	[213]
Pd/NiFeO$_x$	310@10 mA/cm^2	175.06	75@10 mA/cm^2	103.01	[214]
Bi–B/BiB$_3$O$_6$@HC	-	-	88.5@10 mA/cm^2	53.8	[215]
Bi$_2$O$_3$/NiO-NiF	**242@20 mA/cm^2**	**157.5**	**301@50 mA/cm^2**	**103.3**	**This work**
Bi$_2$O$_3$/NiO-CNTF	**164@20 mA/cm^2**	**94.5**	**268@50 mA/cm^2**	**81.3**	**This work**

In a nutshell, Bi$_2$O$_3$/NiO and Bi$_2$O$_3$/NiO-CNTF was characterized through XRD, SEM, EDX, elemental mapping, XPS techniques. Furthermore, these catalysts were tested for OER in 1M KOH and OER/HER in 1M PBS solution. It is clearly indicated that Bi$_2$O$_3$/NiO-CNTF performed better in both media as compared to Bi$_2$O$_3$/NiO-NiF. For OER in alkaline media, Bi$_2$O$_3$/NiO-CNTF based electrodes reached current density of 150 mA/cm^2 at overpotential of 467 mV with Tafel slope 78.1 mV/dec while Bi$_2$O$_3$/NiO-NiF based electrodes reached to same current density at overpotential of 516 mV with Tafel slope 145.9 mV/dec. Similarly, for OER and HER in 1M PBS, Bi$_2$O$_3$/NiO-CNTF also outperformed (164 mV@20 mA/cm^2 with Tafel slope 94.5 mV/dec and 268 mV@50 mA/cm^2 with Tafel slope 81.3 mV/dec, respectively) than the Bi$_2$O$_3$/NiO-NiF (242 mV@20 mA/cm^2 with Tafel slope 157.5 mV/dec and 301 mV@50 mA/cm^2 with Tafel slope 103.3 mV/dec, respectively).

3.1.2. Bi₂O₃/Co₃O₄ Based Mixed Metal Oxides

Characterization and electrochemical studies for Bi_2O_3/Co_3O_4 is given below.

3.1.2.1. Characterization of Materials

Bi_2O_3/Co_3O_4 based mixed metal oxides were characterized through Powder XRD, SEM, EDX, elemental mapping and XPS analysis as discussed below.

Powder XRD Analysis

The PXRD spectra of Bi_2O_3, Co_3O_4, and Bi_2O_3/Co_3O_4 are shown in Figure 3.12a. The sharp and strong peaks indicate the crystallinity of the synthesized materials. Bi_2O_3 diffraction peaks show the monoclinic phase (α). Bi_2O_3 crystal planes and their relative intensities are in good accord with literature. For Co_3O_4, there are four diffraction peaks with crystal planes (311), (400), (511) and (440) having face centred cubic structure, which are in good agreement with the literature (JCPDS 42–1467) [216]. All peaks of Bi_2O_3 and Co_3O_4 are present in the composite. There is no impurity peak in composite. Figure 3.12b depicts the PXRD of Bi_2O_3/Co_3O_4-CNTF which shows that in the amorphous region of CNTF, there are some less intensity diffraction peaks are suppressed. However, the major peaks with crystal planes (120), (311), (400), (302), (242) and (440) clearly indicates the deposition of Bi_2O_3/Co_3O_4 on CNTF surface. This indicates that there is no change in structure after deposition on CNTF. According to Debye Scherrer equation, the particle size of Bi_2O_3/Co_3O_4 and Bi_2O_3/Co_3O_4-CNTF is calculated to be 36.6 and 36.2 nm respectively. Dislocation density, micro strain is also calculated which are mentioned in table 3.6.
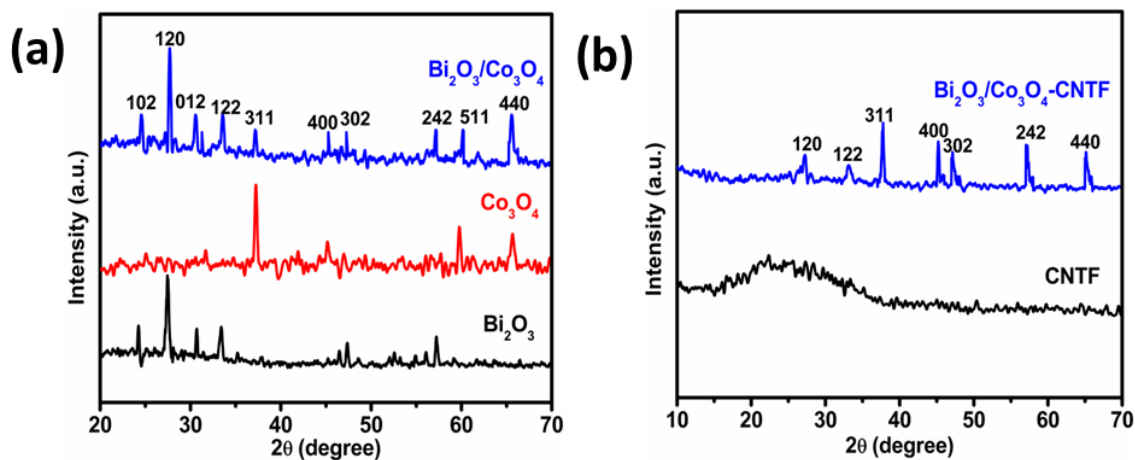
Figure 3.12. PXRD pattern of a) Bi_2O_3/Co_3O_4 b) Bi_2O_3/Co_3O_4-CNTF

Table 3.6. Crystallite size, dislocation density and micro strain

Compound name	Hkl	2θ (degree)	FWHM (degree)	FWHM (radians)	D_{avg} (nm)	δ_D x 10^{15} (m^{-2})	ε_m x 10^{-3}
Bi_2O_3/Co_3O_4	120	27.27	0.5544	0.0097	15.4	4.20	2.3
	012	30.37	0.2432	0.0042	35.7	0.78	1.0
	311	37.26	0.1512	0.0026	58.7	0.29	0.6
Bi_2O_3/Co_3O_4-CNTF	120	27.27	0.2418	0.0042	35.3	0.80	0.1
	122	33.01	0.2213	0.0039	38.7	0.66	0.9
	311	37.26	0.2528	0.0044	34.7	0.83	0.1

D_{avg} Bi_2O_3/Co_3O_4= 15.4 + 35.7 + 58.7 /3 = 36.6 nm

D_{avg} Bi_2O_3/Co_3O_4-CNTF= 35.3 + 38.7 + 34.7 /3 = 36.2 nm

SEM and EDX Analysis

SEM was performed to observe the structural morphology of synthesized composites i.e., Bi_2O_3/Co_3O_4 and Bi_2O_3/Co_3O_4-CNTF. Figure 3.13(a-c) shows the SEM images of Bi_2O_3/Co_3O_4 at different resolutions, in which Bi_2O_3 has flat rod like and Co_3O_4 has spherical morphology. Figure 3.13(d-e) shows the uniform deposition of Bi_2O_3/Co_3O_4 on the surface of CNTF. Morphology remains same after deposition of Bi_2O_3/Co_3O_4 on CNTF.

Furthermore, to determine the elemental and compositional properties, EDX and elemental mapping was performed for Bi_2O_3/Co_3O_4 and Bi_2O_3/Co_3O_4-CNTF. Figure 3.14a depicts the EDX spectrum of Bi_2O_3/Co_3O_4 which shows that elements i.e., cobalt (Co), bismuth (Bi), oxygen (O), carbon (C) were all present. It clearly confirms the purity of synthesized composite because no impurity peak of any other element is present in the spectrum. Figure 3.14b indicates the EDX layered image of Bi_2O_3/Co_3O_4 and figure 3.14c represents the elemental mapping which successfully supports the EDX data. Moreover, EDX spectrum of Bi_2O_3/Co_3O_4-CNTF is shown in figure 3.15a which shows all the elements (Co, Bi, O and C) are present in Bi_2O_3/Co_3O_4-CNTF are present. Layered images and elemental mapping of Bi_2O_3/Co_3O_4-CNTF is also shown in figure 3.15(b-c).
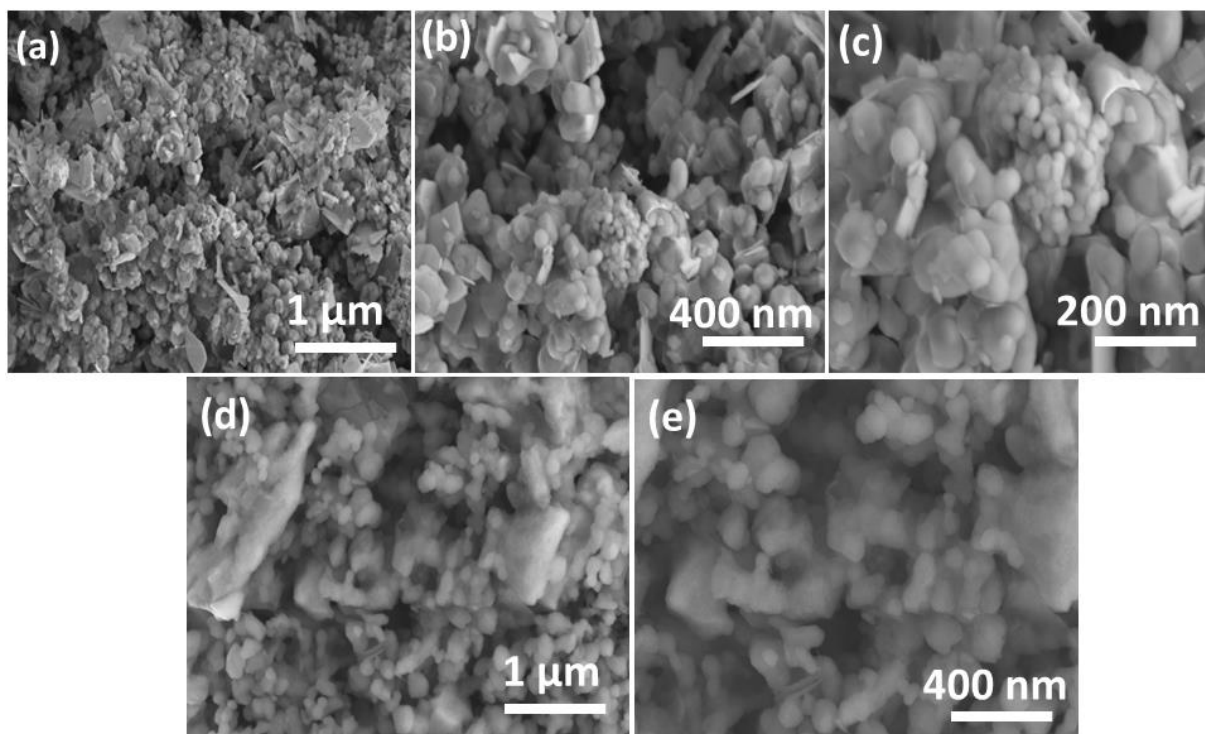
Figure 3.13. SEM images a-c) Bi_2O_3/Co_3O_4 composites with different resolution, and d-e) Bi_2O_3/Co_3O_4-CNTF with different resolution.
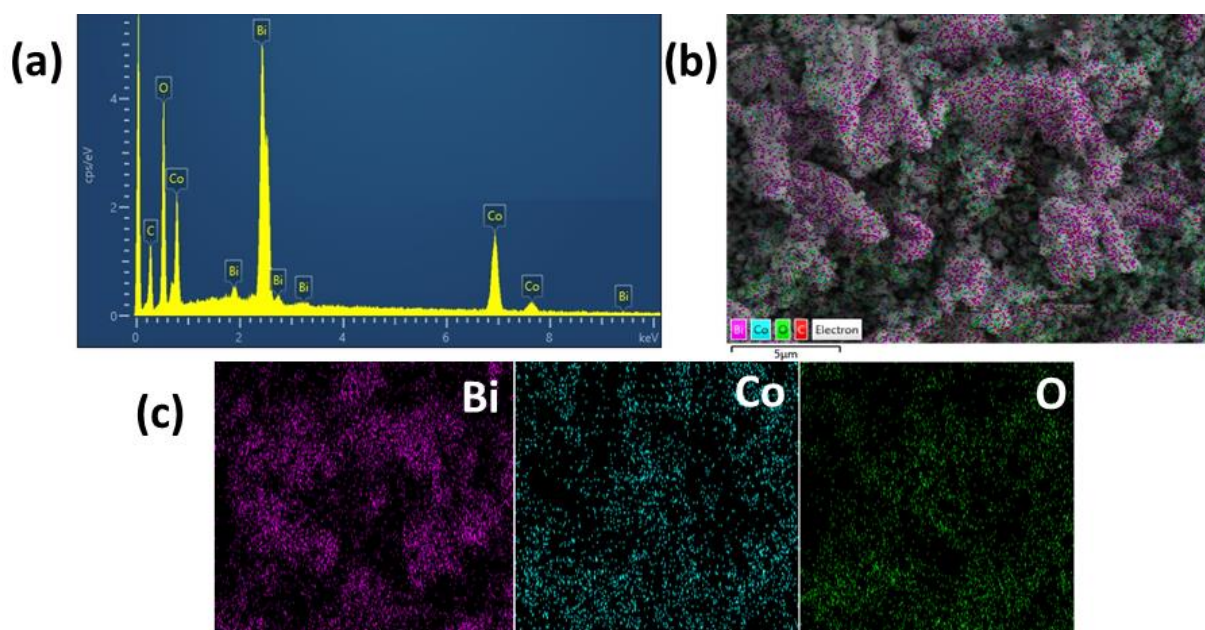
Figure 3.14. EDX spectrum a) Bi_2O_3/Co_3O_4, b) EDX layered image of Bi_2O_3/Co_3O_4, c) elemental mapping of Bi_2O_3/Co_3O_4
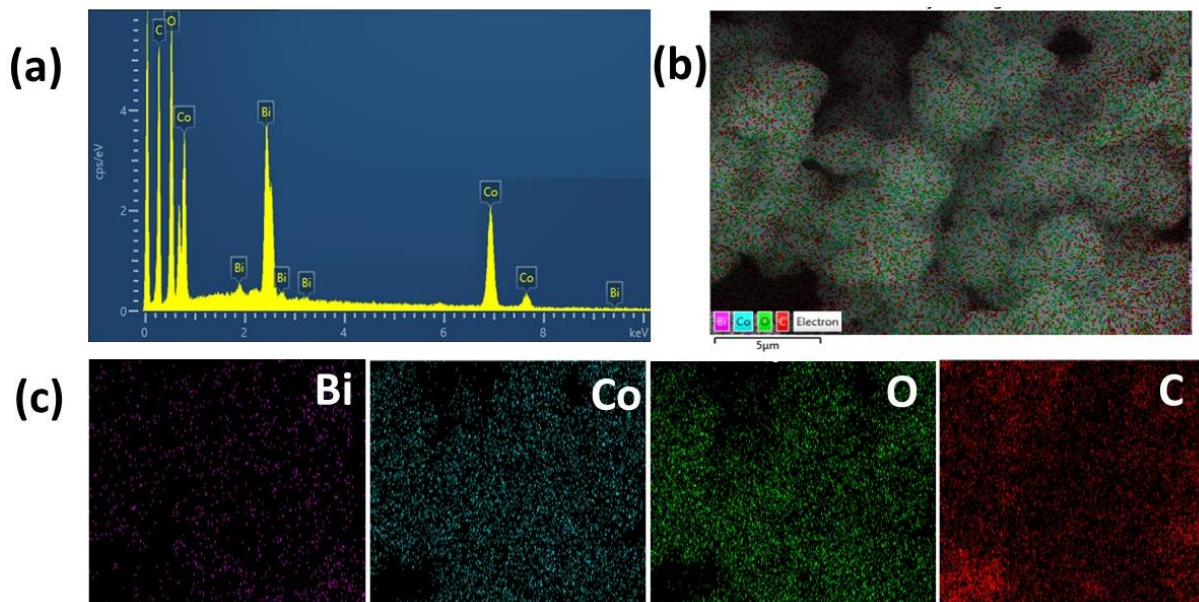
Figure 3.15. EDX spectrum a) Bi$_2$O$_3$/Co$_3$O$_4$-CNTF, b) EDX layered image of Bi$_2$O$_3$/Co$_3$O$_4$-CNTF, c) elemental mapping of Bi$_2$O$_3$/Co$_3$O$_4$-CNTF

XPS Analysis

In figure 3.16a, an overview spectrum of Bi$_2$O$_3$/Co$_3$O$_4$ is shown, which contains typical photoelectron and Auger peaks corresponding to cobalt, oxygen, bismuth, and carbon. In figure 3.16b, the spectrum of Bi 4f reveals a doublet with binding energy of 160.8 eV and 166.2 eV for Bi 4f$_{7/2}$ and 4f$_{5/2}$, respectively, which is attributed to the 3+ oxidation state of bismuth in the compound [205]. Figure 3.16c depicts the Co 2p spectra which showed two peaks having binding energies i.e., 779.9 and 795.1 eV. The spin-orbit doublet 2p spectral profile of Co$_3$O$_4$ was influenced by the tetrahedral and octahedral forms of Co2+ and Co3+ [217]. The present weak satellite peak detected in the higher binding-energy side of the 2p$_{3/2}$ and 2p$_{l/2}$ transitions demonstrates the co-existence of Co(II) and Co(III) on the material's surface. The comparatively intense peak widths be consistent 2p$_{1/2}$ to 2p$_{3/2}$ with a spacing of 15.2 eV. The XPS spectrum of Co$_3$O$_4$ and the Co 2p spectrum are well consistent [218, 219].
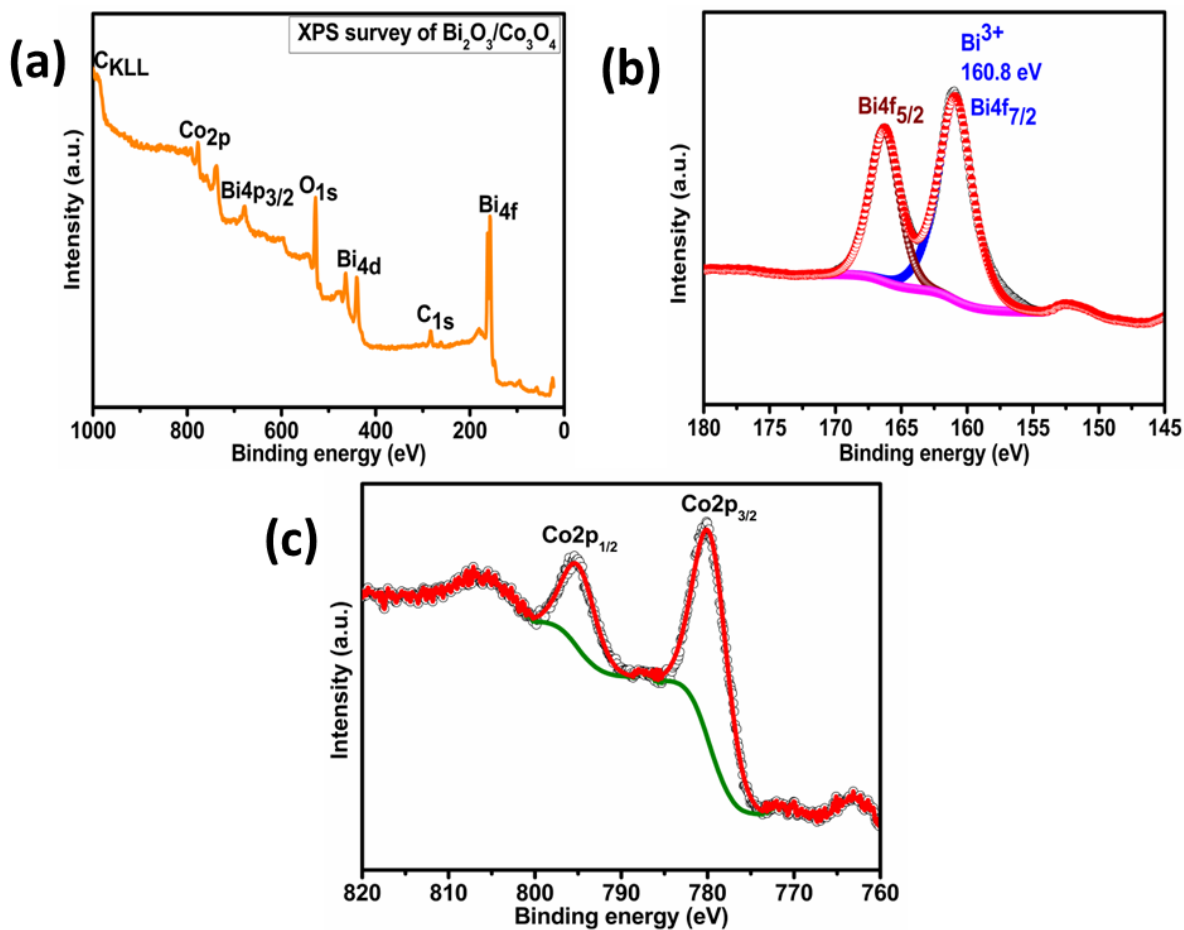
Figure 3.16. XPS spectra; a) survey scan, high resolution spectra of b) Bi 4f and c) Co 2p

3.1.2.2. Electrochemical Studies

Electrochemical HER Activity

The HER performance of both series of electrodes was examined in neutral media. Figure 3.17 depicts LSV polarization curves and Tafel slopes which were used to determine the HER activity of the working electrodes.

Figure 3.17a shows the LSV curves for Bi_2O_3/Co_3O_4-NiF in neutral media and it achieved 354 mV at 50 mA/cm^2 which was less than other working electrodes in series and showed Tafel slope value of 128.3 mV/dec (figure 3.17b). While Bi_2O_3/Co_3O_4-CNTF in neutral media (figure 3.17c-d) i.e., had low overpotential of 301 mV at 50 mA/cm^2 with a Tafel slope of 92.7 mV/dec. It clearly indicated that Bi_2O_3/Co_3O_4-CNTF had better HER performance than Bi_2O_3/Co_3O_4-NiF in neutral media.
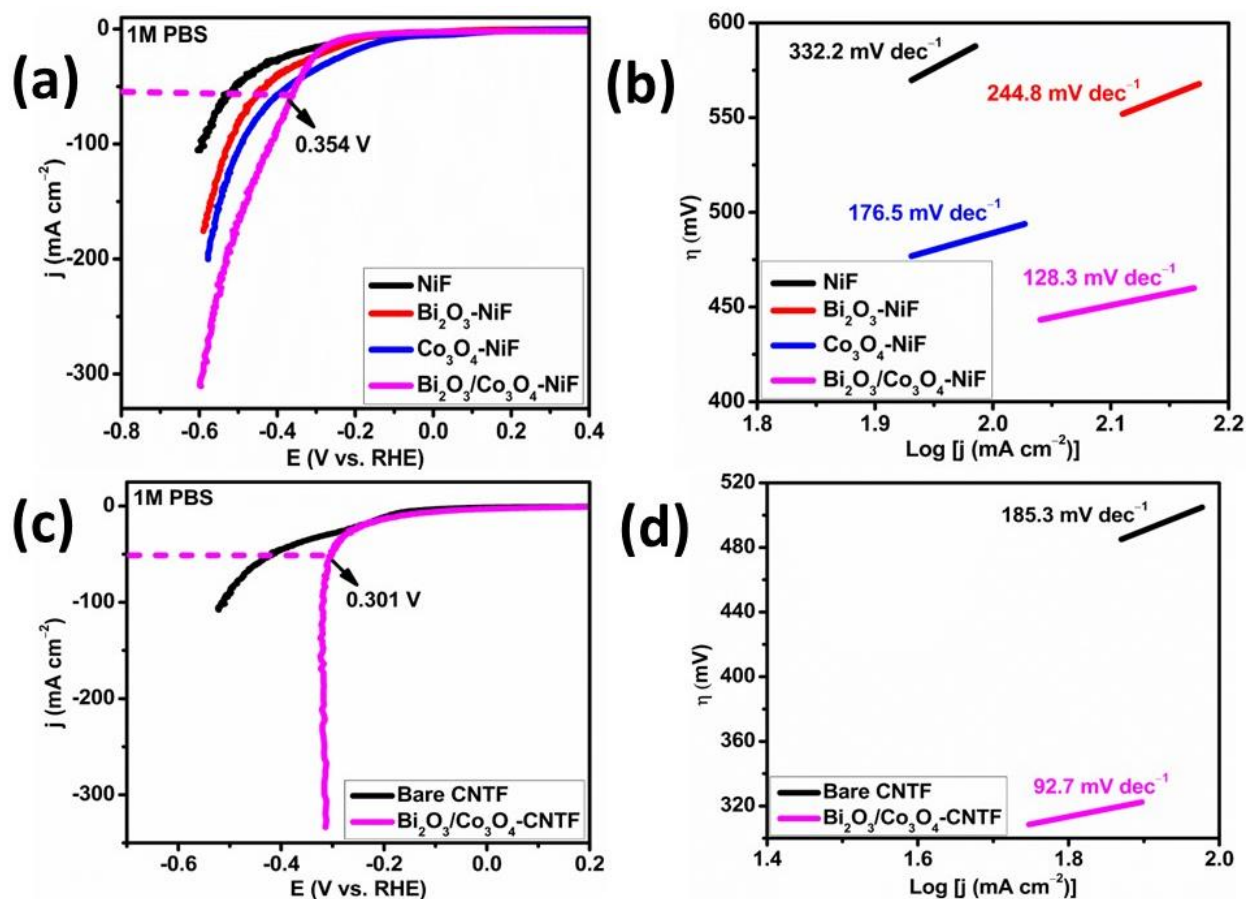
Figure 3.17. HER polarization curves and Tafel plots for a, b) Bi_2O_3/Co_3O_4-NiF and c, d) Bi_2O_3/Co_3O_4-CNTF in 1M PBS

Electrochemical OER Activity

LSV polarization curves were used to determine the OER performance of NiF based and CNTF based electrodes in basic and neutral media. The LSV data for NiF based electrodes in alkaline media reveals that Bi_2O_3/Co_3O_4-NiF exhibited superior performance compared to the other electrodes of its series (see Figure 3.18a). The required overpotential values for Bi_2O_3/Co_3O_4-NiF and Co_3O_4-NiF to generate a current density of 150 mA/cm^2 are found to be 586 and 714 mV, respectively. While Bi_2O_3-NiF and bare NiF both exhibited very little OER activity. In case of Co_3O_4-NiF, high anodic peak current in the range of 1.45 - 1.55 V vs. RHE justifies the oxidation of Co^{3+} to Co^{4+} forming CoO_2 [220]. According to literature, Co^{4+} active centers catalyze the OER reaction and the main active species for the high OER activity for Bi_2O_3/Co_3O_4-NiF bimetallic and Co_3O_4-NiF catalysts is the oxidized CoO(OH) species [221]. Tafel plots were further constructed

to investigate the kinetics of OER activity. Figure 3.18b represents the Tafel slope value of 168.8 mV/dec for Bi_2O_3/Co_3O_4-NiF which is the lowest among NiF-based series in basic medium showing faster kinetics and supports the OER activity of Bi_2O_3/Co_3O_4-NiF. Furthermore, the electrocatalytic OER activity of bimetallic system over CNTF (see Figure 3.18c and d) exhibited an overpotential of 512 mV at the current density of 150 mA/cm^2 with a Tafel slope value of 100.2 mV/dec which is comparatively much lower than that for Bi_2O_3/Co_3O_4-NiF in alkaline media.

Similarly, when the OER activity of Bi_2O_3/Co_3O_4-NiF in performed in neutral medium, the results revealed that the Bi_2O_3/Co_3O_4-NiF achieved 251 mV@ 20 mA/cm^2 with Tafel slope value of 171.9 mV/dec, while Bi_2O_3-NiF, Co_3O_4-NiF and bare NiF exhibited very little OER activity (see Figure 3.18e and f). Moreover, performing the OER activity on CNTF as a substrate, Bi_2O_3/Co_3O_4-CNTF achieved 222 mV@ 20 mA/cm^2 with a Tafel slope 121.4 mV/dec (Figure 3.18g and h). The OER results in both media shows that the CNTF-based electrodes exhibited better electrochemical performance than NiF-based electrodes which can be attributed to the tubular channelled structure of CNTF that provides large surface area and more active sites. Table 3.7 shows OER and HER parameters (overpotential and Tafel slope) for both types of working electrodes in alkaline and neutral media. Comparative studies for OER and HER in alkaline and neutral media are shown in table 3.9 and 3.10.
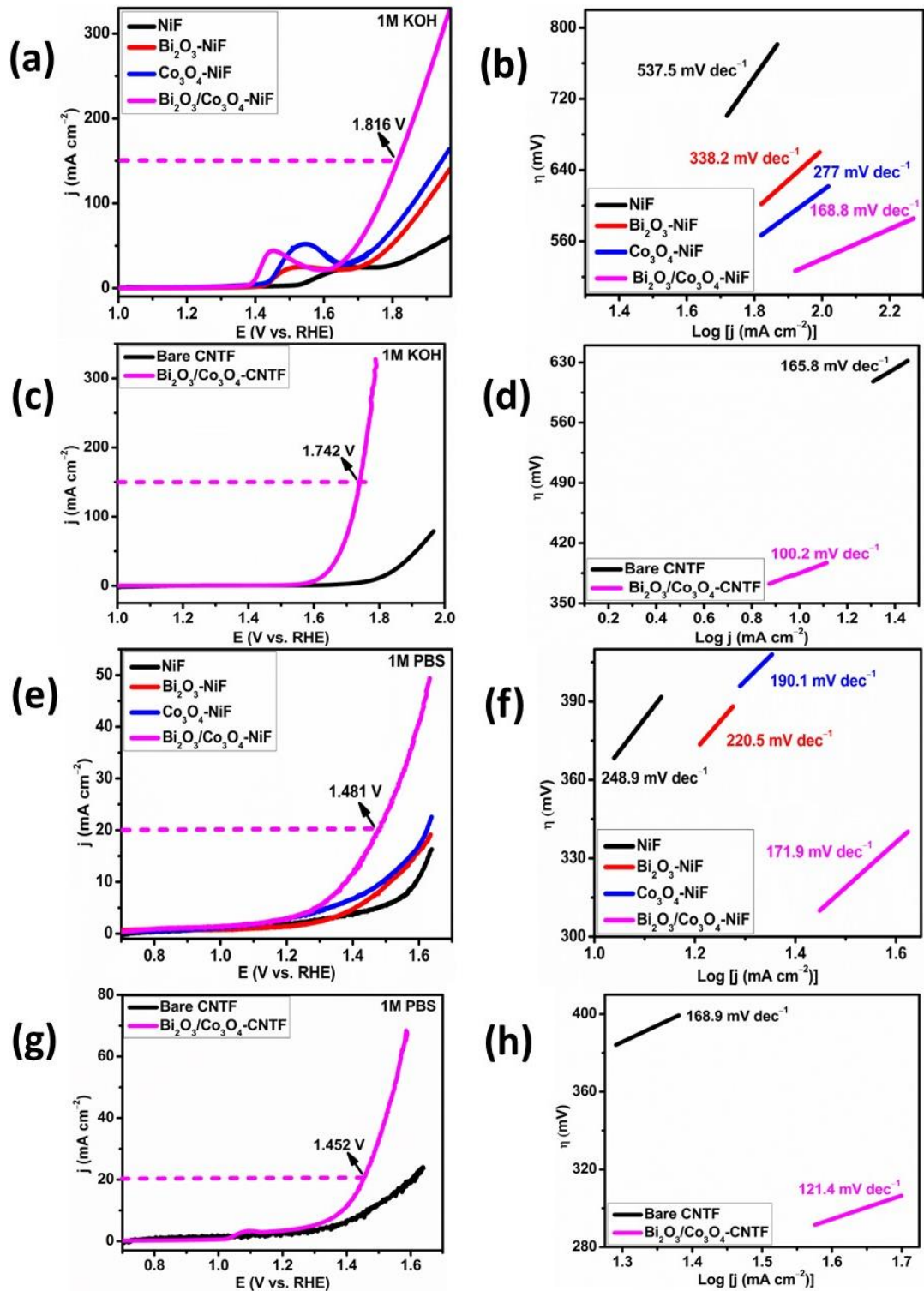
Figure 3.18. OER polarization curves and Tafel plots; a, b) NiF-based electrodes in basic medium, c, d) CNTF-based electrodes in basic medium, e, f) NiF-based electrodes in neutral medium, g, h) CNTF-based electrodes in neutral medium

Table 3.7. OER and HER parameters for Bi_2O_3/Co_3O_4-NiF and Bi_2O_3/Co_3O_4-CNTF in alkaline and neutral medium

Electrocatalyst	Medium	OER		HER	
		η (mV) @mA/cm^2	Tafel slope (mV/dec)	η (mV) @mA/cm^2	Tafel slope (mV/dec)
Bi_2O_3/Co_3O_4-NiF	Alkaline	586@150	168.8	-	-
Bi_2O_3/Co_3O_4-CNTF	-	512@150	100.2	-	-
Bi_2O_3/Co_3O_4-NiF	Neutral	251@20	171.9	354@50	128.3
Bi_2O_3/Co_3O_4-CNTF	-	222@20	121.4	301@50	92.7

Furthermore, CV analysis was performed in non-faradic region at various scan rates ranging from 50 to 250 mV/s for both series of fabricated electrodes in alkaline and neutral media to calculate the ECSA and C_{dl}. Figures 3.19a and c depict the CV graphs of Bi_2O_3/Co_3O_4-NiF and Bi_2O_3/Co_3O_4-CNTF in alkaline media while figures 3.19e and g represent the CV graphs of same electrodes in neutral media. By comparing the C_{dl} values defined from figure 3.19b and d, Bi_2O_3/Co_3O_4-CNTF possesses high C_{dl} values than Bi_2O_3/Co_3O_4-NiF. The same trend is followed while performing the measurements in neutral media (figures 3.19f and h). Furthermore, ECSA and RF was also calculated. Table 3.8 shows the C_{dl}, ECSA and RF for both types of working electrodes in alkaline and neutral media.

Table 3.8. C_{dl}, ECSA and RF in alkaline and neutral media

Electrocatalysts	Medium	C_{dl} (mF)	ECSA (cm^2)	RF
Bi_2O_3/Co_3O_4-NiF	Alkaline	1.24	31	44
Bi_2O_3/Co_3O_4-CNTF	-	1.44	36	643
Bi_2O_3/Co_3O_4-NiF	Neutral	0.871	21.77	31
Bi_2O_3/Co_3O_4-CNTF	-	0.99	24.75	442
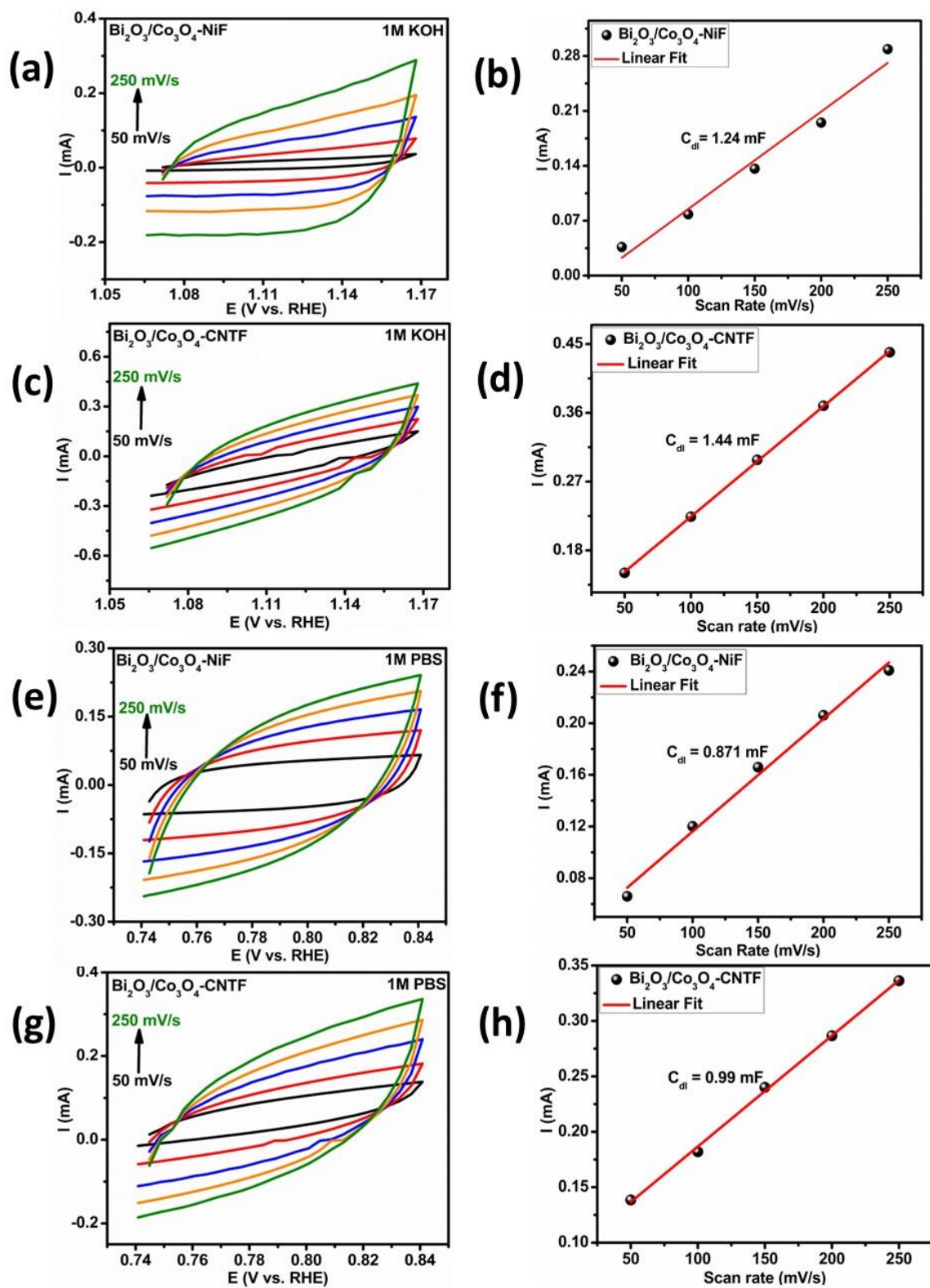
Figure 3.19. CV and C_{dl} plots for a, b) Bi_2O_3/Co_3O_4-NiF in 1M KOH c, d) Bi_2O_3/Co_3O_4-CNTF in 1M KOH, e, f) Bi_2O_3/Co_3O_4-NiF in 1M PBS, g, h) Bi_2O_3/Co_3O_4-CNTF in 1M PBS

To further investigate the OER kinetics, EIS was performed at frequency range of 0.1 to 10^5 Hz at 10 mV AC voltage. Figure 3.20a and b depicts the Nyquist plot for Bi_2O_3/Co_3O_4-NiF and Bi_2O_3/Co_3O_4-CNTF in alkaline media which clearly reveals that Bi_2O_3/Co_3O_4-CNTF had small diameter as compared to the Bi_2O_3/Co_3O_4-NiF. The same trend is observed for Bi_2O_3/Co_3O_4-NiF and Bi_2O_3/Co_3O_4-CNTF in neutral media (see Figure 3.20c and d). A small semicircle justifies the low R_{ct} and faster kinetics.
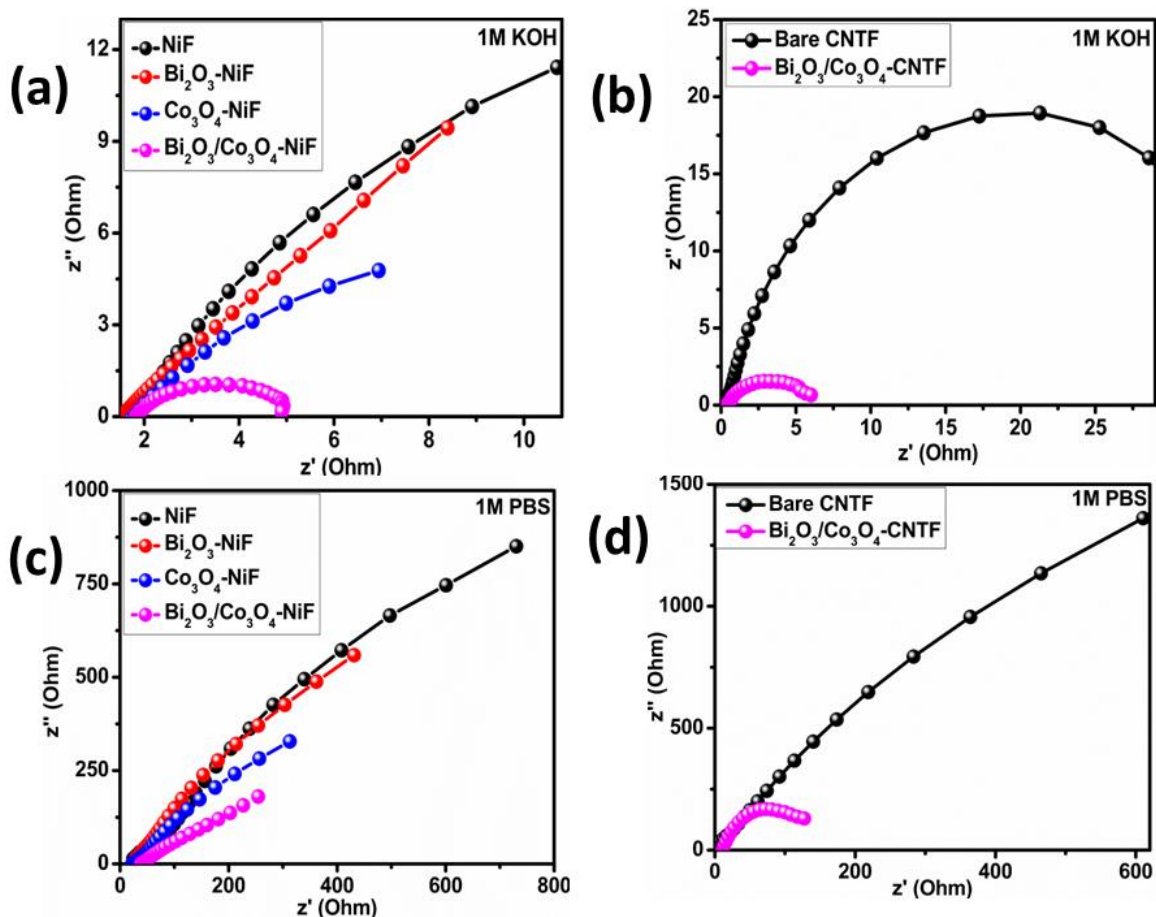
Figure 3.20. Nyquist plots for a) Bi_2O_3/Co_3O_4-NiF and b) Bi_2O_3/Co_3O_4-CNTF in 1M KOH, c) Bi_2O_3/Co_3O_4-NiF and d) Bi_2O_3/Co_3O_4-CNTF in 1M PBS

For the stability test, chronoamperometry was performed for Bi_2O_3/Co_3O_4-CNTF being the best electrocatalyst among series of fabricated electrodes, for 24 h in both alkaline and neutral media (see Figure 3.21a and b) at the applied potential of 1.742 V (150 mA/cm^2 current density) and 1.452 V (20 mA/cm^2 current density) vs RHE, respectively. The electrocatalyst maintained for 24

h at the current density of 150 mA/cm^2 and 20 mA/cm^2 in basic and neutral media, respectively with a minor change under constant potentiostatic electrolysis.
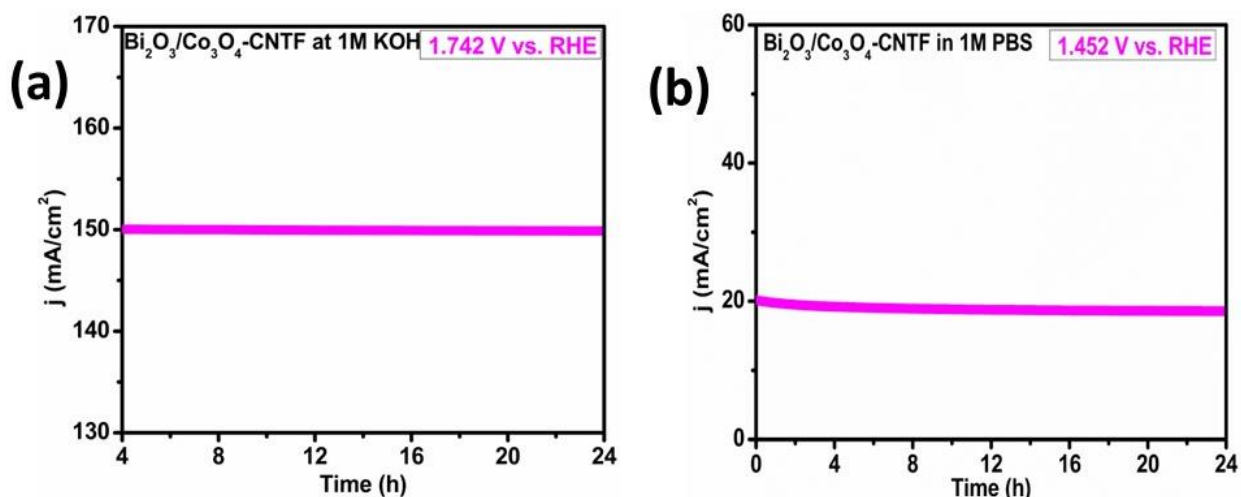
Figure 3.21. Chronoamperometry test for a) Bi$_2$O$_3$/Co$_3$O$_4$-CNTF in 1M KOH and b) Bi$_2$O$_3$/Co$_3$O$_4$-CNTF in 1M PBS

Table 3.9. Comparative OER performance of the electrocatalysts in alkaline media with literature.

Electrocatalyst	OER		References
	η (mV)	Tafel slope (mV/dec)	
Co$_3$O$_4$ quantum dots	315@10 mA/cm^2	49	[222]
Co$_3$O$_4$–Mo$_2$N NFs	220@10 mA/cm^2	87.8	[223]
CoO/Co$_3$O$_4$-CC	260@10 mA/cm^2	54	[224]
Porous spinel Co$_3$O$_4$	361@10 mA/cm^2	87.54	[225]
Co$_{0.89}$Fe$_{11}$O-N	360@50 mA/cm^2	52.7	[226]
CoO–MoO$_2$	312@10 mA/cm^2	69	[227]
Bi$_1$-Co$_9$-BO$_3$@RT	420@10 mA/cm^2	37	[228]
NiCo$_2$O$_4$ nanowire arrays	294@10 mA/cm^2	-	[229]
Bi$_2$O$_3$/Co$_3$O$_4$-NiF	**586@150 mA/cm^2**	**168.8**	**This work**
Bi$_2$O$_3$/Co$_3$O$_4$-CNTF	**512@150 mA/cm^2**	**100.2**	**This work**

Table 3.10. Comparative OER and HER performance of the electrocatalysts in neutral media with literature.

Electrocatalyst	OER		HER		References
	Ƞ (mV)	Tafel slope (mV/dec)	Ƞ (mV)	Tafel slope (mV/dec)	
Co_3O_4-UNA	$379@50$ mA/cm^2	60	$240@100$ mA/cm^2	97	[230]
Co/Co_3O_4-NC	-	243.4	$551@10$ mA/cm^2	-	[231]
$Ni_{0.33}Co_{0.67}S_2$	-	-	$118@100$ mA/cm^2	67.8	[232]
Bi_2O_3/Co_3O_4-NiF	**$251@20$ mA/cm^2**	**171.9**	**$354@50$ mA/cm^2**	**128.3**	**This work**
Bi_2O_3/Co_3O_4-CNTF	**$222@20$ mA/cm^2**	**121.4**	**$301@50$ mA/cm^2**	**92.7**	**This work**

In a nutshell, Bi_2O_3/Co_3O_4 and Bi_2O_3/Co_3O_4-CNTF was characterized through XRD, SEM, EDX, elemental mapping, XPS techniques. Furthermore, these catalysts were tested for OER in 1M KOH and OER/HER in 1M PBS solution. It is clearly indicated that Bi_2O_3/Co_3O_4-CNTF performed better in both media as compared to Bi_2O_3/Co_3O_4-NiF. For OER in alkaline media, Bi_2O_3/Co_3O_4-CNTF based electrodes reached current density of 150 mA/cm^2 at overpotential of 512 mV with Tafel slope 100.2 mV/dec while Bi_2O_3/Co_3O_4-NiF based electrodes reached to same current density at overpotential of 586 mV with Tafel slope 168.8 mV/dec. Similarly, for OER and HER in 1M PBS, Bi_2O_3/Co_3O_4-CNTF also outperformed (222 mV@20 mA/cm^2 with Tafel slope 121.4 mV/dec and 301 mV@50 mA/cm^2 with Tafel slope 92.7 mV/dec, respectively) than the Bi_2O_3/Co_3O_4-NiF (251 mV@20 mA/cm^2 with Tafel slope 171.9 mV/dec and 354 mV@50 mA/cm^2 with Tafel slope 128.3 mV/dec, respectively).

3.1.3. Bi$_2$O$_3$/Fe$_2$O$_3$ Based Mixed Metal Oxides

Characterization and electrochemical studies for Bi$_2$O$_3$/Fe$_2$O$_3$ is given below.

3.1.3.1.Characterization of Materials

Bi$_2$O$_3$/Fe$_2$O$_3$ based mixed metal oxides were characterized through PXRD, SEM, EDX, elemental mapping and XPS analysis as discussed below.

Powder XRD Analysis

The PXRD spectra of Bi$_2$O$_3$, Fe$_2$O$_3$, and Bi$_2$O$_3$/Fe$_2$O$_3$ are shown in Figure 3.22a. The sharp and strong peaks indicate the crystallinity of the synthesized materials. Bi$_2$O$_3$ diffraction peaks show the monoclinic phase (α). Bi$_2$O$_3$ crystal planes and their relative intensities are in good accord with literature. For Fe$_2$O$_3$, there are six diffraction peaks with crystal planes (102), (104), (110), (024), (116), (214) and (300) confirms the synthesis of α-Fe$_2$O$_3$, having rhombohedral structure. which are in good agreement with the literature (JCPDS No. 33-0664) [233]. All peaks of Bi$_2$O$_3$ and Fe$_2$O$_3$ are present in the composite. There is no impurity peak in composite. Figure 3.22b depicts the PXRD of Bi$_2$O$_3$/Fe$_2$O$_3$-CNTF which shows that in the amorphous region of CNTF, there are some less intensity diffraction peaks are suppressed. However, the major peaks with crystal planes (102), (012), (104), (110), (214) and (300) clearly indicates the deposition of Bi$_2$O$_3$/Fe$_2$O$_3$ on CNTF surface. This indicates that there is no change in structure after deposition on CNTF. According to Debye Scherrer equation, the particle size of Bi$_2$O$_3$/Fe$_2$O$_3$ and Bi$_2$O$_3$/Fe$_2$O$_3$-CNTF is calculated to be 35.2 and 34.3 nm respectively. Dislocation density, micro strain is also calculated which are mentioned in table 3.11.
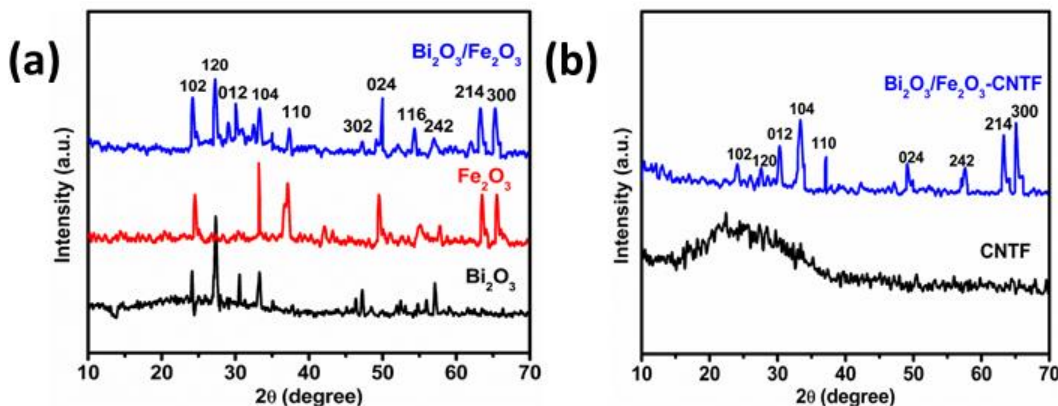
Figure 3.22. PXRD pattern of a) Bi$_2$O$_3$/Fe$_2$O$_3$ b) Bi$_2$O$_3$/Fe$_2$O$_3$-CNTF

Table 3.11. Crystallite size, dislocation density and micro strain

Compound name	Hkl	2θ (degree)	FWHM (degree)	FWHM (radians)	D_{avg} (nm)	$\delta_D \times 10^{15}$ (m^{-2})	$\varepsilon_m \times 10^{-3}$
Bi_2O_3/Fe_2O_3	120	27.27	0.5723	0.0099	15.0	4.44	0.24
	012	30.37	0.2251	0.0039	38.5	0.67	0.94
	104	33.22	0.1713	0.0029	52.2	0.36	0.69
Bi_2O_3/Fe_2O_3-CNTF	120	27.27	0.2322	0.0040	37.3	0.72	0.97
	104	33.22	0.2219	0.0038	39.7	0.63	0.91
	300	65.04	0.3812	0.0066	26.0	1.47	1.39

D_{avg} Bi_2O_3/Fe_2O_3= 15.0+ 38.5+ 52.2 /3 = 35.2 nm

D_{avg} Bi_2O_3/Fe_2O_3-CNTF= 37.3+ 39.7+ 26.0 /3 = 34.3 nm

SEM and EDX Analysis

SEM was performed to observe the structural morphology of synthesized composites i.e., Bi_2O_3/Fe_2O_3 and Bi_2O_3/Fe_2O_3-CNTF. Figure 3.23(a-c) shows the SEM images of Bi_2O_3/Fe_2O_3 at different resolutions, in which Bi_2O_3 has flat rod like and Fe_2O_3 has nanowires like morphology. Figure 3.13(d-e) shows the uniform deposition of Bi_2O_3/Fe_2O_3 on the surface of CNTF. Morphology remains same after deposition of Bi_2O_3/Fe_2O_3 on CNTF.

Furthermore, to determine the elemental and compositional properties, EDX and elemental mapping was performed for Bi_2O_3/Fe_2O_3 and Bi_2O_3/Fe_2O_3-CNTF. Figure 3.24a depicts the EDX spectrum of Bi_2O_3/Fe_2O_3 which shows that elements i.e., iron (Fe), bismuth (Bi), oxygen (O), carbon (C) were all present. It clearly confirms the purity of synthesized composite because no impurity peak of any other element is present in the spectrum. Figure 3.24b indicates the EDX layered image of Bi_2O_3/Fe_2O_3 and figure 3.24c represents the elemental mapping which successfully supports the EDX data. Moreover, EDX spectrum of Bi_2O_3/Fe_2O_3-CNTF is shown in figure 3.25a which shows all the elements (Fe, Bi, O and C) are present in Bi_2O_3/Fe_2O_3-CNTF are present. Layered images and elemental mapping of Bi_2O_3/Fe_2O_3-CNTF is also shown in figure 3.25(b-c).
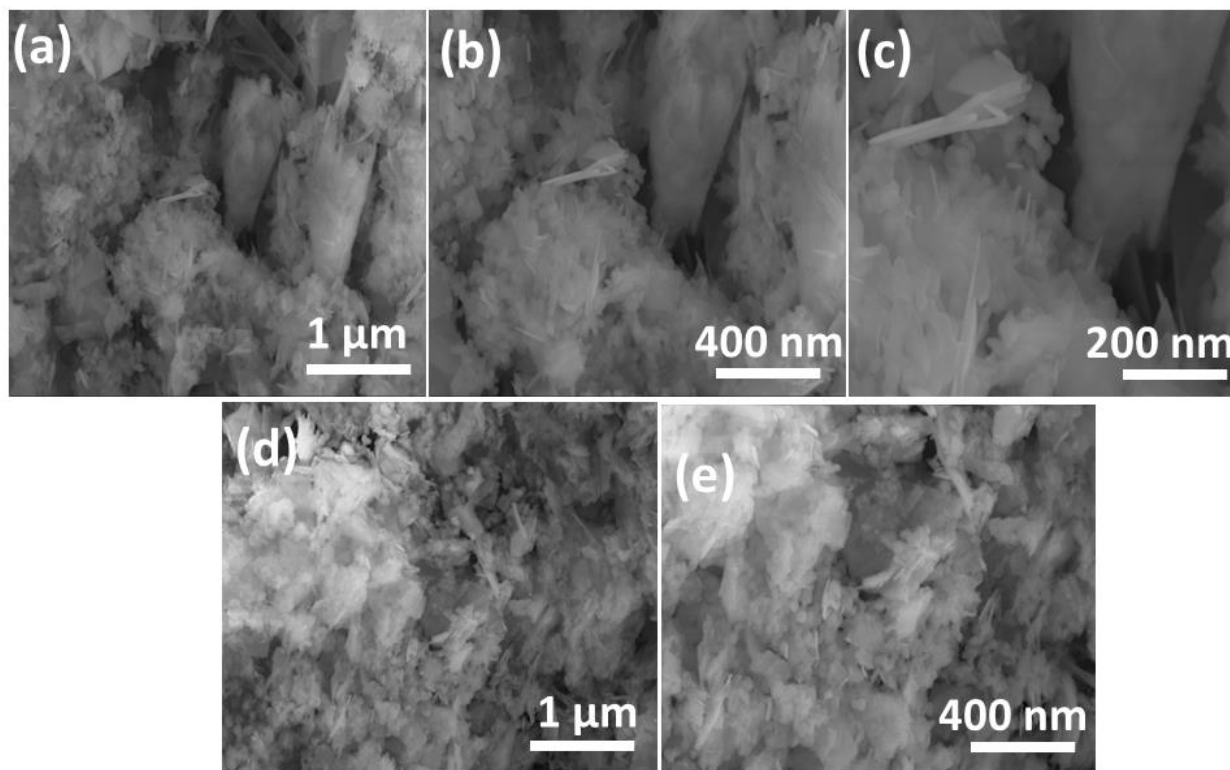
Figure 3.23. SEM images a-c) Bi_2O_3/Fe_2O_3 composites with different resolution, and d-e) Bi_2O_3/Fe_2O_3-CNTF with different resolution.
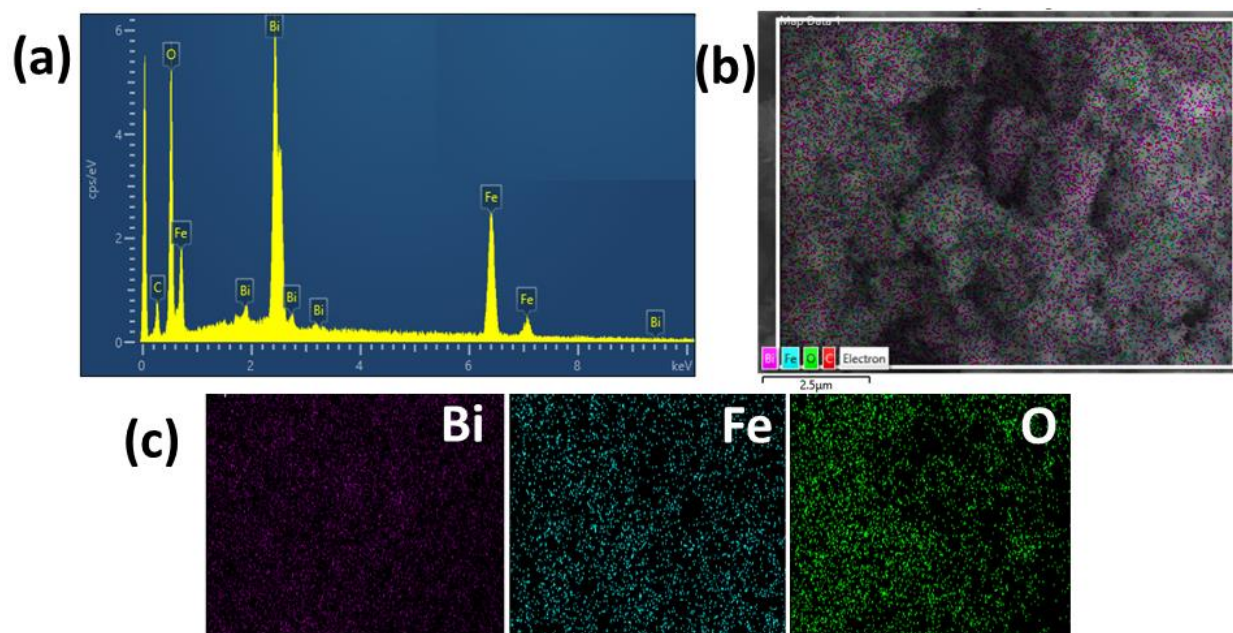
Figure 3.24. EDX spectrum a) Bi_2O_3/Fe_2O_3, b) EDX layered image of Bi_2O_3/Fe_2O_3, c) elemental mapping of Bi_2O_3/Fe_2O_3
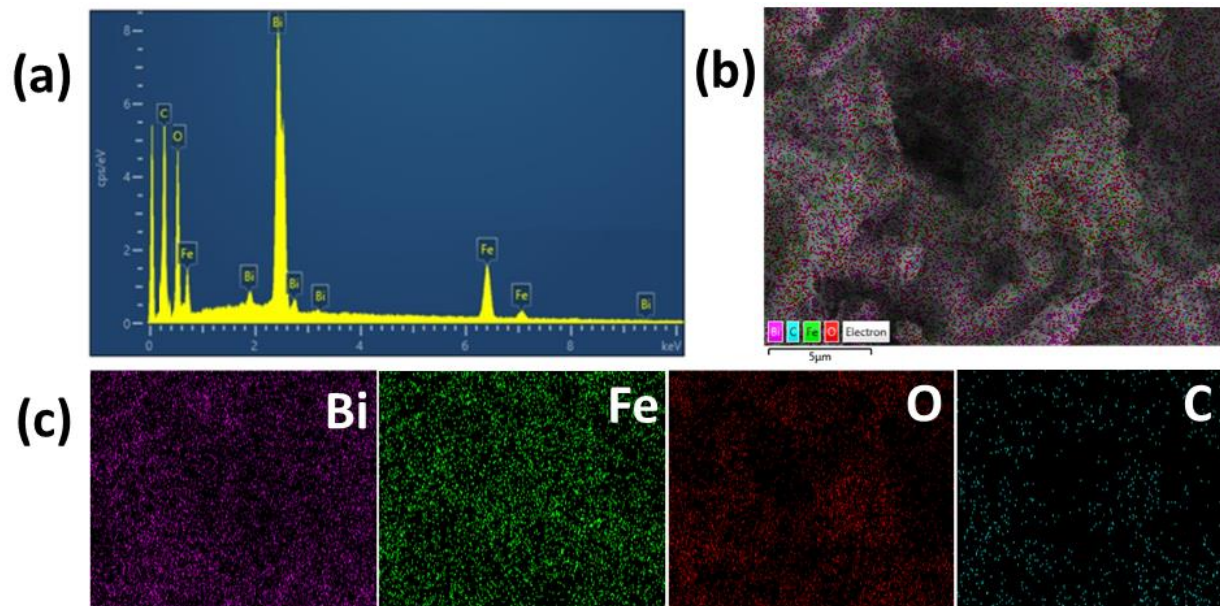
Figure 3.25. EDX spectrum a) Bi_2O_3/Fe_2O_3-CNTF, b) EDX layered image of Bi_2O_3/Fe_2O_3-CNTF, c) elemental mapping of Bi_2O_3/Fe_2O_3-CNTF

XPS Analysis

In figure 3.26a, an overview spectrum of Bi_2O_3/Fe_2O_3 is shown, which contains typical photoelectron and Auger peaks corresponding to iron, oxygen, bismuth, and carbon. In figure 3.26b, the spectrum of Bi 4f reveals a doublet with binding energy of 160.8 eV and 166.2 eV for Bi $4f_{7/2}$ and $4f_{5/2}$, respectively, which is attributed to the 3+ oxidation state of bismuth in the compound [205]. Figure 3.26c depicts the Fe 2p spectra which showed two peaks at binding energies of Fe $2p_{3/2}$ at 711.9 and Fe $2p_{1/2}$ at 725.2 eV. The minute intensity satellite peak detected at 719.2 eV which is the confirmation of Fe_2O_3 [234].
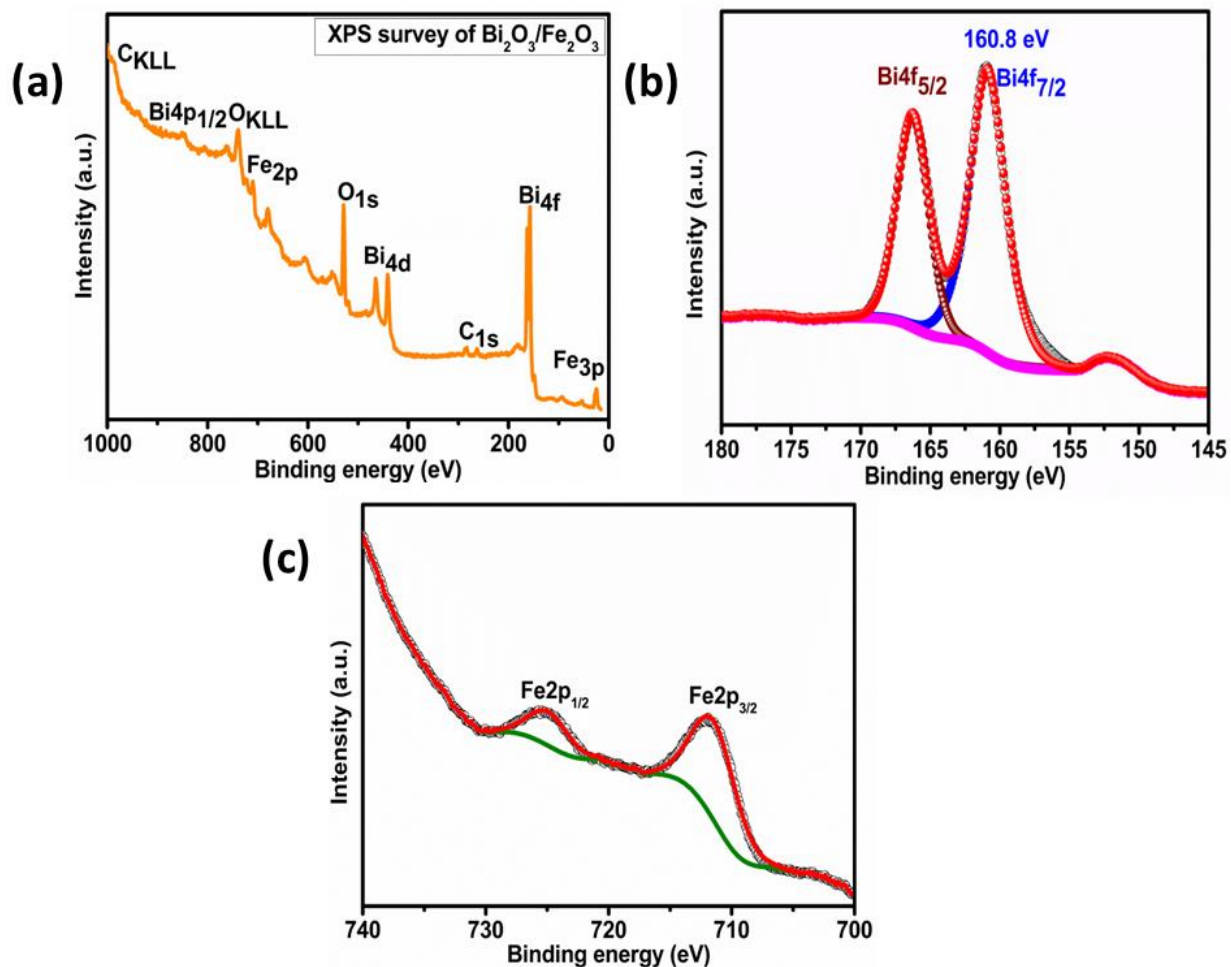
Figure 3.26. XPS spectra; a) survey scan, high resolution spectra of b) Bi 4f and c) Fe 2p

3.1.3.2. Electrochemical Studies

Electrochemical HER Activity

The HER performance of both series of electrodes was examined in neutral media. Figure 3.27 depicts LSV polarization curves and Tafel slopes which were used to determine the HER activity of the working electrodes.

Figure 3.27a shows the LSV curves for Bi_2O_3/Fe_2O_3-NiF in neutral media and it achieved 366 mV at 50 mA/cm^2 which was less than other working electrodes in series and showed Tafel slope value of 164.3 mV/dec (figure 3.27b). While Bi_2O_3/Fe_2O_3-CNTF in neutral media (figure 3.27c-d) i.e., had low overpotential of 340 mV at 50 mA/cm^2 with a Tafel slope of 135.9 mV/dec. It clearly

indicated that Bi_2O_3/Fe_2O_3-CNTF had better HER performance than Bi_2O_3/Fe_2O_3-NiF in neutral media.
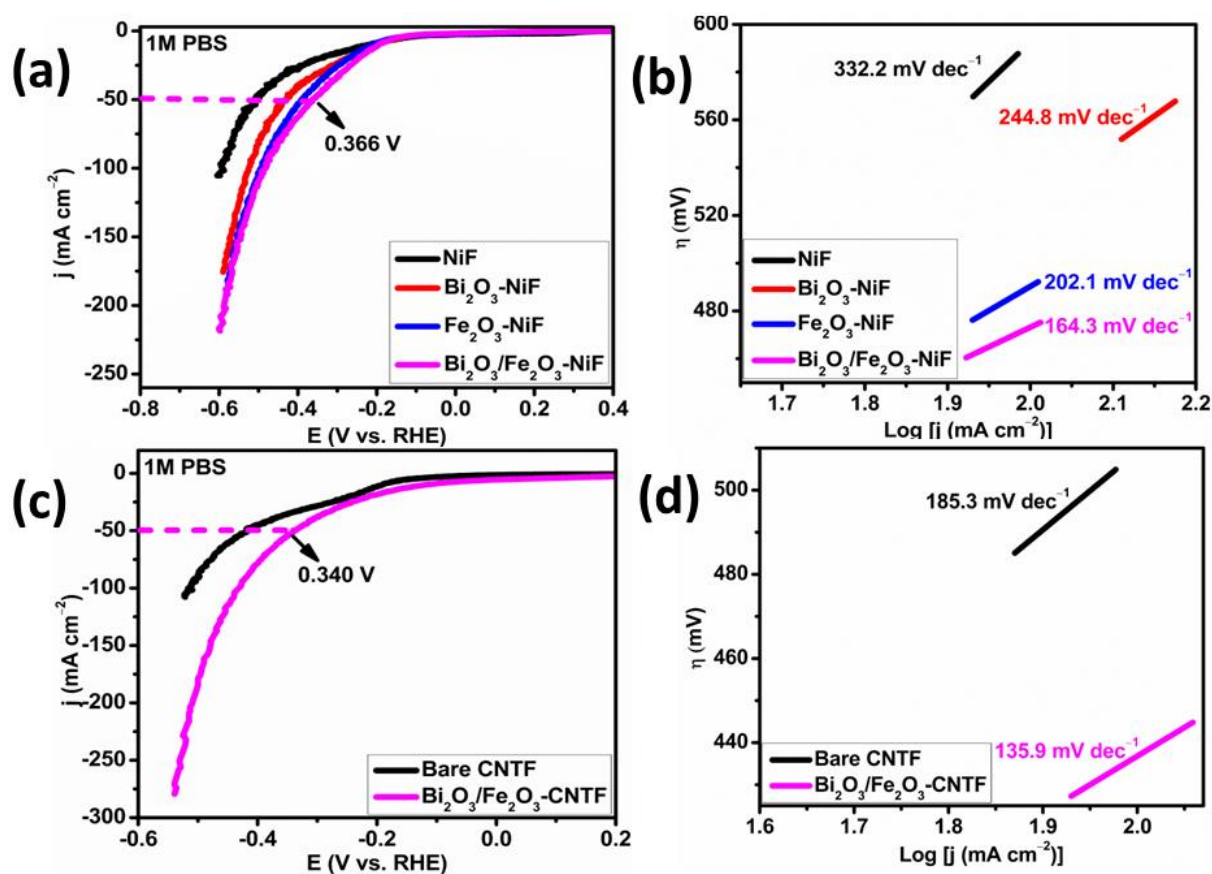
Figure 3.27. HER polarization curves and Tafel plots for a, b) Bi_2O_3/Fe_2O_3-NiF and c, d) Bi_2O_3/Fe_2O_3-CNTF in 1M PBS

Electrochemical OER Activity

LSV polarization curves were used to determine the OER performance of NiF based and CNTF based electrodes in basic and neutral media. The LSV data for NiF based electrodes in alkaline media reveals that Bi_2O_3/Fe_2O_3-NiF exhibited superior performance compared to the other electrodes of its series (see Figure 3.28a). The required overpotential values for Bi_2O_3/Fe_2O_3-NiF and Fe_2O_3-NiF to generate a current density of 150 mA/cm^2 are found to be 622 and 718 mV, respectively. While Bi_2O_3-NiF and bare NiF both exhibited very little OER activity. In case of Fe_2O_3-NiF, oxidation of Fe^{3+} to Fe^{4+} occur and according to literature, Fe^{4+} active centers catalyze the OER reaction [235]. So, the main active species for the high OER activity for Bi_2O_3/Fe_2O_3-

NiF bimetallic and Fe_2O_3-NiF catalysts is the oxidized FeOOH species. Tafel plots were further generated to investigate the kinetics of OER activity. Figure 3.28b represents the Tafel slope value of 194 mV/dec for Bi_2O_3/Fe_2O_3-NiF which is the lowest among NiF-based series in basic medium showing faster kinetics and supports the OER activity of Bi_2O_3/Fe_2O_3-NiF. Furthermore, the electrocatalytic OER activity of bimetallic system over CNTF (see Figure 3.28c and d) exhibited 572 mV@150 mA/cm^2 with a Tafel slope value of 123.1 mV/dec which is comparatively much lower than that for Bi_2O_3/Fe_2O_3-NiF in alkaline media.

Similarly, when the OER activity of Bi_2O_3/Fe_2O_3-NiF in performed in neutral medium, the results revealed that the Bi_2O_3/Fe_2O_3-NiF achieved 323 mV@20 mA/cm^2 with Tafel slope value of 184.2 mV/dec, while Bi_2O_3-NiF, Fe_2O_3-NiF and bare NiF exhibited very little OER activity (see Figure 3.28e and f). Moreover, performing the OER activity on CNTF as a substrate, Bi_2O_3/Fe_2O_3-CNTF exhibited 239 mV@20 mA/cm^2 with a Tafel slope 133.1 mV/dec (Figure 3.28g and h). The OER results in both media shows that the CNTF-based electrodes exhibited better electrochemical performance than NiF-based electrodes which can be attributed to the tubular channelled structure of CNTF that provides large surface area and more active sites. Table 3.12 shows OER and HER parameters (overpotential and Tafel slope) for both types of working electrodes in alkaline and neutral media. Comparative studies for OER and HER in alkaline and neutral media are shown in table 3.14 and 3.15.
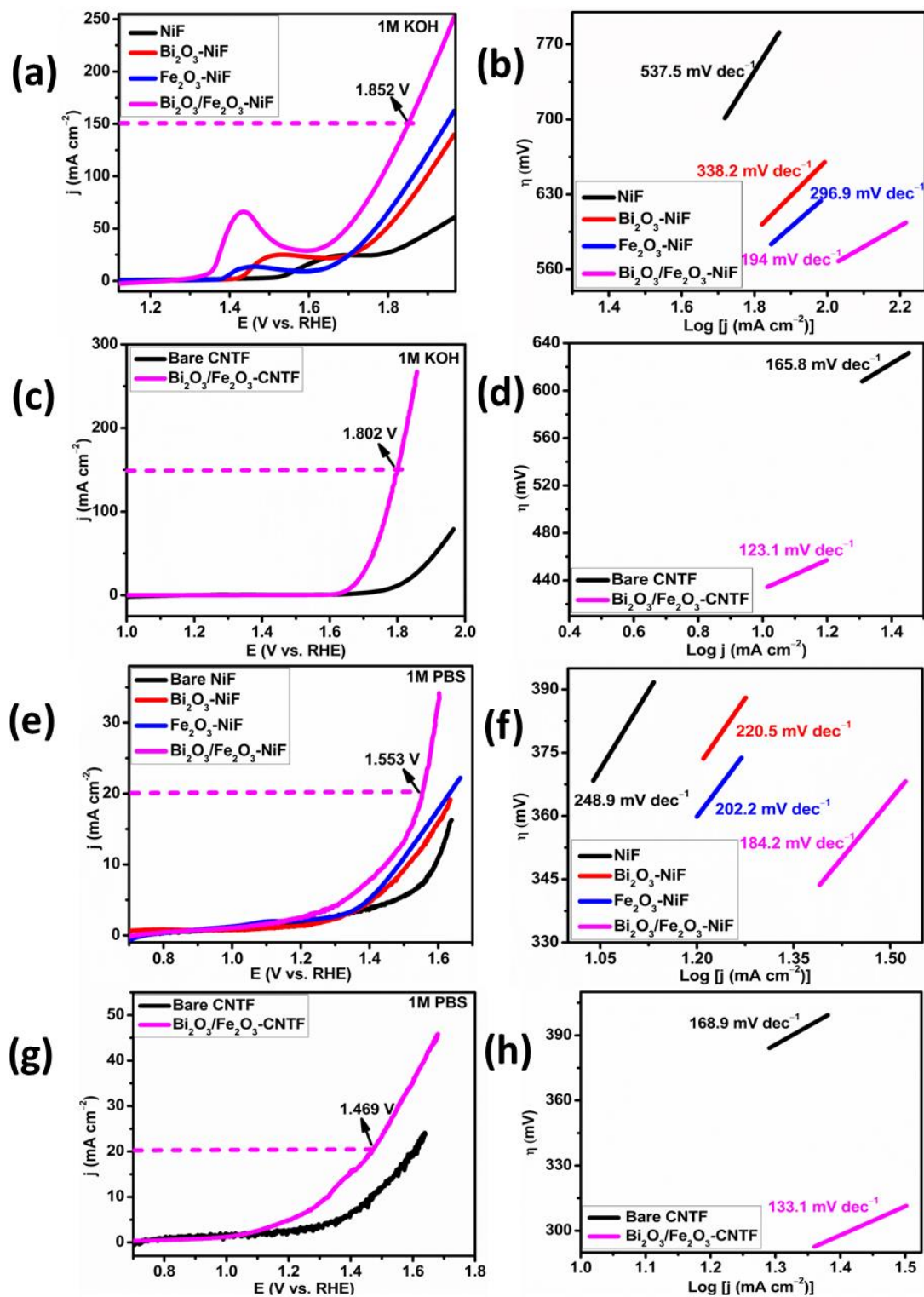
Figure 3.28. OER polarization curves and Tafel plots; a, b) NiF-based electrodes in basic medium, c, d) CNTF-based electrodes in basic medium, e, f) NiF-based electrodes in neutral medium, g, h) CNTF-based electrodes in neutral medium

Table 3.12. OER and HER parameters for Bi_2O_3/Fe_2O_3-NiF and Bi_2O_3/Fe_2O_3-CNTF in alkaline and neutral medium

Electrocatalyst	Medium	OER		HER	
		η (mV) @mA/cm^2	Tafel slope (mV/dec)	η (mV) @mA/cm^2	Tafel slope (mV/dec)
Bi_2O_3/Fe_2O_3-NiF	Alkaline	622@150	194	-	-
Bi_2O_3/Fe_2O_3-CNTF	-	572@150	123.1	-	-
Bi_2O_3/Fe_2O_3-NiF	Neutral	323@20	184.2	366@50	164.3
Bi_2O_3/Fe_2O_3-CNTF	-	239@20	133.1	340@50	135.9

Furthermore, CV analysis was performed in non-faradic region at various scan rates ranging from 50 to 250 mV/s for both series of fabricated electrodes in alkaline and neutral media to calculate the ECSA and C_{dl}. Figures 3.29a and c depict the CV graphs of Bi_2O_3/Fe_2O_3-NiF and Bi_2O_3/Fe_2O_3-CNTF in alkaline media while figures 3.29e and g represent the CV graphs of same electrodes in neutral media. By comparing the C_{dl} values defined from figure 3.29b and d, Bi_2O_3/Fe_2O_3-CNTF possesses high C_{dl} values than Bi_2O_3/Fe_2O_3-NiF. The same trend is followed while performing the measurements in neutral media (figures 3.29f and h). Furthermore, ECSA and RF was also calculated. Table 3.13 shows the C_{dl}, ECSA and RF for both types of working electrodes in alkaline and neutral media.

Table 3.13. C_{dl}, ECSA and RF in alkaline and neutral media

Electrocatalysts	Medium	C_{dl} (mF)	ECSA (cm^2)	RF
Bi$_2$O$_3$/Fe$_2$O$_3$-NiF	Alkaline	1.06	26.5	37
Bi$_2$O$_3$/Fe$_2$O$_3$-CNTF	-	1.34	33.5	598
Bi$_2$O$_3$/Fe$_2$O$_3$-NiF	Neutral	0.572	14.3	20
Bi$_2$O$_3$/Fe$_2$O$_3$-CNTF	-	0.87	21.75	388
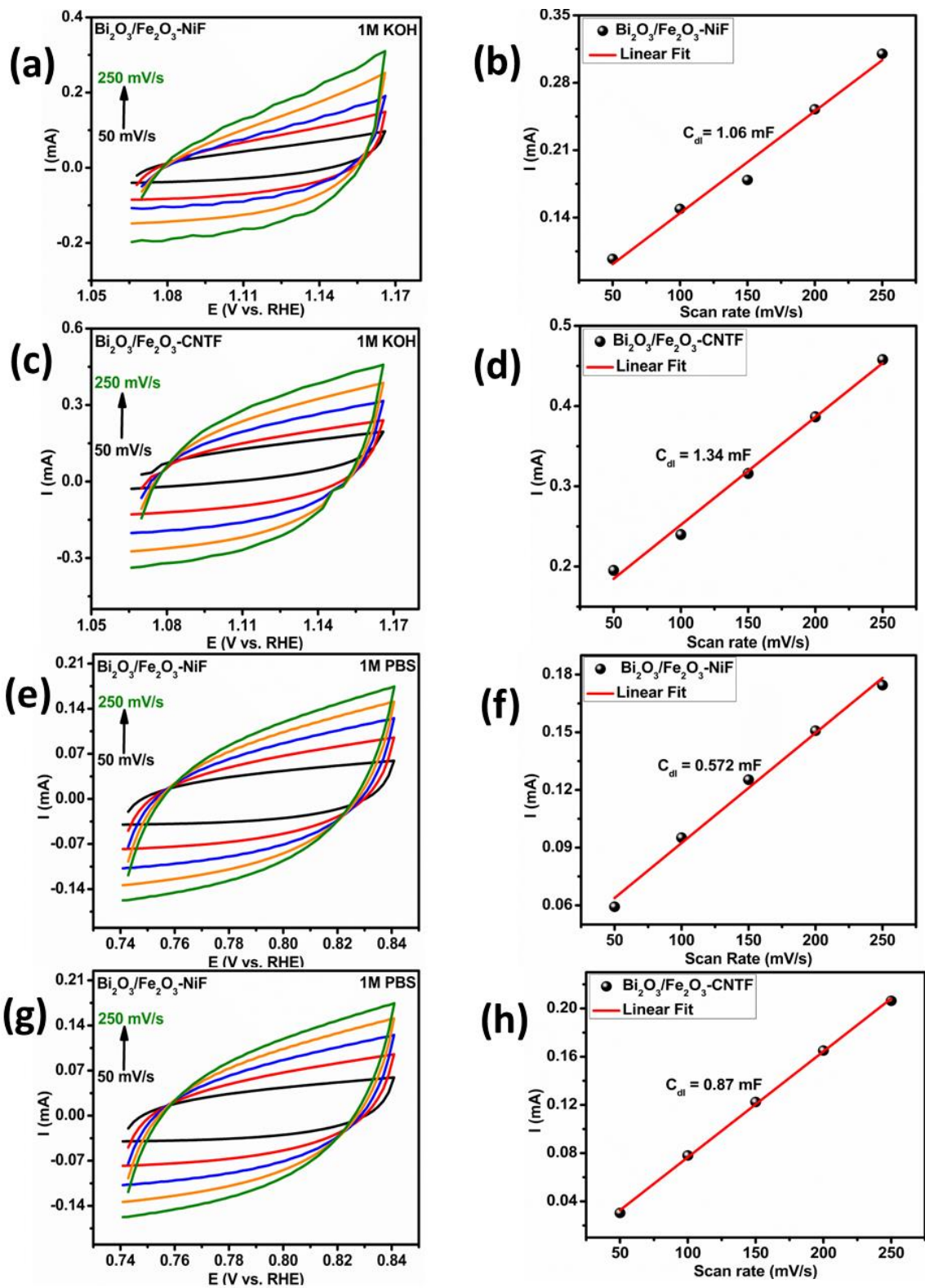
Figure 3.29. CV and C_{dl} plots for a, b) Bi_2O_3/Fe_2O_3-NiF in 1M KOH c, d) Bi_2O_3/Fe_2O_3-CNTF in 1M KOH, e, f) Bi_2O_3/Fe_2O_3-NiF in 1M PBS, g, h) Bi_2O_3/Fe_2O_3-CNTF in 1M PBS

To further investigate the OER kinetics, EIS was performed at 0.1 to 10^5 Hz frequency range by applying 10 mV AC voltage. Figure 3.30a and b depicts the Nyquist plot for Bi_2O_3/Fe_2O_3-NiF and Bi_2O_3/Fe_2O_3-CNTF in alkaline media which clearly reveals that Bi_2O_3/Fe_2O_3-CNTF had small diameter as compared to the Bi_2O_3/Fe_2O_3-NiF. The same trend is observed for Bi_2O_3/Fe_2O_3-NiF and Bi_2O_3/Fe_2O_3-CNTF in neutral media (see Figure 3.30c and d). A small semicircle justifies the low R_{ct} and faster kinetics.
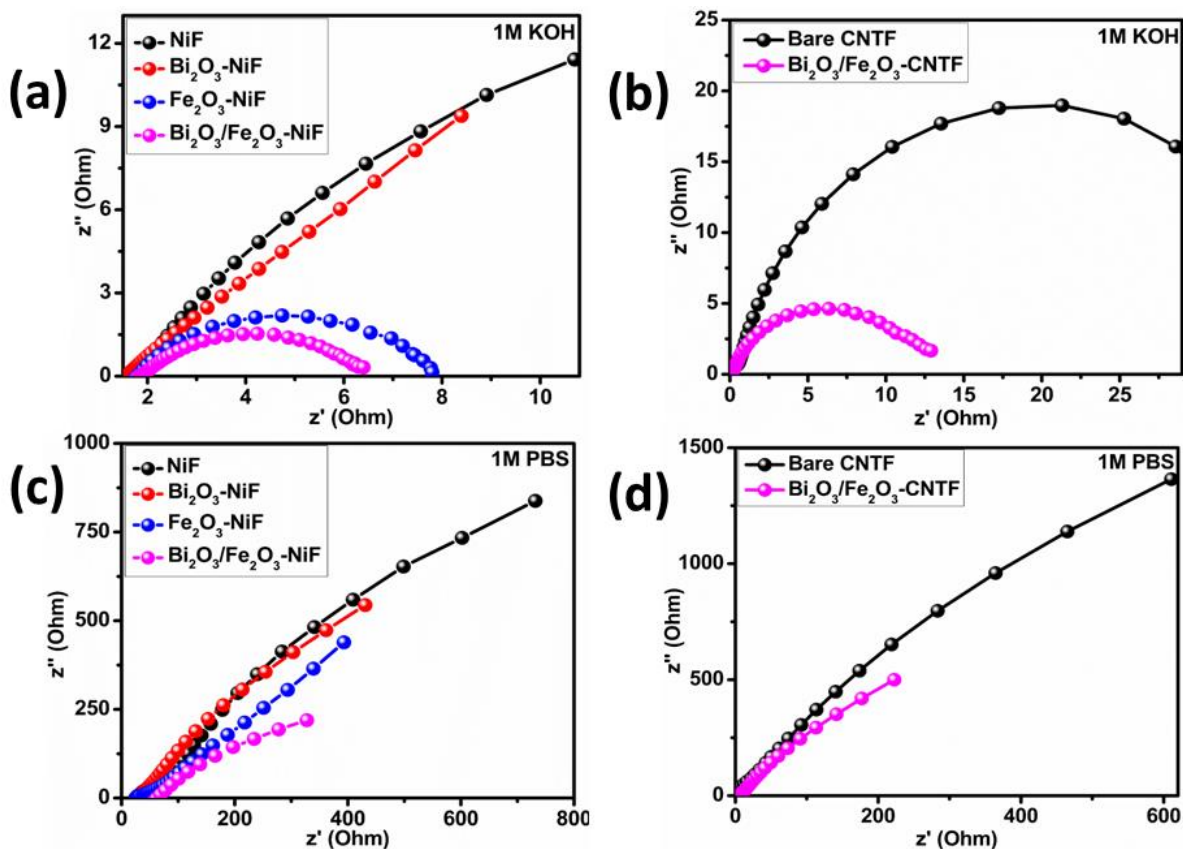
Figure 3.30. Nyquist plots for a) Bi_2O_3/Fe_2O_3-NiF and b) Bi_2O_3/Fe_2O_3-CNTF in 1M KOH, c) Bi_2O_3/Fe_2O_3-NiF and d) Bi_2O_3/Fe_2O_3-CNTF in 1M PBS

For the stability test, chronoamperometry was performed for Bi_2O_3/Fe_2O_3-CNTF being the best electrocatalyst among series of fabricated electrodes, for 24 h in both alkaline and neutral media (see Figure 3.31a and b) at the applied potential of 1.802 V (150 mA/cm^2 current density) and 1.469 V (20 mA/cm^2 current density) vs RHE, respectively. The electrocatalyst maintained for 24 h at the current density of 150 mA/cm^2 and 20 mA/cm^2 in basic and neutral media, respectively with a minor change under constant potentiostatic electrolysis.
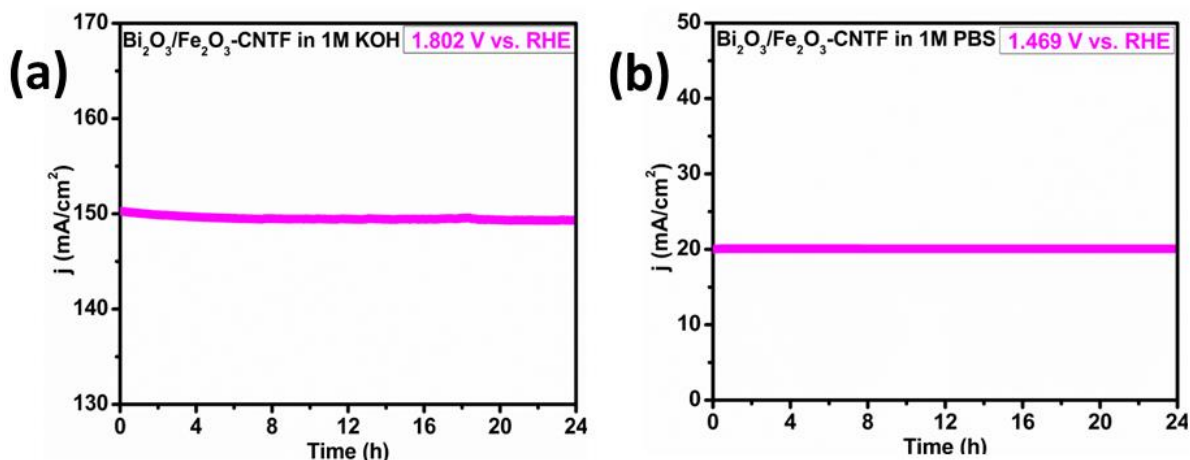
Figure 3.31. Chronoamperometry test for a) Bi_2O_3/Fe_2O_3-CNTF in 1M KOH and b) Bi_2O_3/Fe_2O_3-CNTF in 1M PBS

Table 3.14. Comparative OER performance of the electrocatalysts in alkaline media with literature.

Electrocatalyst	OER		References
	$Ŋ$ (mV)	Tafel slope (mV/dec)	
α-Fe_2O_3@g-C_3N_4-NCs	425@10 mA/cm^2	280	[236]
Fe_2O_3/$ZnCo_2O_4$	212@10 mA/cm^2	56.2	[237]
MnFeO-NF-0.8	157@10 mA/cm^2	-	[238]
FeO_x/$FeNi_3$/NF	269@50 mA/cm^2	78.6	[239]
Co_2FeO_4@PdO	259@20 mA/cm^2	59	[240]
$BiFeO_3$ nanorods	-	229	[241]
CoO_x/FeO_x/CNTs	308@10 mA/cm^2	43	[242]
Bi_2O_3/Fe_2O_3-NiF	**622@150 mA/cm^2**	**194.9**	**This work**
Bi_2O_3/Fe_2O_3-CNTF	**572@150 mA/cm^2**	**123.1**	**This work**

Table 3.15. Comparative OER and HER performance of the electrocatalysts in neutral media with literature.

Electrocatalyst	OER		HER		References
	η (mV)	Tafel slope (mV/dec)	η (mV)	Tafel slope (mV/dec)	
CoP/CeO$_2$-FeO$_x$H	248@10 mA/cm^2	-	37@10 mA/cm^2	-	[243]
FeO$_x$/FeP	-	-	96@10 mA/cm^2	47	[244]
Bi$_2$O$_3$/Fe$_2$O$_3$-NiF	**323@20 mA/cm^2**	**184.2**	**366@50 mA/cm^2**	**164.3**	**This work**
Bi$_2$O$_3$/Fe$_2$O$_3$-CNTF	**239@20 mA/cm^2**	**133.1**	**340@50 mA/cm^2**	**135.9**	**This work**

In a nutshell, Bi$_2$O$_3$/Fe$_2$O$_3$ and Bi$_2$O$_3$/Fe$_2$O$_3$-CNTF was characterized through XRD, SEM, EDX, elemental mapping, XPS techniques. Furthermore, these catalysts were tested for OER in 1M KOH and OER/HER in 1M PBS solution. It is clearly indicated that Bi$_2$O$_3$/Fe$_2$O$_3$-CNTF performed better in both media as compared to Bi$_2$O$_3$/Fe$_2$O$_3$-NiF. For OER in alkaline media, Bi$_2$O$_3$/Fe$_2$O$_3$-CNTF based electrodes reached current density of 150 mA/cm^2 at overpotential of 572 mV with Tafel slope 123.1 mV/dec while Bi$_2$O$_3$/Fe$_2$O$_3$-NiF based electrodes reached to same current density at overpotential of 622 mV with Tafel slope 194.9 mV/dec. Similarly, for OER and HER in 1M PBS, Bi$_2$O$_3$/Fe$_2$O$_3$-CNTF also outperformed (239 mV@20 mA/cm^2 with Tafel slope 133.1 mV/dec and 340 mV@50 mA/cm^2 with Tafel slope 135.9 mV/dec, respectively) than the Bi$_2$O$_3$/Fe$_2$O$_3$-NiF (323 mV@20 mA/cm^2 with Tafel slope 184.2 mV/dec and 366 mV@50 mA/cm^2 with Tafel slope 164.3 mV/dec, respectively).

3.1.4. Bi$_2$O$_3$/MnO Based Mixed Metal Oxides

Characterization and electrochemical studies for Bi$_2$O$_3$/MnO is given below.

3.1.4.1. Characterization of Materials

Bi_2O_3/MnO based mixed metal oxides were characterized through PXRD, SEM, EDX, elemental mapping and XPS analysis as discussed below.

Powder XRD Analysis

The PXRD spectra of Bi_2O_3, MnO, and Bi_2O_3/MnO are shown in Figure 3.32a. The sharp and strong peaks indicate the crystallinity of the synthesized materials. Bi_2O_3 diffraction peaks show the monoclinic phase (α). Bi_2O_3 crystal planes and their relative intensities are in good accord with literature. For MnO, there are three diffraction peaks with crystal planes (111), (200) and (220) confirms the synthesis of MnO, having cubic crystal structure. which are in good agreement with the literature (JCPDS Card No: 07-0230) [245]. All peaks of Bi_2O_3 and MnO are present in the composite. There is no impurity peak in composite. Figure 3.32b depicts the PXRD of Bi_2O_3/MnO-CNTF which shows the major peaks with crystal planes (120), (012), (122), (111), (200), (302) and (220) clearly indicates the deposition of Bi_2O_3/MnO on CNTF surface. This indicates that there is no change in structure after deposition on CNTF. According to Debye Scherrer equation, the crystallite size of Bi_2O_3/MnO and Bi_2O_3/MnO-CNTF is calculated to be 36.7 and 33.3 nm respectively. Dislocation density, micro strain is also calculated which are mentioned in table 3.16.
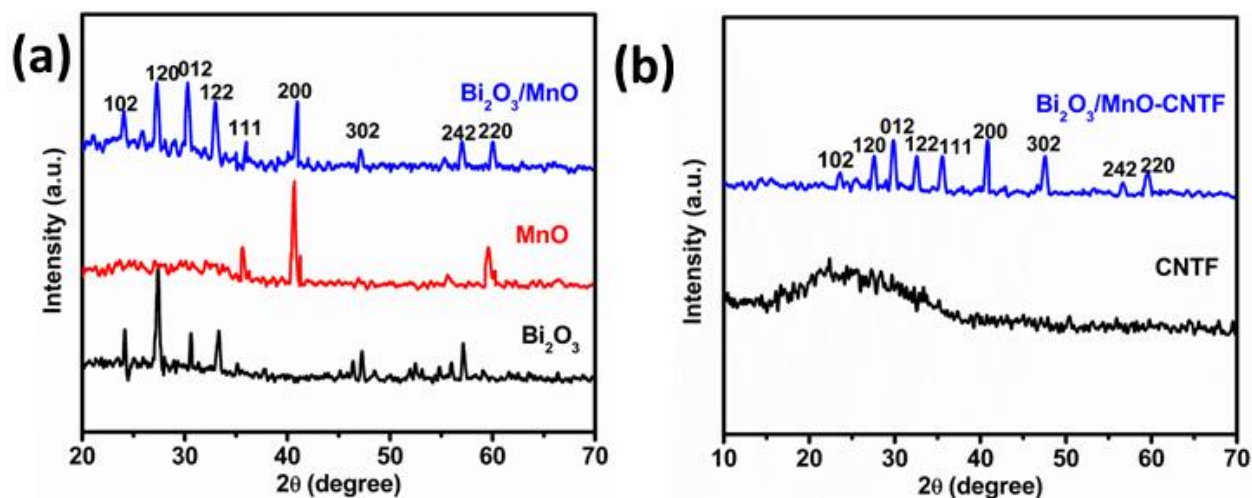
Figure 3.32. PXRD pattern of a) Bi_2O_3/MnO b) Bi_2O_3/MnO-CNTF

Table 3.16. Crystallite size, dislocation density and micro strain

Compound name	Hkl	2θ (degree)	FWHM (degree)	FWHM (radians)	D_{avg} (nm)	$\delta_D \times 10^{15}$ (m^{-2})	$\varepsilon_m \times 10^{-3}$
Bi$_2$O$_3$/MnO	120	27.27	0.5320	0.0092	16.1	3.85	2.2
	012	30.37	0.1956	0.0034	44.1	0.51	0.8
	200	40.90	0.1819	0.0031	49.9	0.40	0.7
Bi$_2$O$_3$/MnO-CNTF	120	27.27	0.2416	0.0042	35.4	0.79	1.0
	012	33.37	0.2572	0.0044	34.3	0.84	1.0
	200	40.90	0.2956	0.0051	30.3	1.08	1.1

D_{avg} Bi$_2$O$_3$/MnO = 16.1 + 44.1 + 49.9 /3 = 36.7 nm

D_{avg} Bi$_2$O$_3$/MnO-CNTF = 35.4 + 34.3 + 30.3 /3 = 33.3 nm

SEM and EDX Analysis

SEM was examined to observe the structural morphology of synthesized composites i.e., Bi$_2$O$_3$/MnO and Bi$_2$O$_3$/MnO-CNTF. Figure 3.33(a-c) shows the SEM images of Bi$_2$O$_3$/MnO at different resolutions, in which Bi$_2$O$_3$ has flat rod like and MnO has nanoneedles like morphology. Figure 3.33(d-e) shows the uniform deposition of Bi$_2$O$_3$/MnO on the surface of CNTF. Morphology remains same after deposition of Bi$_2$O$_3$/MnO on CNTF.

Furthermore, to determine the elemental and compositional properties, EDX and elemental mapping was performed for Bi$_2$O$_3$/MnO and Bi$_2$O$_3$/MnO-CNTF. Figure 3.34a depicts the EDX spectrum of Bi$_2$O$_3$/MnO which shows that elements i.e., manganese (Mn), bismuth (Bi), oxygen (O), carbon (C) were all present. It clearly confirms the purity of synthesized composite because no impurity peak of any other element is present in the spectrum. Figure 3.34b indicates the EDX layered image of Bi$_2$O$_3$/MnO and figure 3.34c represents the elemental mapping which successfully supports the EDX data. Moreover, EDX spectrum of Bi$_2$O$_3$/MnO-CNTF is shown in figure 3.35a which shows all the elements (Mn, Bi, O and C) are present in Bi$_2$O$_3$/MnO-CNTF are present. Layered images and elemental mapping of Bi$_2$O$_3$/MnO-CNTF is also shown in figure 3.35(b-c).
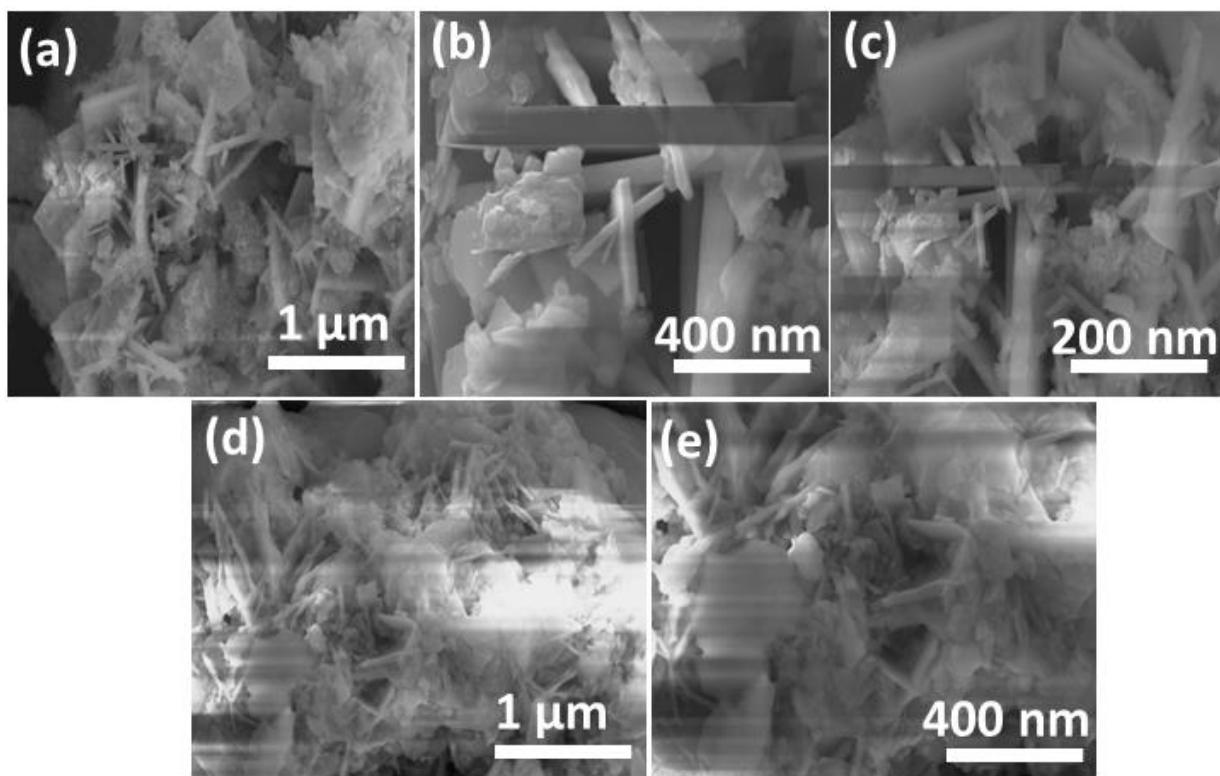
Figure 3.33. SEM images a-c) Bi$_2$O$_3$/MnO composites with different resolution, and d-e) Bi$_2$O$_3$/MnO-CNTF with different resolution.
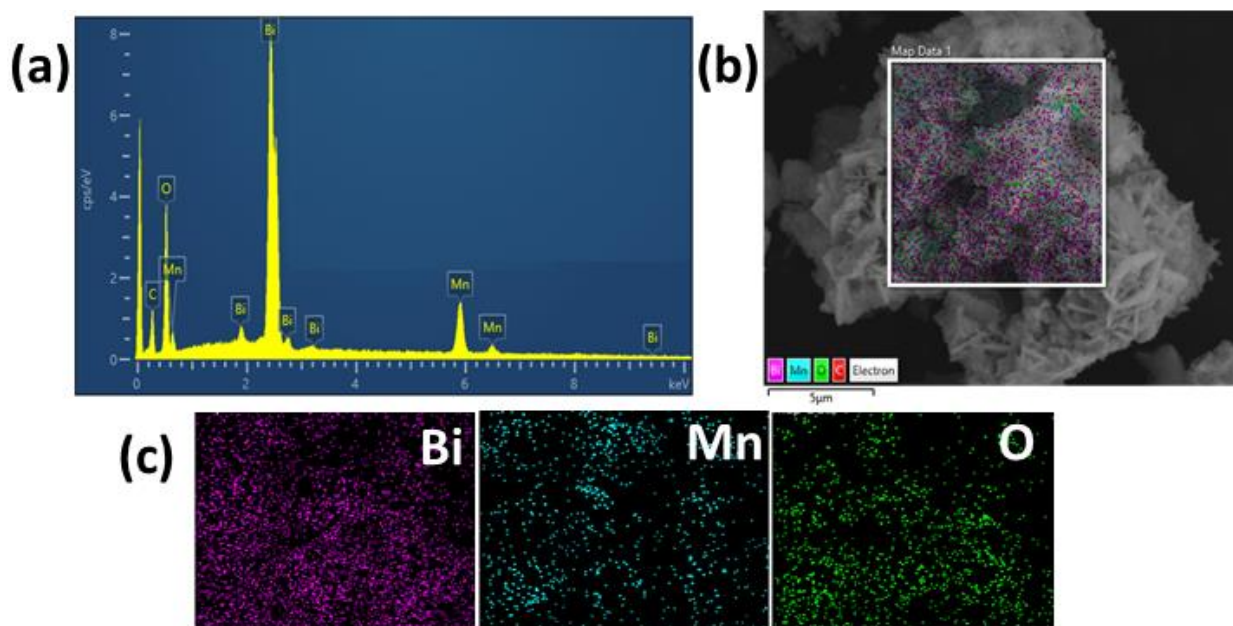
Figure 3.34. EDX spectrum a) Bi$_2$O$_3$/MnO, b) EDX layered image of Bi$_2$O$_3$/MnO, c) elemental mapping of Bi$_2$O$_3$/MnO
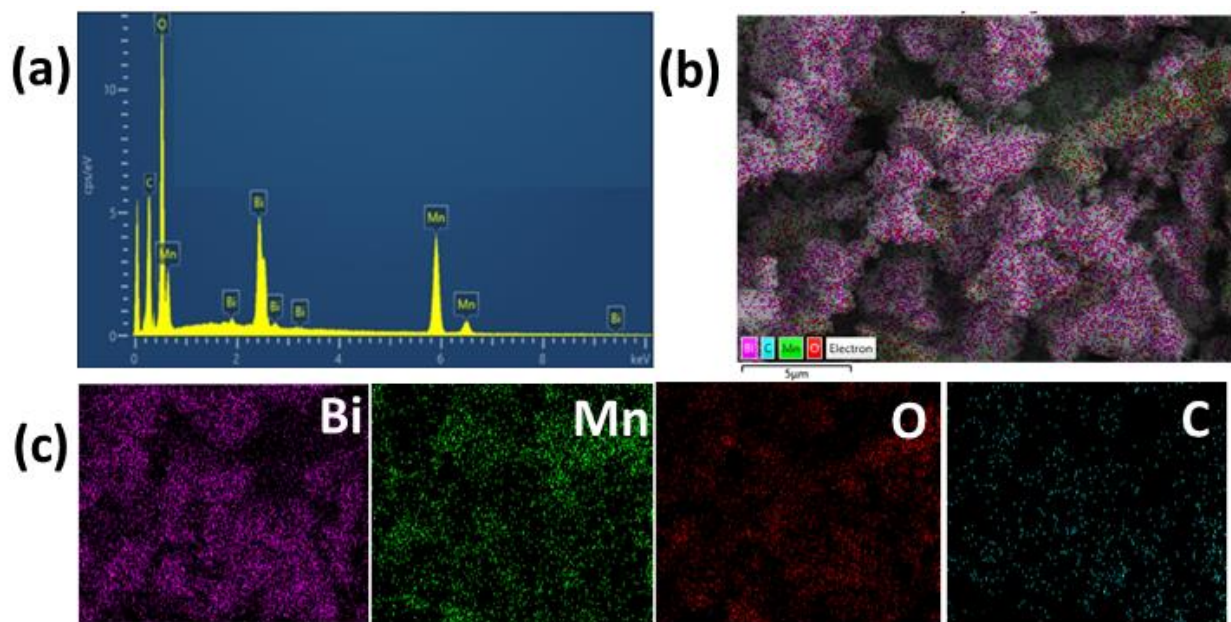
Figure 3.35. EDX spectrum a) Bi_2O_3/MnO_2-CNTF, b) EDX layered image of Bi_2O_3/MnO-CNTF, c) elemental mapping of Bi_2O_3/MnO-CNTF

XPS Analysis

In figure 3.36a, an overview spectrum of Bi_2O_3/MnO is shown, which contains typical photoelectron and Auger peaks corresponding to manganese, oxygen, bismuth, and carbon. In figure 3.36b, the spectrum of Bi 4f reveals a doublet with binding energy of 160.8 eV and 166.2 eV for Bi $4f_{7/2}$ and $4f_{5/2}$, respectively, which is attributed to the 3+ oxidation state of bismuth in the compound [205]. Upon closely examining the Mn 2p (Fig. 3.36c), peaks at 642.4 and 654.2 eV, which correspond to Mn $2p_{3/2}$ and Mn $2p_{1/2}$, respectively. MnO crystallisation is further confirmed by the spin orbit splitting between Mn $2p_{3/2}$ and Mn $2p_{1/2}$, which is 11.8 eV [246].
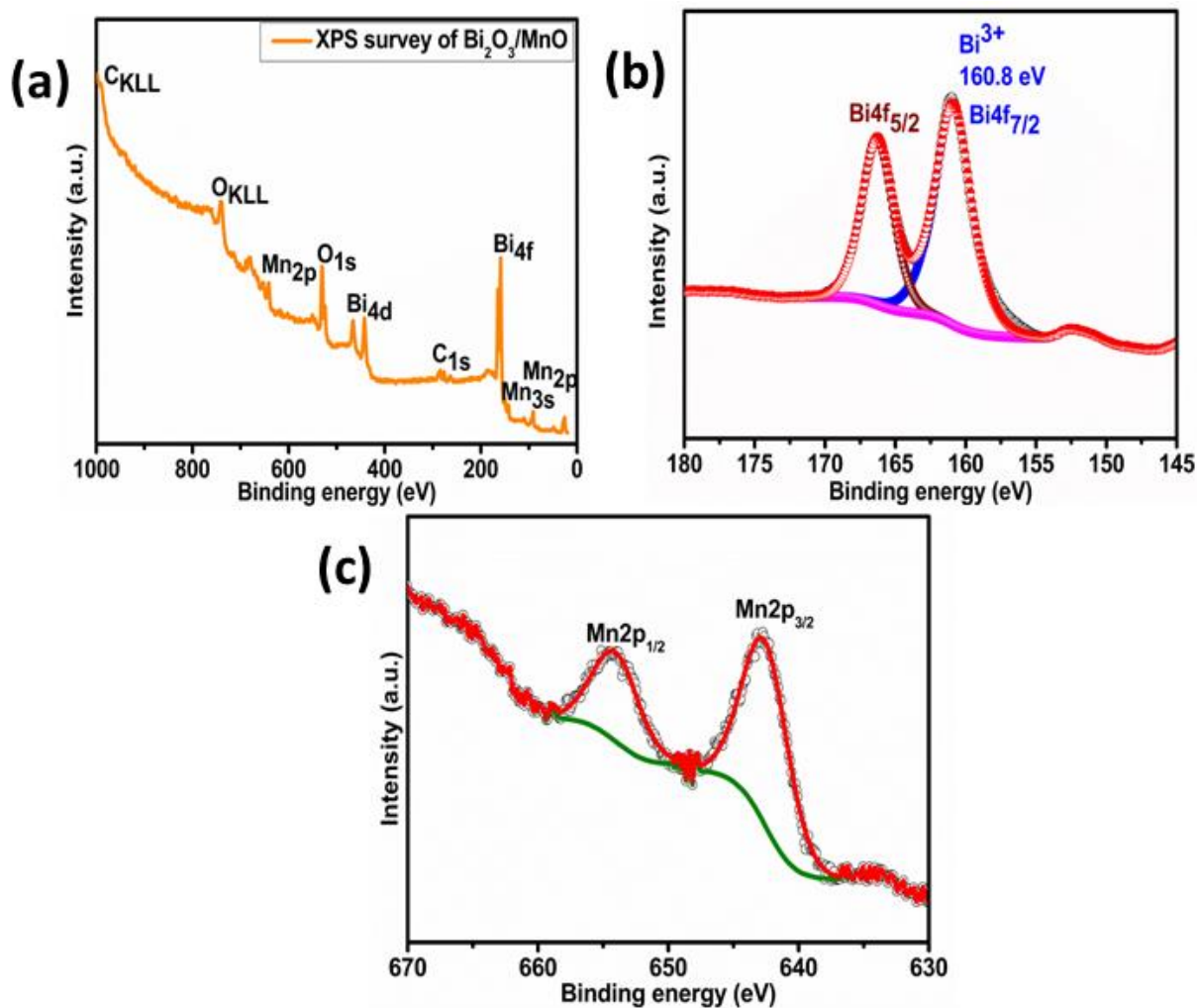
Figure 3.36. XPS spectra; a) survey scan, high resolution spectra of b) Bi 4f and c) Mn 2p

3.1.4.2. Electrochemical Studies

Electrochemical HER Activity

The HER performance of both series of electrodes was examined in neutral media. Figure 3.37 depicts LSV polarization curves and Tafel slopes which were used to determine the HER activity of the working electrodes.

Figure 3.37a shows the LSV curves for Bi_2O_3/MnO-NiF in neutral media and it achieved 375 mV at 50 mA/cm^2 which was less than other working electrodes in series and showed Tafel slope of 195 mV/dec (figure 3.37b). While Bi_2O_3/MnO-CNTF in neutral media (figure 3.37c-d) i.e., had

low overpotential of 356 mV at 50 mA/cm^2 with a Tafel slope of 144.2 mV/dec. It clearly indicated that Bi$_2$O$_3$/MnO-CNTF had better HER performance than Bi$_2$O$_3$/MnO-NiF in neutral media.
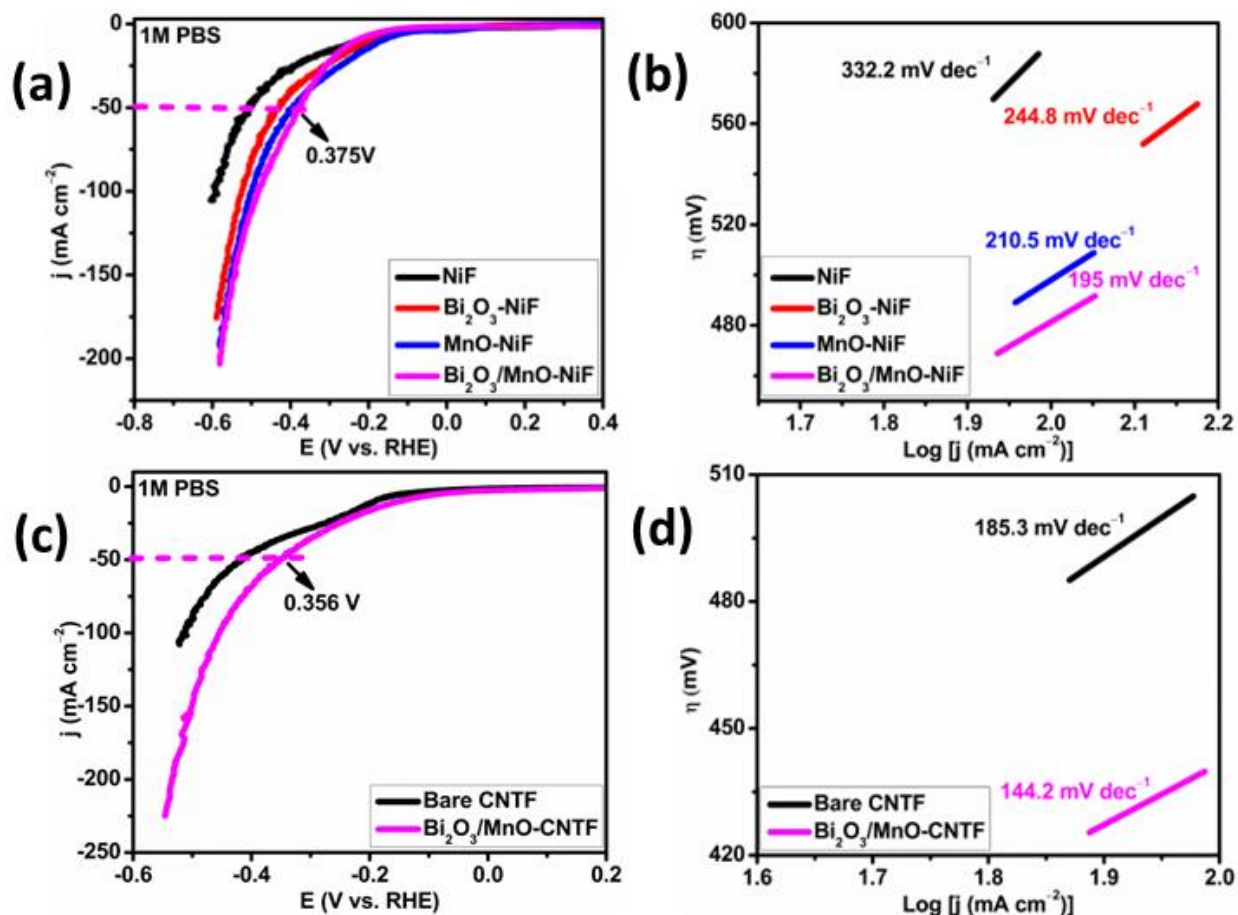
Figure 3.37. HER polarization curves and Tafel plots for a, b) Bi$_2$O$_3$/MnO-NiF and c, d) Bi$_2$O$_3$/MnO-CNTF in 1M PBS

Electrochemical OER Activity

LSV polarization curves were used to determine the OER performance of NiF based and CNTF based electrodes in basic and neutral media. The LSV data for NiF based electrodes in alkaline media reveals that Bi$_2$O$_3$/MnO$_2$-NiF exhibited superior performance compared to the other electrodes of its series (see Figure 3.38a). The required overpotential values for Bi$_2$O$_3$/MnO$_2$-NiF and MnO$_2$-NiF to generate a current density of 150 mA/cm^2 are found to be 674 and 726 mV, respectively. While Bi$_2$O$_3$-NiF and bare NiF both exhibited very little OER activity. In case of MnO$_2$-NiF, oxidation of Mn^{2+} to Mn^{3+} occur and according to literature, Mn^{3+} active centers catalyze the OER reaction. So, the main active species for the high OER activity for Bi$_2$O$_3$/MnO-

NiF bimetallic and MnO-NiF catalysts is the oxidized MnOOH species [247]. Tafel plots were further plotted to investigate the kinetics of OER activity. Figure 3.38b represents the Tafel slope value of 222.5 mV/dec for Bi_2O_3/MnO-NiF which is the lowest among NiF-based series in basic medium showing faster kinetics and supports the OER activity of Bi_2O_3/MnO-NiF. Furthermore, the electrocatalytic OER activity of bimetallic system over CNTF (see Figure 3.38c and d) exhibited an overpotential of 637 mV at the current density of 150 mA/cm^2 with a Tafel slope value of 138.5 mV/dec which is comparatively much lower than that for Bi_2O_3/MnO-NiF in alkaline media.

Similarly, when the OER activity of Bi_2O_3/MnO-NiF in performed in neutral medium, the results revealed that the Bi_2O_3/MnO-NiF achieved 361 mV@20 mA/cm^2 with Tafel slope value of 206.8 mV/dec, while Bi_2O_3-NiF, MnO-NiF and bare NiF exhibited very little OER activity (see Figure 3.38e and f). Moreover, performing the OER activity on CNTF as a substrate, Bi_2O_3/MnO-CNTF achieved 283 mV@20 mA/cm^2 with a Tafel slope 153 mV/dec (Figure 3.38g and h). The OER results in both media shows that the CNTF-based electrodes exhibited better electrochemical performance than NiF-based electrodes which can be attributed to the tubular channelled structure of CNTF that provides large surface area and more active sites. Table 3.17 shows OER and HER parameters (overpotential and Tafel slope) for both types of working electrodes in alkaline and neutral media. Comparative studies for OER and HER in alkaline and neutral media are shown in table 3.19 and 3.20.
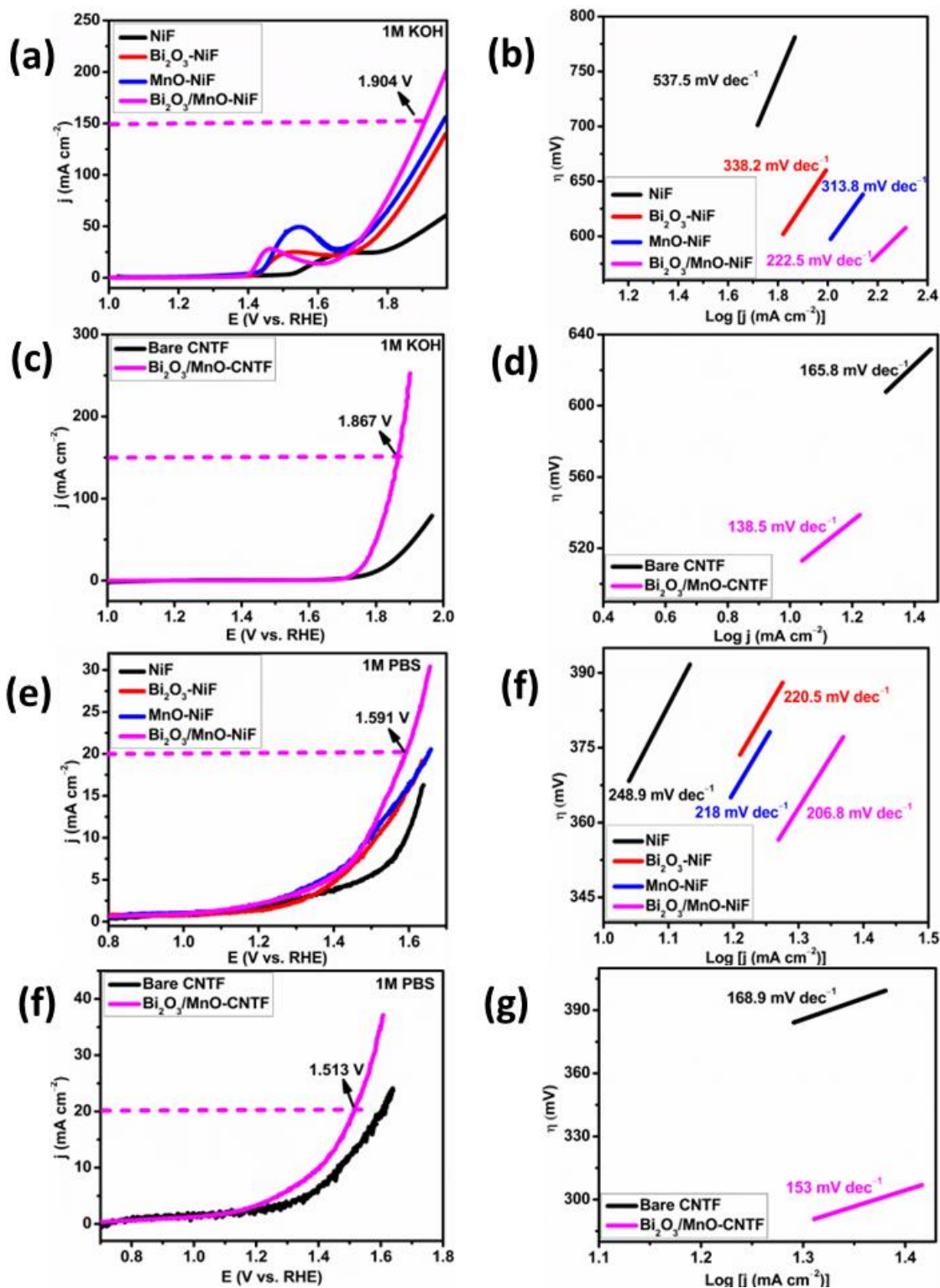
Figure 3.38. OER polarization curves and Tafel plots; a, b) NiF-based electrodes in basic medium, c, d) CNTF-based electrodes in basic medium, e, f) NiF-based electrodes in neutral medium, g, h) CNTF-based electrodes in neutral medium

Table 3.17. OER and HER parameters for Bi_2O_3/MnO-NiF and Bi_2O_3/MnO-CNTF in alkaline and neutral medium

Electrocatalyst	Medium	OER		HER	
		η (mV) @mA/cm^2	Tafel slope (mV/dec)	η (mV) @mA/cm^2	Tafel slope (mV/dec)
Bi_2O_3/MnO-NiF	Alkaline	674@150	222.5	-	-
Bi_2O_3/MnO-CNTF	-	637@150	138.5	-	-
Bi_2O_3/MnO-NiF	Neutral	361@20	206.8	375@50	195
Bi_2O_3/MnO-CNTF	-	283@20	153	356@50	144.2

Furthermore, CV analysis was performed in non-faradic region at various scan rates ranging from 50 to 250 mV/s for both series of fabricated electrodes in alkaline and neutral media to calculate the ECSA and C_{dl}. Figures 3.39a and c depict the CV graphs of Bi_2O_3/MnO-NiF and Bi_2O_3/MnO-CNTF in alkaline media while figures 3.39e and g represent the CV graphs of same electrodes in neutral media. By comparing the C_{dl} values defined from figure 3.39b and d, Bi_2O_3/MnO-CNTF possesses high C_{dl} values than Bi_2O_3/MnO-NiF. The same trend is followed while performing the measurements in neutral media (figures 3.39f and h). Furthermore, ECSA and RF was also calculated. Table 3.18 shows the C_{dl}, ECSA and RF for both types of working electrodes in alkaline and neutral media.

Table 3.18. C_{dl}, ECSA and RF in alkaline and neutral media

Electrocatalysts	Medium	C_{dl} (mF)	ECSA (cm^2)	RF
Bi_2O_3/MnO-NiF	Alkaline	0.95	23.75	34
Bi_2O_3/MnO-CNTF	-	1.11	27.75	495
Bi_2O_3/MnO-NiF	Neutral	0.493	12.32	18
Bi_2O_3/MnO-CNTF	-	0.57	14.25	254
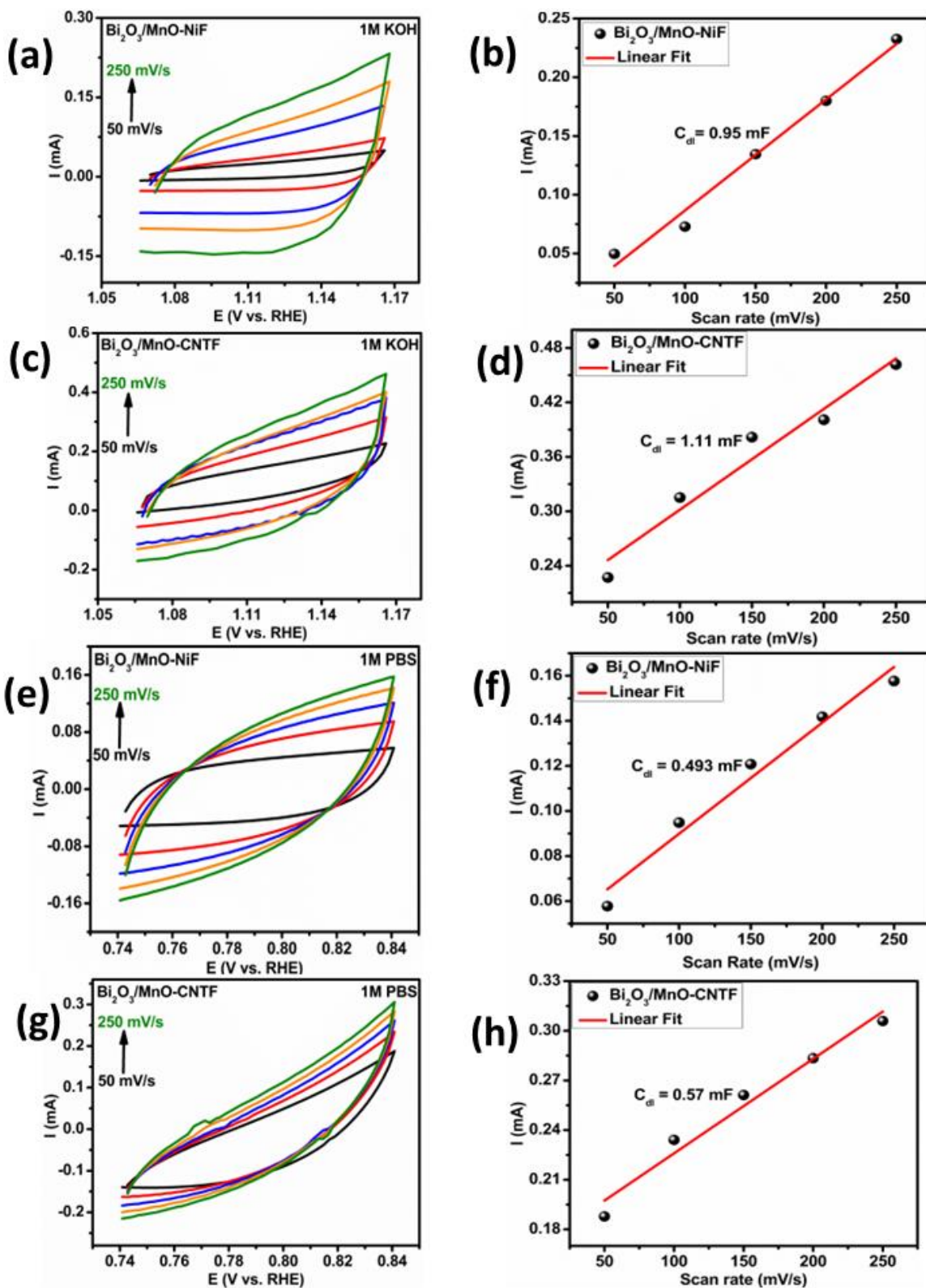
Figure 3.39. CV and C_dl plots for a, b) Bi₂O₃/MnO-NiF in 1M KOH c, d) Bi₂O₃/MnO-CNTF in 1M KOH, e, f) Bi₂O₃/MnO-NiF in 1M PBS, g, h) Bi₂O₃/MnO-CNTF in 1M PBS

To further investigate the OER kinetics, EIS was performed at 0.1 to 10^5 Hz frequency range by applying 10 mV AC voltage. Figure 3.40a and b depicts the Nyquist plot for Bi_2O_3/MnO-NiF and Bi_2O_3/MnO-CNTF in alkaline media which clearly reveals that Bi_2O_3/MnO-CNTF had small diameter as compared to the Bi_2O_3/MnO-NiF. The same trend is observed for Bi_2O_3/MnO-NiF and Bi_2O_3/MnO-CNTF in neutral media (see Figure 3.40c and d). A small semicircle justifies the low R_{ct} and faster kinetics.
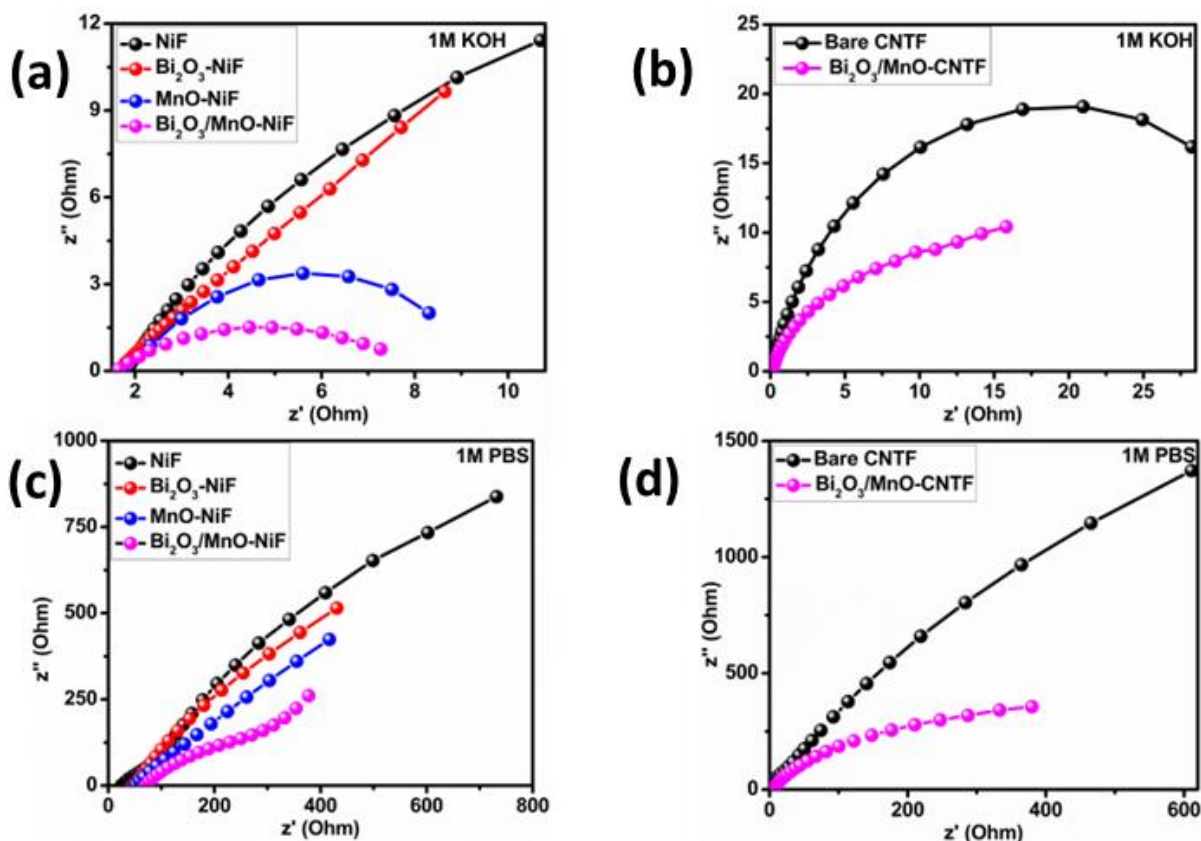
Figure 3.40. Nyquist plots for a) Bi_2O_3/MnO-NiF and b) Bi_2O_3/MnO-CNTF in 1M KOH, c) Bi_2O_3/MnO-NiF and d) Bi_2O_3/MnO-CNTF in 1M PBS

For the stability test, chronoamperometry was performed for Bi_2O_3/MnO-CNTF being the best electrocatalyst among series of fabricated electrodes, for 24 h in both alkaline and neutral media (see Figure 3.41a and b) at the applied potential of 1.867 V (150 mA/cm^2 current density) and 1.513 V (20 mA/cm^2 current density) vs RHE, respectively. The electrocatalyst maintained for 24 h at the current density of 150 mA/cm^2 and 20 mA/cm^2 in basic and neutral media, respectively with a minor change under constant potentiostatic electrolysis.
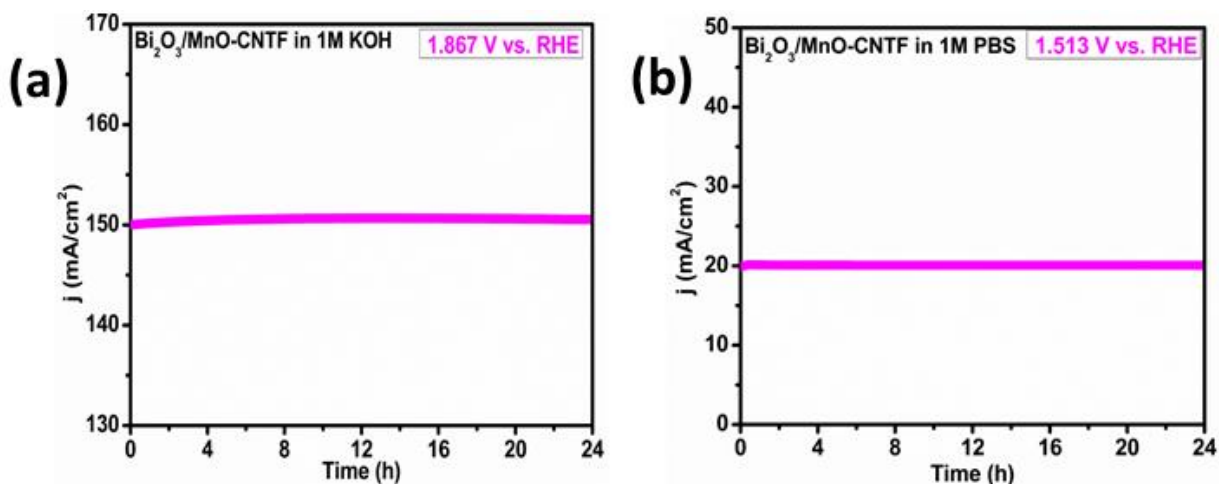
Figure 3.41. Chronoamperometry test for a) Bi$_2$O$_3$/MnO-CNTF in 1M KOH and b) Bi$_2$O$_3$/MnO-CNTF in 1M PBS

Table 3.19. Comparative OER performance of the electrocatalysts in alkaline media with literature.

Electrocatalyst	OER		References
	η (mV)	Tafel slope (mV/dec)	
Co/MnO@GC-700	358@10 mA/cm^2	-	[248]
Ni–MnO/rGO	370@10 mA/cm^2	67	[245]
Fe$_2$O$_3$-MnO/NF	370@10 mA/cm^2	66	[249]
Ni doped MnO$_2$	445@50 mA/cm^2	-	[250]
MnO/Co-CNTs	360@100 mA/cm^2	59.18	[251]
α-MnO$_2$	450@100 mA/cm^2	-	[252]
Bi$_2$O$_3$/MnO-NiF	**674@150 mA/cm^2**	**222.5**	**This work**
Bi$_2$O$_3$/MnO-CNTF	**637@150 mA/cm^2**	**138.5**	**This work**

Table 3.20. Comparative OER and HER performance of the electrocatalysts in neutral media with literature.

Electrocatalyst	OER		HER		References
	Ƞ (mV)	Tafel slope (mV/dec)	Ƞ (mV)	Tafel slope (mV/dec)	
Mn–Co–Bi/CC	366@10 mA/cm^2	193	293@10 mA/cm^2	-	[253]
Mn$_3$O$_4$ NPs	395@10 mA/cm^2	-	-	-	[254]
MnOx-300	330@1 mA/cm^2	92	-	-	[255]
Bi$_2$O$_3$/MnO-NiF	**361@20 mA/cm^2**	**206.8**	**375@50 mA/cm^2**	**195**	**This work**
Bi$_2$O$_3$/MnO-CNTF	**283@20 mA/cm^2**	**153**	**356@50 mA/cm^2**	**144.2**	**This work**

In a nutshell, Bi$_2$O$_3$/MnO and Bi$_2$O$_3$/MnO-CNTF was characterized through XRD, SEM, EDX, elemental mapping, XPS techniques. Furthermore, these catalysts were tested for OER in 1M KOH and OER/HER in 1M PBS solution. It is clearly indicated that Bi$_2$O$_3$/MnO -CNTF performed better in both media as compared to Bi$_2$O$_3$/MnO -NiF. For OER in alkaline media, Bi$_2$O$_3$/MnO -CNTF based electrodes reached current density of 150 mA/cm^2 at overpotential of 637 mV with Tafel slope 138.5 mV/dec while Bi$_2$O$_3$/MnO -NiF based electrodes reached to same current density at overpotential of 674 mV with Tafel slope 222.5 mV/dec. Similarly, for OER and HER in 1M PBS, Bi$_2$O$_3$/MnO -CNTF also outperformed (283 mV@20 mA/cm^2 with Tafel slope 153.1 mV/dec and 356 mV@50 mA/cm^2 with Tafel slope 144.2 mV/dec, respectively) than the Bi$_2$O$_3$/MnO -NiF (361 mV@20 mA/cm^2 with Tafel slope 206.8 mV/dec and 375 mV@50 mA/cm^2 with Tafel slope 195 mV/dec, respectively).

3.1.5. Ni4POM Based Mixed Metal Oxides

Characterization and electrochemical studies for Ni4POM is given below.

3.1.5.1. Characterization of Materials

Ni4POM based electrodes were characterized through FT-IR, PXRD, SEM, EDX and elemental mapping as discussed below.

FT-IR Analysis

To confirm the synthesis of Ni4POM, FT-IR analysis was performed and compared with the reported one [256]. Figure 3.42 demonstrates the FT-IR spectrum of Ni4POM which shows many distinct vibration peaks. These vibrations at 938, 884, and 811 cm^{-1} are attributed to the corner-sharing $v_{as}(W-O_b)$, edge-sharing $v_{as}(W-O_c)$ and $v_{as}(W-O-W)$ vibrations, respectively [256]. Furthermore, the P-O symmetric stretching vibration of Ni4POM can be assigned to a distinctive peak located around 1015 cm^{-1}. The Ni-O stretching vibration peak is present at 804 cm^{-1}. All these peaks clearly confirm the synthesis of Ni4POM.
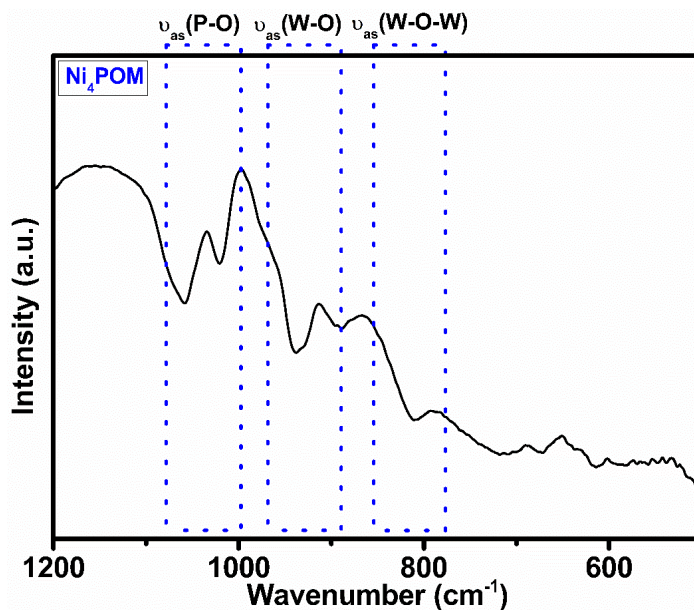
Figure 3.42. FT-IR spectrum of Ni4POM

Powder XRD Analysis

The fabricated electrode (Ni$_4$POM@CNTF) was characterized through PXRD technique. Figure 3.43 shows that CNTF had an amorphous pattern, whereas that of Ni$_4$POM@CNTF had prominent peaks at 7°, 8°, and 10° 2θ values, which confirmed the deposition of Ni$_4$POM on the surface of CNTF. Crystallite size was calculated by Debye Scherrer equation, and it was found that crystallite size was 41.2 nm. Dislocation density and micro strain were also calculated. Table 3.21 depicts the crystallite size, dislocation density and micro strain of electrocatalysts deposited on CNTF.
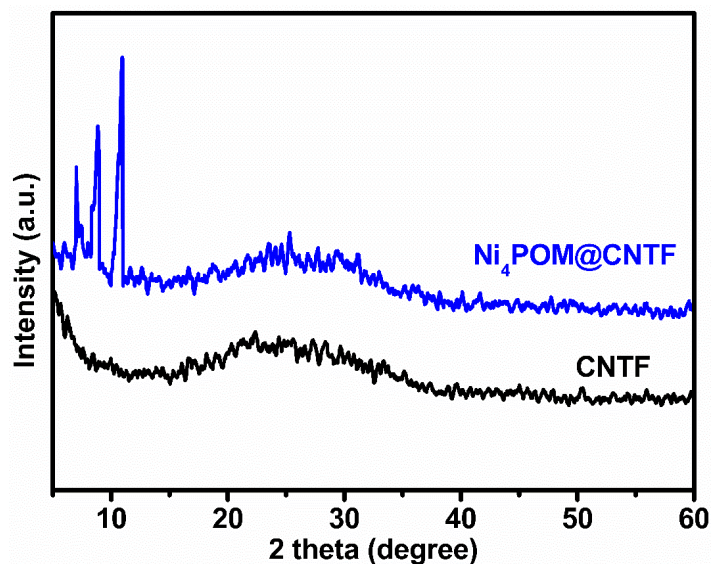
Figure 3.43. PXRD pattern of Ni$_4$POM and bare CNTF

Table 3.21. Crystallite size, dislocation density and micro strain of Ni$_4$POM@CNTF

Compound name	2θ (degree)	FWHM (degree)	FWHM (radians)	D_{avg} (nm)	δ_D x 10^{15} (m^{-2})	ε_m x 10^{-3}
Ni$_4$POM@CNTF	7.02	0.2252	0.0039	37.2	0.72	0.9
	8.87	0.1476	0.0025	58.1	0.29	0.6
	10.89	0.2952	0.0051	28.5	1.23	1.2

D_{avg} Ni$_4$POM@CNTF = 37.2 + 58.1 + 28.5 /3 = 41.2 nm

SEM and EDX Analysis

The morphological features of bare CNTF and Ni$_4$POM@CNTF were investigated through SEM analysis. Figure 3.44a, b depicts the SEM images of bare CNTF at different magnifications. The

SEM images of Ni$_4$POM@CNTF show that Ni$_4$POM was uniformly distributed on the surface of CNTFs (Figure 3.44c, d).

Moreover, EDX spectroscopy was used to determine the elemental composition of Ni$_4$POM@CNTF. The modified electrode derived from Ni$_4$POM had the following elements: nickel, tungsten, phosphorus, oxygen, potassium, and sodium as shown in Figure 3.45a. The EDX-layered image shown in Figure 3.45b shows that the Ni$_4$POM is evenly distributed over the CNTF surface. Moreover, elemental mapping confirmed that the corresponding elements are present in the manufactured electrode (Figure 3.45c).
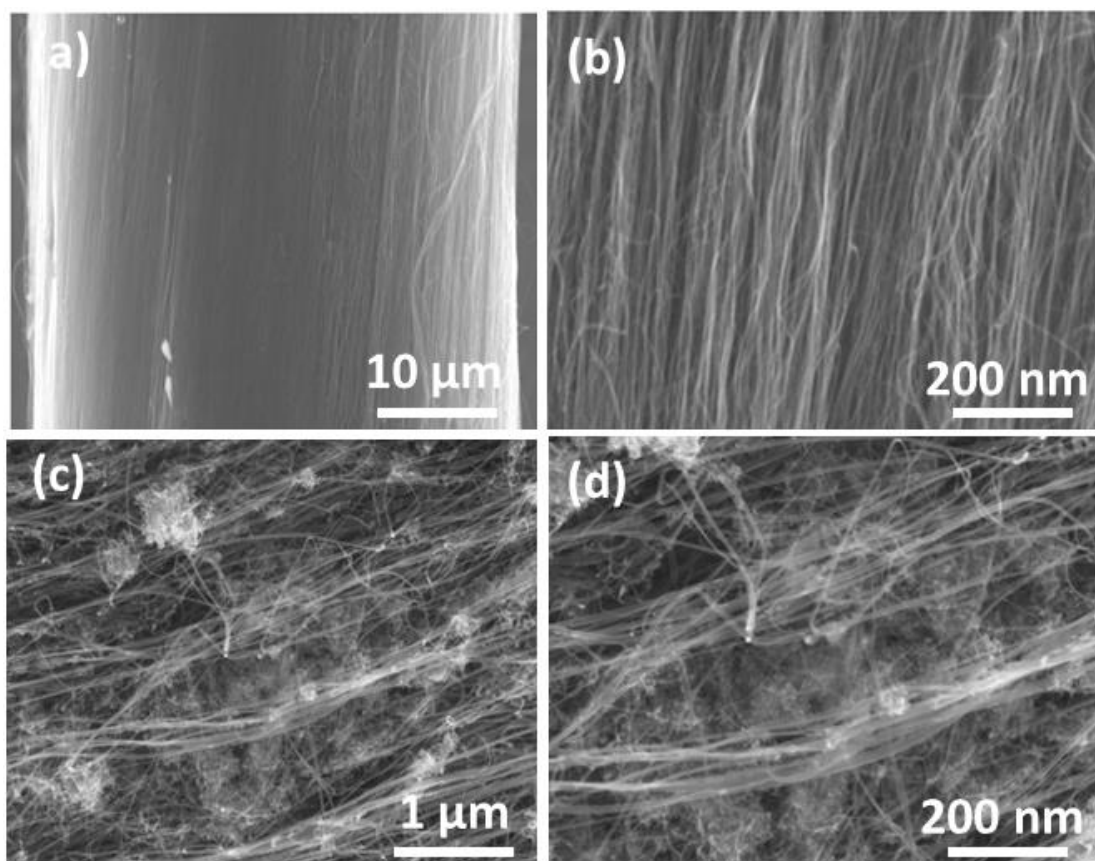
Figure 3.44. SEM images a-b) bare CNTF with different resolution, and d-e) Ni$_4$POM@CNTF with different resolution.
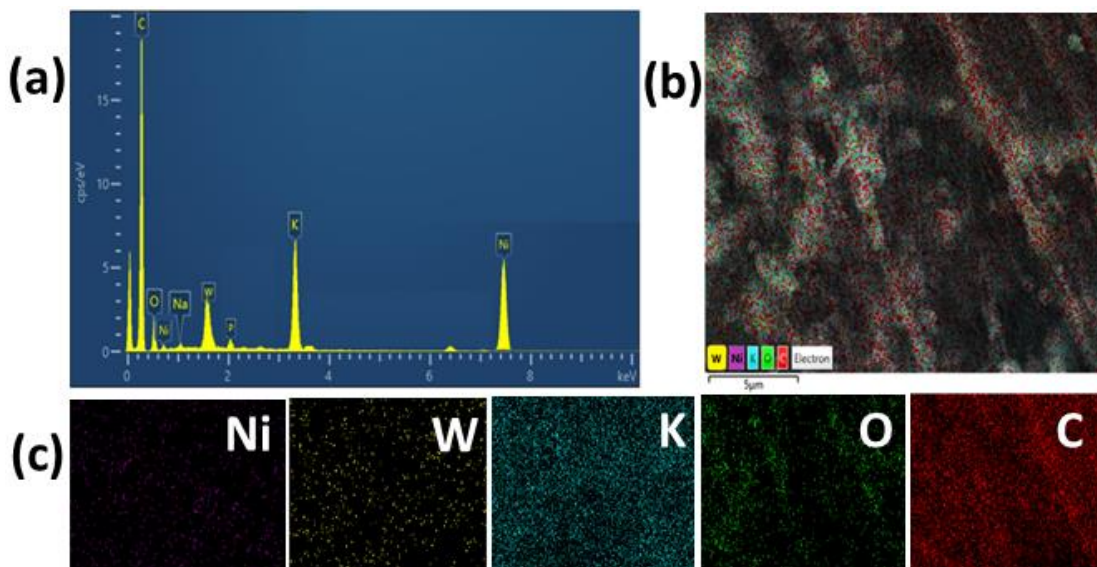
Figure 3.45. EDX spectrum a) Ni$_4$POM@CNTF, b) EDX layered image of Ni$_4$POM@CNTF, c) elemental mapping of Ni$_4$POM@CNTF

3.1.5.2. Electrochemical Studies

Ni$_4$POM@CNTF was employed as a working electrode to examine its OER activity in a three-electrode system at pH 13.5 (0.1M KOH). By comparing the LSV curves of bare CNTF with the POM-modified electrode (Figure 3.46a), OER activity was significantly increased by the immobilization of Ni$_4$POM over CNTF. Ni$_4$POM@CNTF demonstrated a remarkable increase in current density and significantly lower overpotential of 260 mV@10 mA/cm^2 compared to the bare CNTF, which needed overpotential of 737 mV for the same anodic current density. The low overpotential exhibited by the Ni$_4$POM@CNTF can be attributed to the tubular shape of CNTF that provided a high surface area and more active sites. Moreover, the high current-carrying capability and ballistic electron transport of CNTF increased electrical conductivity and current density due to its uniform nanochannels, which are superior to most of the Ni-based heterogeneous electrocatalysts in basic media.

The Tafel plots of as-prepared catalyst and bare CNTF were built using the LSV curves, as shown in Figure 3.46b. Compared to the bare CNTF with Tafel slope value of 288 mV/dec, Ni$_4$POM@CNTF exhibited a Tafel slope value of 42 mV/dec, showing the enhanced reaction kinetics of the modified electrode. The faster rate of the multiple electron transfer process presented in Ni$_4$POM@CNTF complimented the modified electrode's higher activity and current-

carrying ability. The high activity of the modified electrode can be attributed to the self-activation of Ni_4POM through restructuring in basic media that generated Nickel oxide and hydroxide as catalytic sites for OER.

Figure 3.46c depicts the cyclic voltammograms at different scan rates, i.e., from 50 to 250 mV/s in the non-Faradic region, to assess the ECSA of bare and Ni_4POM-modified electrodes. The plot of anodic current versus scan rate at a potential from 0 to 0.1 V versus RHE, as illustrated in Figure 3.46d, yielded a straight line where the slope obtained with linear fitting showed the double-layer capacitance (C_{dl}) of the respective electrodes. When the C_{dl} values of $Ni_4POM@CNTF$ and bare CNTF were compared, $Ni_4POM@CNTF$ had a higher C_{dl} value of 1.62 mF because it had a larger surface area and more active sites, which translated into higher efficiency. A calculation of ECSA was also made; it is directly correlated with C_{dl}, with a greater C_{dl} indicating a larger ECSA. Similarly, the RF is another surface characteristic and an important parameter for the electrocatalytic activity of the electrode material and can be calculated with the ratio of ECSA and the geometric area of the electrode. The higher ECSA and RF calculated for $Ni_4POM@CNTF$ than those for the bare CNTF confirm its improved electrochemical OER activity (see Table 3.22).
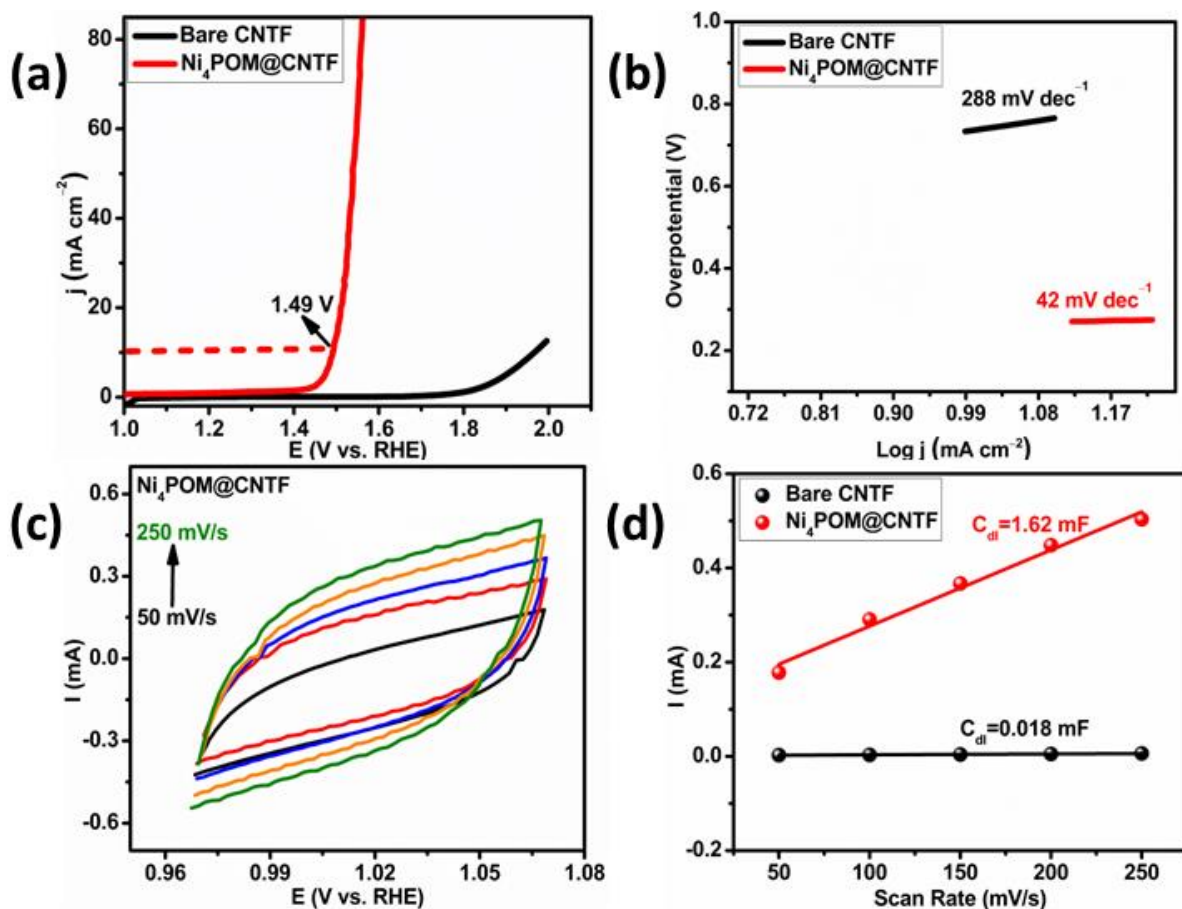
Figure 3.46. OER parameters (a, b) LSV polarization curves and Tafel plots for CNTF and Ni$_4$POM@CNTF (c) cyclic voltammograms for Ni$_4$POM@CNTF (d) C$_{dl}$ plot

Table 3.22. Electrochemical parameters of Ni$_4$POM

Electrocatalysts	η at 10 mA/cm^2 (mV)	Tafel slope mV/dec	C$_{dl}$ (mF)	ECSA (cm^2)	RF
Bare CNTF	737	288	0.018	0.45	8
Ni$_4$POM@CNTF	260	42	1.62	40.5	723
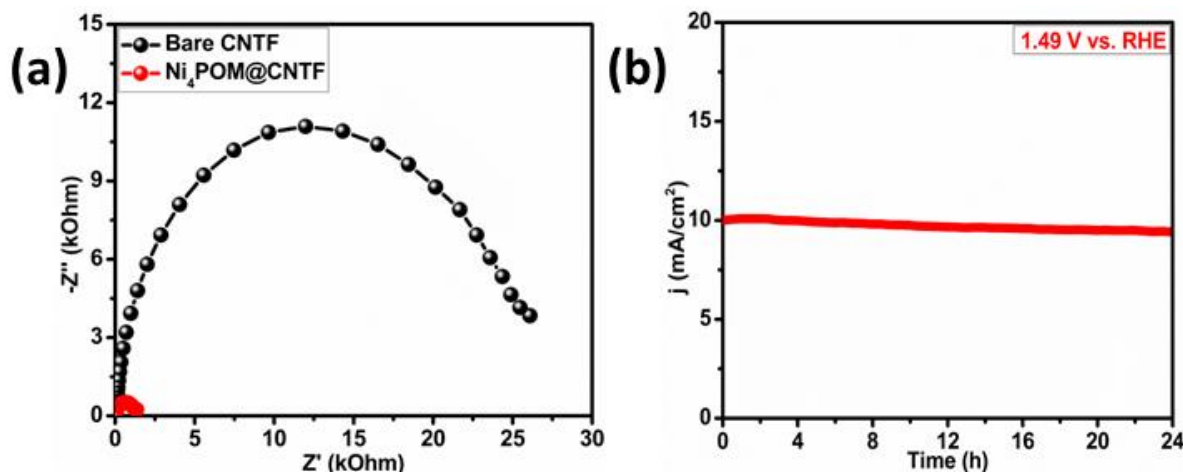
Figure 3.47. (a) Nyquist plots and (b) Chronoamperometry for Ni₄POM

3.1.6. Co₄POM Based Mixed Metal Oxides

Characterization and electrochemical studies for Co₄POM is given below.

3.1.6.1. Characterization of Materials

Co₄POM based electrodes were characterized through FT-IR, PXRD, SEM, EDX and elemental mapping as discussed below.

FT-IR Analysis

To confirm the synthesis of Co₄POM, FT-IR analysis was performed. Figure 3.48 depicts the FT-IR spectrum of Co₄POM which displays many distinct vibration peaks. These vibrations at 929, 881, and 790 cm^{-1} are assigned to the corner-sharing ν_{as}(W−O$_b$), edge-sharing ν_{as}(W−O$_c$) and ν_{as}(W-O-W) vibrations, respectively. Furthermore, the P-O symmetric stretching vibration of Ni₄POM can be attributed to a distinctive peak located around 1033 cm^{-1}. The Co-O stretching vibration peak is present at 721 cm^{-1}. All these peaks clearly confirm the synthesis of Co₄POM.

120
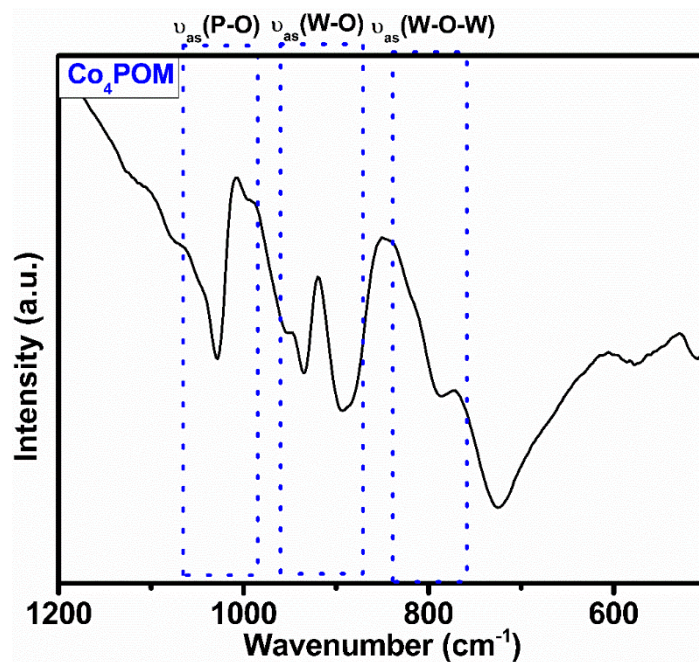
Figure 3.48. FT-IR spectrum of Co$_4$POM

Powder XRD Analysis

The fabricated electrode was characterized through PXRD. Figure 3.49 shows that CNTF had an amorphous pattern, whereas that of Co$_4$POM@CNTF had prominent peaks at 6°, 8°, and 12° 2θ values, which confirmed the deposition of Co$_4$POM on the surface of CNTF [87]. The peaks at 2θ values from 22° to 32° were not dominant due to the presence of the amorphous CNTF phase. The crystallite was calculated to be 40.1 nm. Dislocation density and micro strain was also calculated (Table 3.23)
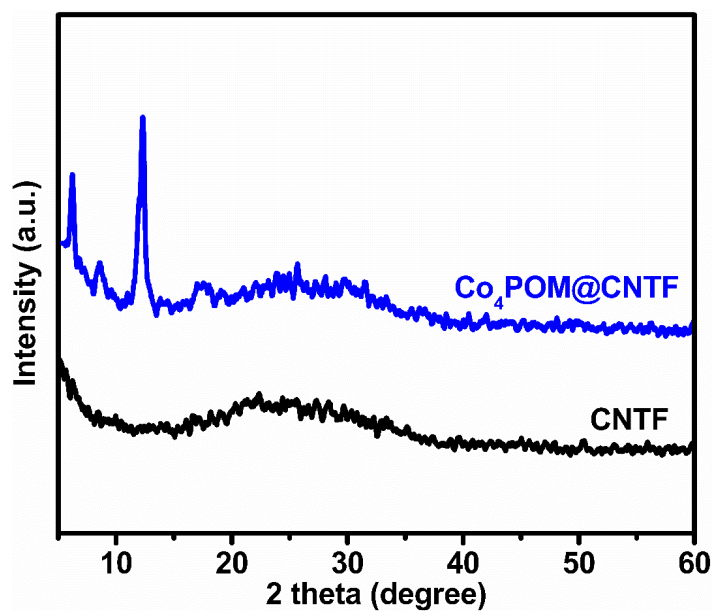
Figure 3.49. PXRD pattern of Co₄POM and bare CNTF

Table 3.23. Crystallite size, dislocation density and micro strain of Co₄POM@CNTF

Compound name	2θ (degree)	FWHM (degree)	FWHM (radians)	D_{avg} (nm)	δ_D x 10^{15} (m^{-2})	ε_m x 10^{-3}
Co₄POM@CNTF	6.25	0.2232	0.0038	38.1	0.68	0.9
	8.58	0.1568	0.0027	53.8	0.34	0.6
	12.28	0.2956	0.0051	28.5	1.23	1.2

D_{avg} Co₄POM@CNTF = 38.1 + 53.8 + 28.5 /3 = 40.1 nm

SEM and EDX Analysis

The morphological features of Co₄POM@CNTF were investigated through SEM analysis. Figure 3.50a, b shows the SEM images of Co₄POM@CNTF show that Co₄POM was uniformly distributed on the surface of CNTF.

Furthermore, Co₄POM@CNTF was characterized through EDX spectroscopy. Figure 3.51a shows that cobalt, oxygen, phosphorus, potassium, tungsten and sodium were all present in the modified electrode that stemmed from Co₄POM. A peak observed in the range from 0.1 to 0.2 keV was assigned to carbon, which is attributed to the CNTF substrate. The iron catalyst utilized in the chemical vapor deposition (CVD) method of CNTF synthesis produced the iron (Fe) peak, which occurred between 6.2 and 6.6 keV [257]. The EDX-layered image shown in Figure 3.51b shows

122

that the colored dots, or components, of Co4POM were evenly distributed across the CNTF surface. Additionally, elemental mapping confirmed that the corresponding elements were present in the manufactured electrode. (see Figure 3.51c).
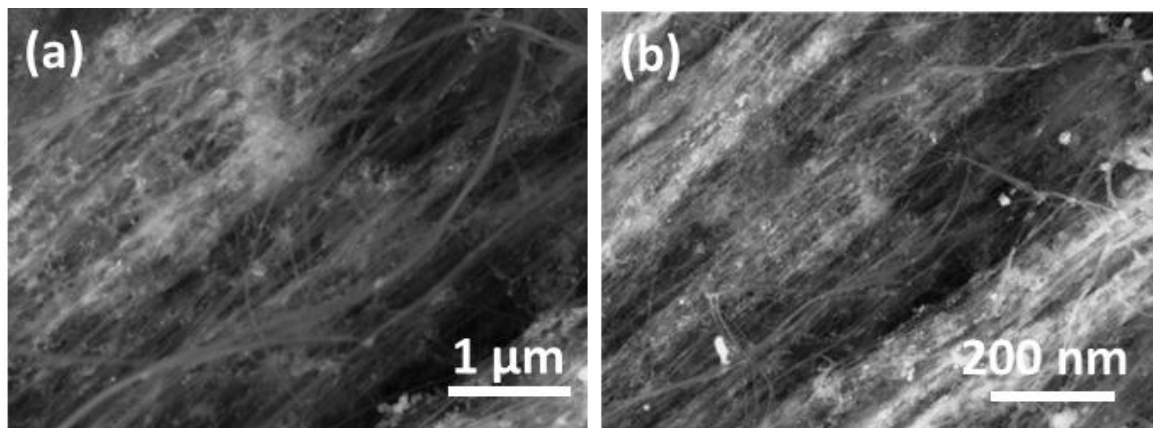
Figure 3.50. SEM images a-b) Co₄POM@CNTF with different resolution
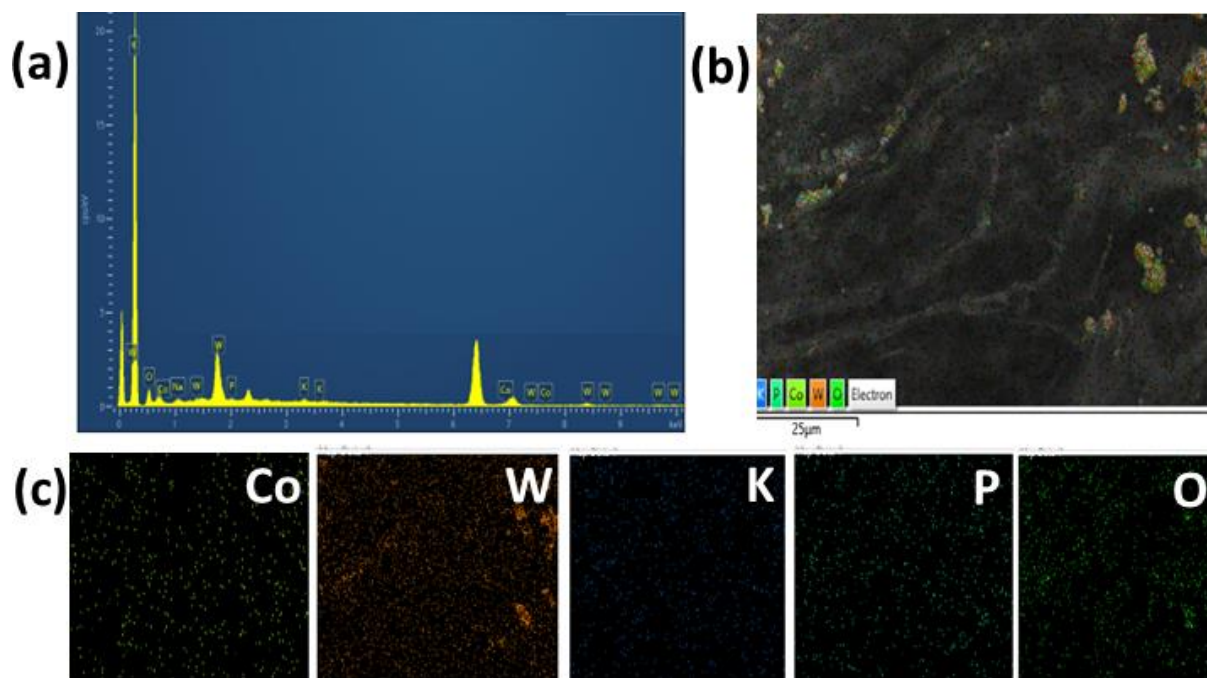
Figure 3.51. EDX spectrum a) Co₄POM@CNTF, b) EDX layered image of Co₄POM@CNTF, c) elemental mapping of Co₄POM@CNTF

3.1.6.2. Electrochemical Studies

Co₄POM@CNTF was used as a working electrode to examine its OER activity. By comparing the LSV curves of bare CNTF with the POM-modified electrode (Figure 3.52a), OER activity was

significantly increased by the immobilization of Co_4POM over CNTF. $Co_4POM@CNTF$ demonstrated a remarkable increase in current density and significantly lower overpotential of 323 $mV@10 mA/cm^2$ compared to the bare CNTF, which needed overpotential of 737 mV for the same anodic current density.

Tafel plots of synthesized catalyst and bare CNTF were built, as shown in Figure 3.52b. The improved reaction kinetics of the modified electrode were demonstrated by $Co_4POM@CNTF$, which displayed a Tafel slope value of 69 mV/dec in comparison to the bare CNTF's 288 mV/dec. The faster rate of the multiple electron transfer process presented in $Co_4POM@CNTF$ complimented the modified electrode's higher activity and current-carrying ability.

Figure 3.52c, d depicts the CV cycles at different scan rates, i.e., from 50 to 250 mV/s in the non-Faradic region and C_{dl} plots to assess the ECSA of bare and Co_4POM-modified electrodes. When the C_{dl} values of $Co_4POM@CNTF$ and bare CNTF were compared, $Co_4POM@CNTF$ had a higher C_{dl} value of 0.9 mF because it had a larger surface area and more active sites, which translated into higher efficiency. ECSA and RF were also calculated which supports the highest OER performance of $Co_4POM@CNTF$ (see Table 3.24).

Table 3.24. Electrochemical parameters of Co_4POM

Electrocatalysts	η at 10 mA/cm^2 (mV)	Tafel slope mV/dec	C_{dl} (mF)	ECSA (cm^2)	RF
Bare CNTF	737	288	0.018	0.45	8
$Co_4POM@CNTF$	323	69	0.9	22.5	402

Moreover, electron transport kinetics in bare and Co_4POM-modified CNTF electrodes were examined using EIS. The Nyquist plot obtained with EIS presents the criterion for the efficient electrocatalyst having small charge transfer resistance in terms of the smaller diameter of the semicircle in the high-frequency region. In Figure 3.53a, the real and imaginary component's Nyquist plot reveals that, for $Co_4POM@CNTF$, the semicircle had a smaller diameter than that of the bare CNTF owing to the smaller R_{ct} from the electrode. This shows that, during OER, electron transport in the modified electrode is faster than that in the bare CNTF.

Chronoamperometry was used to investigate the resilience and stability of $Co_4POM@CNTF$ under continuous oxygen generation for 24 hours at 1.55 V vs. RHE. Figure 3.53b showed that

throughout the test, Co₄POM@CNTF was stable at the current density of 10 mA/cm^2. Based on the chronoamperometric stability test, Co₄POM-modified electrode is a potential candidate electrocatalyst for OER that is stable for several hours.
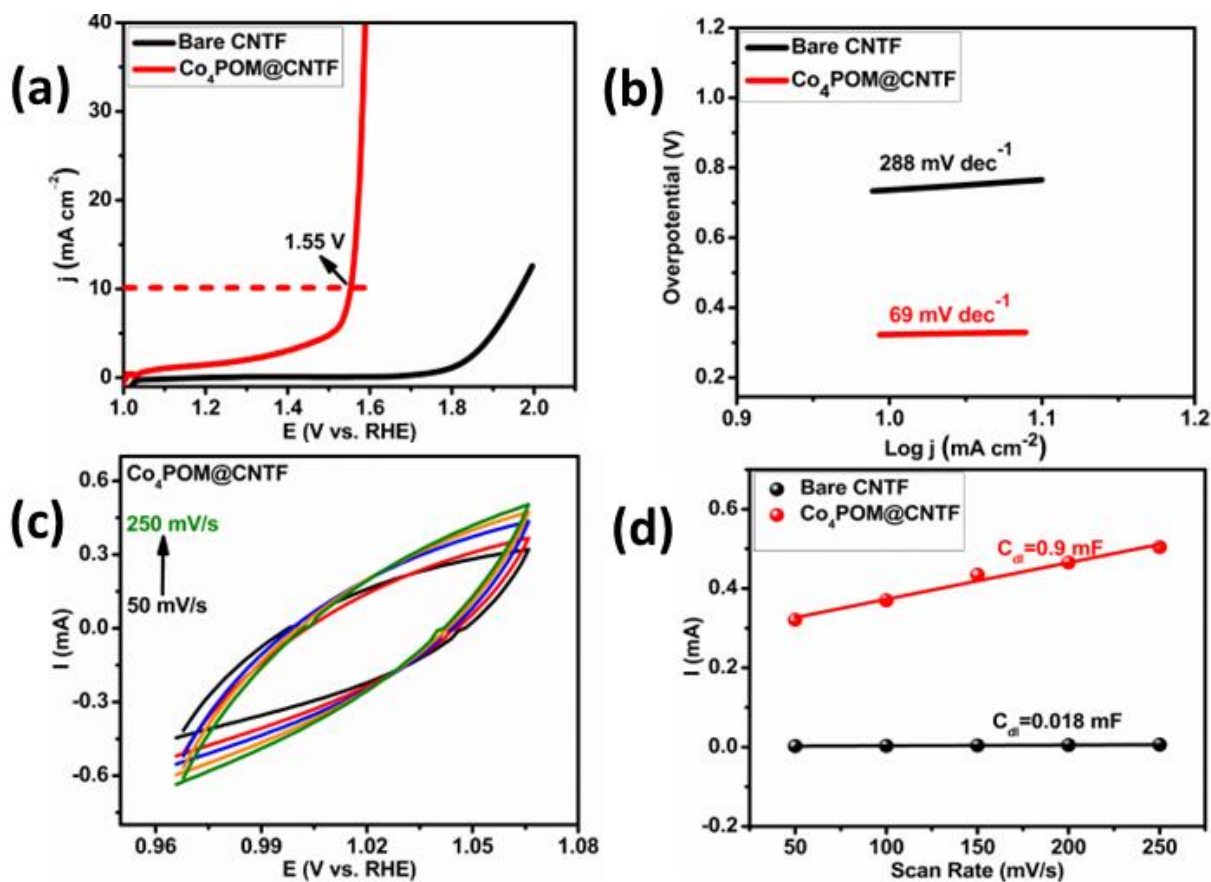
Figure 3.52. OER parameters (a, b) LSV polarization curves and Tafel plots for CNTF and Co₄POM@CNTF (c) cyclic voltammograms for Co₄POM@CNTF (d) C_{dl} plot
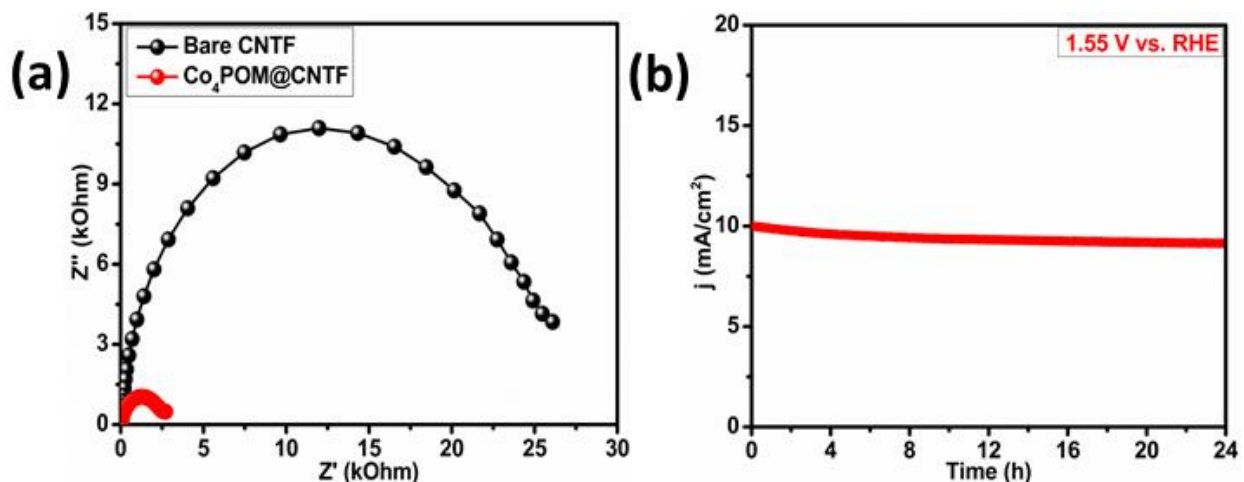
Figure 3.53. (a) Nyquist plots and (b) chronoamperometry for Co$_4$POM

The high activity of the modified electrode can be attributed to the self-activation of Co$_4$POM through restructuring in basic media that generated cobalt oxide and hydroxide as catalytic sites for OER. This self-activation, because of the restructuring of POM, was discussed in detail by the group Streb [258-259].

3.1.7. Fe$_4$POM Based Mixed Metal Oxides

Characterization and electrochemical studies for Fe$_4$POM is given below.

3.1.7.1. Characterization of Materials

Fe$_4$POM based electrodes were characterized through FT-IR, PXRD, SEM, EDX and elemental mapping as discussed below.

FT-IR Analysis

To confirm the synthesis of Fe$_4$POM, FT-IR analysis was performed. Figure 3.54 depicts the FT-IR spectrum of Fe$_4$POM which displays many distinct vibration peaks. These vibrations at 956, 880 and 783 cm^{-1} are assigned to the corner-sharing ν_{as}(W−O$_b$), edge-sharing ν_{as}(W−O$_c$) and ν_{as}(W-O-W) vibrations, respectively. Furthermore, the P-O symmetric stretching vibration of Ni$_4$POM can be attributed to a distinctive peak located around 1059 cm^{-1}. The Fe-O stretching vibration peak is present at 640 cm^{-1}. All these peaks clearly confirm the synthesis of Fe$_4$POM.
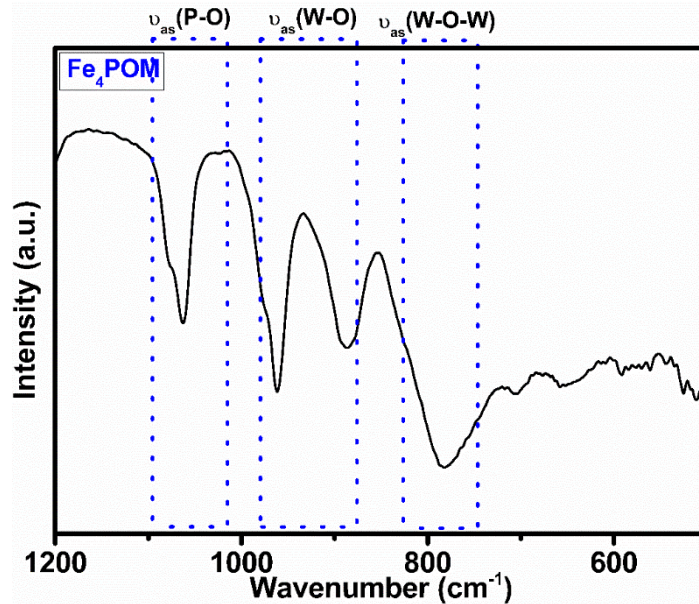
Figure 3.54. FT-IR spectrum of Fe$_4$POM

Powder XRD Analysis

The fabricated electrode (Fe$_4$POM@CNTF) was characterized through PXRD technique. Figure 3.55 shows that CNTF had an amorphous pattern, whereas that of Fe$_4$POM@CNTF had prominent peaks at 10° and 25° 2θ values, which confirmed the deposition of Fe$_4$POM on the surface of CNTF. Crystallite size was calculated to be 35.3 nm. Dislocation density and micro strain were also calculated. Table 3.25 depicts all the parameters i.e., crystallite size, dislocation density and micro strain.
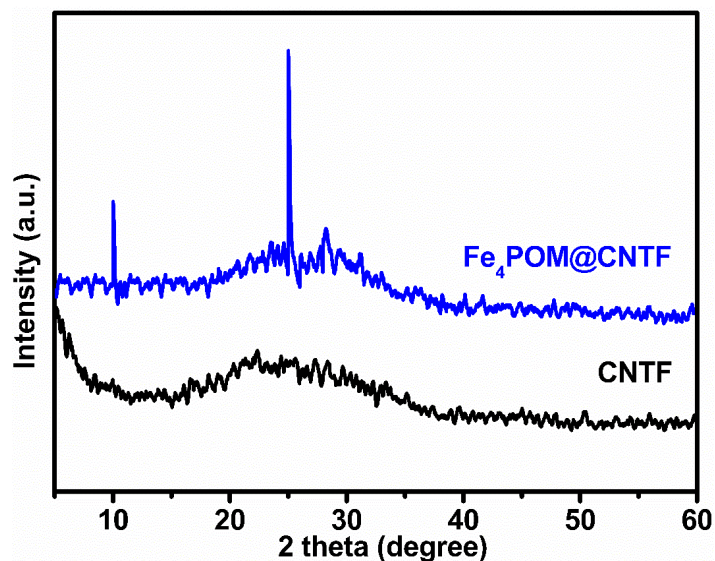
Figure 3.55. PXRD pattern of Fe₄POM and bare CNTF

Table 3.25. Crystallite size, dislocation density and micro strain of Fe₄POM@CNTF

Compound Name	2θ (degree)	FWHM (degree)	FWHM (radians)	D_{avg} (nm)	$\delta_D \times 10^{15}$ (m^{-2})	$\varepsilon_m \times 10^{-3}$
Fe₄POM@CNTF	10.03	0.2103	0.0036	40.4	0.61	0.8
	25.01	0.2816	0.0049	30.2	1.09	1.1

D_{avg} Fe₄POM@CNTF = 40.4 + 30.2 /2 = 35.3 nm

SEM and EDX Analysis

The morphological features of Fe₄POM@CNTF were investigated through SEM analysis. Figure 3.56a, b depicts the SEM images of Fe₄POM@CNTF show that Fe₄POM was uniformly distributed on the surface of CNTF.

Furthermore, Fe₄POM@CNTF was characterized through EDX spectroscopy to identify its elemental composition. Figure 3.57a shows that iron, tungsten, oxygen, potassium, sodium, and carbon were all present in the modified electrode that stemmed from Fe₄POM. Figure 3.57b illustrates the EDX-layered image depicting that all the components of Fe₄POM were uniformly spread throughout the surface of CNTF. Furthermore, elemental mapping supported the presence of the corresponding elements in the fabricated electrode (Figure 3.57c).
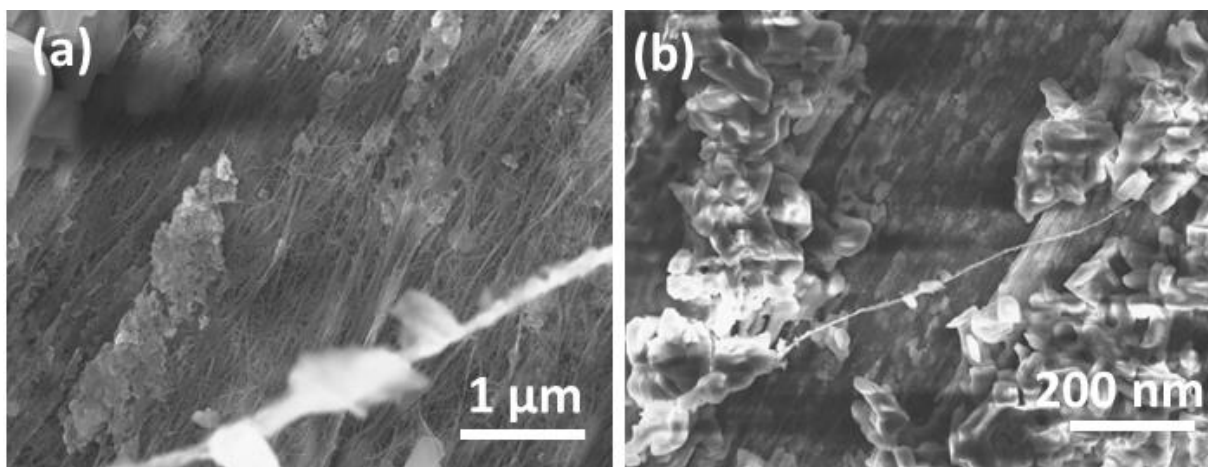
Figure 3.56. SEM images a-b) Co$_4$POM@CNTF with different resolution
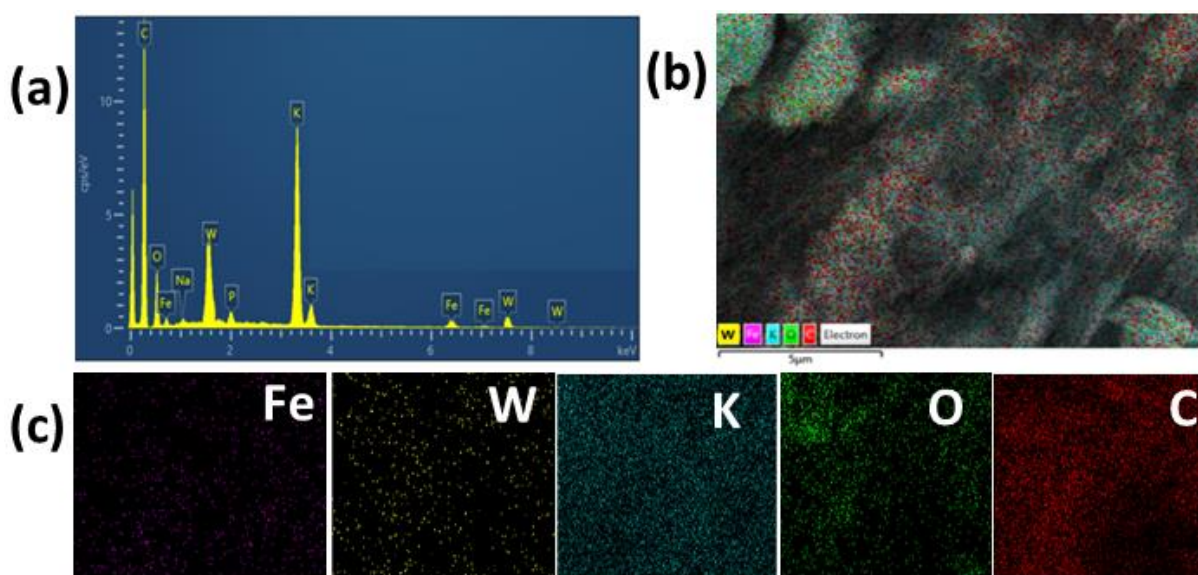
Figure 3.57. EDX spectrum a) Fe$_4$POM@CNTF, b) EDX layered image of Fe$_4$POM@CNTF, c) elemental mapping of Fe$_4$POM@CNTF

3.1.7.2. Electrochemical Studies

To investigate Fe$_4$POM@CNTF's OER activity, a working electrode was utilized. Fe$_4$POM immobilization over CNTF resulted in a considerable increase in OER activity, as shown by comparing the LSV curves of the POM-modified electrode with those of bare CNTF (Figure 3.58a). Comparing Fe$_4$POM@CNTF to bare CNTF, which needed an overpotential of 737 mV for the same anodic current density, showed a notable improvement in current density and a substantially reduced overpotential of 510 mV for anodic current density of 10 mA/cm^2.

Tafel plots of as-prepared catalyst and bare CNTF were built, as shown in Figure 3.58b. The modified electrode, Fe$_4$POM@CNTF, demonstrated improved reaction kinetics with a Tafel slope value of 89 mV/dec, in contrast to the bare CNTF's 288 mV/dec. Fe$_4$POM@CNTF demonstrated a faster rate of multiple electron transfer, which complemented the modified electrode's increased activity and capacity to transport current.

Figure 3.58c, d depicts the CV cycles at different scan rates, i.e., from 50 to 250 mV/s in the non-Faradic region and C$_{dl}$ plots to assess the ECSA of bare and Fe$_4$POM-modified electrodes. Fe$_4$POM@CNTF had a higher C$_{dl}$ value of 0.32 mF when compared to the bare CNTF because it had a larger surface area and more active sites, which translated into higher efficiency. ECSA and RF were also calculated which supports the highest OER performance of Co$_4$POM@CNTF (see Table 3.26).

Table 3.26. Electrochemical parameters of Fe$_4$POM

Electrocatalysts	η at 10 mA/cm^2 (mV)	Tafel slope mV/dec	C$_{dl}$ (mF)	ECSA (cm^2)	RF
Bare CNTF	737	288	0.018	0.45	8
Fe$_4$POM@CNTF	510	89	0.32	8	142
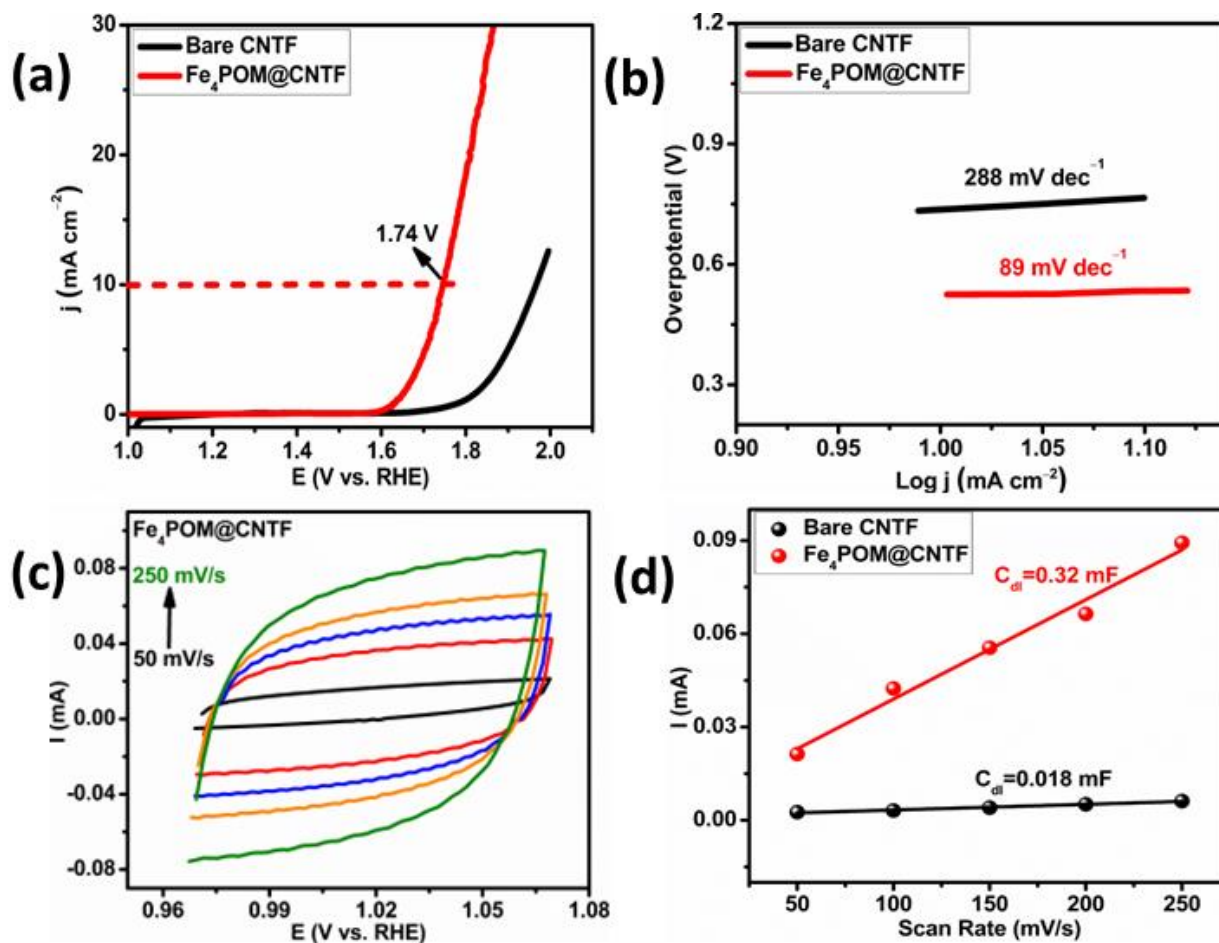
Figure 3.58. OER parameters (a, b) LSV polarization curves and Tafel plots for CNTF and Fe$_4$POM@CNTF (c) cyclic voltammograms for Fe$_4$POM@CNTF (d) C$_{dl}$ plot

Furthermore, EIS was performed to investigate the electron transport kinetics in bare and Fe$_4$POM modified CNTF electrodes. The Nyquist plot obtained with EIS presents the criterion for the efficient electrocatalyst having small charge transfer resistance in terms of the smaller diameter of the semicircle in the high-frequency region. In Figure 3.59a, the Nyquist plot reveals that, for Fe$_4$POM@CNTF, the semicircle had a smaller diameter than that of the bare CNTF owing to the smaller R$_{ct}$ from the electrode. This shows that, during OER, electron transport in the modified electrode is faster than that in the bare CNTF.

Chronoamperometry was used to investigate the robustness and stability of Fe$_4$POM@CNTF under continuous oxygen generation for 24 hours at 1.74 V vs. RHE. Figure 3.59b showed that throughout the test, Fe$_4$POM@CNTF was not very stable at 10 mA/cm^2.
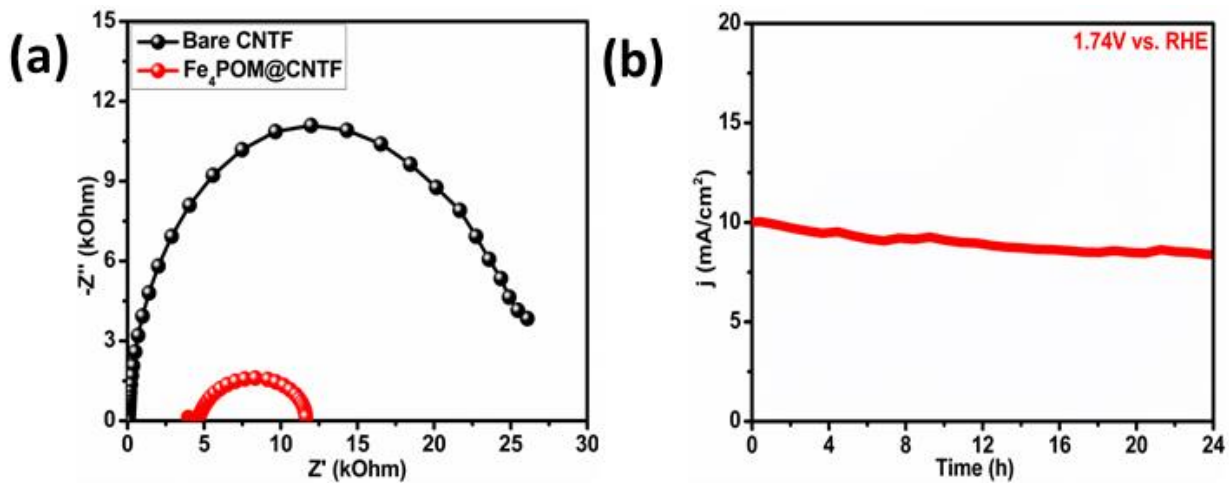
Figure 3.59. (a) Nyquist plots and (b) Chronoamperometry for Fe$_4$POM

Table 3.27. Comparative OER performance of the electrocatalysts in alkaline media with literature.

Electrocatalyst	OER		References
	η (mV)	Tafel slope (mV/dec)	
NiCo-POM/Ni	360@10 mA/cm^2	126	[88]
Co$_2$P@Co$_2$P/Co-POM	336@50 mA/cm^2	-	[260]
ZIF-8@ZIF-67@POM	490@10 mA/cm^2	88	[261]
Yolk shell/ZIF-8/POM	287@10 mA/cm^2	58	[89]
Co$_4$POM@TiO$_2$@PEI	490@10 mA/cm^2	60	[258]
PBA-POM	440@10 mA/cm^2	73	[262]
MOF-74 derived NC @POM	400@10 mA/cm^2	-	[263]
POM@ZnCoS NW	200@20 mA/cm^2	-	[90]
Ni$_4$POM@CNTF	**260@10 mA/cm^2**	**42**	**This work**
Co$_4$POM@CNTF	**320@50 mA/cm^2**	**69**	**This work**
Fe$_4$POM@CNTF	**510@50 mA/cm^2**	**89**	**This work**

In a nutshell, Ni₄POM-CNTF, Co₄POM-CNTF and Fe₄POM-CNTF was characterized through FT-IR, XRD, SEM, EDX, elemental mapping techniques. Furthermore, these catalysts were tested for OER in 1M KOH. It is clearly indicated that Ni₄POM-CNTF (260 mV@10 mA/cm² with Tafel slope of 42 mV/dec) performed better as compared to Co₄POM-CNTF (320 mV@10 mA/cm² with Tafel slope of 69 mV/dec) and Fe₄POM-CNTF (510 mV@10 mA/cm² with Tafel slope of 89 mV/dec).

3.2. Bifunctional Catalysts for Biodiesel Production

3.2.1. Characterization of Materials

Catalysts for biodiesel production were characterized through PXRD, SEM, EDX and BET/BJH analysis as discussed below.

Powder XRD Analysis

PXRD was performed for the composites to determine the phase purity and crystallinity. Figure 3.60a depicts the PXRD pattern of MgO@WO₃@MCM-41 which shows that MCM-41 had amorphous nature. All the peaks of WO₃@MCM-41 present in composite material. In the composite material, there are three diffraction peaks for MgO nanoparticles with crystal planes (111), (200), (220) and (311) at 2θ 36.4°, 42.6°, 62.9° and 75.8° respectively, which are according to the literature (JCPDS 89-7746) [264]. There is no impurity peak present in composite material which confirms the purity. According to Debye Scherrer equation, the particle size of MgO@WO₃@MCM-41 is calculated to be 39 nm. Figure 3.60b represents the PXRD pattern of CaO@WO₃@MCM-41 which shows that all the peaks of WO₃@MCM-41 present in composite material. In the composite material, there are four diffraction peaks for CaO nanoparticles with crystal planes (111), (200), (311) and (222) at 2θ 32°, 37.8°, 64.5° and 67.7° respectively, which are according to the literature (JCPDS 82-1691) [265]. The crystallite size of CaO@WO₃@MCM-41 was calculated to be 35.4 nm. Figure 3.60c represents the PXRD pattern of SrO@WO₃@MCM-41 which shows that all the peaks of WO₃@MCM-41 present in composite material. In the composite material, there are three diffraction peaks for SrO nanoparticles with crystal planes (110), (200) and (311) at 2θ 30.3°, 35.5° and 60.1° respectively, which are according to the literature (JCPDS 74-1227) [266]. The crystallite size of SrO@WO₃@MCM-41 was calculated to be 37.1 nm. Figure 3.60d represents the PXRD pattern of BaO@WO₃@MCM-41 which shows

that all the peaks of WO₃@MCM-41 present in composite material. In the composite material, there are three diffraction peaks for BaO nanoparticles with crystal planes (211), (212), (111), (200) and (112) at 2θ 24.5°, 34.8°, 40.5°, 42.9° and 45.6° respectively, which are according to the literature (JCPDS 26-0178) [267]. The crystallite size of BaO@WO₃@MCM-41 was calculated to be 37.2 nm. Dislocation density, micro strain is also calculated which are mentioned in table 3.28.
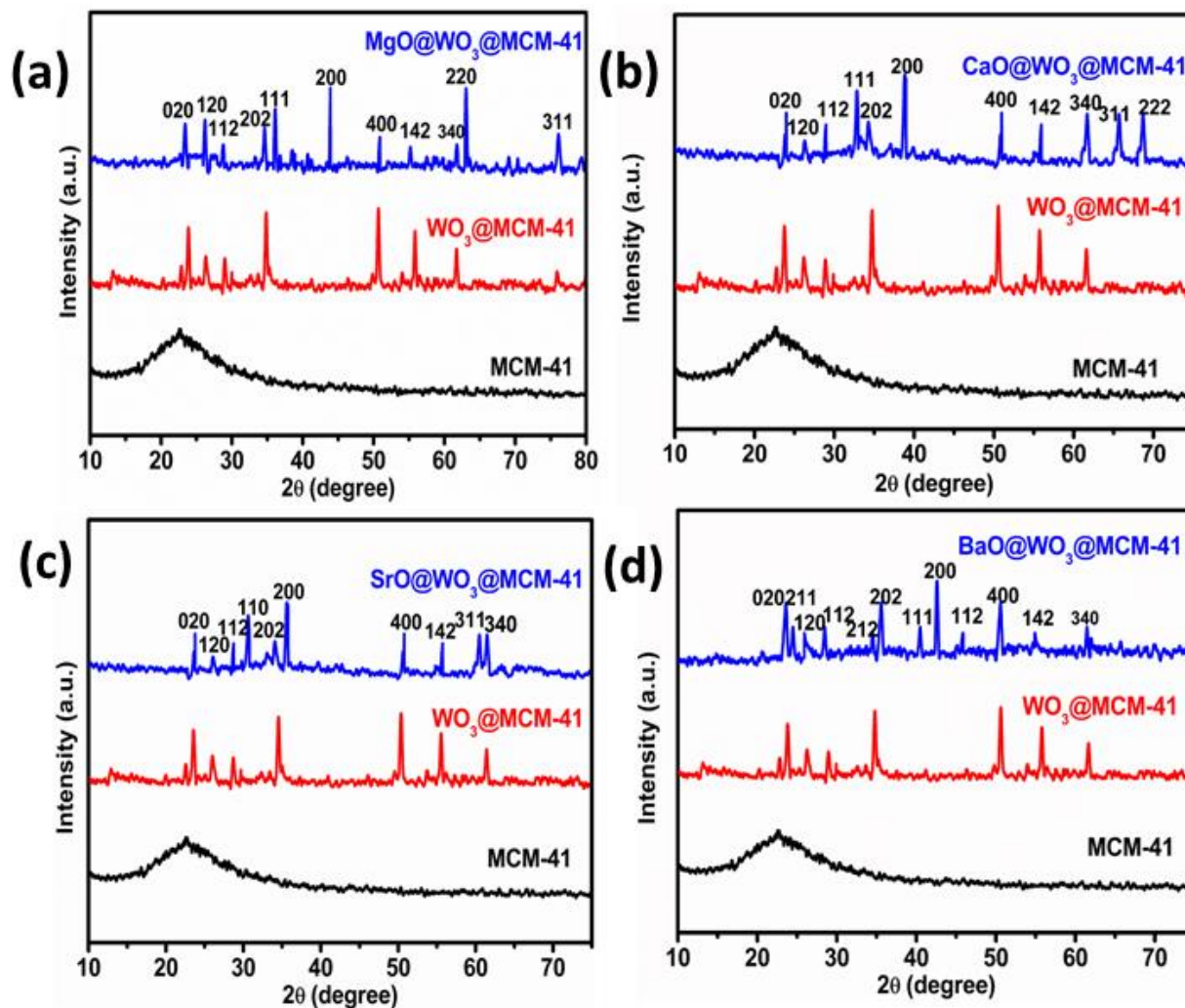
Figure 3.60. PXRD pattern a) MgO@WO₃@MCM-41, b) CaO@WO₃@MCM-41, c) SrO@WO₃@MCM-41, and d) MgO@WO₃@MCM-41

Table 3.28. All the parameters i.e., crystallite size, dislocation density and micro strain

Compound Name	hkl	2θ (degree)	FWHM (degree)	FWHM (radians)	D_{avg} (nm)	δ_D x 10^{15} (m^{-2})	ε_m x 10^{-3}
MgWM	111	36.4	0.2312	0.0040	38.1	0.68	0.9
	200	42.6	0.2732	0.0047	33.1	0.91	1.0
	220	62.9	0.2114	0.0037	45.9	0.47	0.7
CaWM	020	24.0	0.2031	0.0035	42.3	0.55	0.8
	111	32.0	0.2611	0.0045	33.5	0.89	1.0
	200	37.8	0.2873	0.0050	30.6	1.06	1.1
SrWM	020	24.0	0.1932	0.0033	44.9	0.49	0.8
	110	30.3	0.2472	0.0043	34.8	0.82	1.0
	200	35.5	0.2781	0.0048	31.6	1.00	1.1
BaWM	202	35.8	0.2132	0.0037	41.1	0.59	0.8
	200	42.9	0.2951	0.0051	30.5	1.07	1.1
	400	50.6	0.2345	0.0040	40.0	0.62	0.9

D_{avg} MgO@WO$_3$@MCM-41 = 38.1 + 33.1 + 45.9 /3 = 39.0 nm

D_{avg} CaO@WO$_3$@MCM-41 = 42.3 + 33.5 + 30.6 /3 = 35.4 nm

D_{avg} SrO@WO$_3$@MCM-41 = 44.9 + 34.8 + 31.6 /3 = 37.1 nm

D_{avg} BaO@WO$_3$@MCM-41   = 41.1 + 30.5 + 40.0 /3 = 37.2 nm

SEM and EDX Analysis

To determine morphological features, SEM analysis was carried out for all the samples (i.e., MgWM, CaWM, SrWM and BaWM) at different magnifications as seen in figure 3.61 (a-h). were determined using SEM. The SEM image of MgWM (figure 3.61a, b) shows MgO particles are uniformly distributed on the support WO$_3$@MCM-41 and morphology is spores like. Figure. 3.61c, d shows the morphology of CaWM which depicts the CaO particles as spherical agglomerated morphology. In the (figure 3.61e, f), it is indicated that SrWM has flakes like

structure which are uniformly distributed. Figure 3.61g, h shows the morphology of BaWM which depicts the BaO particles as spherical spongy rod like morphology.

Furthermore, EDX was performed to determine the elemental composition of all the composite materials. Figure 3.62a demonstrates the EDX spectra of MgWM which shows that all the elements like magnesium (Mg), tungsten (W), silicon (Si), oxygen (O) were present with high phase purity. Figure 3.62 b depicts the EDX spectra of CaWM, which shows that all the elements like calcium (Ca), tungsten (W), silicon (Si), oxygen (O) were present. Figure 3.62 c shows the EDX spectra of SrWM which shows that all the elements like strontium (Sr), tungsten (W), silicon (Si), oxygen (O) were present with high phase purity. Figure 3.62 d demonstrates the EDX spectra of BaWM which shows that all the elements like Barium (Ba), tungsten (W), silicon (Si), oxygen (O) were present.
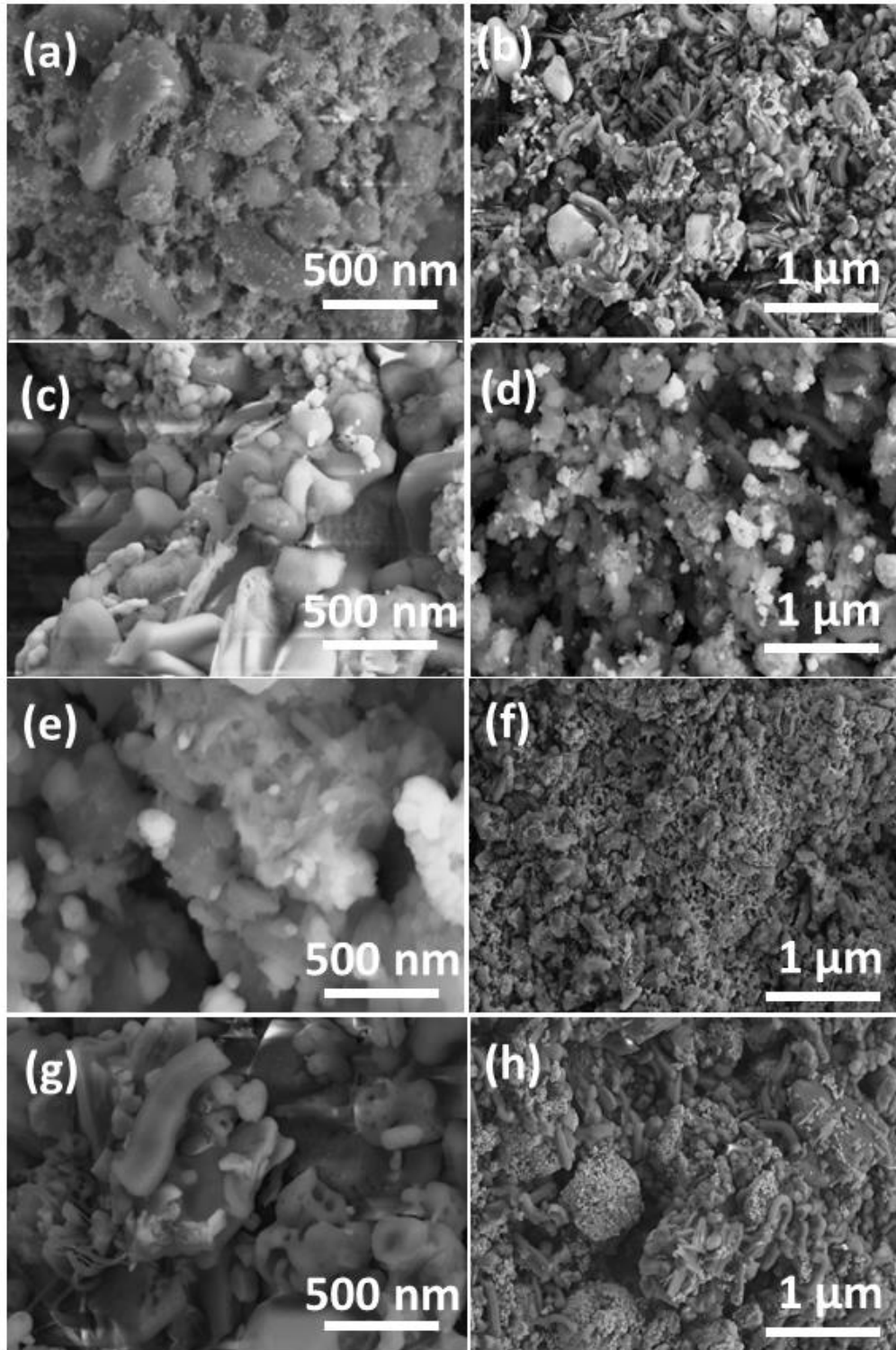
Figure 3.61. SEM images a-b) MgWM composite with different resolution, c-d) CaWM composite with different resolution, e-f) SrWM composite with different resolution, and g,h) BaWM composite with different resolution
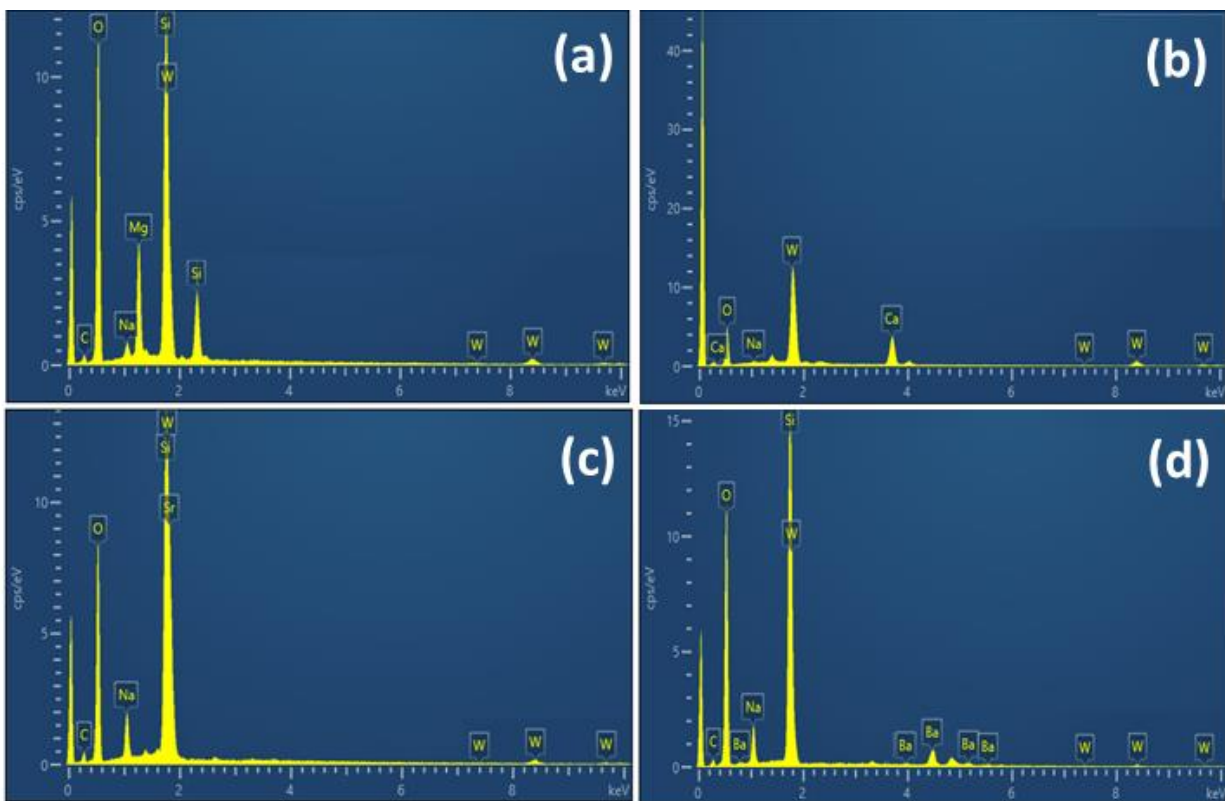
Figure 3.62. EDX spectrum a) MgWM composite, b) CaWM composite, c) SrWM composite, and d) BaWM composite

BET Analysis

To investigate surface area and pore size distribution of synthesized materials, BET analysis was performed. Nitrogen sorption isotherms and pore size distribution were measured from this, and the curves are shown in Figure 3.63. All the synthesized materials' N_2 sorption isotherms are shown in Figure 3.63a. They all show a type-IV isotherm with a hysteresis loop and the feature of capillary condensation with remarkably large surface area, extended pore volume, and large pore size distribution. The inflection points present at the relative pressure (P/P0) in the 0.4–0.6 range, which indicates that mesopores are constantly being stuffed. P/P0 > 0.6 in the isotherm suggests multilayered adsorption on the exterior surface of particles, whereas P/P0 < 0.4 in the isotherm implies single layer adsorption of N_2 on the mesopore walls. [268]. Figure 3.63b represents the BJH pore diameter of the synthesized materials which showed that surface area and pore size of composite material decreased in the same trend. Textural properties of mesoporous materials are given in table 3.29.
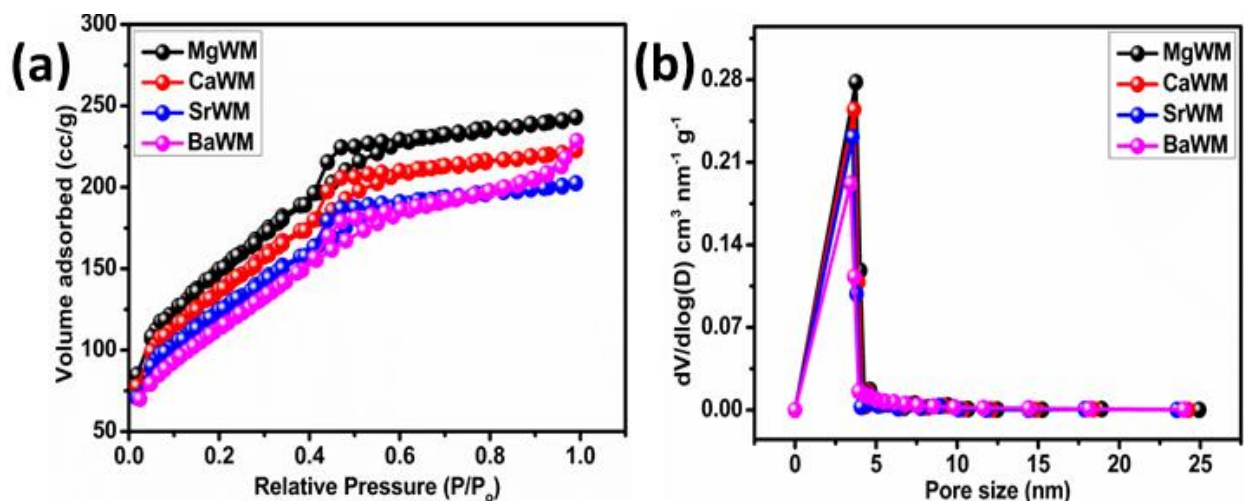
Figure 3.63. BET analysis a) N_2 adsorption-desorption isotherm of MgWM, CaWM, SrWM, and BaWM /b) BJH pore size distribution plots

Table 3.29. textural properties of synthesized mesoporous materials

Compound name	BET surface area (m^2/g)	Pore volume (cc/g)	Pore size (nm)
MgWM	579	0.354	3.74
CaWM	490	0.314	3.65
SrWM	445	0.345	3.54
BaWM	401	0.408	3.42

3.2.2. Esterification/Transesterification Reaction

Esterification/transesterification reaction for corn and waste cooking oil is given below.

3.2.2.1. Biodiesel Production from Corn and Waste Cooking Oil

Some parameters i.e., methanol to oil ratio, effect of time, catalyst dose and effect of temperature were optimized for biodiesel production.

Effect of Methanol to Oil Ratio

The methanol to oil molar ratio was used to calculate the amount of methanol needed for transesterification. A full transesterification requires a stoichiometric methanol to oil ratio of 3/1.

Though, this is not enough to finish the transesterification reaction. To accelerate the reaction's completion, a greater molar ratio is needed. The methanol/oil molar ratio was altered from 3:1 to 15:1 for this experiment. Figures 3.64 and 3.65 demonstrate the biodiesel production parameters for corn oil biodiesel and waste cooking oil biodiesel respectively. In the case of both biodiesels, the molar ratio of methanol to oil was raised, the reaction rate increased. In figure 3.64a, for corn oil biodiesel, the highest yield (96%) for the SrWM catalyst was attained at a 6:1 molar ratio and molar ratio of 9:1 for the BaWM catalyst achieved the maximum yield of 91%. and the yield decreased at higher molar ratios. In Figure 3.65a, the greatest yield of 94% and 87%, respectively, was generated by the SrWM and BaWM catalysts at a 6:1 molar ratio for the biodiesel made from waste cooking oil. However, when the methanol/oil ratio was exceeded to 9:1, an excess of methanol began to impede the separation of glycerin due to an increase in solubilization, which followed a drop in the yield of biodiesel [269]. The optimum methanol to oil molar ratio of 12:1 was achieved to produce the highest output utilizing CaWM and MgWM in case of corn oil biodiesel while for waste cooking oil biodiesel the molar ratios were 9:1.

In terms of catalytic activity, SrWM and BaWM catalysts were superior to MgWM and CaWM. Although surface area of MgWM and CaWM was higher than SrWM and BaWM, but transesterification reaction majorly depends upon the acidic/basic sites. Among SrWM and BaWM, SrWM had excellent catalytic activity due to the low alkalinity and high stability as compared to BaWM [270]. Although basicity of BaO based composite was high and more basic sites are responsible for transesterification, but there are some other factors like leaching involved for the less biodiesel production through BaWM [271].

Effect of Reaction Time

Figure 3.64b illustrates how reaction time affects biodiesel yield produced by corn oil. For corn oil, transesterification tests were performed at a constant stirring rate for intervals between 3 to 12 hours. When utilizing BaWM, SrWM, CaWM, and MgWM, the highest yield for corn oil was reached at 7 (94%), 5 (95%), 10 (42%), and 10 (40%) hours, respectively.

Figure 3.65b depicts the effect of reaction time on waste cooking oil biodiesel production. For this oil, transesterification tests were performed from 3 to 18 hours. The maximum yield for waste cooking oil when using BaWM, SrWM, CaWM, and MgWM was attained after 8 (89%), 6 (95%),

12 (50%) and 12 (38%) hours, respectively. The biodiesel yield from both oils remained almost relatively stable after optimized time, indicating that the transesterification reaction reached equilibrium at that time.

Effect of Catalyst Dose

Figure 3.64c depicts the impact of catalyst concentration on corn oil biodiesel production. In a range of 10 to 40 mg, the catalyst concentration has been changed to study this effect. BaWM, SrWM, CaWM, and MgWM all produced corn oil biodiesel at a maximum yield of 89%, 95%, 40% and 36% respectively at concentration of 10mg for SrWM and 20 mg for all others. It was discovered that the manufacturing yield either decreased marginally or remained unchanged with an increase in catalyst concentration. The mass transfer diffusion resistance is the reason why the reaction rate may slow down at larger concentrations [272].

Similarly, Figure 3.65c shows the impact of catalyst concentration on the production of biodiesel from waste cooking oil. The catalyst concentration has been varied to investigate this impact within a range of 10 to 40 mg. BaWM, SrWM, CaWM, and MgWM all produced corn oil biodiesel at maximum yields of 87%, 94%, 69%, and 45% respectively at concentrations of 20 mg for SrWM and 30 mg for the other systems.

Effect of Temperature

Figure 3.64d represents the effect of temperature on corn oil biodiesel production. The temperature range was 60°C to 120°C. Raising the reaction temperature can speed up the process and boost the amount of biodiesel produced. It is due to the increase in the number of high energy collisions which faster the reaction rate. Figure 3.65d shows that at low temperatures, the reaction rate was slow for all the catalysts. The optimized temperatures for BaWM, SrWM, CaWM and MgWM were 80°C and the maximum yield was 90%, 96%, 42% and 39% respectively. Figure 3.67d shows the temperature effect on waste cooking oil biodiesel production and it shows that optimized temperature for all the catalysts were 100°C and the maximum yield was 86%, 93%, 62% and 44% respectively for BaWM, SrWM, CaWM and MgWM.

All the optimized parameters for all catalysts are given in table 3.30 and 3.31 for corn oil biodiesel and waste cooking oil biodiesel.
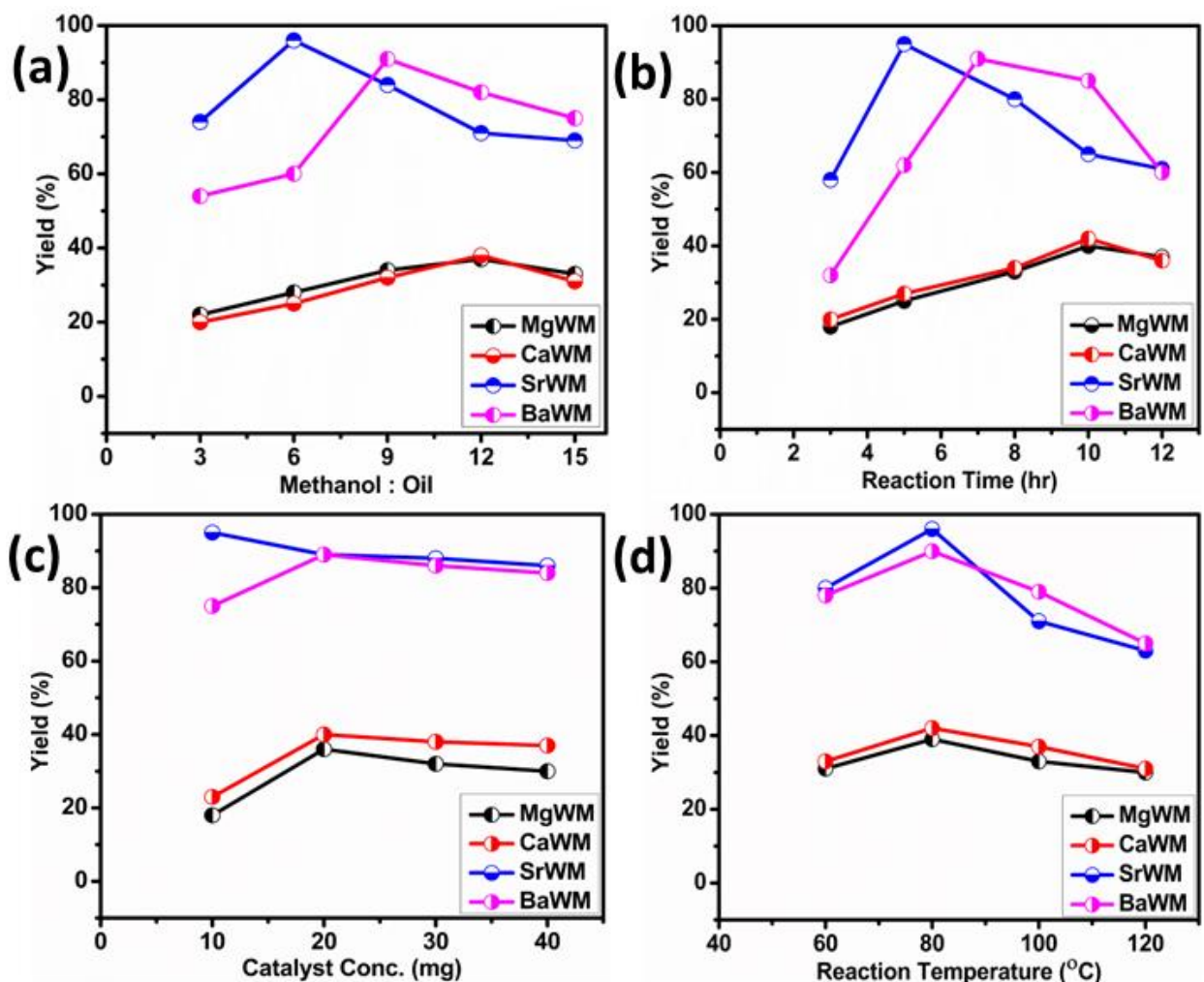
Figure 3.64. Impact of various parameters on transesterification reaction on the conversion of corn oil to biodiesel a) Oil: methanol ratio effects b) Reaction time effects c) Catalyst concentration effects d) Reaction temperature effects
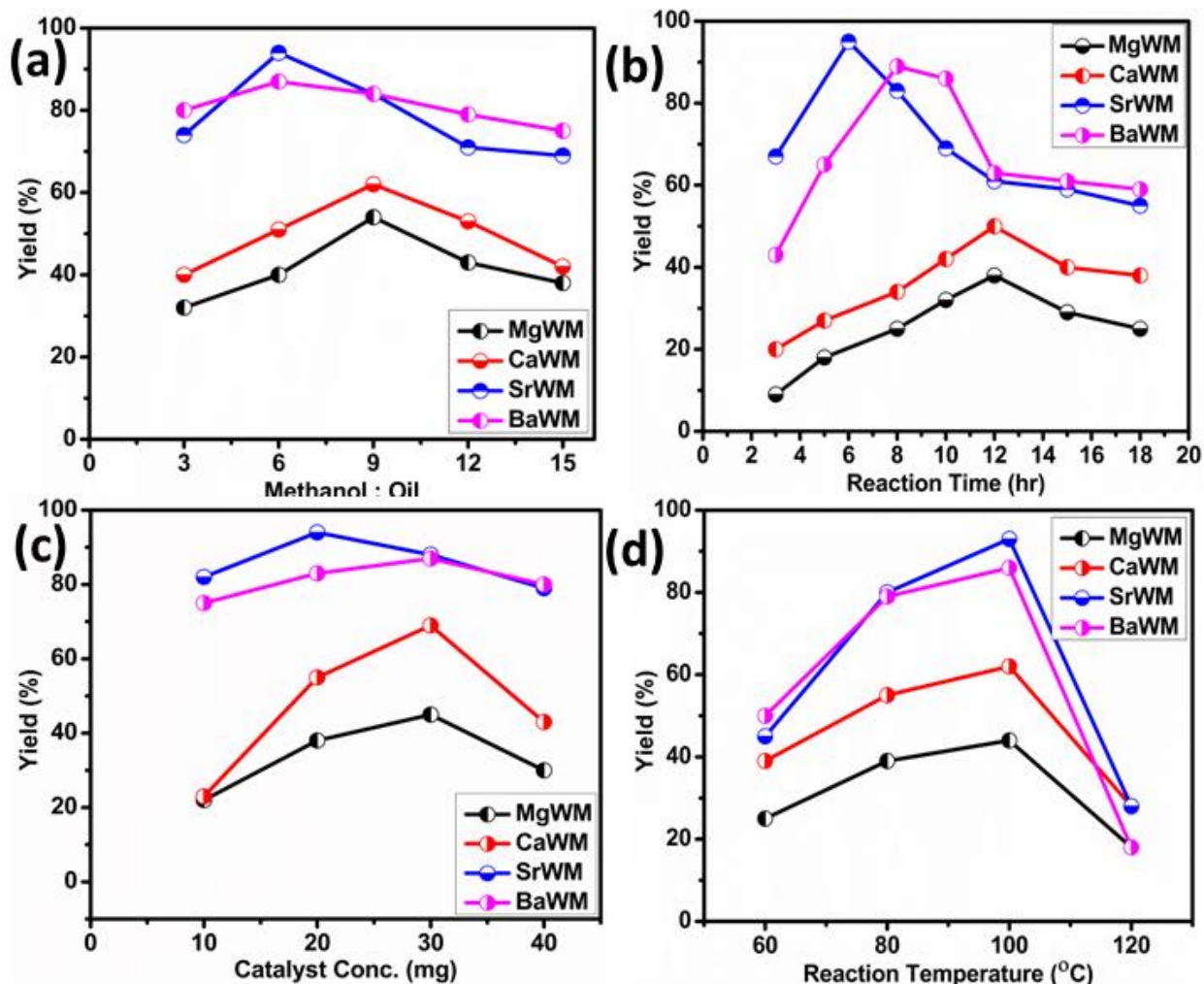
Figure 3.65. Impact of various parameters on transesterification reaction on the conversion of waste cooking oil to biodiesel a) Oil: methanol ratio effects b) Reaction time effects c) Catalyst concentration effects d) Reaction temperature effects

3.2.2.2. Characterization for Biodiesel Production from Corn oil and Waste Cooking Oil

^{1}H NMR was performed to confirm the biodiesel production. Figure 3.66-3.69 depicts the ^{1}H NMR spectra of biodiesel production from corn oil. The biodiesel spectrum of wasted corn through BaWM, SrWM, CaWM and MgWM contains the strong peak for methoxy proton within the range of 3.1 ppm to 3.6 ppm as a singlet. The methylene protons peak appeared within the range of 2.3 to 2.7 ppm as a multiplet. Percentage conversion of biodiesel was calculated by using Eq. 36 from integration values at methoxy protons and methylene protons and observed to be 85%, 92%, 42% and 32% for BaWM, SrWM, CaWM and MgWM respectively. Figures 3.70-3.73 depict the NMR

spectra of biodiesel production from waste cooking oil through BaWM, SrWM, CaWM and MgWM which shows the biodiesel yield of 80%, 91%, 60% and 41% respectively. The biodiesel yield which was calculated practically from the initial amount of oil taken is slightly less than calculated from ^{1}H NMR. This may be improved by leaving extra time for biodiesel mixture to settle down or by using centrifuge procedures. Table 3.30 and 3.31 show ^{1}H NMR biodiesel yield from corn oil and waste cooking oil respectively.

%age conversion = $(2A_{Me} / 3A_{CH2}) * 100$
= $(2(3.54) / 3(2.76)) *100$
= 85

Methoxy peak

Methylene (CH$_2$) peak
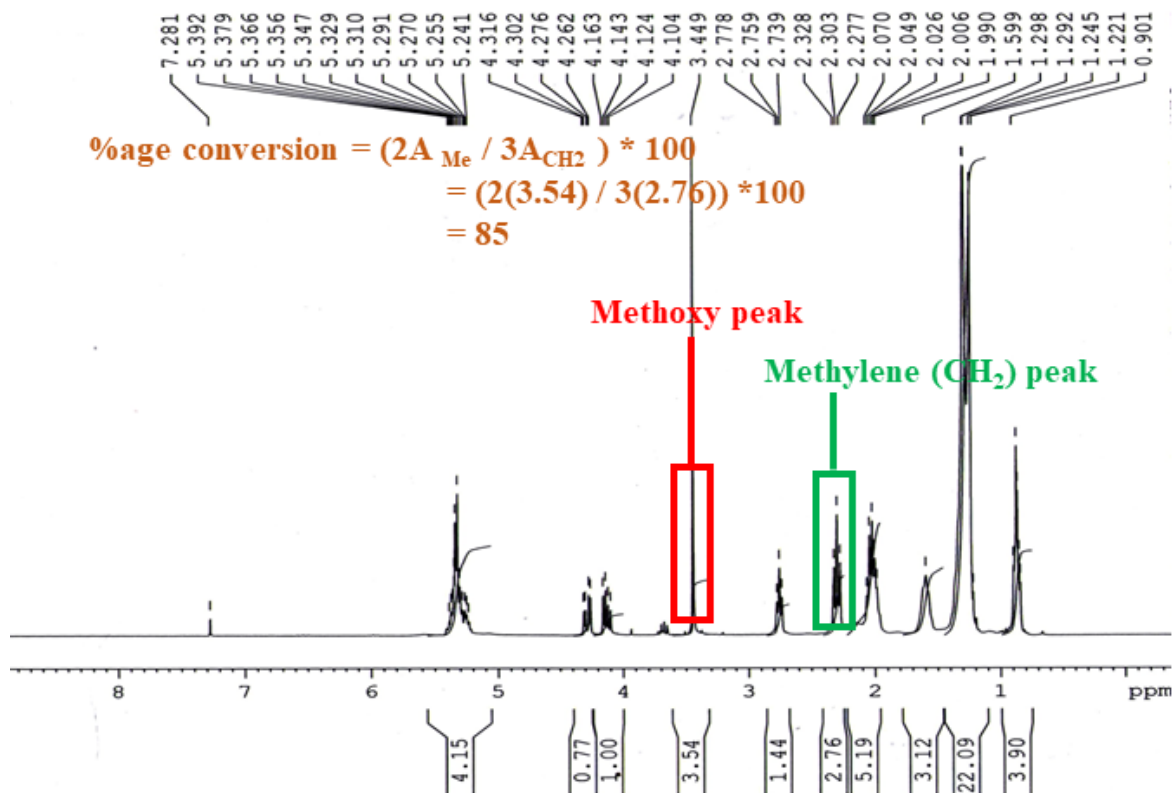
Figure 3.66. ^{1}H NMR spectra of corn oil biodiesel production through BaWM
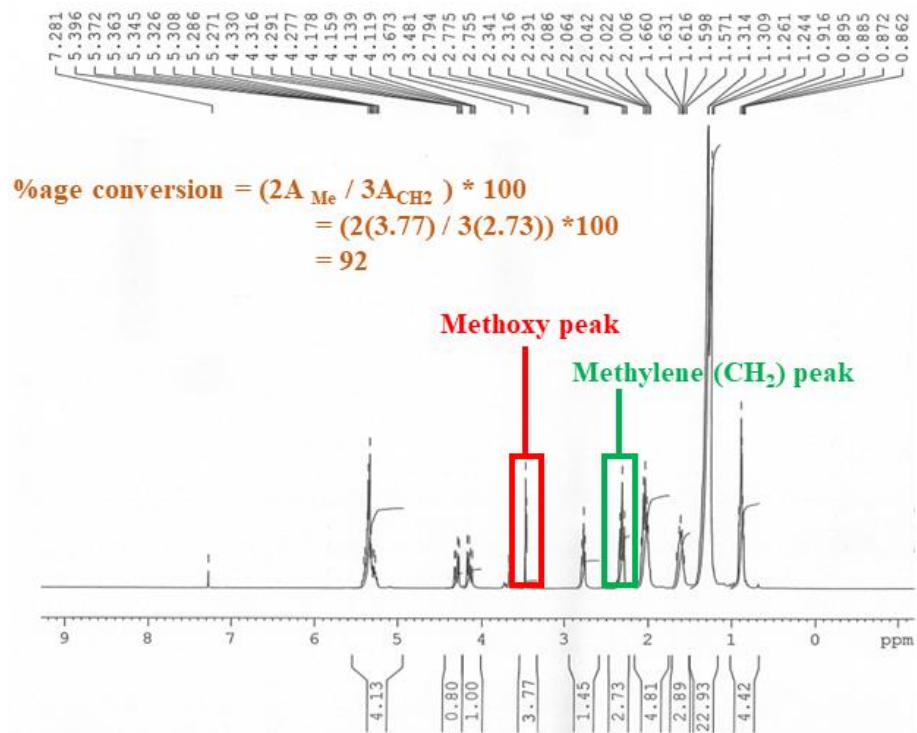
Figure 3.67. ^{1}H NMR spectra of corn oil biodiesel production through SrWM

%age conversion = $(2A_{Me} / 3A_{CH2}) * 100$
= $(2(3.77) / 3(2.73)) * 100$
= 92

Methoxy peak

Methylene (CH$_2$) peak
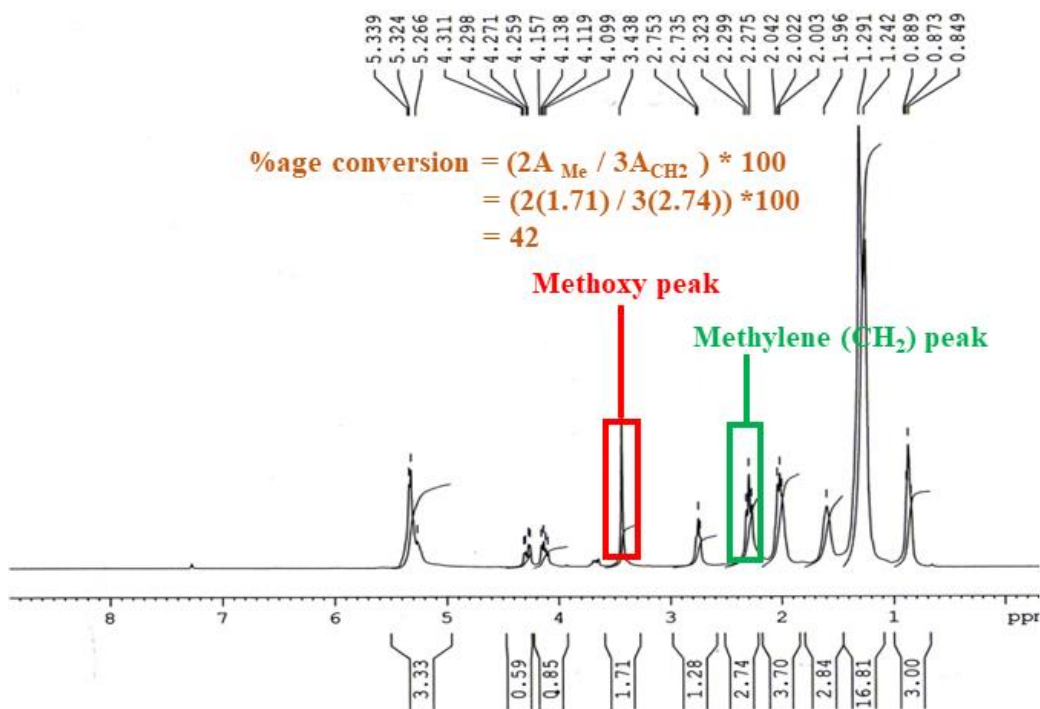
Figure 3.68. ^{1}H NMR spectra of corn oil biodiesel production through CaWM

%age conversion = $(2A_{Me} / 3A_{CH2}) * 100$
= $(2(1.71) / 3(2.74)) * 100$
= 42

Methoxy peak

Methylene (CH$_2$) peak

145

$$\text{%age conversion} = (2A_{Me} / 3A_{CH2}) * 100$$
$$= (2(0.99) / 3(2.02)) *100$$
$$= 32$$

Methoxy peak

Methylene (CH₂) peak
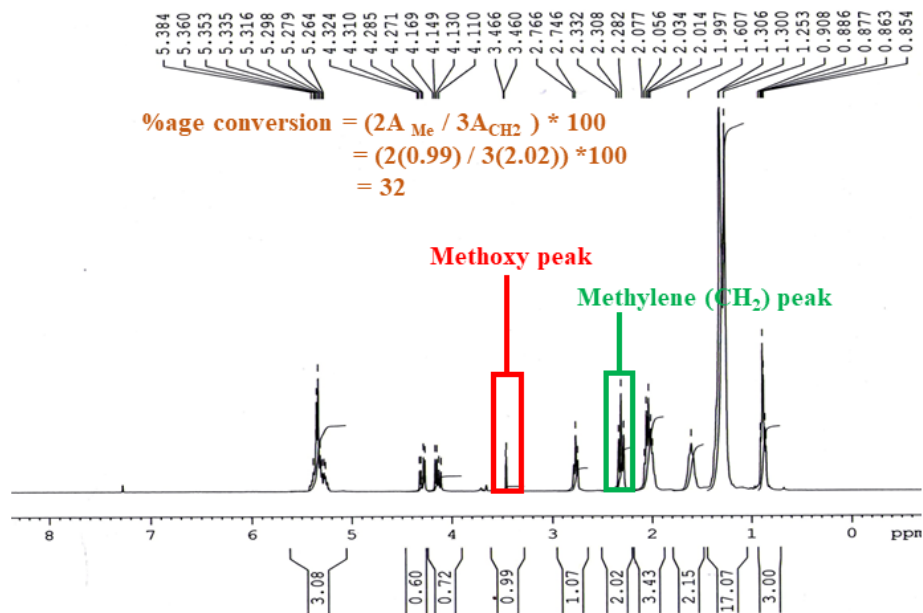
Figure 3.69. ^{1}H NMR spectra of corn oil biodiesel production through MgWM

$$\text{%age conversion} = (2A_{Me} / 3A_{CH2}) * 100$$
$$= (2(3.15) / 3(2.62)) *100$$
$$= 80$$

Methoxy peak

Methylene (CH₂) peak
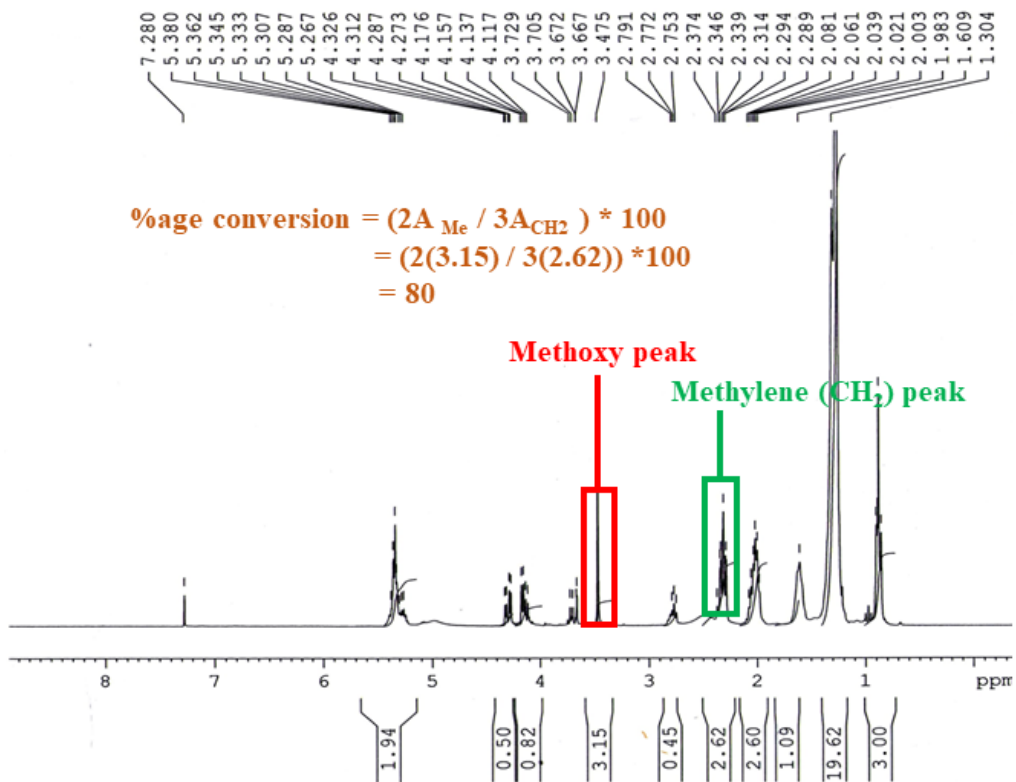
Figure 3.70. ^{1}H NMR spectra of waste cooking oil biodiesel production through BaWM
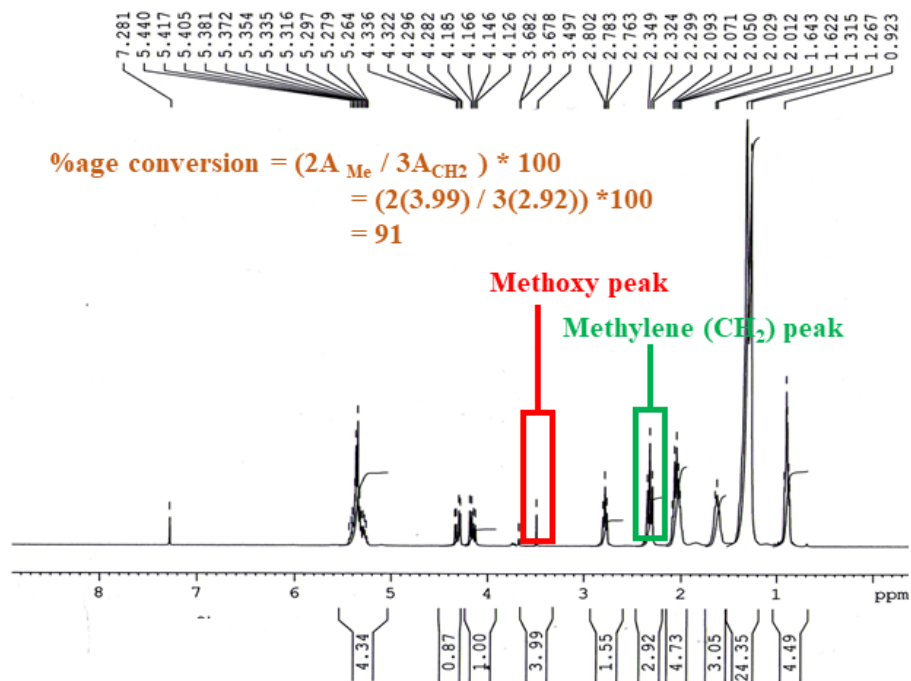
Figure 3.71. ^{1}H NMR spectra of waste cooking oil biodiesel production through SrWM
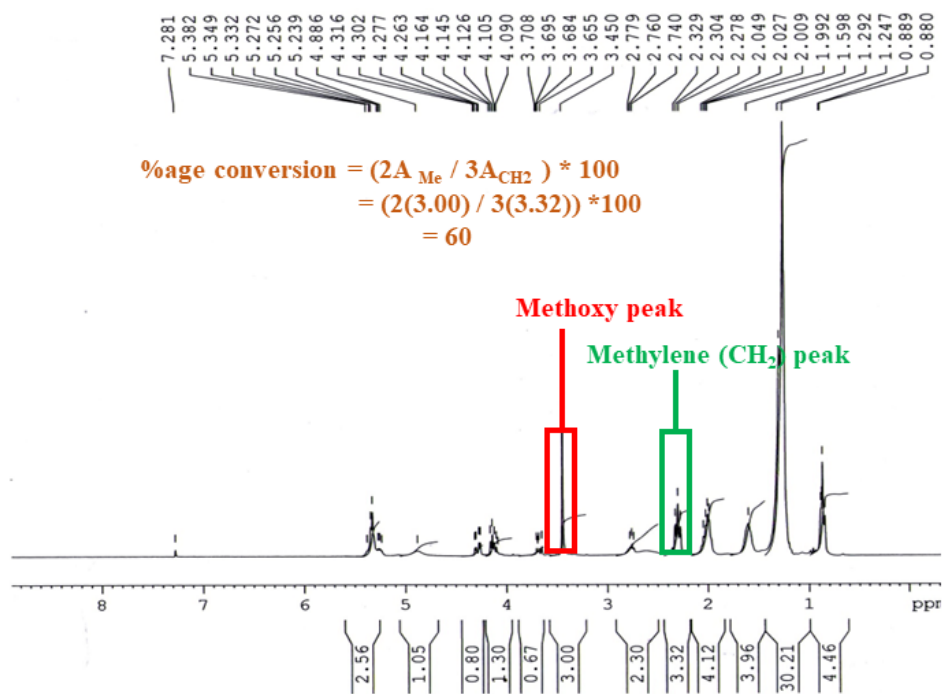
Figure 3.72. ^{1}H NMR spectra of waste cooking oil biodiesel production through CaWM

147
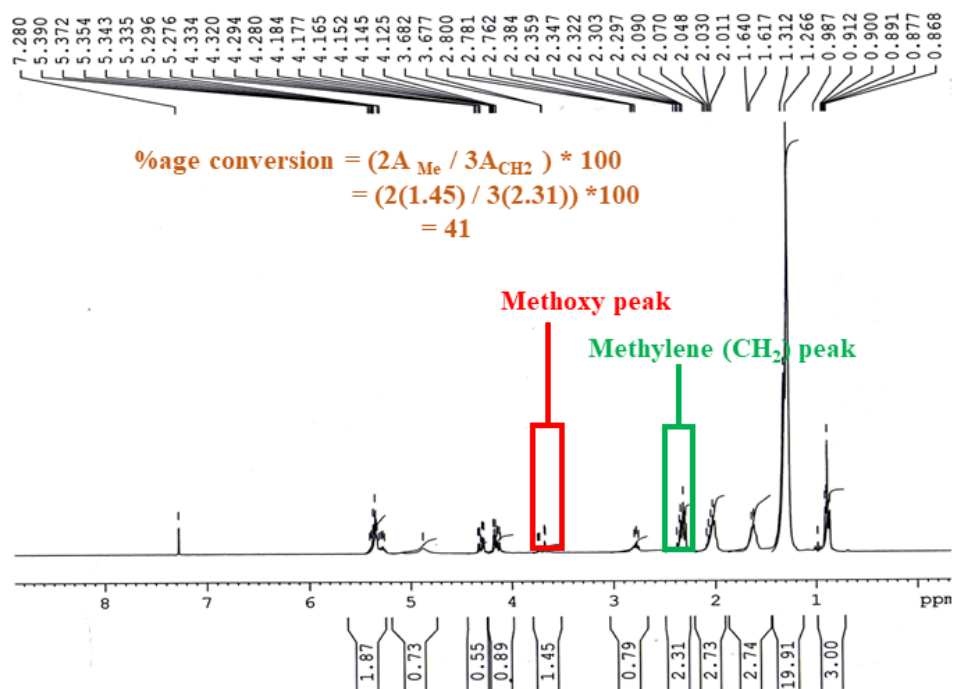
Figure 3.73. ^{1}H NMR spectra of waste cooking oil biodiesel production through MgWM

Table 3.30. Optimized parameters for biodiesel production from corn oil

Composite material	Methanol/oil ratio	Reaction time (h)	Reaction Temperature (°C)	Catalyst Concentration (mg)	Experimental Yield (%)	^{1}H NMR yield (%)
MgWM	12:1	10	80	20	39	32
CaWM	12:1	10	80	20	42	42
SrWM	6:1	5	80	10	96	92
BaWM	9:1	7	80	20	91	85

Table 3.31. Optimized parameters for biodiesel production from waste cooking oil

Composite material	Methanol/oil ratio	Reaction time (h)	Reaction temperature (°C)	Catalyst concentration (mg)	Experimental yield (%)	^{1}H NMR yield (%)
MgWM	9:1	12	100	30	44	41
CaWM	9:1	12	100	30	62	60
SrWM	6:1	6	100	20	93	91
BaWM	6:1	8	100	30	86	80

Table 3.32. Comparative biodiesel production from corn and waste cooking oil through synthesized catalyst

Compound name	Source	Yield (%)	References
TiO_2-MgO	Waste cooking oil	85	[144]
WO_3-ZrO_2@MCM-41	Ankol seed oil	98	[273]
MgO/CeMCM-41	Waste cooking oil	88	[274]
ZnO/MCM-41	Jatropha oil	99	[275]
MgO/clinoptilolite	Corn oil	94	[276]
MgO/clinoptilolite	Palm oil	97	[276]
SrO-ZnO/Al_2O_3	Corn oil	71	[277]
SrO-CaO-Al_2O_3	Palm oil	98	[186]
WO_3/$ZnCo_2O_4$@CeO_2	Levulinic acid	78	[278]
CaO/Zr-MCM41	Waste cooking oil	88	[202]
MgWM	**Corn oil**	**39**	**This work**
CaWM	**Corn oil**	**42**	**This work**
SrWM	**Corn oil**	**96**	**This work**
BaWM	**Corn oil**	**91**	**This work**
MgWM	**Waste cooking oil**	**44**	**This work**
CaWM	**Waste cooking oil**	**62**	**This work**
SrWM	**Waste cooking oil**	**93**	**This work**
BaWM	**Waste cooking oil**	**86**	**This work**

In a nutshell, MgWM, CaWM, SrWM and BaWM was characterized through XRD, SEM, EDX, elemental mapping, BET/BJH techniques. Furthermore, these catalysts were tested for biodiesel production through corn and waste cooking oil. It is clearly indicated that SrWM produce highest biodiesel yield through both feedstocks. From corn oil, MgWM, CaWM, SrWM and BaWM produced biodiesel yield of 39%, 42%, 96% and 91% respectively while from waste cooking oil, MgWM, CaWM, SrWM and BaWM produced biodiesel yield of 44%, 62%, 93% and 86% respectively. Furthermore, biodiesel was characterized through ^{1}H-NMR spectroscopy. From corn

oil, MgWM, CaWM, SrWM and BaWM produced biodiesel yield of 32%, 42%, 92% and 85% respectively while from waste cooking oil, MgWM, CaWM, SrWM and BaWM produced biodiesel yield of 41%, 60%, 91% and 80% respectively.

3.3.   Conclusions

In this research work, bifunctional composites based on post transition-metal oxide (Bi_2O_3) and 3d-transition metal oxides (Ni, Co, Fe, Mn) were synthesized and characterized through multitude analytical techniques including powder XRD analysis, SEM, EDX, XPS and used for electrochemical water splitting applications. For this, composites were supported on nickel foam (NiF) and carbon nanotube fiber (CNTF) as electrode materials for oxygen evolution reaction (OER) in basic medium (1M KOH) while OER/hydrogen evolution reaction (HER) in neutral (1M PBS) medium. The electrochemical OER results revealed that CNTF based electrodes outperformed as compared to NiF based electrodes in both media. One dimensional alignment of arrays of CNTs as fibers have a higher electrocatalytic activity due to their uniform electron transport nano channels. Among CNTF based electrodes, Bi_2O_3/NiO-CNTF based electrodes outperformed in 1M KOH (467 mV@150 mA/cm^2 with Tafel slope 78.1 mV/dec) compared other CNTF based fabricated electrodes. Similarly, for OER and HER in 1M PBS, Bi_2O_3/NiO-CNTF also outperformed (164 mV@20 mA/cm^2 with Tafel slope 94.5 mV/dec and 268 mV@50 mA/cm^2 with Tafel slope 81.3 mV/dec, respectively) than the other fabricated electrodes. Keeping in view the performance of mixed metal oxides, three different transition metal-based polyoxometalates (POMs) were also synthesized and fabricated on the surface of CNTF. The electrochemical water oxidation activity in 1M KOH reveals that Ni based was more efficient POM (260 mV@10 mA/cm^2 with Tafel slope 42 mV/dec) than other synthesized analogues.

For biodiesel production, bifunctional catalysts based on tungsten oxide (WO_3) over mesoporous material MCM-41 impregnated with alkaline earth metal oxides (Mg, Ca, Sr, Ba) were synthesized and characterized through PXRD, SEM/EDX and BET/BJH techniques. These composites were tested for biodiesel production using corn and waste cooking oil as feedstocks. The results revealed that strontium-based composite was an efficient bifunctional (esterification/trans-esterification simultaneously) catalyst for biodiesel production with 96% and 93% yield from corn oil and waste cooking oil, respectively. Strong basic and acidic sites on strontium-based composites supported the highest biodiesel production. The synthesized biodiesel was characterized through ^{1}H-NMR spectroscopy, and it revealed that biodiesel yield was 92% and 91% from corn oil and waste cooking oil, respectively.

References

1. Gür T M, (2018) Review of electrical energy storage technologies, materials and systems: challenges and prospects for large-scale grid storage. *Energy & Environmental Science*, 11(10), 2696-2767.
2. Uddin R, Raza Khan H, Arfeen A, Shirazi MA, Rashid A, Shahbaz Khan U, (2021) Energy storage for energy security and reliability through renewable energy technologies: a new paradigm for energy policies in Turkey and Pakistan. *Sustainability*, 13(5), 2823.
3. Rasheed R, Rizwan A, Javed H, Yasar A, Tabinda A B, Bhatti S G, Su Y, (2020) An analytical study to predict the future of Pakistan's energy sustainability versus rest of South Asia. *Sustainable Energy Technologies and Assessments*, 39, 100707.
4. Ardo S, Rivas D F, Modestino M A, Greiving V S, Abdi F F, Llado E A, Artero V, Ayers K, Battaglia C, Becker J P, Bederak D, (2018) Pathways to electrochemical solar-hydrogen technologies. *Energy & Environmental Science*, 11(10), 2768-2783.
5. Hoekman S K, Broch A, Robbins C, Ceniceros E, Natarajan M, (2012) Review of biodiesel composition, properties, and specifications. *Renewable and Sustainable Energy Reviews*, 16(1), 143-169.
6. Salvi B, N Panwar, (2012) Biodiesel resources and production technologies–A review. *Renewable and Sustainable Energy Reviews,* 16(6), 3680-3689.
7. Holladay J D, Hu J, King D L, Wang Y, (2009) An overview of hydrogen production technologies. *Catalysis Today,* 139(4), 244-260.
8. Ibn Shamsah S M, (2021) Earth-abundant electrocatalysts for water splitting: current and future directions. Catalysts, 11(4), 429.
9. Raveendran A, M Chandran, R Dhanusuraman, (2023) A comprehensive review on the electrochemical parameters and recent material development of electrochemical water splitting electrocatalysts. *RSC Advances*, 13(6), 3843-3876.
10. Goncalves J M, Kumar A, da Silva M I, Toma, H E, Martins P R, Araki K, Bertotti M, Angnes L, (2021), Nanoporous gold-based materials for electrochemical energy storage and conversion. *Energy Technology,* 9(5), 2000927.
11. Joya K S, Y F Joya, H J De Groot, (2014) Ni-Based Electrocatalyst for Water Oxidation Developed In-Situ in a HCO_3^-/CO_2 System at Near-Neutral pH. *Advanced Energy Materials*, 4(9), 1301929.
12. Wei J, Zhou M, Long A, Xue Y, Liao H, Wei C, Xu Z J, (2018) Heterostructured electrocatalysts for hydrogen evolution reaction under alkaline conditions. *Nano-Micro Letters*, 10, 1-15.
13. Bockris J M, Reddy A K N, Gamboa Aldeco M, Peter L M, (2002) Comprehensive Modern Electrochemistry: Modern Electrochemistry, in 3 Volumes: Volume 1 Ionics, 1998, 767 pages, Volume 2A Fundamentals of Electrodics, 2000, 763 pages, Volume 2B Electrodics in Chemistry, Engineering, Biology and Environmental Science, 2000, 514 pages. *Platinum Metals Review,* 46(1), 15-17.
14. Trasatti S, (1972) Work function, electronegativity, and electrochemical behaviour of metals: III. Electrolytic hydrogen evolution in acid solutions. *Journal of Electroanalytical Chemistry and Interfacial Electrochemistry*, 39(1), 163-184.
15. Hinnemann B, Moses P G, Bonde J, Jørgensen K P, Nielsen J H, Horch S, Chorkendorff I, Nørskov J K, (2005) Biomimetic hydrogen evolution: MoS2 nanoparticles as catalyst for hydrogen evolution. *Journal of the American Chemical Society*, 127(15), 5308-5309.

16. Jin H, Guo C, Liu X, Liu J, Vasileff A, Jiao Y, Zheng Y, Qiao S Z, (2018) Emerging two-dimensional nanomaterials for electrocatalysis. *Chemical Reviews*, 118(13), 6337-6408.
17. Suen N T, Hung S F, Quan Q, Zhang N, Xu Y J, Chen H M, (2017) Electrocatalysis for the oxygen evolution reaction: recent development and future perspectives. *Chemical Society Reviews*, 46(2), 337-365.
18. Medford A J, Vojvodic A, Hummelshøj J S, Voss J, Abild Pedersen F, Studt F, Bligaard T, Nilsson A, Nørskov J K, (2015) From the Sabatier principle to a predictive theory of transition-metal heterogeneous catalysis. *Journal of Catalysis*, 328, 36-42.
19. Bosserez T, Geerts L, Rongé J, Ceyssens F, Haussener S, Puers R, Martens J A, (2016) Minimization of ionic transport resistance in porous monoliths for application in integrated solar water splitting devices. *The Journal of Physical Chemistry C*, 120(38), 21242-21247.
20. Brodsky C N, Hadt R G, Hayes D, Reinhart B J, Li N, Chen L X, Nocera D G, (2017) In situ characterization of cofacial Co (IV) centers in Co_4O_4 cubane: Modeling the high-valent active site in oxygen-evolving catalysts. *Proceedings of the National Academy of Sciences*, 114(15), 3855-3860.
21. Burstein G, (2005) A hundred years of Tafel's Equation: 1905-2005. *Corrosion Science*, 47(12), 2858-2870.
22. Vrubel H, Moehl T, Grätzel M, Hu X, (2013) Revealing and accelerating slow electron transport in amorphous molybdenum sulphide particles for hydrogen evolution reaction. *Chemical Communications,* 49(79), 8985-8987.
23. Anantharaj S, Ede S R, Karthick K, Sankar S S, Sangeetha K, Karthik P E, Kundu S, (2018) Precision and correctness in the evaluation of electrocatalytic water splitting: revisiting activity parameters with a critical assessment. *Energy & Environmental Science*, 11(4), 744-771.
24. Chen J, Liu J, Xie J Q, Ye H, Fu X Z, Sun R, Wong C P, (2019) Co-Fe-P nanotubes electrocatalysts derived from metal-organic frameworks for efficient hydrogen evolution reaction under wide pH range. *Nano Energy*, 56, 225-233.
25. Huang J, Y Zhang, Y Ding, (2017) Rationally designed/constructed CoO x/WO3 anode for efficient photoelectrochemical water oxidation. *ACS Catalysis*, 7(3), 1841-1845.
26. Schalenbach M, Carmo M, Fritz D L, Mergel J, Stolten D, (2013) Pressurized PEM water electrolysis: Efficiency and gas crossover. *International Journal of Hydrogen Energy*, 38(35), 14921-14933.
27. Xie J, Y C Lu, (2020) A retrospective on lithium-ion batteries. *Nature Communications*, 11(1), 2499.
28. Subbaraman R, Tripkovic D, Strmcnik D, Chang K C, Uchimura M, Paulikas A P, Stamenkovic V, Markovic N M, (2011) Enhancing hydrogen evolution activity in water splitting by tailoring Li+-Ni (OH) 2-Pt interfaces. *Science,* 334(6060), 1256-1260.
29. Lee S W, Carlton C, Risch M, Surendranath Y, Chen S, Furutsuki S, Yamada A, Nocera D G, Shao Horn Y (2012) The nature of lithium battery materials under oxygen evolution reaction conditions. *Journal of the American Chemical Society*, 134(41), 16959-16962.
30. Wang H, Lee H W, Deng Y, Lu Z, Hsu P C, Liu Y, Lin D, Cui Y, (2015) Bifunctional non-noble metal oxide nanoparticle electrocatalysts through lithium-induced conversion for overall water splitting. *Nature Communications*, 6(1), 7261.
31. Li Z, Wang S, Tian Y, Li B, jun Yan H, Zhang S, Liu Z, Zhang Q, Lin Y, Chen L, (2020) Mg-Doping improves the performance of Ru-based electrocatalysts for the acidic oxygen evolution reaction. *Chemical Communications*, 56(11), 1749-1752.

32. Xu J, Wang S, Yang C, Li T, Liu Q, Kong X, (2021) Free-standing two-dimensional ruthenium-beryllium nanosheets for alkaline hydrogen evolution. *Chemical Engineering Journal*, 421, 129741.
33. Lima A J, Silva V D, Raimundo R A, Morales M A, Simoes T A, Loureiro F J, Fagg D P, Macedo D A, Nascimento R M, (2021) Fe-doped calcium cobaltites as electrocatalysts for oxygen evolution reaction. *Ceramics International*, 47(18), 26109-26118.
34. Shi Y, Xie R, Liu X, Zhang N, Aruta C, Yang N, (2019) Tunable pH-dependent oxygen evolution activity of strontium cobaltite thin films for electrochemical water splitting. *Physical Chemistry Chemical Physics*, 21(29), 16230-16239.
35. Li M, Zhuang L, Wang Z, ur Rehman A, Liu L X, Zhu Z, (2019) Strontium-doped lanthanum iron nickelate oxide as highly efficient electrocatalysts for oxygen evolution reaction. *Journal of Colloid and Interface Science*, 553, 813-819.
36. Xu X, Pan Y, Zhong Y, Ge L, Shao Z, (2020) From scheelite BaMoO4 to perovskite BaMoO3: Enhanced electrocatalysis toward the hydrogen evolution in alkaline media. *Composites Part B: Engineering*, 198, 108214.
37. Chen C F, King G, Dickerson R M, Papin P A, Gupta S, Kellogg W R, Wu G, (2015) Oxygen-deficient BaTiO$_{3-x}$ perovskite as an efficient bifunctional oxygen electrocatalyst. *Nano Energy*, 13, 423-432.
38. Zhang R, Tang C, Kong R, Du G, Asiri A M, Chen L, Sun X, (2017) Al-Doped CoP nanoarray: a durable water-splitting electrocatalyst with superhigh activity. *Nanoscale,* 9(14), 4793-4800.
39. Li Z, Niu W, Zhou L, Yang Y, (2018) Phosphorus and aluminum codoped porous NiO nanosheets as highly efficient electrocatalysts for overall water splitting. *ACS Energy Letters*, 3(4), 892-898.
40. Kakoria A, Devi B, Anand A, Halder A, Koner R R, Sinha Ray S, (2018) Gallium oxide nanofibers for hydrogen evolution and oxygen reduction. *ACS Applied Nano Materials*, 2(1), 64-74.
41. Kakoria A, Devi B, Anand A, Halder A, Koner R R, Sinha-Ray S, (2019) Synthesis of popcorn-shaped gallium-platinum (GaPt$_3$) nanoparticles as highly efficient and stable electrocatalysts for hydrogen evolution reaction. *Electrochimica Acta*, 297, 288-296.
42. Jing T, Liang D, Deng M, Cai S, Qi X, (2021) Density functional theory studies of heteroatom-doped graphene-like GaN monolayers as electrocatalysts for oxygen evolution and reduction. *ACS Applied Nano Materials*, 4(7), 7125-7133.
43. Wang J, Zheng X, Cao Y, Li L, Zhong C, Deng Y, Han X, Hu W, (2020) Developing indium-based ternary spinel selenides for efficient solid flexible Zn-air batteries and water splitting. *ACS Applied Materials & Interfaces*, 12(7), 8115-8123.
44. Shamraiz U, Badshah A, Alfantazi A, Hussain H, Raza B, Ullah S, Green I R, (2021) Solvent mediated fabrication of Ditched Hollow Indium sulfide (In$_2$S$_3$) spheres for overall electrocatalytic water splitting. *Journal of The Electrochemical Society*, 168(6), 066510.
45. Jian J, Kou X, Wang H, Chang L, Zhang L, Gao S, Xu Y, Yuan H, (2021) Fascinating Tin Effects on the Enhanced and Large-Current-Density Water Splitting Performance of Sn–Ni (OH) 2. *ACS Applied Materials & Interfaces*, 13(36), 42861-42869.
46. Yu J, Ma F X, Du Y, Wang P P, Xu C Y, Zhen L, (2017) In Situ Growth of Sn-Doped Ni$_3$S$_2$ Nanosheets on Ni Foam as High-Performance Electrocatalyst for Hydrogen Evolution Reaction. *ChemElectroChem*, 4(3), 594-600.

47. Lang L, Lang L, Shi Y, Wang J, Wang F B, Xia X H, (2015) Hollow core–shell structured Ni–Sn@ C nanoparticles: a novel electrocatalyst for the hydrogen evolution reaction. *ACS Applied Materials & Interfaces*, 7(17), 9098-9102.

48. Syah R, Ahmad A, Davarpanah A, Elveny M, Ramdan D, Albaqami M D, Ouladsmane M, (2021) Incorporation of Bi_2O_3 residuals with metallic bi as high performance electrocatalyst toward hydrogen evolution reaction. *Catalysts*, 11(9), 1099.

49. Khatun S, Roy P, (2020) Bismuth iron molybdenum oxide solid solution: a novel and durable electrocatalyst for overall water splitting. *Chemical Communications*, 56(53), 7293-7296.

50. Aziz S T, Ummekar M, Karajagi I, Riyajuddin S K, Siddhartha K V R, Saini A, Potbhare A, Chaudhary R G, Vishal V, Ghosh P C, Dutta A, (2022) A Janus cerium-doped bismuth oxide electrocatalyst for complete water splitting. *Cell Reports Physical Science*,. 3(11).

51. Lao J, Li D, Jiang C, Luo R, Peng H, Qi R, Lin H, Huang R, Waterhouse, G I, Luo C, (2020) Efficient overall water splitting using nickel boride-based electrocatalysts. *International Journal of Hydrogen Energy*, 45(53), 28616-28625.

52. He Y, Wang T L, Zhang M, Wang T W, Wu L F, Zeng L, Wang X, Boubeche M, Wang S, Yan K, Lin S H, (2021) Discovery and facile synthesis of a new silicon based family as efficient hydrogen evolution reaction catalysts: a computational and experimental investigation of metal monosilicides. *Small*, 17(8), 2006153.

53. Chiani E, S N Azizi, S Ghasemi, (2021) PdCu bimetallic nanoparticles decorated on ordered mesoporous silica (SBA-15)/MWCNTs as superior electrocatalyst for hydrogen evolution reaction. *International Journal of Hydrogen Energy*, 46(50), 25468-25485.

54. Hausmann J N, Khalaniya R A, Das C, Remy-Speckmann I, Berendts S, Shevelkov A V, Driess M, Menezes P W, (2021) Intermetallic Fe 6 Ge 5 formation and decay of a core–shell structure during the oxygen evolution reaction. *Chemical Communications*, 57(17), 2184-2187.

55. Gauthier J A, King L A, Stults F T, Flores R A, Kibsgaard J, Regmi Y N, Chan, K, Jaramillo T F, (2019) Transition metal arsenide catalysts for the hydrogen evolution reaction. *The Journal of Physical Chemistry C*, 123(39), 24007-24012.

56. Lu S, Huynh H L, Lou F, Guo K, Yu Z, (2021) Single transition metal atom embedded antimonene monolayers as efficient trifunctional electrocatalysts for the HER, OER and ORR: a density functional theory study. *Nanoscale*, 13(30), 12885-12895.

57. Yang L, Xu H, Liu H, Cheng D, Cao D, (2019) Active site identification and evaluation criteria of in situ grown CoTe and NiTe nanoarrays for hydrogen evolution and oxygen evolution reactions. *Small Methods*, 3(5), 1900113.

58. Shi H, Liang H, Ming F, Wang Z, (2017) Efficient overall water-splitting electrocatalysis using lepidocrocite VOOH hollow nanospheres. *Angewandte Chemie*, 129(2), 588-592.

59. Zhang P, L Gong, Y Tan, (2021) Ni $_{1-2x}$ Mo $_x$ Se nanowires@ ammonium nickel phosphate–MoO x heterostructures as a high performance electrocatalyst for water splitting. *Sustainable Energy & Fuels*, 5(21), 5581-5593.

60. Zhang Z, He B, Chen L, Wang H, Wang R, Zhao L, Gong Y, (2018) Boosting overall water splitting via FeOOH nanoflake-decorated PrBa0. 5Sr0. 5Co2O5+ δ nanorods. *ACS Applied Materials & Interfaces*, 10(44), 38032-38041.

61. Rajan A G, E A Carter, (2020) Microkinetic model for pH-and potential-dependent oxygen evolution during water splitting on Fe-doped β-NiOOH. *Energy & Environmental Science*, 13(12), 4962-4976.`

62. Rathore D, A Banerjee, S Pande, (2022) Bifunctional tungsten-doped Ni (OH)$_2$/NiOOH nanosheets for overall water splitting in an alkaline medium. *ACS Applied Nano Materials*, 5(2), 2664-2677.

63. Zhang B, Shan J, Wang W, Tsiakaras P, Li Y, (2022) Oxygen Vacancy and Core–Shell Heterojunction Engineering of Anemone-Like CoP@ CoOOH Bifunctional Electrocatalyst for Efficient Overall Water Splitting. *Small*, 18(12), 2106012.

64. Elakkiya R, R Ramkumar, G Maduraiveeran, (2019) Flower-like nickel-cobalt oxide nanomaterials as bi-functional catalyst for electrochemical water splitting. *Materials Research Bulletin*, 116, 98-105.

65. Zhang B, Zhang X, Wei Y, Xia L, Pi C, Song H, Zheng Y, Gao B, Fu J, Chu P K, (2019) General synthesis of NiCo alloy nanochain arrays with thin oxide coating: a highly efficient bifunctional electrocatalyst for overall water splitting. *Journal of Alloys and Compounds*, 797, 1216-1223.

66. Han L, Guo L, Dong C, Zhang C, Gao H, Niu J, Peng Z, Zhang Z, (2019) Ternary mesoporous cobalt-iron-nickel oxide efficiently catalyzing oxygen/hydrogen evolution reactions and overall water splitting. *Nano Research*, 12, 2281-2287.

67. Liao H, Guo X, Hou Y, Liang H, Zhou Z, Yang, H, (2020) Construction of defect-rich Ni-Fe-doped K$_{0.23}$MnO$_2$ cubic nanoflowers via etching prussian blue analogue for efficient overall water splitting. *Small*, 16(10), 1905223.

68. Ma L, Ting L R L, Molinari V, Giordano C, Yeo B S, (2015) Efficient hydrogen evolution reaction catalyzed by molybdenum carbide and molybdenum nitride nanocatalysts synthesized via the urea glass route. *Journal of Materials Chemistry A*, 3(16), 8361-8368.

69. Liu R, Anjass M, Greiner S, Liu S, Gao D, Biskupek J, Kaiser U, Zhang G, Streb C, (2020) Bottom-up design of bimetallic cobalt–molybdenum carbides/oxides for overall water splitting. *Chemistry–A European Journal*, 26(18), 4157-4164.

70. Zhang Y, Liu Z, Guo F, Li M, Bo X, (2022) Morphological modulation of iron carbide embedded nitrogen-doped hierarchically porous carbon by manganese doping as highly efficient bifunctional electrocatalysts for overall water splitting. *Journal of Colloid and Interface Science*, 618, 149-160.

71. Yu H, Yang X, Xiao X, Chen M, Zhang Q, Huang L, Wu J, Li T, Chen S, Song L, Gu L, (2018) Atmospheric-pressure synthesis of 2D nitrogen-rich tungsten nitride. *Advanced Materials*, 30(51), 1805655.

72. Zhou X, Mo Y, Yu F, Liao L, Yong X, Zhang F, Li D, Zhou Q, Sheng T, Zhou H, (2023) Engineering active iron sites on nanoporous bimetal phosphide/nitride heterostructure array enabling robust overall water splitting. *Advanced Functional Materials*, 33(6), 2209465.

73. Peng X, Huang C, Dai J, Liu Y, (2022) Uniform cobalt grafted on vanadium nitride as a high efficient oxygen evolution reaction catalyst. *International Journal of Hydrogen Energy*, 47(7), 4386-4393.

74. Wang Z, Qu J, He Y, Xiong T, Huang Z, Wang F, Balogun M S, (2023) Exceptional alkaline hydrogen evolution by molybdenum-oxide-nitride-based electrocatalysts with fast water-dissociation and hydrogen-adsorption kinetics. *Materials Chemistry Frontiers*.

75. Kagkoura A, Pelaez-Fernandez M, Arenal R, Tagmatarchis N, (2019) Sulfur-doped graphene/transition metal dichalcogenide heterostructured hybrids with electrocatalytic activity toward the hydrogen evolution reaction. *Nanoscale Advances*, 1(4), 1489-1496.

76. He W, Liu H, Cheng J, Mao J, Chen C, Hao Q, Zhao J, Liu C, Li Y, Liang L, (2021) Designing Zn-doped nickel sulfide catalysts with an optimized electronic structure for enhanced hydrogen evolution reaction. *Nanoscale*, 13(22), 10127-10132.

77. Mao X, Liu Y, Chen Z, Fan Y, Shen P, (2022) Fe and Co dual-doped Ni3S4 nanosheet with enriched high-valence Ni sites for efficient oxygen evolution reaction. *Chemical Engineering Journal*, 427, 130742.

78. Zhu X, Nguyen D C, Prabhakaran S, Kim D H, Kim N H, Lee J H, (2023) Activating catalytic behavior of binary transition metal sulfide-shelled carbon nanotubes by iridium incorporation toward efficient overall water splitting. *Materials Today Nano*, 21, 100296.

79. Xia X, Wang L, Sui N, Colvin V L, William W Y, (2020) Recent progress in transition metal selenide electrocatalysts for water splitting. *Nanoscale*, 12(23), 12249-12262.

80. Liu H, Wang K, He W, Zheng X, Gong T, Li Y, Zhao J, Zhang J, Liang L, (2021) Phosphorus-doped nickel selenides nanosheet arrays as highly efficient electrocatalysts for alkaline hydrogen evolution. *International Journal of Hydrogen Energy*, 46(2), 1967-1975.

81. Guo Y, Zhang C, Zhang J, Dastafkan K, Wang K, Zhao C, Shi Z, (2021) Metal–organic framework-derived bimetallic NiFe selenide electrocatalysts with multiple phases for efficient oxygen evolution reaction. *ACS Sustainable Chemistry & Engineering*, 9(5), 2047-2056.

82. Wu H, Wang Z, Li Z, Ma Y, Ding F, Li F, Bian H, Zhai Q, Ren Y, Shi Y, Yang Y, (2023) Medium-Entropy Metal Selenides Nanoparticles with Optimized Electronic Structure as High-Performance Bifunctional Electrocatalysts for Overall Water Splitting. *Advanced Energy Materials*,.13(28), 2300837.

83. Yan L, Zhang B, Zhu J, Liu Z, Zhang H, Li Y, (2019) Callistemon-like Zn & S codoped CoP nanorod clusters as highly efficient electrocatalysts for neutral-pH overall water splitting. *Journal of Materials Chemistry A*, 7(39), 22453-22462.

84. Li R, Zang J, Li W, Li J, Zou Q, Zhou S, Su J, Wang Y, (2020) Three-Dimensional Transition Metal Phosphide Heteronanorods for Efficient Overall Water Splitting. *ChemSusChem*, 13(14), 3718-3725.

85. Xu S, Qi Y, Lu Y, Sun S, Liu Y, Jiang D, (2021) Fe-Doped CoP holey nanosheets as bifunctional electrocatalysts for efficient hydrogen and oxygen evolution reactions. *International Journal of Hydrogen Energy*, 46(52), 26391-26401.

86. Sun X, Wei P, He Z, Cheng F, Tang L, Li Q, Han J, He J, (2023) Novel transition-metal phosphides@ N, P-codoped carbon electrocatalysts synthesized via a universal strategy for overall water splitting. *Journal of Alloys and Compounds*, 932, 167253.

87. Tariq I, Asghar M A, Ali A, Badshah A, Abbas S M, Iqbal W, Zubair M, Haider A, Zaman S, (2022) Surface reconstruction of cobalt-based polyoxometalate and CNT fiber composite for efficient oxygen evolution reaction. *Catalysts*, 12(10), 1242.

88. Luo W, Hu J, Diao H, Schwarz B, Streb C, Song Y F, (2017) Robust polyoxometalate/nickel foam composite electrodes for sustained electrochemical oxygen evolution at high pH. *Angewandte Chemie International Edition*, 56(18), 4941-4944.

89. Li Q Y, Zhang L, Xu Y X, Li Q, Xue H, Pang H, (2019) Smart yolk/shell ZIF-67@ POM hybrids as efficient electrocatalysts for the oxygen evolution reaction. *ACS Sustainable Chemistry & Engineering*, 7(5), 5027-5033.

90. Gautam J, Liu Y, Gu J, Ma Z, Zha J, Dahal B, Zhang L N, Chishti A N, Ni L, Diao G, Wei Y, (2021) Fabrication of polyoxometalate anchored zinc cobalt sulfide nanowires as a

remarkable bifunctional electrocatalyst for overall water splitting. *Advanced Functional Materials*, 31(46), 2106147.

91. Gautam J, Wang P, Chishti A N, Ma Z, Liu Y, Jiang X, Zha J, Zhang L N, Diao G, Wei Y, Ni, L, (2023) Heterointerface engineering of hierarchically assembling polyoxometalate on zinc/iron layered double hydroxide nanosheet as a remarkable bifunctional electrocatalyst for overall water splitting. *Journal of Power Sources*, 581, 233502.

92. Ravi A, S Mulkapuri, S K Das, (2023) Hydroxylated Polyoxometalate with Cu (II)-and Cu (I)-Aqua Complexes: A Bifunctional Catalyst for Electrocatalytic Water Splitting at Neutral pH. *Inorganic Chemistry.*

93. Li D, Guo Z, Zhao R, Ren H, Huang Y, Yan Y, Cui W, Yao X, (2024) An efficient cerium dioxide incorporated nickel cobalt phosphide complex as electrocatalyst for All-pH hydrogen evolution reaction and overall water splitting. *Journal of Colloid and Interface Science*, 653, 1725-1742.

94. Majhi K C, M Yadav, (2022) Neodymium oxide doped neodymium phosphate as efficient electrocatalyst towards hydrogen evolution reaction in acidic medium. *Journal of Environmental Chemical Engineering*, 10(3), 107416.

95. Ouyang Q, Cheng S, Yang C, Lei Z, (2023) Ni, Co, and Yb Cation Co-doping and Defect Engineering of FeOOH Nanorods as an Electrocatalyst for the Oxygen Evolution Reaction. *Inorganic Chemistry*, 62(4), 1719-1727.

96. Singh S, D Singh, (2010) Biodiesel production through the use of different sources and characterization of oils and their esters as the substitute of diesel: a review. *Renewable and sustainable energy reviews*, 14(1), 200-216.

97. Mofijur M, Siddiki S Y A, Shuvho M B A, Djavanroodi F, Fattah I R, Ong H C, Chowdhury M A, Mahlia T M I, (2021) Effect of nanocatalysts on the transesterification reaction of first, second and third generation biodiesel sources-A mini-review. *Chemosphere*, 270, 128642.

98. Singh D, Sharma D, Soni S L, Sharma S, Kumari D, (2019) Chemical compositions, properties, and standards for different generation biodiesels: A review. *Fuel*, 253, 60-71.

99. Mahdavi M, E Abedini, A hosein Darabi, (2015) Biodiesel synthesis from oleic acid by nano-catalyst (ZrO_2/Al_2O_3) under high voltage conditions. *RSC Advances*, 5(68), 55027-55032.

100. Aransiola E F, Ojumu T V, Oyekola O O, Madzimbamuto T F, Ikhu-Omoregbe D I O, (2014) A review of current technology for biodiesel production: State of the art. *Biomass and bioenergy*, 61, 276-297.

101. Eryilmaz T, Yesilyurt M K, Cesur C, Gokdogan O, (2016) Biodiesel production potential from oil seeds in Turkey. *Renewable and Sustainable Energy Reviews*, 58, 842-851.

102. Moser B R, (2012) Preparation of fatty acid methyl esters from hazelnut, high-oleic peanut and walnut oils and evaluation as biodiesel. *Fuel*, 92(1), 231-238.

103. Fadhil A B, W S Abdulahad, (2014) Transesterification of mustard (Brassica nigra) seed oil with ethanol: Purification of the crude ethyl ester with activated carbon produced from de-oiled cake. *Energy Conversion and Management*, 77, 495-503.

104. Demirbas A, (2008) A Realistic Fuel Alternative for Diesel Engines. *Springer London2008*.

105. Shaah M A H, Hossain M S, Allafi F A S, Alsaedi A, Ismail N, Ab Kadir M O, Ahmad M I, (2021) A review on non-edible oil as a potential feedstock for biodiesel:

physicochemical properties and production technologies. *RSC advances*, 11(40), 25018-25037.

106.   Peer M S, Kasimani R, Rajamohan S, Ramakrishnan P, (2017) Experimental evaluation on oxidation stability of biodiesel/diesel blends with alcohol addition by rancimat instrument and FTIR spectroscopy. *Journal of Mechanical Science and Technology*, 31, 455-463.

107.   Tariq M, S Ali, N Khalid, (2012) Activity of homogeneous and heterogeneous catalysts, spectroscopic and chromatographic characterization of biodiesel: A review. *Renewable and Sustainable Energy Reviews*, 16(8), 6303-6316.

108.   Verma P, M Sharma, G Dwivedi, (2016) Impact of alcohol on biodiesel production and properties. *Renewable and Sustainable Energy Reviews*, 56, 319-333.

109.   Mata T M, A A Martins, N S Caetano, (2010) Microalgae for biodiesel production and other applications: a review. *Renewable and sustainable energy reviews*, 14(1), 217-232.

110.   Hwang J, C Bae, T Gupta, (2016) Application of waste cooking oil (WCO) biodiesel in a compression ignition engine. *Fuel*, 176, 20-31.

111.   Cameron D E, C J Bashor, J J Collins, (2014) A brief history of synthetic biology. *Nature Reviews Microbiology*, 12(5), 381-390.

112.   Knothe G, (2006) Analyzing biodiesel: standards and other methods. *Journal of the American Oil Chemists' Society*, 83(10), 823-833.

113.   Foglia T A, Jones K C, Haas M J, Scott K M, (2000) Technologies supporting the adoption of biodiesel as an alternative fuel. *The cotton gin and oil mill presses*.

114.   ukuda H, A Kondo, H Noda, (2001) Biodiesel fuel production by transesterification of oils. *Journal of Bioscience and Bioengineering*, 92(5), 405-416.

115.   Koh M Y, T I M Ghazi, (2011) A review of biodiesel production from Jatropha curcas L. oil. *Renewable and Sustainable Energy Reviews*, 15(5), 2240-2251.

116.   Ma F, M A Hanna, (1999) Biodiesel production: a review. *Bioresource Technology*, 70(1), 1-15.

117.   Balat M, H Balat, (2010) Progress in biodiesel processing. *Applied Energy*, 87(6), 1815-1835.

118.   Lappi H, R Alén, (2011) Pyrolysis of vegetable oil soaps—palm, olive, rapeseed and castor oils. *Journal of Analytical and Applied Pyrolysis*, 91(1), 154-158.

119.   Maher K, D Bressler, (2007) Pyrolysis of triglyceride materials for the production of renewable fuels and chemicals. *Bioresource Technology*, 98(12), 2351-2368.

120.   Lima D G, Soares V C, Ribeiro E B, Carvalho D A, Cardoso É C, Rassi F C, Mundim K C, Rubim J C, Suarez P A, (2004) Diesel-like fuel obtained by pyrolysis of vegetable oils. *Journal of Analytical and Applied Pyrolysis*, 71(2), 987-996.

121.   Lappi H, R Alén, (2009) Production of vegetable oil-based biofuels—thermochemical behavior of fatty acid sodium salts during pyrolysis. *Journal of Analytical and Applied Pyrolysis*, 86(2), 274-280.

122.   Hossain M N, Siddik Bhuyan M S U, Md Ashraful Alam A H, Seo Y C, (2019) Optimization of biodiesel production from waste cooking oil using S–TiO2/SBA-15 heterogeneous acid catalyst. *Catalysts*, 9(1), 67.

123.   Ramli A, Farooq M, Naeem A, Khan S, Hummayun M, Iqbal A, Ahmed S, Shah L A, (2017) Bifunctional heterogeneous catalysts for biodiesel production using low cost feedstocks: a future perspective. *Frontiers in Bioenergy and Biofuels*, 285, 285-299.

124. Thangaraj B, Solomon P R, Muniyandi B, Ranganathan S, Lin L, (2019) Catalysis in biodiesel production—a review. *Clean Energy*, 3(1), 2-23.

125. Avhad M, J Marchetti, (2015) A review on recent advancement in catalytic materials for biodiesel production. *Renewable and Sustainable Energy Reviews*, 50, 696-718.

126. Ni J, F Meunier, (2007) Esterification of free fatty acids in sunflower oil over solid acid catalysts using batch and fixed bed-reactors. *Applied Catalysis A: General*, 333(1), 122-130.

127. Thiruvengadaravi K V, Nandagopal J, Baskaralingam P, Bala V S S, Sivanesan S, (2012) Acid-catalyzed esterification of karanja (Pongamia pinnata) oil with high free fatty acids for biodiesel production. *Fuel*, 98, 1-4.

128. Zhang J, L Jiang, (2008) Acid-catalyzed esterification of Zanthoxylum bungeanum seed oil with high free fatty acids for biodiesel production. *Bioresource Technology*, 99(18), 8995-8998.

129. Abbas A S, R N Abbas, (2015) Preparation and characterization of NaY zeolite for biodiesel production. *Iraqi Journal of Chemical and Petroleum Engineering*, 16(2), 19-29.

130. Schuchardt U, R Sercheli, R M Vargas, (1998) Transesterification of vegetable oils: a review. *Journal of the Brazilian Chemical Society*, 9, 199-210.

131. Ataya F, M A Dubé, M Ternan, (2007) Acid-catalyzed transesterification of canola oil to biodiesel under single-and two-phase reaction conditions. *Energy & Fuels*, 21(4), 2450-2459.

132. Srinivas D, R Srivastava, P Ratnasamy, (2004) Transesterifications over titanosilicate molecular sieves. *Catalysis Today*, 96(3), 127-133.

133. Miao X, R Li, H Yao, (2009) Effective acid-catalyzed transesterification for biodiesel production. *Energy Conversion and Management*, 50(10), 2680-2684.

134. Meher L C, D V Sagar, S Naik, (2006) Technical aspects of biodiesel production by transesterification—a review. *Renewable and Sustainable Energy Reviews*, 10(3), 248-268.

135. Alamu O J, Akintola T A, Enweremadu C C, Adeleke A E, (2008) Characterization of palm-kernel oil biodiesel produced through NaOH-catalysed transesterification process. *Scientific Research and Essay*, 3(7), 308-311.

136. Jamil F, Kumar P S M, Al-Haj L, Myint M T Z, Ala'a H, (2021) Heterogeneous carbon-based catalyst modified by alkaline earth metal oxides for biodiesel production: Parametric and kinetic study. *Energy Conversion and Management: X*, 10, 100047.

137. Arzamendi G, Arguinarena E, Campo I, Zabala S, Gandía L M, (2008) Alkaline and alkaline-earth metals compounds as catalysts for the methanolysis of sunflower oil. *Catalysis Today*, 133, 305-313.

138. Marchetti J, V Miguel, A Errazu, (2007) Possible methods for biodiesel production. *Renewable and Sustainable Energy Reviews*, 11(6), 1300-1311.

139. Di Serio M, Tesser R, Dimiccoli M, Cammarota F, Nastasi M, Santacesaria E, (2005) Synthesis of biodiesel via homogeneous Lewis acid catalyst. *Journal of Molecular Catalysis A: Chemical*, 239(1-2), 111-115.

140. Wang Y, Ou S, Liu P, Zhang Z, (2007) Preparation of biodiesel from waste cooking oil via two-step catalyzed process. *Energy Conversion and Management*, 48(1), 184-188.

141. Dehkhoda A M, (2010) Developing biochar-based catalyst for biodiesel production. *University of British Columbia*.

142.   Vicente G, M Martınez, J Aracil, (2004) Integrated biodiesel production: a comparison of different homogeneous catalysts systems. *Bioresource Technology*, 92(3), 297-305.

143.   Enweremadu C C, M Mbarawa, (2009) Technical aspects of production and analysis of biodiesel from used cooking oil—A review. *Renewable and Sustainable Energy Reviews*, 13(9), 2205-2224.

144.   Wen Z, Yu X, Tu S T, Yan J, Dahlquist E, (2010) Biodiesel production from waste cooking oil catalyzed by TiO_2–MgO mixed oxides. *Bioresource Technology*, 101(24), 9570-9576.

145.   Cannilla C, Bonura G, Rombi E, Arena F, Frusteri F, (2010) Highly effective MnCeOx catalysts for biodiesel production by transesterification of vegetable oils with methanol. *Applied Catalysis A: General*, 382(2), 158-166.

146.   Jiménez-López A, Jiménez-Morales I, Santamaría-González J, Maireles-Torres P, (2011) Biodiesel production from sunflower oil by tungsten oxide supported on zirconium doped MCM-41 silica. *Journal of Molecular Catalysis A: Chemical*, 335(1-2), 205-209.

147.   Guo H, Cheng J, Mao Y, Qian L, Shao Y, Yang X, Yang W, (2022) Acid-base bifunctional catalyst with coordinatively unsaturated cobalt-nitrogen sites for the simultaneous conversion of microalgal triglycerides and free fatty acids into biodiesel. *Bioresource Technology*, 350, 126862.

148.   Al-Saadi A, B Mathan, Y He, (2020) Biodiesel production via simultaneous transesterification and esterification reactions over SrO–ZnO/Al2O3 as a bifunctional catalyst using high acidic waste cooking oil. *Chemical Engineering Research and Design*, 162, 238-248.

149.   Dai Y M, Li Y Y, Chen B Y, Chen C C, (2021) One-pot synthesis of acid-base bifunctional catalysts for biodiesel production. *Journal of Environmental Management*, 299, 113592.

150.   Knothe G, (2005) The Biodiesel Handbook. 1-302. Knothe, G., Van Gerpen, J., and Krahl, *J. ed: AOCS Press, Urbana, IL*.

151.   Tabatabaei M, Aghbashlo M, Dehhaghi M, Panahi H K S, Mollahosseini A, Hosseini M, Soufiyan M M, (2019) Reactor technologies for biodiesel production and processing: A review. *Progress in Energy and Combustion Science*, 74, 239-303.

152.   Amani H, Z Ahmad, B Hameed, (2014) Highly active alumina-supported Cs–Zr mixed oxide catalysts for low-temperature transesterification of waste cooking oil. *Applied Catalysis A: General*, 487, 16-25.

153.   Ezebor F, Khairuddean M, Abdullah A Z, Boey P L, (2014) Oil palm trunk and sugarcane bagasse derived solid acid catalysts for rapid esterification of fatty acids and moisture-assisted transesterification of oils under pseudo-infinite methanol. *Bioresource Technology*, 157, 254-262.

154.   Gomaa M A, Gombocz N, Schild D, Mjalli F S, Al-Harrasi A, Abed R M, (2021) Effect of organic solvents and acidic catalysts on biodiesel yields from primary sewage sludge, and characterization of fuel properties. *Biofuels*, 12(4), 405-413.

155.   Alamu O J, Waheed M A, Jekayinfa S O, Akintola T A, (2007) Optimal transesterification duration for biodiesel production from Nigerian palm kernel oil. *Agricultural Engineering International: CIGR Journal*.

156.   Mathiyazhagan M, A Ganapathi, (2011) Factors affecting biodiesel production. *Research in plant Biology*, 1(2).

157.	Monteiro M R, Ambrozin A R P, Lião L M, Ferreira A G, (2008) Critical review on analytical methods for biodiesel characterization. *Talanta*, 77(2), 593-605.

158.	O'Donnell S, Demshemino I, Yahaya M, Nwadike I, Okoro L, (2013) A review on the spectroscopic analyses of biodiesel. *European International Journal of Science and Technology*, 2(7), 137-146.

159.	Rezende M J, Lima A L D, Silva B V, Mota C J, Torres E A, Rocha G O D, Cardozo I M, Costa K P, Guarieiro L L, Pereira P A, Martinez S, (2021) Biodiesel: an overview II. *Journal of the Brazilian Chemical Society*, 32, 1301-1344.

160.	Meng X, G Chen, Y Wang, (2008) Biodiesel production from waste cooking oil via alkali catalyst and its engine test. *Fuel Processing Technology*, 89(9), 851-857.

161.	Rashid U, Anwar F, Ansari T M, Arif M, Ahmad M, (2009) Optimization of alkaline transesterification of rice bran oil for biodiesel production using response surface methodology. *Journal of Chemical Technology & Biotechnology*, 84(9), 1364-1370.

162.	Yusup S, M A Khan, (2010) Base catalyzed transesterification of acid treated vegetable oil blend for biodiesel production. *Biomass and Bioenergy*, 34(10), 1500-1504.

163.	Atadashi I M, Aroua M K, Aziz A A, Sulaiman N M N, (2013) The effects of catalysts in biodiesel production: A review. *Journal of Industrial and Engineering Chemistry*, 19(1), 14-26.

164.	Veljković V B, Lakićević S H, Stamenković O S, Todorović Z B, Lazić M L, (2006) Biodiesel production from tobacco (Nicotiana tabacum L.) seed oil with a high content of free fatty acids. *Fuel*, 85(17-18), 2671-2675.

165.	Ehiri R, I Ikelle, O Ozoaku, (2014) Acid-catalyzed transesterification reaction of beef tallow for biodiesel production by factor variation. *Am. J. Eng. Res*, 3, 174-177.

166.	Dalvand P, L Mahdavian, (2018) Calculation of the properties of biodiesel produced from castor seed by eggshell catalyst. *Biofuels*, 9(6), 705-710.

167.	Ma Y, Wang Q, Sun X, Wu C, Gao Z, (2017) Kinetics studies of biodiesel production from waste cooking oil using FeCl3-modified resin as heterogeneous catalyst. *Renewable Energy*, 107, 522-530.

168.	Chozhavendhan S, Singh M V P, Fransila B, Kumar R P, Devi G K, (2020) A review on influencing parameters of biodiesel production and purification processes. *Current Research in Green and Sustainable Chemistry*, 1, 1-6.

169.	Gaurav A, Dumas S, Mai C T, Ng F T, (2019) A kinetic model for a single step biodiesel production from a high free fatty acid (FFA) biodiesel feedstock over a solid heteropolyacid catalyst. *Green Energy & Environment*, 4(3), 328-341.

170.	Farabi M A, Ibrahim M L, Rashid U, Taufiq-Yap Y H, (2019) Esterification of palm fatty acid distillate using sulfonated carbon-based catalyst derived from palm kernel shell and bamboo. *Energy Conversion and Management*, 181, 562-570.

171.	Xie W, T Wang, (2013) Biodiesel production from soybean oil transesterification using tin oxide-supported WO3 catalysts. *Fuel Processing Technology*, 109, 150-155.

172.	Zhang Q, Li H, Liu X, Qin W, Zhang Y, Xue W, Yang S, (2013) Modified porous Zr–Mo mixed oxides as strong acid catalysts for biodiesel production. *Energy Technology*, 1(12), 735-742.

173.	Suzuta T, Toba M, Abe Y, Yoshimura Y, (2012) Iron oxide catalysts supported on porous silica for the production of biodiesel from crude Jatropha oil. *Journal of the American Oil Chemists' Society*, 89(11), 1981-1989.

174.   Thirunavukkarasu K, Sankaranarayanan T M, Pandurangan A, Shanthi R V, Sivasanker S, (2014) The role of surface Zn 2+ ions in the transesterification of vegetable oils over ZnO supported on Al 2 O 3 and Fe 2 O 3. *Catalysis Science & Technology*, 4(3), 851-860.

175.   Lam M K, K T Lee, A R Mohamed, (2009) Sulfated tin oxide as solid superacid catalyst for transesterification of waste cooking oil: an optimization study. *Applied Catalysis B: Environmental*, 93(1-2), 134-139.

176.   Gardy J, Hassanpour A, Lai X, Ahmed M H, Rehan M, (2017) Biodiesel production from used cooking oil using a novel surface functionalised TiO2 nano-catalyst. *Applied Catalysis B: Environmental*, 207, 297-310.

177.   Kresge C T, Vartuli J C, Roth W J, Leonowicz M E, (2004) The discovery of ExxonMobil's M41S family of mesoporous molecular sieves, in Studies in Surface Science and catalysis., Elsevier. 53-72.

178.   Tuel A, (1999) Modification of mesoporous silicas by incorporation of heteroelements in the framework. *Microporous and Mesoporous Materials*, 27(2-3), 151-169.

179.   Samart C, C Chaiya, P Reubroycharoen, (2010) Biodiesel production by methanolysis of soybean oil using calcium supported on mesoporous silica catalyst. *Energy Conversion and Management*, 51(7), 1428-1431.

180.   Sharma R V, C Baroi, A K Dalai, (2014) Production of biodiesel from unrefined canola oil using mesoporous sulfated Ti-SBA-15 catalyst. *Catalysis Today*, 237, 3-12.

181.   Karnjanakom S, Kongparakul S, Chaiya C, Reubroycharoen P, Guan G, Samart C, (2016) Biodiesel production from Hevea brasiliensis oil using SO3H-MCM-41 catalyst. *Journal of Environmental Chemical Engineering*, 4(1), 47-55.

182.   Negm N A, Betiha M A, Alhumaimess M S, Hassan H M, Rabie A M, (2019) Clean transesterification process for biodiesel production using heterogeneous polymer-heteropoly acid nanocatalyst. *Journal of Cleaner Production*, 238, 117854.

183.   Alcañiz-Monge J, El Bakkali B, Trautwein G, Reinoso S, (2018) Zirconia-supported tungstophosphoric heteropolyacid as heterogeneous acid catalyst for biodiesel production. *Applied Catalysis B: Environmental*, 224, 194-203.

184.   Esmi F, A K Dalai, Y Hu, (2023) Optimization and kinetic studies of 12-tungstophosphoric supported mesoporous aluminosilicate through response surface methodology for biodiesel production using green seed canola oil. *Fuel*, 348, 128594.

185.   Rasouli H, H Esmaeili, (2019) Characterization of MgO nanocatalyst to produce biodiesel from goat fat using transesterification process. *3 Biotech*, 9(11), 429.

186.   Zhang Y, Niu S, Han K, Li Y, Lu C, (2021) Synthesis of the SrO–CaO–Al2O3 trimetallic oxide catalyst for transesterification to produce biodiesel. *Renewable Energy*, 168, 981-990.

187.   Booramurthy V K, Kasimani R, Pandian S, Subramanian D, (2022) Magnetic nano-catalyzed synthesis of biodiesel from tannery sludge: characterization, optimization and kinetic studies. *Arabian Journal for Science and Engineering*, 47(5), 6341-6353.

188.   Hameed A, Naqvi S R, Sikandar U, Chen W H, (2022) One-step biodiesel production from waste cooking oil using CaO promoted activated carbon catalyst from Prunus persica seeds. *Catalysts*, 12(6), 592.

189. Kaur M, A Ali, (2015) An efficient and reusable Li/NiO heterogeneous catalyst for ethanolysis of waste cottonseed oil. *European Journal of Lipid Science and Technology*, 117(4), 550-560.

190. Baskar G, Gurugulladevi A, Nishanthini T, Aiswarya R, Tamilarasan K J R E, (2017) Optimization and kinetics of biodiesel production from Mahua oil using manganese doped zinc oxide nanocatalyst. *Renewable Energy*, 103, 641-646.

191. Seffati K, Honarvar B, Esmaeili H, Esfandiari N, (2019) Enhanced biodiesel production from chicken fat using CaO/CuFe2O4 nanocatalyst and its combination with diesel to improve fuel properties. *Fuel*, 235, 1238-1244.

192. Kawashima A, K Matsubara, K Honda, (2008) Development of heterogeneous base catalysts for biodiesel production. *Bioresource Technology*, 99(9), 3439-3443.

193. Madhuvilakku R, S Piraman, (2013) Biodiesel synthesis by TiO2–ZnO mixed oxide nanocatalyst catalyzed palm oil transesterification process. *Bioresource Technology*, 150, 55-59.

194. Banerjee S, S Sahani, Y C Sharma, (2019) Process dynamic investigations and emission analyses of biodiesel produced using Sr–Ce mixed metal oxide heterogeneous catalyst. *Journal of Environmental Management*, 248, 109218.

195. Farooq M, A Ramli, D Subbarao, (2013) Biodiesel production from waste cooking oil using bifunctional heterogeneous solid catalysts. *Journal of Cleaner Production*, 59, 131-140.

196. Sulaiman N F, Bakar W A, Toemen S, Kamal N M, Nadarajan R, (2019) In depth investigation of bi-functional, Cu/Zn/γ-Al2O3 catalyst in biodiesel production from low-grade cooking oil: Optimization using response surface methodology. *Renewable Energy*, 135, 408-416.

197. Li Y, Niu S, Hao Y, Zhou W, Wang J, Liu J, (2022) Role of oxygen vacancy on activity of Fe-doped SrTiO3 perovskite bifunctional catalysts for biodiesel production. *Renewable Energy*, 199, 1258-1271.

198. Rafiei S, Tangestaninejad S, Horcajada P, Moghadam M, Mirkhani V, Mohammadpoor-Baltork I, Kardanpour R, Zadehahmadi F, (2018) Efficient biodiesel production using a lipase@ ZIF-67 nanobioreactor. *Chemical Engineering Journal*, 334, 1233-1241.

199. Jayaraman J, Alagu K, Appavu P, Joy N, Jayaram P, Mariadoss A, (2020) Enzymatic production of biodiesel using lipase catalyst and testing of an unmodified compression ignition engine using its blends with diesel. *Renewable Energy*, 145, 399-407.

200. Zulkifli Z A, K A Razak, W N W A Rahman, (2018) The effect of reaction temperature on the particle size of bismuth oxide nanoparticles synthesized via hydrothermal method. in *AIP conference proceedings*. AIP Publishing.

201. Rahman M A, R Radhakrishnan, R Gopalakrishnan, (2018) Structural, optical, magnetic and antibacterial properties of Nd doped NiO nanoparticles prepared by co-precipitation method. *Journal of Alloys and Compounds*, 742, 421-429.

202. Dehghani S, M Haghighi, (2020) Sono-enhanced dispersion of CaO over Zr-Doped MCM-41 bifunctional nanocatalyst with various Si/Zr ratios for conversion of waste cooking oil to biodiesel. *Renewable Energy*, 153, 801-812.

203. Salomão P E, Gomes D S, Ferreira E J, Moura F, Nascimento L L, Patrocínio A O, Pereira M C, (2019) Photoelectrochemical hydrogen production from water splitting using

heterostructured nanowire arrays of Bi2O3/BiAl oxides as a photocathode. *Solar Energy Materials and Solar Cells*, 194, 276-284.

204.   Ren J T, Z Y Yuan, (2021) Heterojunction-induced nickel-based oxygen vacancies on N-enriched porous carbons for enhanced alkaline hydrogen oxidation and oxygen reduction. *Materials Chemistry Frontiers*, 5(5), 2399-2408.

205.   Morgan W E, W J Stec, J R Van Wazer, (1973) Inner-orbital binding-energy shifts of antimony and bismuth compounds. *Inorganic Chemistry*, 12(4), 953-955.

206.   Ashfaq H T, Asghar M A, Nisar T, Wagner V, Mansoor M A, Haider A, Ali S, (2023) Electrochemical synthesis of Co-, Ni- and NiCo-based hexacyanocobaltates as efficient electrocatalysts for water oxidation studies. *Inorganic Chemistry Communications*, 154, 110916.

207.   Yu X, Qu L, Lee C, Peng J, Yan Q, Bai H, Yao M, (2022) Bismuth–nickel bimetal nanosheets with a porous structure for efficient hydrogen production in neutral and alkaline media. *Nanoscale*, 14(46), 17210-17221.

208.   Jo S G, Kim C S, Kim S J, Lee J W, (2021) Phase-controlled NiO nanoparticles on reduced graphene oxide as electrocatalysts for overall water splitting. *Nanomaterials*, 11(12), 3379.

209.   Bruno L, Battiato S, Scuderi M, Priolo F, Terrasi A, Mirabella S, (2022) Physical insights into alkaline overall water splitting with NiO microflowers electrodes with ultra-low amount of Pt catalyst. *International Journal of Hydrogen Energy*, 47(80), 33988-33998.

210.   Bruno L, Scuderi M, Priolo F, Mirabella S, (2022) Enhanced electrocatalytic activity of low-cost NiO microflowers on graphene paper for the oxygen evolution reaction. *Sustainable Energy & Fuels*, 6(19), 4498-4505.

211.   Yang H, Chen Z, Hao W, Xu H, Guo Y, Wu R, (2019) Catalyzing overall water splitting at an ultralow cell voltage of 1.42 V via coupled Co-doped NiO nanosheets with carbon. *Applied Catalysis B: Environmental*, 252, 214-221.

212.   Wu Z, Zou Z, Huang J, Gao F, (2018) Fe-doped NiO mesoporous nanosheets array for highly efficient overall water splitting. *Journal of Catalysis*, 358, 243-252.

213.   Liu J, Zhu D, Ling T, Vasileff A, Qiao S Z, (2017) S-NiFe2O4 ultra-small nanoparticle built nanosheets for efficient water splitting in alkaline and neutral pH. *Nano Energy*, 40, 264-273.

214.   Zhang W, Jiang X, Dong Z, Wang J, Zhang N, Liu J, Xu G R, Wang L, (2021) Porous Pd/NiFeOx nanosheets enhance the pH-universal overall water splitting. *Advanced Functional Materials*, 31(51), 2107181.

215.   Fan J, Hao W, Fu C, Chen Z, Liang R, Lian C, Zhang Q, Li G, (2022) Construction of efficient bismuth/boron-based flexible electrodes in organic media toward neutral hydrogen evolution. *Journal of Materials Chemistry A*, 10(3), 1535-1546.

216.   Yue X M, Liu Z J, Xiao C C, Ye M, Ge Z P, Peng C, Gu Z Y, Zhu J S, Zhang S Q, (2021) Synthesis of Co 3 O 4/reduced graphene oxide by one step-hydrothermal and calcination method for high-performance supercapacitors. *Ionics*, 27, 339-349.

217.   Tyuliev G, S Angelov, (1988) The nature of excess oxygen in Co3O4+ ε. *Applied Surface Science*, 32(4), 381-391.

218.   Younis A, Chu D, Lin X, Lee J, Li S, (2013) Bipolar resistive switching in p-type Co 3 O 4 nanosheets prepared by electrochemical deposition. *Nanoscale Research Letters*, 8, 1-5.

219. Raquet B, Mamy R, Ousset J C, Negre N, Goiran M, Guerret-Piécourt C, (1998) Preparation and magnetic properties of the CoO/Co bilayer. *Journal of Magnetism and Magnetic Materials*, 184(1), 41-48.

220. Doyle R L, Godwin I J, Brandon M P, Lyons M E, (2013) Redox and electrochemical water splitting catalytic properties of hydrated metal oxide modified electrodes. *Physical Chemistry Chemical Physics*, 15(33), 13737-13783.

221. Stumm C, Bertram M, Kastenmeier M, Speck F D, Sun Z, Rodríguez-Fernández J, Lauritsen J V, Mayrhofer K J, Cherevko S, Brummel O, Libuda J, (2021) Structural dynamics of ultrathin cobalt oxide nanoislands under potential control. *Advanced Functional Materials*, 31(13), 2009923.

222. Tong Y, Mao H, Xu Y, Liu J, (2019) Oxygen vacancies confined in Co 3 O 4 quantum dots for promoting oxygen evolution electrocatalysis. *Inorganic Chemistry Frontiers*, 6(8), 2055-2060.

223. Wang T, Wang P, Zang W, Li X, Chen D, Kou Z, Mu S, Wang J, (2022) Nanoframes of Co3O4–Mo2N Heterointerfaces Enable High-Performance Bifunctionality toward Both Electrocatalytic HER and OER. *Advanced Functional Materials*, 32(7), 2107382.

224. He D, Song X, Li W, Tang C, Liu J, Ke Z, Jiang C, Xiao X, (2020) Active electron density modulation of Co3O4-based catalysts enhances their oxygen evolution performance. *Angewandte Chemie International Edition*, 59(17), 6929-6935.

225. Acedera R A E, Gupta G, Mamlouk M, Balela M D L, (2020) Solution combustion synthesis of porous Co_3O_4 nanoparticles as oxygen evolution reaction (OER) electrocatalysts in alkaline medium. *Journal of Alloys and Compounds*, 836, 154919.

226. Du Q, Su P, Cao Z, Yang J, Price C A H, Liu J, (2021) Construction of N and Fe co-doped CoO/Co_xN interface for excellent OER performance. *Sustainable Materials and Technologies*, 29, e00293.

227. Lyu F, Bai Y, Li Z, Xu W, Wang Q, Mao J, Wang L, Zhang X, Yin Y, (2017) Self-Templated Fabrication of $CoO–MoO_2$ Nanocages for Enhanced Oxygen Evolution. *Advanced Functional Materials*, 27(34), 1702324.

228. Thomas B, Tang C, Ramírez-Hernández M, Asefa T, (2023) Incorporation of Bismuth Increases the Electrocatalytic Activity of Cobalt Borates for Oxygen Evolution Reaction. *ChemPlusChem*, 88(5), e202300104.

229. Wei B, Wu J, Mei G, Qi Z, Hu W, Wang Z, (2019) $NiCo_2O_4$ nanowire arrays rich in oxygen deficiencies for hydrogen evolution reaction. *International Journal of Hydrogen Energy*, 44(13), 6612-6617.

230. Zhang L, Liu B, Zhang N, Ma M, (2018) Electrosynthesis of Co_3O_4 and $Co(OH)_2$ ultrathin nanosheet arrays for efficient electrocatalytic water splitting in alkaline and neutral media. *Nano Research*, 11, 323-333.

231. Chen Y, Zhao X, Zhang Q, Miao X, Chen Y, Yang W, Pan Q, (2023) Carbon fiber supported Co/Co3O4-embedded N-doped carbon microparticles for efficient overall seawater splitting and oxygen reduction. *International Journal of Hydrogen Energy*, 48(10), 3759-3767.

232. Peng Z, Jia D, Al-Enizi A M, Elzatahry A A, Zheng G, (2015) From water oxidation to reduction: homologous Ni–Co based nanowires as complementary water splitting electrocatalysts. *Advanced Energy Materials*, 5(9), 1402031.

233.   Wang F, Qin X F, Meng Y F, Guo Z L, Yang L X, Ming Y F, (2013) Hydrothermal synthesis and characterization of α-Fe$_2$O$_3$ nanoparticles. *Materials Science in Semiconductor Processing*, 16(3), 802-806.

234.   Zhu X, Zhu Y, Murali S, Stoller M D, Ruoff R S, (2011) Nanostructured reduced graphene oxide/Fe2O3 composite as a high-performance anode material for lithium ion batteries. *ACS Nano*, 5(4), 3333-3338.

235.   Fu G, Li W, Zhang J Y, Li M, Li C, Li N, He Q, Xi S, Qi D, MacManus-Driscoll J L, Cheng J, (2021) Facilitating the Deprotonation of OH to O through Fe^{4+}-Induced States in Perovskite LaNiO3 Enables a Fast Oxygen Evolution Reaction. *Small*, 17(12), 2006930.

236.   Alduhaish O, Ubaidullah M, Al-Enizi A M, Alhokbany N, Alshehri S M, Ahmed J, (2019) Facile synthesis of mesoporous α-Fe$_2$O$_3$@ g-C$_3$N$_4$-NCs for efficient bifunctional electro-catalytic activity (OER/ORR). *Scientific Reports*, 9(1), 14139.

237.   Karuppasamy L, Gurusamy L, Ananan S, Barton S C, Liu C H, Wu J J, (2023) Metal-organic frameworks derived interfacing Fe2O3/ZnCo2O4 multimetal oxides as a bifunctional electrocatalyst for overall water splitting. *Electrochimica Acta*, 449, 142242.

238.   Luo J, Guo W H, Zhang Q, Wang X H, Shen L, Fu H C, Wu L L, Chen X H, Luo H Q, Li N B, (2020) One-pot synthesis of Mn–Fe bimetallic oxide heterostructures as bifunctional electrodes for efficient overall water splitting. *Nanoscale*, 12(38), 19992-20001.

239.   Qayum A, Peng X, Yuan J, Qu Y, Zhou J, Huang Z, Xia H, Liu Z, Tan D Q, Chu P K, Lu F, (2022) Highly Durable and Efficient Ni-FeO$_x$/FeNi$_3$ Electrocatalysts Synthesized by a Facile In Situ Combustion-Based Method for Overall Water Splitting with Large Current Densities. *ACS Applied Materials & Interfaces*, 14(24), 27842-27853.

240.   Hanan A, Lakhan M N, Shu D, Hussain A, Ahmed M, Soomro I A, Kumar V, Cao D, (2023) An efficient and durable bifunctional electrocatalyst based on PdO and Co2FeO4 for HER and OER. *International Journal of Hydrogen Energy*, 48(51), 19494-19508.

241.   Rani B J, Ravi G, Yuvakkumar R, Thambidurai M, (2019) Perovskite BiFeO 3 nanocatalysts for electrochemical water oxidation. *Journal of Sol-Gel Science and Technology*, 91, 247-254.

242.   Yang X, Sun X, Gan L Y, Sun L, Mi H, Zhang P, Ren X, Li Y, (2020) A CoO$_x$/FeO x heterojunction on carbon nanotubes prepared by plasma-enhanced atomic layer deposition for the highly efficient electrocatalysis of oxygen evolution reactions. *Journal of Materials Chemistry A*, 8(30), 15140-15147.

243.   Tan Y, Q Che, Q Li, (2021) Constructing Double-Layer CoP/CeO$_2$–FeO$_x$H Hybrid Catalysts for Alkaline and Neutral Water Splitting. *ACS Sustainable Chemistry & Engineering*, 9(35), 11981-11990.

244.   Huang J, Su Y, Zhang Y, Wu W, Wu C, Sun Y, Lu R, Zou G, Li Y, Xiong J, (2018) FeO x/FeP hybrid nanorods neutral hydrogen evolution electrocatalysis: insight into interface. *Journal of Materials Chemistry A*, 6(20), 9467-9472.

245.   Fu G, Yan X, Chen Y, Xu L, Sun D, Lee J M, Tang Y, (2018) Boosting bifunctional oxygen electrocatalysis with 3D graphene aerogel-supported Ni/MnO particles. *Advanced Materials*, 30(5), 1704609.

246.   Li M, Lei W, Yu Y, Yang W, Li J, Chen D, Xu S, Feng M, Li H, (2018) High-performance asymmetric supercapacitors based on monodisperse MnO nanocrystals with high energy densities. *Nanoscale*, 10(34), 15926-15931.

247.   Jin K, Chu A, Park J, Jeong D, Jerng S E, Sim U, Jeong H Y, Lee C W, Park Y S, Yang K D, Kumar Pradhan G, (2015) Partially oxidized sub-10 nm MnO nanocrystals with high activity for water oxidation catalysis. *Scientific Reports*, 5(1), 10279.

248.   Xu J, Zhang H, Xu P, Wang R, Tong Y, Lu Q, Gao F, (2018) In situ construction of hierarchical Co/MnO@ graphite carbon composites for highly supercapacitive and OER electrocatalytic performances. *Nanoscale*, 10(28), 13702-13712.

249.   Kim J, Heo J N, Do J Y, Chava R K, Kang M, (2019) Electrochemical synergies of heterostructured Fe2O3-MnO catalyst for oxygen evolution reaction in alkaline water splitting. *Nanomaterials*, 9(10), 1486.

250.   Bera K, Karmakar A, Karthick K, Sankar S S, Kumaravel S, Madhu R, Kundu S, (2021) Enhancement of the OER kinetics of the less-explored α-MnO$_2$ via nickel doping approaches in alkaline medium. *Inorganic Chemistry*, 60(24), 19429-19439.

251.   Zhang W, Zong L, Fan K, Cui L, Zhang Q, Zhao J, Wang L, Feng S, (2021) Enabling highly efficient electrocatalytic oxygen reduction and evolution reaction by established strong MnO/Co-support interaction. *Journal of Alloys and Compounds*, 874, 159965.

252.   Han G Q, Liu Y R, Hu W H, Dong B, Li X, Shang X, Chai Y M, Liu Y Q, Liu C G, (2015) Crystallographic structure and morphology transformation of MnO2 nanorods as efficient electrocatalysts for oxygen evolution reaction. *Journal of The Electrochemical Society*, 163(2), H67.

253.   Hao S, Y Yang, (2017) Water splitting in near-neutral media: using an Mn–Co-based nanowire array as a complementary electrocatalyst. *Journal of Materials Chemistry A*, 5(24), 12091-12095.

254.   Cho K H, Seo H, Park S, Lee Y H, Lee M Y, Cho N H, Nam K T, (2020) Uniform, assembled 4 nm Mn3O4 nanoparticles as efficient water oxidation electrocatalysts at neutral pH. *Advanced Functional Materials*, 30(10), 1910424.

255.   Zhang B, Chen H, Daniel Q, Philippe B, Yu F, Valvo M, Li Y, Ambre R B, Zhang P, Li F, Rensmo H, (2017) Defective and "c-disordered" hortensia-like layered MnO x as an efficient electrocatalyst for water oxidation at neutral pH. *ACS Catalysis*, 7(9), 6311-6322.

256.   Tang L, Hu Y, Tang H, Sun L, Jiang H, Wang W, Su H, Hu J, Wang L, Liu Q, (2022) Incorporating Ni-Polyoxometalate into the S-Scheme Heterojunction to Accelerate Charge Separation and Resist Photocorrosion for Promoting Photocatalytic Activity and Stability. *The Journal of Physical Chemistry Letters*, 13(50), 11778-11786.

257.   Ali A, Shah S M, Bozar S, Kazici M, Keskin B, Kaleli M, Akyürekli S, Günes S, (2016) Metal-free polymer/MWCNT composite fiber as an efficient counter electrode in fiber shape dye-sensitized solar cells. *Nanotechnology*, 27(38), 384003.

258.   Gong R, Gao D, Liu R, Sorsche D, Biskupek J, Kaiser U, Rau S, Streb C, (2021) Self-activation of a polyoxometalate-derived composite electrocatalyst for the oxygen evolution reaction. *ACS Applied Energy Materials*, 4(11), 12671-12676.

259.   Stracke J J, R G Finke, (2011) Electrocatalytic water oxidation beginning with the cobalt polyoxometalate [Co$_4$(H$_2$O)$_2$(PW$_9$O$_{34}$)$_2$]$^{10-}$: identification of heterogeneous CoO x as the dominant catalyst. *Journal of the American Chemical Society*, 133(38), 14872-14875.

260.   Zhang L, Ding X, Cong M, Wang Y, Zhang X, (2019) Self-adaptive amorphous Co2P@ Co2P/Co-polyoxometalate/nickel foam as an effective electrode for

electrocatalytic water splitting in alkaline electrolyte. *International journal of hydrogen energy*, 44(18), 9203-9209.

261.   Wang Y, Wang Y, Zhang L, Liu C S, Pang H, (2019) Core–shell-type ZIF-8@ ZIF-67@ POM hybrids as efficient electrocatalysts for the oxygen evolution reaction. *Inorganic Chemistry Frontiers*, 6(9), 2514-2520.

262.   Wang Y, Wang Y, Zhang L, Liu C S, Pang H, (2019) PBA@ POM hybrids as efficient electrocatalysts for the oxygen evolution reaction. *Chemistry–An Asian Journal*, 14(16), 2790-2795.

263.   Abdelkader-Fernandez V K, Fernandes D M, Cunha-Silva L, Fernandes A J, Freire C, (2021) Decorating MOF-74-derived nanocarbons with a sandwich-type polyoxometalate to enhance their OER activity: Exploring the underestimated bulk-deposition approach. *Electrochimica Acta*, 389, 138719.

264.   Dhineshbabu N R, Karunakaran G, Suriyaprabha R, Manivasakan P, Rajendran V, (2014) Electrospun MgO/Nylon 6 hybrid nanofibers for protective clothing. *Nano-Micro Letters*, 6, 46-54.

265.   Balázsi C, Wéber F, Kövér Z, Horváth E, Németh C, (2007) Preparation of calcium–phosphate bioceramics from natural resources. *Journal of the European Ceramic Society*, 27(2-3), 1601-1606.

266.   Harish S, Sabarinathan M, Archana J, Navaneethan M, Nisha K D, Ponnusamy S, Gupta V, Muthamizhchelvan C, Aswal D K, Ikeda H, Hayakawa Y, (2017) Synthesis of ZnO/SrO nanocomposites for enhanced photocatalytic activity under visible light irradiation. *Applied Surface Science*, 418, 147-155.

267.   Ansari M A, N Jahan, (2021) Structural and optical properties of BaO nanoparticles synthesized by facile Co-precipitation method. *Materials Highlights*, 2(1-2), 23-28.

268.   Fadhli M, I Khedher, J M Fraile, (2016) Modified Ti/MCM-41 catalysts for enantioselective epoxidation of styrene. *Journal of Molecular Catalysis A: Chemical*, 420, 282-289.

269.   Kim H J, Kang B S, Kim M J, Park Y M, Kim D K, Lee J S, Lee K Y, (2004) Transesterification of vegetable oil to biodiesel using heterogeneous base catalyst. *Catalysis Today*, 93, 315-320.

270.   Mierczynski P, Ciesielski R, Kedziora A, Maniukiewicz W, Shtyka O, Kubicki J, Albinska J, Maniecki T P, (2015) Biodiesel production on MgO, CaO, SrO and BaO oxides supported on (SrO)(Al 2 O 3) mixed oxide. *Catalysis Letters*, 145, 1196-1205.

271.   Patil P D, S Deng, (2009) Transesterification of camelina sativa oil using heterogeneous metal oxide catalysts. *Energy & Fuels*, 23(9), 4619-4624.

272.   Liu X, He H, Wang Y, Zhu S, (2007) Transesterification of soybean oil to biodiesel using SrO as a solid base catalyst. *Catalysis Communications*, 8(7), 1107-1111.

273.   Manimaran S, Tschentscher R, Pandurangan A, Govindasamy G, (2023) Green and recyclable mesoporous silica supported WO3–ZrO2 solid acid catalyst for biodiesel production by transesterification of Ankol seed oil with methanol. *International Journal of Chemical Reactor Engineering*.

274.   Dehghani S, M Haghighi, (2019) Sono-dispersed MgO over cerium-doped MCM-41 nanocatalyst for biodiesel production from acidic sunflower oil: Surface evolution by altering Si/Ce molar ratios. *Waste Management*, 95, 584-592.

275.　　　Mathimani T, Rene E R, Sindhu R, Al-Ansari M M, Al-Humaid L A, Jhanani G K, Chi N T L, Shanmuganathan R, (2023) Biodiesel production and engine performance study using one-pot synthesised ZnO/MCM-41. *Fuel*, 336, 126830.

276.　　　Basyouny M G, Abukhadra M R, Alkhaledi K, El-Sherbeeny A M, El-Meligy M A, Soliman A T A, Luqman M, (2021) Insight into the catalytic transformation of the waste products of some edible oils (corn oil and palm oil) into biodiesel using MgO/clinoptilolite green nanocomposite. *Molecular Catalysis*, 500, 111340.

277.　　　Al-Saadi A, B Mathan, Y He, (2020) Esterification and transesterification over SrO–ZnO/Al$_2$O$_3$ as a novel bifunctional catalyst for biodiesel production. *Renewable Energy*, 158, 388-399.

278.　　　Perveen F, Farooq M, Ramli A, Naeem A, Khan I W, Saeed T, Khan J, (2022) Levulinic Acid Production from Waste Corncob Biomass Using an Environmentally Benign WO3-Grafted ZnCo$_2$O$_4$@CeO$_2$ Bifunctional Heterogeneous Catalyst. *ACS Omega*, 8(1), 333-345.